Broadband optical characterization of material properties

Abildgaard, Otto Højager Attermann; Dahl, Anders Bjorholm; Larsen, Rasmus

Link to article, DOI:
10.11581/DTU:00000009

Publication date:
2014

Document Version
Publisher's PDF, also known as Version of record

Broadband optical characterization of material properties

Otto Højager Attermann Abildgaard

Kongens Lyngby 2014
COMPUTE-PhD-2014-334

Technical University of Denmark
Department of Applied Mathematics and Computer Science
Building 321, DK-2800 Kongens Lyngby, Denmark
Phone +45 45253351, Fax +45 45882673
compute@compute.dtu.dk
www.compute.dtu.dk COMPUTE-PhD-2014-334

Abstract

Optical inspection of material properties is of great interest to industry because it can perform objective and non-invasive characterisation of large sample quantities. This may be used in various ways to lower production costs and improve product quality. In this thesis the objective has been to develop and investigate the applicability of optical broadband characterization techniques in industrially relevant production process. Both combined broad and high resolution techniques have the potential to provide important information on scattering properties related to particle size distributions, as well as details of the absorption spectrum which relate to chemical composition.

The thesis focuses on two production process from the food industry. The first process is from the dairy industry where discrimination between chemical and structural properties is of importance. To explore the applicability of optical techniques for this purpose, the fermentation of milk into yogurt has been used as a model system. Studies have been conducted on commercially available products, but also of on-line measurement of the fermentation process. The second process is from the aquaculture industry, quantification of the fish feed additive astaxanthin has been investigated. A measurement campaign has been carried out on a series of pellets specially produced for the purpose.

To investigate these process, the following three measurement techniques have been developed and applied. **(I)** A camera based inspection system for spectrally-resolved Static Light Scattering (SLS). **(II)** Photon Time-of-Flight (PToF) spectroscopy, which is a state of the art technique for characterization of turbid media. **(III)** A new hyperspectral imaging system based on full-field illumination by diffuse laser light. This thesis reports on the design and operation of the different measurement techniques together with the necessary theoretical

background for the industrial applications.

For the purpose of milk fermentation this work has demonstrated that the reduced scattering properties of milk change significantly throughout the fermentation process. It has also been shown that the optical inspection methods sense changes to structural properties before any are detected by traditional mechanical rheology. Finally, the developed hyperspectral imaging system was used to quantify the content of astaxanthin in fish feed, and performed at an equal level to a state of the art multi-spectral vision system.

Resume (Danish abstract)

Inspektion af materialers egenskaber baseret på optiske målinger er af stor interesse for industrien, da det kan udføre objektiv karakterisering af store mængder materiale. Dette kan lede til en sænkning af produktionsomkostningerne og forbedring af produktets kvalitet. Formålet med denne afhandling er at udvikle og undersøge anvendelsen af bredbåndede optiske karakteriseringsteknikker i en industriel relevant sammenhæng. Kombinationen af høj spektral opløsning over et bredt dynamikområde kan potentielt give information om spredningsegenskaberne relateret til materiale komposition, og ligeledes detaljer i absorptionsegenskaberne som relater til den kemiske sammensætning.

Afhandlingen fokuser på to produktionsprocesser fra fødevareindustrien. Første proces er fra mejeriindustrien hvor diskriminationen imellem kemiske og strukturelle ændringer er vigtig. For at udforske optiske målemetoders evne til dette formål studeres mælks fermentering til yoghurt som et model system. Studierne bliver udført på kommercielt tilgængelige prøver samt on-line målinger af fermenteringsprocessen. Den anden proces er fra akvakulturindustrien. Her undersøges mulighederne for at kvantificere mængden af astaxanthin som tilføjes fiskepiller. En laboratoriekampagne er udført på piller produceret til studiet.

Til at studere disse processer er følgende tre teknikker udviklet og anvendt. (I) Et kamera baseret inspektionssystem for spektralt opløst statisk lysspredning (SLS). (II) Tidsopløst spektroskopi, som er en anerkendt teknik til karakterisering af lysspredende materialer. (III) Et nyt hyperspektralt visionsystem basseret på diffust laserlys. I denne afhandling reporteres deres design og anvendelse sammen med den nødvendige baggrund for de industrielle produktionsprocesser.

Studierne at mælkefermenteringsprocesserne viser at de reducerede spredningsegenskaber af mælken ændres signifikant igennem mælkefermenteringsprocessen. Det demonstreres også at de optiske målinger kan detektere ændringer tidligere end ved inspektion med traditionel reologi. Som sidste resultat har det hyperspektrale visionsystem været anvendt til inspektion af fiskepiller for prædiktion af astaxanthinkoncentrationen, og det er demonstreret at disse målinger kunne udføres på niveau med kommercielt tilgængelige multispektrale visionsystemer.

Preface

This thesis was prepared at the Department of Applied Mathematics and Computer Science at the Technical University of Denmark (DTU) in partial fulfilment of the requirements for a Ph.D. degree in engineering.

The research was conducted at the Department of Applied Mathematics and Computer Science, DTU; at the Department of Physics, Lund University; and at NKT Photonics A/S. The research was conducted in the period June 15$^{\text{th}}$ - March 27$^{\text{th}}$ 2014. During this period three months were spent on leave of absence at NKT Photonics A/S working as optical design engineer, and three months and two were spent on paternity leave.

The thesis deals with development of optical broadband characterisation methods for quantifying the structure and chemical properties of turbid samples. The thesis consists of five selected peer-reviewed papers and a technical report.

This work was financed by the Centre for Imaging Food Quality project, which is funded by the Danish Council for Strategic Research (contract no 09-067039) within the Programme Commission on Health, Food and Welfare. The Ph.D. project was supervised by

- Anders B. Dahl, Associate Professor, Department of Applied Mathematics and Computer Science, Technical University of Denmark. 2800 Kgs. Lyngby, Denmark.
- Carsten L. Thomsen, Product Development Manager, NKT Photonics A/S. Blokken 84. 3460 Birkerød, Denmark.

Lyngby, 27-March-2014

Otto Højager Attermann Abildgaard

Publications

Papers included in the thesis

[A] **Supercontinuum Light sources for Hyperspectral Subsurface Laser Scattering.** *O. H. A. Nielsen, A. L. Dahl, R. Larsen, F. Møller, F. D. Nielsen, C. L. Thomsen, H. Aanæs and J. M. Carstensen.* Published: Proceedings of Scandinavia Conference on Image Analysis 2011 as part of the section "Application for Food Inspection", 2011 ([1])

[B] **Monitoring Optical Changes during Milk Acidification using Hyperspectral Diffuse Reflectance Images.** *J. L. Skytte, O. H. A. Nielsen, U. Andersen, F. Møller, J. M. Carstensen, A. L. Dahl and R. Larsen.* Submitted: Journal of Spectral Imaging, 2014 ([2])

[C] **Non-invasive assessment of dairy products using spatially resolved diffuse reflectance spectroscopy.** *O. H. A. Nielsen, F. Kamran, A. B. Dahl. J. L. Skytte, F. D. Nielsen, C. L. Thomsen, P. E. Andersen, R. Larsen and J. R. Frisvad.* Submitted: Applied Spectroscopy. ([3])

[D] **Spectral characterizations of dairy products using photon time-of-flight spectroscopy.** *O. H. A. Nielsen, A. A. Subash, F. D. Nielsen, J. L. Skytte, S. Andersson-Engels and D. Khoptyar.* Published: Journal of Near Infrared Spectroscopy, 2013 ([4])

[E] **Evaluation of the ID220 single photon avalanche diode for extended spectral range photon time of flight spectroscopy.** *O. H. A. Nielsen, F. D. Nielsen, C. L. Thomsen, S. Andersson-Engels, D. Khoptyar.* Technical report: Published, 2014 ([5])

[F] **Hyperspectral imaging based on diffused laser light for prediction of astaxanthin coating concentration.** *M. G. Ljungqvist, O. H. A. Nielsen, S. Frosch, M. E. Nielsen, L. H. Clemmensen and B. K. Ersbøll.* Published: Machine Vision and Applications, 2014 ([6])

Additional journal publications

1. **Spectroscopic analysis of pharmaceuticals in the close NIR range using PToF spectroscopy.** *F. Kamran, O. H. A. Nielsen, A. Spaé n, O. Svensson, J. Johansson, S. Anderson-Engels, P. E. Andersen, D. Khoptyar.* Submitted: Applied Spectroscopy, 2014 ([7])

2. **Motion analysis of optically trapped particles and cells using 2D Fourier analysis.** *M. V. Kristensen, P. Ahrendt, T. B. Lindballe; O. H. A. Nielsen, A. P. Kylling, H. Karstoft, A. Imparato, L. Hosta-Rigau, B. Stadler, H. Stapelfeldt and S. R. Keiding.* Published: Optics Express, vol: 20, issue: 3, pages: 1953-1962, 2012 ([8])

3. **Profiling of micrometer-sized laser beams in restricted volumes.** *Y. Miroshnychenko, O. Nielsen, A. Thorsen, and M. Drewsen.* Published: Applied Optics, Vol. 51, Issue 13, pp. 2341-2345, 2012 ([9])

Additional conference contributions

1. **Broadband photon time of flight spectroscopy: advanced spectroscopic analysis for ensuring safety and performance of pharmaceutical tablets.** *F. Kamran, O. H. A. Nielsen, S. Andersson-Engels, D. Khooptyar.* Published: Asia Communications and Photonics Conference, 2013 ([10])

2. **Wide-bandwidth photon time of flight spectroscopy for biomedical and pharmaceutical applications.** *D. Khoptyar, A. A. Subash, M. Saleem, O. H. A. Nielsen, and S. Andersson-Engels.* Published: NIR 2013 - 16th International Conference on Near Infrared Spectroscopy, 2013 ([11])

3. **Decomposition of Diffuse Reflectance Images – Features for Monitoring Structure in Turbid Media.** *J. L. Skytte , O. H. A. Nielsen, U. Andersen, J. M. Carstensen, A. Dahl, R. Larsen, F. Møller, F. Kamran, J. Frisvad.* Published: InsideFood Symposium : Book of proceedings, 2013 ([12])

4. **Monitoring structure development in milk acidification using diffuse reflectance profiles.** *J. L. Skytte, U. Andersen, F. Møller, O. H. A. Nielsen, J. M. Carstensen, A. B. Dahl and R. Larsen.* Published: Conference abstract in proceedings, Part of: Proceedings of the 14th Food Colloids Conference, 2012 ([13])

5. **Regression and Sparse Regression Methods for Viscosity Estimation of Acid Milk From it's SlS Features.** *S. Sharifzadeh, J. L. Skytte, O. H. A. Nielsen, B. K. Ersbøll and L. K. H. Clemmensen.* Published: Article in proceedings, Presented at: 19th International Conference on Systems, Signals and Image Processing (IWSSIP 2012) ([14])

6. **In Depth Analysis of Food Structures, Hyperspectral Subsurface Laser Scattering** *O. H. A. Nielsen, A. L. Dahl, R. Larsen, F. Møller, , F. D. Nielsen, C. L. Thomsen, H. Aanæs and J. M. Carstensen.* Published: Proceedings of Scandinavian workshop on imaging food quality, Ystad, 2014 ([15])

Acknowledgements

From the Department of Applied Mathematics and Computer Science at the Technical University of Denmark, I thank my main supervisor, Associate Professor Anders B. Dahl, for his persistent optimism and his assistance with the scientific papers. Many thanks are owed to Professor Rasmus Lassen for his support which guided the direction of the scientific work on raising the funding for the CIFQ project. Associate Professor Jeppe Frisvad provided excellent knowledge of optical modelling and light-matter interactions in general; I am truly thankful for his assistance. A tremendous thanks to both Ph.D. student Jacob L. Skytte and Dr. Martin Ljungqvist, both of you have truly defined the direction of my work and have been a great pleasure to collaborate with. Thanks also to Associate Professor Line Clemmensen for her excellent teaching and guidance, both during the course Multivariate Data Analysis and the continuing discussion on different aspect of data analysis.

From the National Food Institute at the Technical University of Denmark, I thank Associate Professor Stina Frosch for her guidance on the research into fish feed coating. Likewise, I would like to thank Heidi O. Petersen for providing access and assistance during the measurement campaigns conducted on milk fermentation.

From NKT Photonics A/S, a great token of appreciation to co-supervisor Carsten L. Thomsen for his trust and encouragement throughout the Ph.D. The warmest thanks to Frederik D. Nielsen for teaching, and for deepening my conceptions about on research. Your openness and support have been highly appreciated, and I have always felt that all options were open. I am deeply grateful for your discussions and hands-on experience with all the different aspects of the super-

continuum sources which I have encountered. Many thanks to Mark Denninger and Kristian Nielsen for their assistance on the filtering unit; they provided great practical experience. For assistance on integrating the supercontinuum units in the different measurement routines for SLS and PToF spectroscopy I thank Erik Thomsen.

From Department of Physic at Lund University, many thanks to Prof. Stefan Anderson-Engels for hosting my external stay in the PToF spectroscopy group. Here I enjoyed the teaching on physical models for atom-light interaction by Research Associate Dr. Dmitry Khoptyar. Dmitry and Ph.D. student Arman Ahamed Subash educated me in the use of the PToF spectrometer, knowledge which has been a highly appreciated, even after the duration of my external stay. Arman is especially thanked for his exceedingly hard work on the measurement campaign and his participation in development of the algorithm for the measurement routines.

Lastly, thanks to the staff at Videometer A/S, especially Senior R&D engineer Kåre L. Jensen for his assistance with integrating the VM lab software and supercontinuum laser systems. I thanks software developer Cristian Gleerup for his assistance on interfacing the camera from JAI. Lastly, I thank Associate Professor Jens Michael Carstensen for input on the SLS measurement technique.

Contents

Abstract **i**

Resume (Danish abstract) **iii**

Preface **v**

Publications **vii**

Acknowledgements **xi**

I Summation **1**

1 Introduction **3**
1.1 Aims of the thesis 4
1.2 Motivation 5
1.3 Thesis outline 6
1.4 Overview of scientific papers 8
1.5 Abbreviations 10

2 Applications for optical inspection in industrial production process **13**
2.1 Research on measurement techniques 14
2.2 Dairy production 15
2.3 Aquaculture industry 20

3 Light-Matter Interaction **25**
3.1 Phenomenology 26
3.2 Modelling light transport 36

3.3 Solutions to light propagation 42
3.4 Combining the benefits of time-resolved and static measurements 46

4 Measurement design and analysis of data 49
4.1 Design of experiments 50
4.2 Data exploration 52
4.3 Regression methods 54
4.4 Combining broadband characterisation and sparse quantification 56

5 Instruments for broadband characterization 59
5.1 Supercontinuum generation 60
5.2 Wavelength filtering and selection 62
5.3 Static light scattering vision system 70
5.4 Photon time-of-flight spectroscopy 84
5.5 Hyperspectral camera 90

II Summary of scientific contributions 97

6 Scientific contribution based on SLS 101

7 Scientific contribution in PToF spectroscopy 105

8 Scientific contribution within hyperspectral imaging 109

9 Discussion of methods for in-line monitoring of milk fermentation 111

10 Conclusion 121

A Supercontinuum Light sources for Hyperspectral Subsurface Laser Scattering 125

B Monitoring Optical Changes during Milk Acidification Using Hyperspectral Diffuse Reflectance Images 139

C Non-invasive Assessment of Dairy Products Using Spatially Resolved Diffuse Reflectance Spectroscopy 161

D Spectral characterizations of dairy products using photon time-of-flight spectroscopy. 185

E Evaluation of the ID220 single photon avalanche diode for extended spectral range of photon time-of-flight spectroscopy 199

F Hyperspectral imaging based on diffused laser light for prediction of astaxanthin coating concentration 217

Part I

Summation

Chapter 1

Introduction

The use of material characterization by means of optical properties has expanded drastically over the previous three decades. New inspection methods continue to emerge, largely driven by improvements in light source and detector technology. Such inspection methods are often developed in the field of biomedical optics, and as the technology matures they also become applicable to the industrial sector. For industry, material characterisation can be used for quality assurance of raw materials or end products, and, just as importantly during actual production. Material characterisation adds value to companies in multiple ways. For one ting, it allows cost reductions. This can be by documenting the quality of purchased raw materials, or by validating the quality of final products. The ability to make high quality ingredients or products only has value if it can be documented. Cost may also be reduced by enabling a more well-controlled production process; either by rejecting products at an early stage of production, or by compensating for any unintended performance issues. Along the same lines, material characterisation may enable innovation of the production process, which allows the creation of new products.

Material characterization in general makes use of many different measurement techniques, relying on chemical, electrical, or physical properties. In comparison to other techniques, optically-based inspection excels because it may be implemented in a non-invasive and non-contact way. This facilitates important properties such as labour-free inspection, analysis of large quantities of samples,

and automatic feedback to the production process in real time.

The interaction between light and matter gives rise to a plethora of optical effects, and research is necessary to investigate their individual applicability for a specific aspect of a given production process. As part of this instrumentation and data evaluation go hand-in-hand, as even measurements of the proper optical properties may be corrupted by excessive noise in a real industrial implementations.

1.1 Aims of the thesis

The research objectives for the three inspection techniques illustrated in Figure 1.1 may be summarised as.

- Design nd construct new optical research platforms, and characterise their performance.
- Investigate and combine new models for data evaluation based upon statistical and physical interpretation of light-matter interactions.
- Evaluate the combination of instrumentation and analysis techniques in measurement campaigns, simulating the actual production process, as close as possible.

In collaboration with partners from industry, two production process from within the dairy and aquaculture industries were selected as the focus of this Ph.D. project.

Within dairy production, the acidification of milk into yogurt was investigated, with the objective of quantifying the development of the gel network. The actual fermentation process is transferable to other applications, such as the manufacture of cheese and cream cheese. These products are homogeneous, and the measurements are carried out by illuminating a small point on the sample. The optical properties were then evaluated by investigating how the light spreads though the sample to other areas. This was conducted using two measurement techniques. The first uses spatially resolved measurements, and is illustrated in Figure 1.1(a). Here, images of the light propagation from the entry point to other areas of the sample are captured. The other measurement technique measures the speed with which the light propagates though the sample: the principle is illustrated in Figure 1.1(b). Here the light may take different paths, which broadens it is temporal profile.

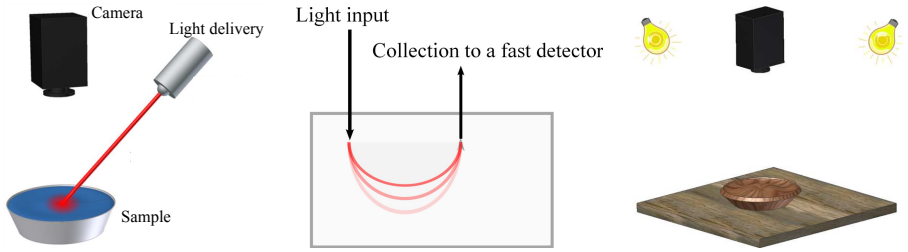

(a) **SLS**. Measurement of homogenous samples using spatially resolved reflectance.

(b) **PToF**. Measurement of homogenous samples using time-resolved reflectance.

(c) **Hyperspectral Imaging**. Illumination of a hetrogeous sample using full field illumination.

Figure 1.1: *Illustrations of the three measurement techniques used and developed during this Ph.D. project.*

The second application was quantification of the carotenoid astaxanthin in fish feed, where it is used as an additive which primarily affects the colour of the fish. As the pellets are heterogeneous materials, and only bulk values of multiple pellets were of interest, the analysis required illumination of larger areas so-called full field illumination, as is illustrated in Figure 1.1(c). The measurement problem is more similar to the classical art of spectral imaging, and a parallel study was conducted with an industrial multispectral vision system.

Evidently, the two applications span very different aspects of both measurement modality and the relevant optical properties. One focusses on structural properties of homogeneous samples, and the other on chemical composition in heterogeneous samples.

1.2 Motivation

The motivation for this thesis work was to develop and apply optical inspection methods with the potential to improve industrial production process, leading to less material waste and higher product quality. Furthermore, the development of new sensor technology may contribute to companies' ability to compete based on innovative production.

With the scientific motivation of making relevant research on novel optical instrumentation for industry, collaboration with external partners has been es-

sential. These key contributors are summarised in Figure 1.2. The contents of the thesis are largely the results of successful collaboration with these partners. Many, but not all, of these partners are part of the Centre for Imaging Food Quality (CIFQ) which financed this Ph.D. project. The collaboration has allowed the thesis work to cover many different aspects from instrument design to analysis of actual measurements campaigns.

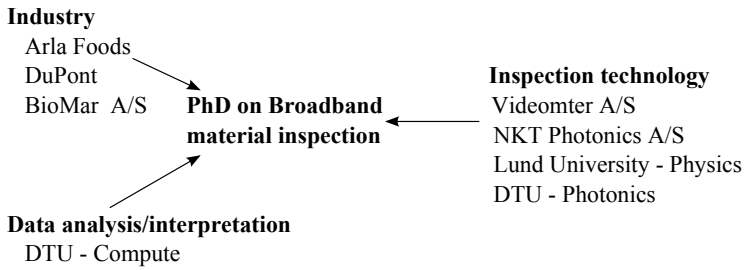

Figure 1.2: *Key collaboration partners who have influenced the work and contents of the thesis.*

The collaboration with industrial partners has succeeded in combining scientific research and industrial relevance. The measurement techniques of Videometer A/S have been the starting point for this Ph.D. project, and their capabilities have been investigated. NKT Photonics A/S have assisted in adapting the supercontinuum light source to the different measurement platforms developed during the Ph.D. project. The Department of Physics at Lund University have contributed with state of the art inspection technology on scattering (turbid) media, which enabled quantification of physically-based optical properties from the dairy samples. Lastly, Department of Photonics at DTU participated in transferring the measurements of physically-based optical properties to camera-based non-contact inspection using the SLS instrument.

1.3 Thesis outline

The thesis consist of two parts. Part I provides the foundation for reading the papers which are compiled in the appendix. As the thesis spans multiple scientific areas, single chapters are devoted to each of the topics illustrated in Figure 1.2. An extra chapter is include on light-matter interactions. Part II gives a summary of the scientific contributions for the different measurement techniques illustrated in Figure 1.1. A final concluding chapter is also provided.

Reading flow It is the intention that the thesis should be read from beginning

to end. Subsequently, the papers in the appendix may be read as individual contributions without loss.

The scope of the individual chapters is briefly outlined below:

Part I - Summation

Chapter 1 provides an introduction to the thesis, describing its aims within the application areas of dairy and fish feed production.

Chapter 2 describes the motivation for the development of both equipment and data analysis for industrial applications. First, a short introduction to dairy production is given, describing the aim of the instrumentation. The key criteria for an inspection instrument are sketched. Following this, the motivation for quantification of pellet coating in fish feed production is given.

Chapter 3 gives a description of light interactions with materials, with a focus on materials which scatter light. It introduces the background for the numerical models used for interpretation of the measurement data from the SLS and time-resolved measurement techniques.

Chapter 4 introduces the methodology of the experimental design and multivariate data analysis. These are key components in the interpretation of the data. This chapter gives a description of how to perform regression on sparse data, together with a description of supervised and unsupervised methods.

Chapter 5 gives a description of the instruments developed and used in the different publications. The chapter starts with a description of the supercotinuum light source and spectral filtering units which have been used for the majority of the work. Following this, different instruments for material characterization are presented. This equipment include the SLS instrument developed at DTU, and the PToF spectrometer used at Lund University. Finally, the system using full field illumination by diffused laser light which has been constructed at DTU is presented.

Part II - Summary of scientific contributions

Chapter 6 provides a summary of the combined work conducted using static light scattering, covering the contents of paper A, B and C. The focus with this measurement platform has been on dairy inspection.

Chapter 7 gives a summary on the work with time-resolved measurements. Paper D provides the first broadband characterisation of dairy products with an analysis technique from diffuse optical spectroscopy. Paper E addresses the possibility of extending the spectral range of the instrumentation used in paper D using a newly available Single Photon Avalanche Diode (SPAD).

Chapter 8 summarises the development of the instrument for hyperspectral imaging with diffused laser light together with the results from this instrument presented in paper F.

Chapter 9 is a comparison of the optical properties of dairy products deduced from PToF spectroscopy and SLS techniques.

Chapter 10 gives a combined conclusion of the scientific work presented in this thesis.

1.4 Overview of scientific papers

Figure 1.3 provides an overview of the scientific work presented in this thesis. The scientific papers which are included are arranged in relation to their measurement technique and the time they were written. Part of the work on SLS was published using the knowledge obtained by studying the optical properties of dairy products during my external stay at Lund University. Likewise, the paper on using the supercontinuum generated light for a vision system with directional illumination benefited from the technical knowledge about instrument interfacing developed in the first paper on SLS.

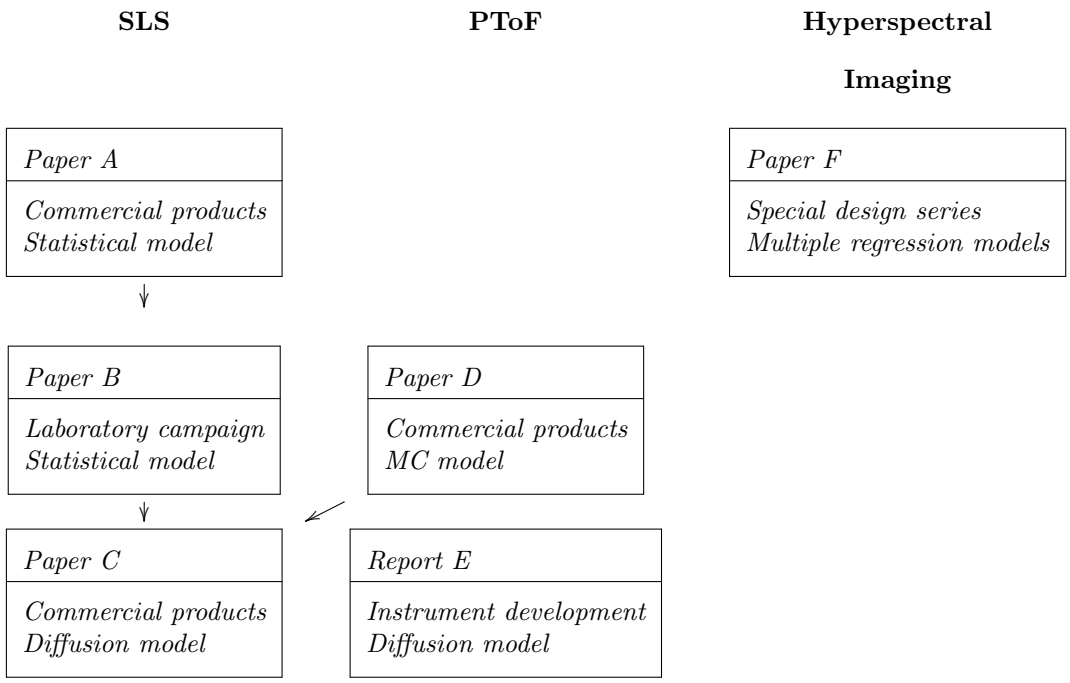

Figure 1.3: *Visualization of how the papers relate.*

1.5 Abbreviations

All abbreviations are spelled out the first time they are used. As the papers compiled in the appendix are intended to be readable individually the abbreviations are also spelled out in each paper when used for the first time. The following list provides a single section where the reader may find all of the abbreviations used in this thesis.

Abbreviations

ADC Analog-to-Digital Converter

ANOVA Analysis of Variance

AOTF Acousto-Optical Tunable Filter

CFD Constant Fraction Discriminator

CIFQ Centre for Imaging Food Quality

DDS Direct Digital Synthesizer

DE Diffusion Equation

DLS Dynamic Light Scattering

DTU Technical University of Denmark

DWS Dynamic Wave Spectroscopy

EN The Elastic Net

FDS Fiber Delivery System

FWHM Full Width at Half Maximum

HDR High Dynamic Range

HPLC High Performance Liquid Chromatography

IRF Instrument Response Function

LED Light Emitting Diode

MANOVA Multivariate analysis of variance

MFP Mean Free Path

NA Numerical Aperture

NIR Near Infra-Red

NIST National Institute of Standards and Technology

OIR Oblique Incidence Reflectometry

OLS Ordinary Least Squares

PCA Principal Component Analysis

PCF Photonic Crystal Fibre

PLS Partial Least Square

ppm parts pr. million

PToF Photon Time-of-Flight

RF Radio Frequency

RTE Radiative Transfer Equation

SAOR Small Amplitude Oscillatory Rheology

SEP Standard Error of Prediction

SLS Static Light Scattering

SPAD Single Photon Avalanche Diode

TAC Time-to-Amplitude Converter

TCSPC Time-Correlated Single Photon Counting

ToF Time-of-Flight

TR Time Reference

UHT Ultra-high Temperature Treatment

WMCL White Monte Carlo Light

Chapter 2

Applications for optical inspection in industrial production process

This chapter serves as an introduction to those aspects of the application of the instrument design and the production process which have been investigated. As the focus of the Ph.D. project has been to investigate new measurement modalities for process inspection, the considerations addressed here concerning the design of each instrument have been essential. For this reason, the first topic is a general discussion of how instrument design affects the measurement data. Following this, the two application areas are discussed, starting with the dairy industry and followed by aquaculture. For each of the production processes some relevant optical inspection techniques are discussed. For dairy production this includes other measurement techniques, largely based on optical probes. For the aquaculture industry this consists of a description of hyperspectral imaging. For both applications, the prospects for new optical inspection techniques are summarised at the end of their respective section so as to give a clear formulation of the desired properties of the inspection technology from a research point of view.

2.1 Research on measurement techniques

Before looking into the details of the individual industrial applications, it is instructive to consider the inspection techniques in a more general framework, as is illustrated by Figure 2.1. Here the measurement process truncates the amount of information which is available. For the present work, the focus is on optical inspection, therefore the process which is inspected should have some direct or indirect influence on how the sample interacts with light. More specifically, it is important to consider whether the optical changes are expressed as changes in absorption, scattering florescences, or some other effect. Making the link between changes in the sample and a measurable optical property is critical to create a successful inspection technique. For this reason, it is important to focus the development of each measurement technique only on cases where it may be applicable. As a result the spot illumination methods (SLS and PToF) have only been applied to homogeneous samples. Similarly full field illumination was only applied to heterogeneous samples.

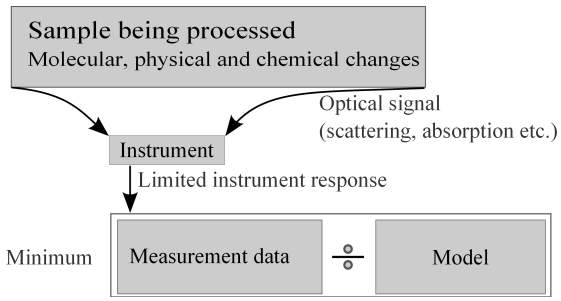

Figure 2.1: *Conceptual drawing of the information reduction process, starting in the real world and ending with final evaluation of some optimal model from the measured data.*

When appropriate instrumentation and measurement technique has been assigned to a given process, the next challenge is to optimize the instrument design for that specific application. In many ways this entails quantification of the Instrument Response Function (IRF), to ensure that the sample characteristics are resolved. The limitations of an instrument are always seen in relation to the model, which is applied afterwards. The length scale for the different optical phenomena forms the topic of Section 3.2.
To make these discussions more concrete, the following aspects were considered during instrument development for the three platforms. For the SLS instrument the field of view was investigated to include measurement characteristics of the reflectance profiles' asymmetric shape and speckle structure, which can only be quantified close to where the light enters the surface. For PToF, the finite time

response of the detector and illumination system was considered. Lastly, for the diffused laser light platform, the homogeneity of the illuminated area was investigated. The objective here was to ensure that the structure of the illuminating diffuse light was smaller than the pellets under investigation.

2.2 Dairy production

Dairy products are consumed globally and often in processed forms such as yoghurt, cheese, cream cheese, or milk powder. However, because milk is not a unique composition of simple chemical constituents, but a complex emulsion displaying biological diversity, control and standardisation is essential to maintain high product quality[16].

Although this thesis is focused on the formation of yoghurt gels, this has been used as a model system, and it is intended that the technique should be transferable to other forms of dairy production. The long term objective with the present work is to investigate and develop optically-based techniques which can measure the structural properties not covered by existing methods such as rheology.
The development of new sensors may therefore provide added value for dairy production in the following ways: **I** Inspection of other production process which also rely on a time-critical fermentation process, such as cheese-making [17]. **II** Reduction of the energy consumption of dairy plants. A typical mass involved in the industrial production of yoghurt is ~ 200 tonne per day. As the production requires both heating and cooling of the dairy goods, technology which reduces the time for the individual steps may also reduce energy consumption. **III** To improve the transfer of dairy production from one plant to another. Cheese in particular is highly dependent on the specific bacteria culture at a particular plant, but yoghurt may also experience variation because of differences in milk composition or bacteria culture. New sensor technology may form part of the characterisation, which will ease production transfer and allow more uniform production. **IV** Product innovation. For examples, there is a drive to reduce the fat content in food products. The low fat products exhibit a higher degree of syneresis [18] but may also have the unintended sandy mouth feel of a yoghurt [19]. New sensor technologies, able to quantify structural properties, could form part of this product innovation process. **V** Lastly the availability of cheap sensors could be used for quality control of the auxiliary equipment such as pumps, piping and stirring instruments. Here cheap on-line measurement at multiple sites may give early warnings of equipment wear or contamination which might damage the gels.

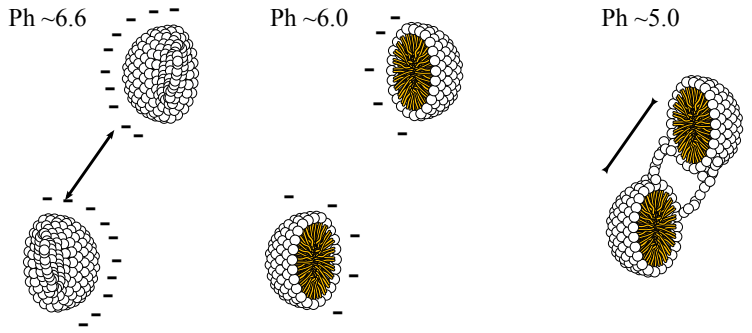

Figure 2.2: *Illustration of the casein micelles (protein) during milk acidification, starting as repulsing spheres which open and finally aggregate.*

2.2.1 Milk fermentation

This section describes the main steps in the process of milk fermentation into yoghurt. The description is for production of stirred yoghurt, and a more detailed review of the production process and the impact of the individual steps is given by Lee and Lucey [20]. The production chain starts with standardization of the milk, which entails preheat treatment and homogenization. After this preprocessing, the milk temperature is raised and the starter culture is added. This begins the actual fermentation process.

At this initial stage, the milk's fat and protein are suspended in the water. The casein (which is a protein) is amphipathic and is combined in clusters as a micelle with a hydrophilic exterior. Because the of the hydrophilic surface, the micelles repulse each other. The size of these micelles is $\sim 50 - 600$ nm[21], in comparison the fat globules is $0.1 - 10$ μm. During the fermentation process the pH value of the milk drops, as the bacteria produce acid. The pH of the milk changes the surface charge on the micelles. When the pH of the milk becomes lower than ~ 6.0 the electrostatic charge on the micelles' exterior starts to decrease, and the repulsion between the micelles consequently also decreases. Simultaneously, the micelles begin to open. For the opened micelles the inner structure may attract other micelles, which cause an aggregation into chain-like structures. This structure constitutes the gel on a microscopic scale. This process is captured in a sequence of confocal microscopy images are shown in Figure 2.3(a), where the white dots are the protein. The black void in between is largely filled with fat and water. The aggregation of the micelles also changes the viscosity of the samples, which was measured by Small Amplitude Oscillatory Rheology (SAOR) in paper B. A typical development of the pH and rheology is presented in Figure 2.3(b). The development of structure is not given

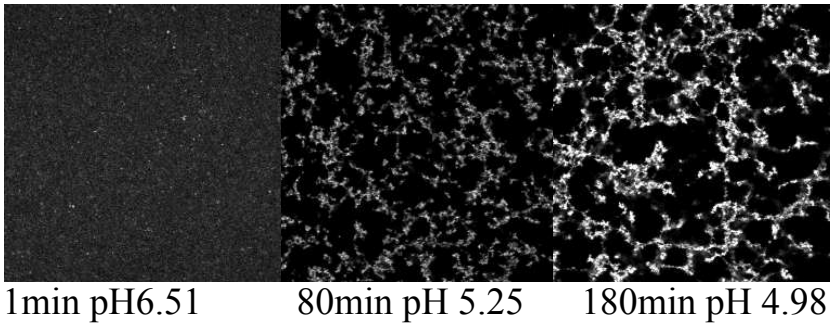

(a) Confocal microscopy images of protein structure during skimmed milk acidification by GDL. Recreated from Auty *et al.* [23].

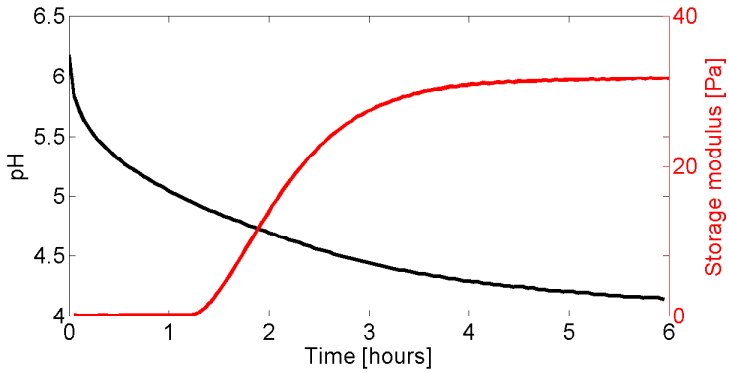

(b) Time development of viscosity and pH during GDL acidification from paper B, the measurements starts a minute after the addition of GDL, which explains the lower ph ($\sim$ 6pH) in the start.

Figure 2.3: *Changes in milk structure during an acidification process with GDL to yoghurt.*

uniquely by the development of the pH [22], but it depends upon temperature and pretreatment, among other factors. The casein forms a gel, which may be quantified as "particles". However, this will not reflect the actual structure of the sample [20].

The final gel has a complex microstructure form by the protein network, which affects the viscosity and water mobility. The microstructure, as described by Bijnen *et al.* [24], is an important part of the consumers perception of the gel's "mouthfeel" and "creaminess" [25].

2.2.2 Optical quantification of structure formation

A comparison of the development of an optical signal with classical analysis methods for inspection of milk fermentation is reproduced in Figure 2.4(a) taken from O'Callaghan*et al.* [26]. The Gelograph (Gel Instrumente AG, Oberuzwil, Switzerland) and TxPro (Zellweger Analytics SA, Emerainville, France) are both transmission sensors, while CoAguLite (Tetra Pak, Lausanne, Switzerland) measures reflection. It is evident that some optical changes occur together, and that they also do so before the changes detected by rheology. This suggests, that new information on the fermentation process may be obtained if the gel's optical properties are also characterised. Optical inspection systems have been described which focus on total reflectance measurements [27]. Based on such systems, the curd cutting time and curd composition during cheese production have been investigated [17]. A detailed description of the time development of the optical signals during cheese formation is obtained, and the optical changes take place sooner than those seen in rheology [28]. Similar work has been conducted on cottage cheese [29].
These optical sensors (Gelograph, TxPro and CoAguLite) are commercially available technologies for inspecting the fermentation process, and rely on quantifying **light attenuation** by the sample. These methods typically rely on fibre probes, and they quantify only light attenuation, often at a single wavelength. Work have been conducted presented for broadband inspection by Mateo *et al.* [30], and also in the NIR wavelength range by Saputra *et al.* [31]. Because the measurements detect a static light reflection, and are performed with a single detector fibre, it is not possible to discriminate whether the light is attenuated by light scattering or by absorption.

Another optical inspection technique is to quantify the water mobility. This is performed by Dynamic Light Scattering (DLS) and Dynamic Wave Spectroscopy (DWS). In this technique, the movement of the sample's particles induces a Doppler shift which can be detected as **speckle** on a detector. Additional details of the phenomenon are given in section 3.1.4. The technique is used in the Rheolight (NTS Optel, Nijmegen , The Netherlands), a commercially available instrument which has been applied to dairy inspection. A demonstration of DLS for characterization of milk renneting has been reported by Alexander and Dalgleish [33].

As the particles aggregate during acidification another approach to quantify the process may be by monitoring the particle size distribution. This is possible using the light **diffraction or directionality of scattering process** which is performed in the instrument Mastersizer 3000 (Malvern, United Kingdom). The diffraction process is described as a single scattering phase function in this thesis. However, this technique does rely on light only exhibiting a single scattering

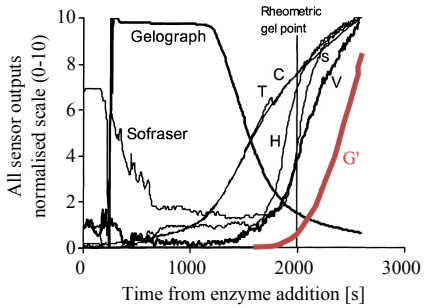

(a) *Comparison of the response of the optical sensors Gelograph, TxPro(T) and CoAguLite (C) with rheology (G') presented by O'Callaghan* et al. *[26]*

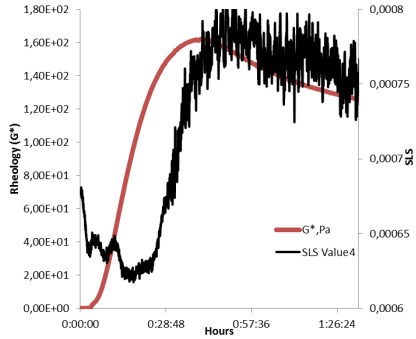

(b) Time development of optical and rheological properties as presented by Møller and Carstensen[32]

Figure 2.4: *Examples of measurements during milk fermentation for different optical and rheological instruments. In both figures the rheological development is marked in red.*

event, and therefore require dilution of milk and yoghurt samples. It is thus not suitable for quantifying the acidification process in-line. Furthermore, as stated by Lee and Lucey [20] the dilution of fermented milk products can change the particle size distribution or can even be responsible for creating it. For this reason, the measurements do not reflect the actual properties of the samples as intended. Some work on the technology has, however, been conducted on milk gels [34].

An alternative approach is taken by Møller and Carstensen [32, 35] using camera-based inspection of SLS. The time development of the optical signal in relation to rheology is reproduced in Figure 2.4(b). The results show some promising correlation between the optical and rheological properties.

2.2.3 Prospects for new optical inspection methods in the dairy industry

In summary, different optical interactions may be relevant for quantification of the acidification process. The techniques discussed in this section quantify the light attenuation, speckle properties and scattering directionality. During the course of this Ph.D.,the camera based measurement modality presented by Carstensen *et al.* [32] has been used as the foundation for the present SLS in-

strument. Camera based inspection may be advantageous in two ways. First, camera based inspection expands the optical characterization of the sample. The measurement can be designed so that it is possible to quantify all of the interactions mentioned before. The SLS technique may thus provide more information than these instruments individually. Furthermore, a combination with a wavelength tunable light source, i.e. the combined supercontinuum system and Acousto-Optical Tunable Filter (AOTF) resolves the wavelength dependence of the interactions. The optical phenomena are the topic of chapter 3, where the requirements for resolving the different optical effects are explained. Secondly, a camera based measurement has two significant features relevant for in-line measurement techniques. The measurements are performed in reflection mode, making it possible to quantify the optical properties independently of the sample volume. Large volumes prevent measurements in transmission mode. Furthermore, the measurements can be conducted without sample extraction and dilution. This Ph.D. has focused on the creation of the SLS instrument, and the quantification of light attenuation and its wavelength dependence. The quantification of speckle and phase function properties is presented in the Thesis by Skytte [36].

2.3 Aquaculture industry

Aquaculture is the farming of fish, water plants or molluscs contained in a controlled environment. Fish in particular form a significant part of our nutrition, and while global landings of openwater fish are stalling, aquaculture continues to grow [1]. For Denmark, the main breed is the trout [2]. An important part of consumer's perception of the quality of the trout is its colour [37, 38, 39]. In nature the trout flesh becomes reddish due to the natural occurrence of the colour pigment astaxanthin in its food. To obtain a similar colour for farmed trout, a pigment is added to the feed. For the fish farm, the amount of astaxanthin must be sufficient to ensure a proper colour of the flesh. As a counterweight, the fish feed producer desires a low content to reduce the production cost. Fore this reason, a need arises for validating the absolute content of astaxanthin in a convenient way during production.

[1] www.fao.org/fishery/statistics/en
[2] www.mst.dk/English/Industry/aquaculture/

2.3.1 Fish feed production process

Fish feed is produced on large scale by an extruder similar to that of Corn flakes. This creates small cylindrical pellets and the fish oil, which contain astaxanthin, is added afterwards in a rotating barrel, through which the pellets are rolled. A complication of the production process is that the pellets are not produced in a constant pace. During production, the holes in the extruder's mask start to fill and block, which affects the production speed of the pellets. For this reason, the flow of fish oil must be adjusted during the production process. The desire from industry is therefore to have a feedback loop, which quantifies the pellets oil composition and then adjusts the oil flow accordingly. The state of the art technique for accessing astaxanthin contents uses chemical extraction and analysis with High Performance Liquid Chromatography (HPLC). This is both labour intensive and time consuming which makes it infeasible for on-line analysis. The technique has been used to obtain ground truth values for the coated pellets used for paper F.

2.3.2 Optical inspection by spectral imaging

One method for performing this quantification of surface chemistry is using spectral imaging. Here, the benefits of spatially resolved measurements are combined with the spectral discernment of a spectrometer. Successful applications of spectral imaging for quantification of surface chemistry include [40, 41, 42, 43, 44, 45, 46, 47]. A variety of techniques have been developed to perform spectral imaging, Figure 2.5 gives an illustration of two multi-spectral methods. These typically only capture a few preselected bands which are customised for the given application. Similarly Figure 2.6 illustrates two methods for hyperspectral imaging. The terms multispectral and hyperspectral are often distinguished by the number of spectral bands. A better approach may be to instead consider where the technique intrinsically support a continuously resolved spectrum: this is the case for the present methods.

The first method presented in Figure 2.5(a) is the use of a bandpass filter, here positioned between the sample and camera. This is performed with the typical Bayer filter on commercial RGB digital cameras, but may also be used for more advanced multispectral systems [48, 49]. Another typical use of the technique is in remote sensing technologies as the Landsat satellite.[3] Here, the filters are typically custom made for specific applications [47], multispectral images are acquired by swapping the bandpass filter. An alternative multispectral approach is instead to control the illumination wavelength, as illustrated in Figure

[3] www.nasa.gov/mission_pages/landsat/main/

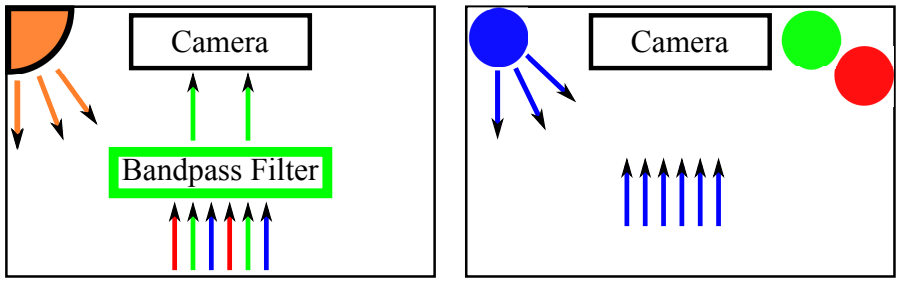

(a) Transmission filters (b) Controlled illumination

Figure 2.5: *Different methods for multispectral imaging*

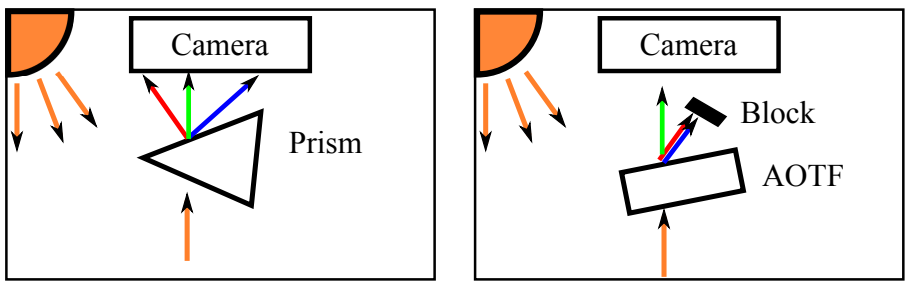

(a) Pushbroom (b) AOTF

Figure 2.6: *Different methods for hyperspectral imaging.*

2.5(b). This may be performed by colour filters on the illumination source, or with lasers or Light Emitting Diode (LED)s. Examples of this technique are given by Merdasa *et al.* [50] and Videometer Lab (Videometer A/S, Hørsholm, Denmark). The Videometer Lab is a commercially available system, which was used in paper F. This technique may accomplish high measurement speeds with a good signal to noise ratio, because the sample is only illuminated with one spectral band. A further advantage of this approach is that by actively controlling the illumination, the data is collected in a more well-defined way. With this measurement technique, mechanical exchange of the filters is avoided, and LEDs are in cheap and available with many different wavelengths.

When it comes to hyperspectral methods, a widely used technique is the push-broom system illustrated in Figure 2.6(a). Here the image is only taken along a single line, the other direction of the camera is then used for the collection of spectral information. The full image is obtained by moving the sample or the imaging system. Dispersive optics, typically a combination of a prism and

a grating, provide a continuous spectrum. The pushbroom technique may be performed with very different settings, changing the field of view and spectral range [51, 52, 53, 54]. The second method is uses an AOTF as is illustrated in Figure 2.6(b). In this method, the image is sent though the active area of an AOTF crystal. This approach has been used by various authors[55, 56, 57]. This has the porential to provide a continuous spectrum without the need for mechanical movement of the sample and the imaging system. It is, however, limited by the small Numerical Aperture (NA) of the crystal.

2.3.3 Prospects for new optical inspection methods in spectral imaging

Multiple approaches exist for integrating spectral and spatially resolved measurements, as has been discussed in the previous section. The aim with the hyperspectral imaging platform constructed in this Ph.D. was to merge the benefits of controlled LED illumination (2.5(b)) and the high spectral resolution of an AOTF based method (2.6(b)). In conjunction, they could create a hyperspectral imaging system with high spectral resolution, but without the requirement of steady movement of either the sample or the imaging system as used in the pushbroom technique.

Chapter 3

Light-Matter Interaction

This chapter introduces some of the interactions between light and matter which make optical based inspection techniques relevant in an industrial setting. Its purpose is to provide a single chapter containing the theoretical background for lights interaction with matter and how they are derived from measurements in the scientific papers written during the Ph.D..

The first section describes the different phenomenons of light-matter interaction which have been relevant for these measurements using different optical inspection techniques. The subsequent section discusses different numerical models used for extracting optical properties. The description is focused on the overall difference between physically-based models with a foundation in MC models and diffusion theory. The objective is to convey a knowledge of how the choice of model influences the inverse modelling and the deduced optical properties (i.e. potential cross-talk). Following this section, different solutions to light propagation are presented and discussed for the different measurement techniques. The objective with this section is to give an overview of how the relevant optical properties may be deduced from the measurement data obtained from PToF and SLS. In the final section of this chapter, the knowledge obtained throughout the previous sections is summarised in a discussion of SLS measurements using the analysis technique Oblique Incidence Reflectometry (OIR).

3.1 Phenomenology

Light consist of electromagnetic radiation that oscillates through space, and we may think of it as both particles and waves. As we will see throughout this section, both descriptions are necessary to understand complex interactions with a material. For each phenomenon a short introduction to its effects is given, with a focus on its relevance for the intended application, and its relevance to the papers is discussed.

The description starts with the simple scenario of a non-scattering medium, which causes refraction and absorption of the light. Following this, light propagation in a scattering medium is presented. The description introduces a scattering coefficient (μ_s) and the directionality of the scattering process. Both absorption and scattering processes are unaffected by the coherence of the laser source, however the coherence of the laser causes a speckle pattern which is described as the final relevant phenomenon for the present instruments.

3.1.1 The refractive index

When light propagates through a medium, the electric field interacts with the dipoles within the medium (i.e. those of its atoms and molecules). This reduces the propagation speed. The ratio of the speed relative to the speed of light in a vacuum is given by the refractive index. The interaction of light with a non-scattering medium is illustrated in Figure 3.1. A beam of light is directed onto the sample's surface where it splits into a transmitted and reflected component. Both the direction and intensity of the transmitted beam is determined by the difference in refractive index. The direction of the transmitted beam is described by Snell's law. The intensity of the transmitted light is described by the Fresnel equations.

Although we are all familiar with the effect of the refractive index, which causes the refraction, for example when looking through water and other clear liquids, it has some more subtle effects which are important for the operation of the SLS instrument and PToF spectrometer.
In paper C, reflectance profiles are analysed using a model OIR, which relies on quantifying a shift in the diffusion profile denote Δx (see definition in Figure 3.13). The refractive index mismatch causes a saturation of the diffusion displacements when changing the incidence angle of the beam. This effect is seen in Figure 3.2(b) for different levels of scattering (absorption is neglected). Figure 3.2(b) also shows the width of the beam projection for the different angles, it is desirable to have a larger displacement than the beam width to ensure a good

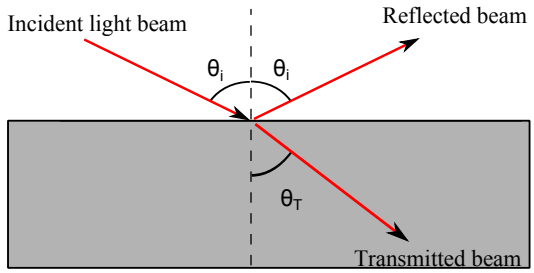

Figure 3.1: *Transmission and reflection of light at the interface between two materials.*

contrast in the centreline of the diffusion profile.
The break in symmetry induced by the oblique incidence angle also makes the transmission intensity depend upon the light's polarization. In general, S-polarised light will have a higher transmission, which was the reason for operating the instrument with this polarization in paper C. Also, choosing an incidence angle close to the Brewster angle (54^o) causes a complete transmission into the sample. The light is polarised due to the AOTF filter used for wavelength selection, so the output polarization is altered by rotating the delivery fibre from the Fiber Delivery System (FDS) around its symmetry axis. This is described in more detail in section 5.2.4. In this way, the refractive index of the sample has a direct impact on the design of the SLS instrument, as it affects both the transmission intensity and the displacement of the oblique incident light. Visualizations of the effects of transmission, diffusion displacement and the projected beam width informed the reasoning behind the choice of incidence angle for the final form of the instrument.

Another subtle effect of the refractive index is reflection at the sample surface *back* into the sample. This is also described theoretically by the Fresnel equations, which place boundary conditions on the analytical solutions to the Radiative Transfer Equation (RTE). The boundary condition is applied to both time-resolved and spatially resolved measurements alike. However, for PToF the optical fibres may be inserted into the sample deeply enough to make the boundary effect negligible. This was the motivation for using submerged fibres in paper D. Finally, as the propagation speed through the medium is proportional to the refractive index, a value for this must be assumed for the evaluation of the PToF measurement as in paper D and E. The deduced optical properties are inversely proportional to the refractive index.

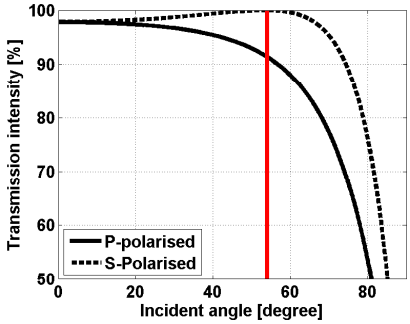

(a) Polarized light transmission.

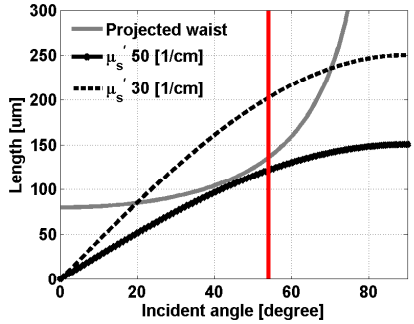

(b) Caculated diffusion displacements for different scattering coefficients

Figure 3.2: *Milk and Yoghurt ($n = 1.348$), the vertical line red lines mark the 54^o used by the final SLS instrument C.*

3.1.2 Absorption

Another significant interaction between light and mater is the process of absorption. Absorption only occurs when the energy of the photons matches a transition energy for molecules or atoms in the sample. This gives rise to chemically-specific fingerprints in the absorption spectrum. For an isolated atom these transitions are very well defined, but for liquids and solid materials, the narrow absorption lines are broadened and smeared out, creating broad absorption bands. The absorption of a photon may cause various changes to a molecule, depending on photon's energy. A molecule may undergo photodissociation, or excitation of its electronic, rotational or vibrational states. Jha [58] gives an introduction to NIR measurements in a setting relevant for food inspection. A review of the different transitions is presented by Osborne [59] for food products. The accessible transitions in the visible to short wave NIR spectral range typically fit higher order vibrational transitions for food products. An excellent text book introduction for different absorption process is given by Bransden and Joachain [60].

For a non-scattering medium the absorption properties may be deduced simply by measuring light attenuation in samples of a known thickness. An example of attenuation measurements is presented in Figure 3.3(a), the line colour represents the visual colour of the respective sample presented in Figure 3.3(b). The samples were combination of coloured vodka drinks and juice. From Figure 3.3(a) it may be seen that the attenuation of each sample causes broad but well defined dips in the transmission spectrum. We also se the edge of the absorption spectra move from green through red as we move though the colours. For

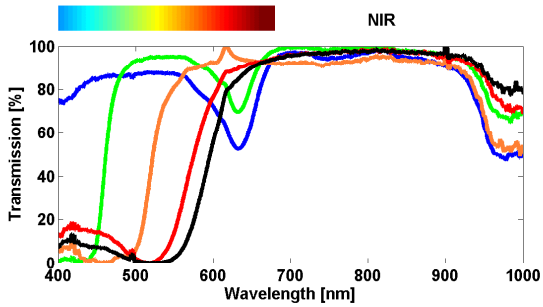

(a) Example of total light attenuation for different beverages

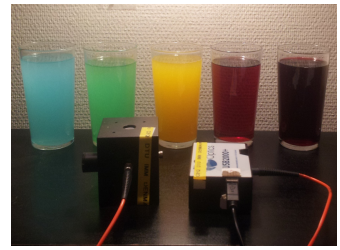

(b) Image of the samples used for the total attenuation measurements in Figure 3.3(a)

Figure 3.3: *Examples of total attenuation measurements on coloured liquids.*

a non-scattering medium, the light attenuation may be solved analytically. The absorption at a position inside the medium is proportional to the light intensity and the probability of a photon being absorbed. This gives rise to a differential equation whose solution is the Lambert-Beer law:

$$I(l, \lambda) = \exp\left[-\mu_{\mathrm{a}}(\lambda) \cdot l\right] \tag{3.1}$$

Here $\mu_{\mathrm{a}}(\lambda)$ is the combined absorption of all the constituents of the samples, which can be expanded as a sum of the absorptions of the individual constituents

$$\mu_{\mathrm{a}}(\lambda) = \sum \sigma_n(\lambda)\rho_n \tag{3.2}$$

Here $\sigma_n(\lambda)$ is the intrinsic absorption cross section for the possible transition at a given wavelength λ. ρ_n is the volume concentration of the n'th constituent. This is the theoretical background for chemometrics based on absorption spectra.

The state of the art for milk and dairy inspection is the MilkoScan$^{\mathrm{TM}}$ (FOSS Electric A/S, Hillerød, Denmark), which measures transmission spectra by Fourier transform Near Infra-Red (NIR) spectroscopy. Using the same measurement technology, total light absorption over the visible to mid infra-red range has been reported to predict the fat, protein and lactose content of raw milk. The spectral range from 450 nm to 2500 nm has been investigated by Tsenkova *et al.* [61] and measurement have been made on the spectral range from 2.00 μm - 10.76 μm by Bittante *et al.* [62]. Likewise the optical properties of fermented milk are presented by Xu *et al.* [63]. The absorption spectra of different fish oils in the spectral range from $\sim$ 380 nm - 2400 nm has been reported by Ljungquist [64]. In this case, the spectra for fish oil with added astaxanthin was presented as well.

In this thesis, absorption properties were investigated in paper C and F. In paper C the absorption spectra of dairy products was investigated using OIR showing absorption for both milk fat and water. In paper F different statistical approaches were used for the prediction of astaxanthin levels on fish feed pellets. This quantification relied on the difference in absorption of fish oil with and without added astaxanthin. Here total attenuation measurements on pure astaxanthin showed good agreement with the loadings of the prediction models.

3.1.3 Scattering

As discussed in the previous section light exhibits both refraction and reflection when it encounters a change in refractive index, this description of light as photons (particles) holds true when the medium has a uniform refractive index. However, many biological samples are composed of multiple different chemical compounds or are disorganised so that the sample does not have a uniform refractive index. This is the case for milk and yoghurt products which largely consist of water ($n_{\text{water}} = 1.333$) with suspended fat globules ($n_{\text{milk fat}} \sim 1.465$ [65]). Often, solids are even less homogeneous and exhibit a higher degree of scattering. When light propagates in such samples it encounters regions with different refractive indices, but on a length scale similar to the wavelength. Because of this the wave nature of light becomes significant, and the light undergoes diffraction by the different perturbations. Effectively, this causes an incoming wave to be re-emitted in another direction. An excellent discussion of this process is given by M. Mishchenko [66].

On a macroscopic scale we see this as light scattering, which causes some of the light to be re-emitted by the sample at another location than the entrance point, as is illustrated in Figure 3.4(a). This form of re-emitted light is often denoted diffuse reflectance [67] or subsurface light scattering [68] and it provides information on both scattering and absorption. As we have briefly touched upon already, we may consider light as both particles and waves.When light is modelled as particles, as in Figure 3.4(a) the wave nature of light is "hidden away" in the actual scattering process. This approach is taken for Monte Carlo models which will be discussed later in this section.

Because the scattering is caused by diffraction, the scattering probability is dependent on the ratio between the light's wavelength and the physical size of the scattering object. In general, longer wavelength light exhibits less scattering because the perturbation of the refractive index becomes smaller relative to the wavelength. Similarly to the absorption process we define a scattering probability μ_s, which is the likelihood of a photon being scattered per unit length as it propagates in the medium.

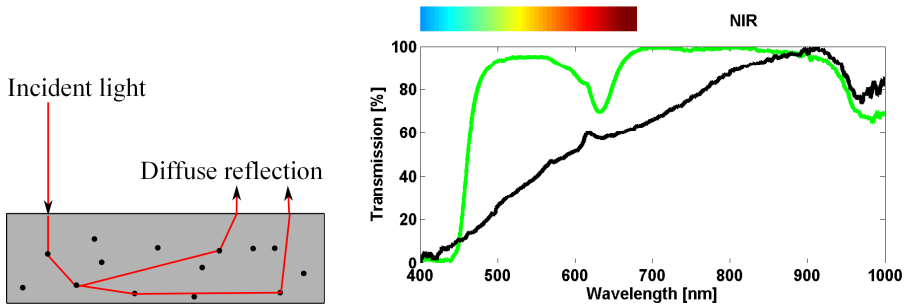

(a) Illustration of the scattering process in a sample on the macroscopic scale. Light emerging from the surface has taken different paths in the sample.

(b) Comparison of the spectral difference in attenuation measurements of a scattering and absorbing sample.

Figure 3.4: *Illustrations of light propagation and attenuation by scattering samples.*

While leaving the actual modelling of the light propagation for the next section, we may still observe that there is a clear difference between light attenuation by scattering and absorbing samples. Concerning light attenuation, we may conduct the same form of attenuation measurements on a scattering sample as was performed on the absorbing samples presented in Figure 3.3(b). The attenuation by milk (0.5 % fat) as a function of wavelength is presented in Figure 3.4(b), and is compared to the attenuation of the green vodka. Unlike the attenuation measured by the non scattering samples in Figure 3.3(a) this attenuation shows a monotonic decrease as a function of wavelength rather than reduction over a specific wavelength range. The exception to this slow variation is the water absorption peak at 970 nm.

Scattering phase function

The scattering process is not deterministic because it arises from diffraction. For an incoming wave with a propagation direction $\mathbf{s}$ the probability of scattering into the direction s' is given by the so called phase function $\mathrm{P}(\mathbf{s}, \mathbf{s'})$. The materials studied in this Ph.D. project, dairy products and fish feed pellets, do not have any inherent direction. The amplitude of the phase function, illustrated in Figure 3.5(a), is therefore only dependent on the angular change of the scattering event (θ).

The most common description of the phase function is the Henyey-Gresnstein

phase function [69], which has a simple closed analytical expression. The Henyey-Gresnstein phase function takes only one argument, which is also the value for the asymmetry factor defined as

$$g = \frac{1}{2\pi} \int_0^{2\pi} \mathrm{P}(\theta) \cos(\theta) d\theta \tag{3.3}$$

Due to normalization of the phase function, its asymmetry value is in the range from $[-1, 1]$, where an asymmetry factor of 0 corresponds to isotropic scattering. The Henyey-Gresnstein phase function does not, however, provide a physical interpretation of the particles' size or shape. This may be accomplished using Lorentz-Mie theory, which calculates the scattering and phase function properties for an uniform spherical scattering particle. For emulsions, this is often an adequate model. Calculating the phase function properties for a given particle is not trivial, but an easily accessible solution is provided by S. Prahl[1]. Frisvad *et al.* [70] have published a numerical model for light scattering specifically for milk. For a given particle size distribution it calculates the wavelength dependence of the effective scattering and phase function properties for a given particle size distributions. Using the latter framework, the phase functions for protein and fat have been calculated and are presented in Figure 3.5. The protein are small and cause a scattering with $g \simeq 0$. This regime is a special case called Rayleigh scattering. For the fat particles in milk, with a size of 500 nm causing $g \simeq 0.8$, the phase function is significantly forward directed. As seen from Figure 3.5, the phase function properties depend on the polarization. This have been studied by Cameron [71], where the polarization on both source and detector was varied.

The effect of the scattering phase function can be measured in two different regimes. The first being the single scattering regime, in which the sample is dilute and thin enough, that the photons only undergo a single scattering event. This measurement form is often denoted small angle light scattering, and an example is given by Agrawal and Meng*üç* [72]. In this sub-field of light scattering, it is also more common to use a more complicated and non analytical solution to the phase function. This may be performed using the T-matrix method [73]. This regime is mostly used for sensing of gases or dilute samples to ensure the single scattering criterion is fulfilled. The diffraction pattern created by the particles may be used for determining the particle size distribution in the commercial Mastersizer 3000 instrument discussed in section 2.2.2. The same measurement principle applied in conjunction with T-matrix simulation for investigation of particle shapes in given in the doctoral theses by Meland [74].
The second regime in which the scattering process may be quantified is the multiple scattering regime. This is used by the SLS instrument developed in

[1] http://omlc.ogi.edu/calc/

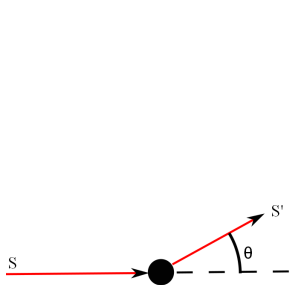

(a) Illustration of the scattering of an incoming photon (travelling in one direction **s**) into an another direction (**s'**).

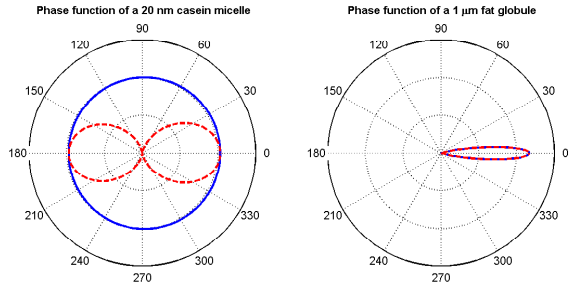

(b) Examples of the phase functions for protein and fat particles present in milk, red is p-polarised and blue is s-polarised light at 650nm.

Figure 3.5: *Illustration of the single scattering phase function.*

this Ph.D.. A description of the instrument is given in 5.3. In this regime the detailed shape of the scattering phase function is smeared out due to multiple scattering events, often it is only possible to evaluate the first one or two moments of the phase function properties. Along the same lines, we define a reduced scattering coefficient

$$\mu_{\mathrm{s}}' = \mu_{\mathrm{s}}(1-g) \tag{3.4}$$

which corresponds to the effective scattering coefficient for an isotropic scattering process. g denotes the average cosine defined in Equation 3.3. In this multiple scattering regime, the particle size effect may be deduced from the first moment of the reflectance profile. A numerical study has been performed for a fibre probe instrument as presented by Bevilacqua and Depeursinge [75], which illustrates some of the very intriguing properties that can be revealed even in the multiple scattering regime. Another approach is to use the inverse model of the particle size distribution from broadband characterizations of the reduced scattering properties, as has been applied by Hajihashemi and Jiang [76] and Li *et al.* [77].

For the present work it have been sufficient to deduced the changes in size distribution using an approximation to the reduced scattering coefficient presented by Graaff *et al.* [78]

$$\mu_{\mathrm{s}}'(\lambda) = A\left(\frac{\lambda}{\lambda_0}\right)^{-\beta} \tag{3.5}$$

Here the coefficient A is the amplitude of the reduced scattering and is related to a combination of the scattering cross-section and the particle density. β is

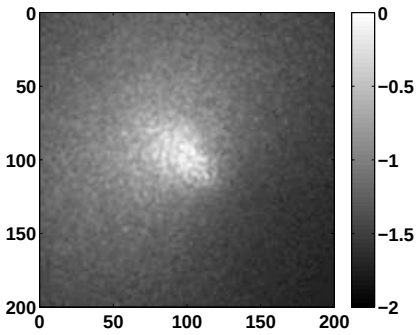

(a) Zoomed view of the laser's entry point with the SLS instrument. Normalized and logarithmic colormap. Light is incident from the bottom right corner.

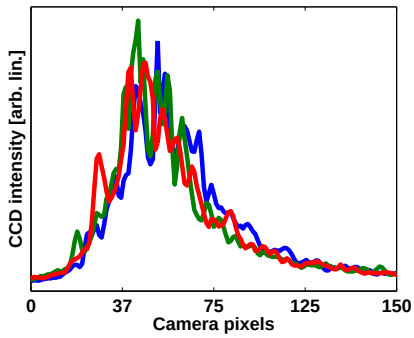

(b) Reflectance profile extracted though the entry point and along the incidence dircetion of an SLS image. Different colurs represent repeated measurements.

Figure 3.6: *Examples of speckle in measurements with the SLS instrument on milk* 1.5 % *fat at* 700 *nm.*

related to the ratio between wavelength and particle diameter. For scattering by relatively small particles $\beta \sim 4$ which correspond to Rayleigh scattering, while for smaller values of β scattering is described by Lorenz-Mie theory. The value of β has previously been used to quantify the average size of the sample's particle size distribution[79], and here a monotonic relationship was found. The constant λ_0 is an arbitrary scaling coefficient. Equation C.10 was used as confirmation of the measurements results in both paper C and D.

Changes in the phase function were observed with the SLS instrument in paper B, which reports a significant difference between both wavelengths and sample structure (milk vs. yoghurt). Finally, the phase function was important in publication D where an assumed value for the phase function was necessary for the MC model. A value of $g = 0.7$ was assumed.

3.1.4 Speckle

The last interaction between light and matter which has been relevant for the work during the Ph.D. project is speckle. Speckle arises due to the wave nature of light, where the waves may interfere constructively or destructively. The effect is measurable with the SLS instrument because the supercontinuum source is semi-coherent and the AOTF filtered light has a narrow bandwidth. Because the supercontinuum light source produces a semi-coherent output, it enables

measurement of the sample's speckle properties. When the AOTF filtered light arrives at the sample surface it is in phase. As described in the previous section, the light will undergo a number of scattering process inside the sample before it is detected by the camera. An effect not addressed in the previous section, however, is the Doppler shift which the scattered photon will experience if the particles is moving. The Doppler shift will slightly alter the wavelength of the light, and thereby the interference pattern as measured on the camera. A close up view of a speckle pattern near an entry point is presented in Figure 3.6(a). The scattering induced wavelength change is often refereed to as quasi-elastic scattering. The theoretical foundation is described by Gillespie[80], and relies on the random phase shift of a coherent beam by particles undergoing Brownian motion[81]. The Brownian motion of the particles in dairy liquids depends on the sample's water mobility, which characterises the degree to which the water is confined by the microstructure. In this way speckle properties may provide another form of quantification of the structure than those given by the scattering probability and directionality.

For a detector which measures the diffuse reflectance, the light may come from multiple different paths as seen in Figure 3.4(a). Each photon contributes with their accumulated phase from the scattering processes and path distances in the sample. The strength of the interference pattern is thus greatest for light which has propagated a well-defined distance, this is seen close to the entry point and in the direction following the light incidence direction, as is observed in Figure 3.6(a).

For the work conducted during this Ph.D., the speckle properties have been significant for a number of publications. Specifically for OIR in paper C the speckle is problematic as it increases the uncertainty of the entry point estimation. This is seen in Figure 3.6(b) which shows the changes in the reflectance profile for repeated measurements. To overcome this, Lindbergh [82] proposed an image smoothing and averaging the result between repetitive images. However, the smoothing operation changes the entry point for our data significantly, and the amount is dependent of the scattering process asymmetry. We used the hyperspectral information to achieve a similar noise reduction, which avoids an additional increase in data acquisition time.
Finally, statistical approaches for quantification of the speckle pattern were used by Skytte *et al.* [12] and by Sharifzadeh *et al.* [83].

As stated in section 2.2.2 the speckle properties are already used in commercially available instruments for monitoring milk coagulation. For this reason, a quantification of the speckle properties with the SLS measurement system may contribute relevant information about the dairy products microstrutural properties.

3.2 Modelling light transport

Now that we are familiar with the different interactions which take place between light and matter, the next topic is how models may be used to extract and distinguish the optical properties. A number of different models have been used during the Ph.D. project and for different measurement techniques. The aim of this section is to give an overview of the methods and to describe why the different approaches were taken. An actual derivation of the individual analytical expressions is not provided references are available in the respective papers.

It is instructive to first separate the different models in two groups. The first are statistics-driven models and the second are models based on a physical interpretation of light propagation. A summary of their use in the different papers is given in Figure 1.3. The two groups are illustrated in Figure 3.7 with a summary of their respective advantages. These observations are somewhat general and not specific to modelling light transport.

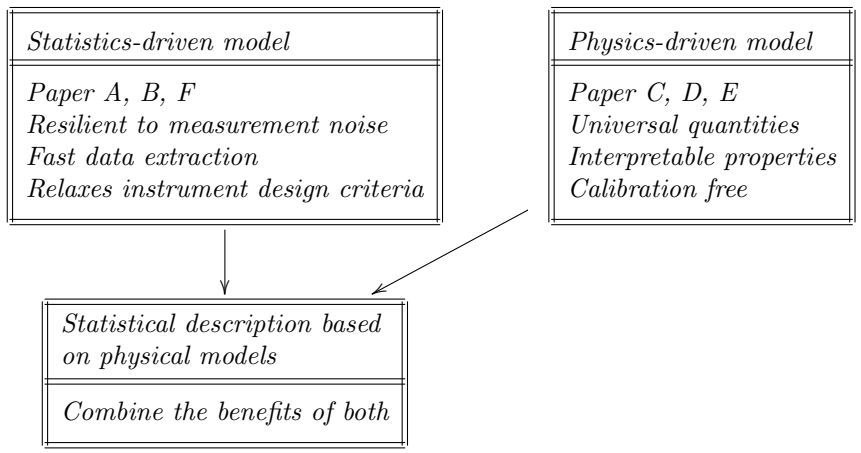

Figure 3.7: *Paradigms for quantification of optical properties*

When modelling light transport, it is clarifying to first define a characteristic length scale, which incorporates both scattering and absorption. This is contained in the transport Mean Free Path (MFP) as defined by Lin *et al.* [84]

$$1\text{mfp} = \frac{1}{0.35\mu_\text{a} + \mu_\text{s}'} \tag{3.6}$$

The MFP is imperative as it quantifies the length scales on which the different optical interactions take place. Its specific dependency on both absorption and scattering asymmetry (g) has been the subject of discussion [82, 85]. For the dairy products inspected in paper C and D, the MFP varied from $\sim$ 0.2 mm of yoghurt (3.5 % fat) at 470 nm to $\sim$ 2 mm for milk (0.5 % fat) at 1020 nm. The values were not considered for the astaxanthin samples in paper F as it was clear in advance that single pellet characterization was not desired.

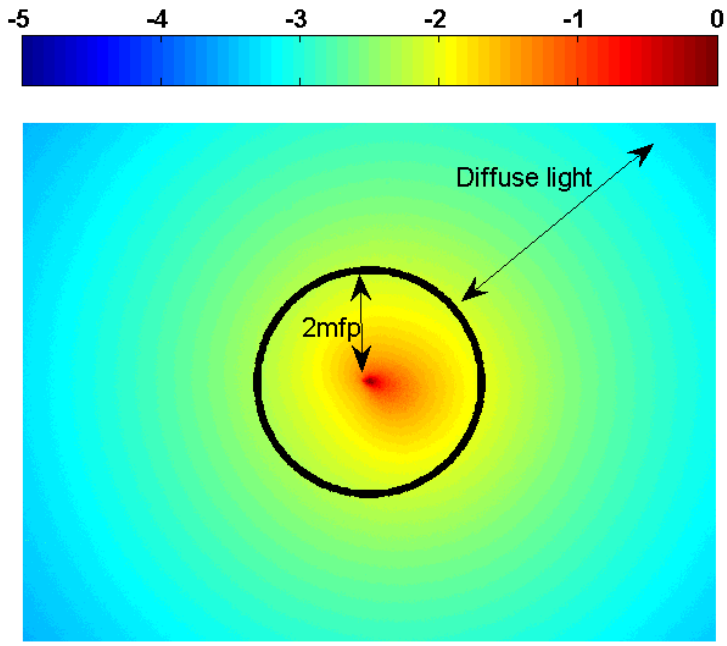

Figure 3.8: *SLS image with oblique incident light, colour scale is logarithmic. The image is of Arla Lærkevang (milk, 1.5 % fat) at 800 nm. The image shows the different regions in which the different optical properties are expressed. The scattering phase function, and speckle pattern are expressed at the entry point and within a distance of 2 MFP, marked as a black circle. Scattering and absorption may be quantified from the diffuse reflectance profile further away from the entry point.*

The spatial regions in which the optical properties are expressed are illustrated in Figure 3.8. As already mentioned in the discussion of both the scattering phase

function and the speckle pattern, these two effects are strongest close to the source. The distance is effectively quantified in units of the MFP. At distances larger than $\sim$ 2 MFP from the entry point, the reflectance profiles become diffuse and have lost information about the original phase and direction[84]. At these distances, the speckle and phase function properties have diminished for both the SLS and PToF instrument.

3.2.1 Introduction to physical based models

The description of the physical based models will take its starting points in the conservation of photons, which leads to the radiative transfer equation. This approach neglects the wave nature of light, and can not model the speckle properties.

Consider an infinitesimal volume element of a medium, which exhibits light transport, and let I denote the light intensity. We may now make a heuristic description of how the different interactions from the previous section may change the light intensity within the volume element along the direction $\vec{s}$. Let the position and time coordinate be implicit for simplicity of the equations. For a time-dependent solutions, the different processes the model must incorporate are the following:

I The time scale for intensity changes, given by the medium's refractive index (n).

II The intensity increase caused by an external source (q)

III The increase and redirection of energy due to scattering (μ_s') over the volume elements' surface area (A)

IV Changes due to the light density gradient which describes a diffusion process ($\cdot\nabla I$)

V Reduction of light intensity due to scattering or absorption proportional to the light intensity.

Combining all of these terms one obtains the RTE 3.7

$$\underbrace{\frac{1}{cn}}_{\mathbf{I}}\frac{\delta I}{\delta t} = \underbrace{q}_{\mathbf{II}} + \mu_s \underbrace{\int_A P(\vec{s},\vec{s'})I da}_{\mathbf{III}} - \underbrace{\vec{s}\cdot\nabla I}_{\mathbf{IV}} - \underbrace{I(\mu_s+\mu_a)}_{\mathbf{V}} \tag{3.7}$$

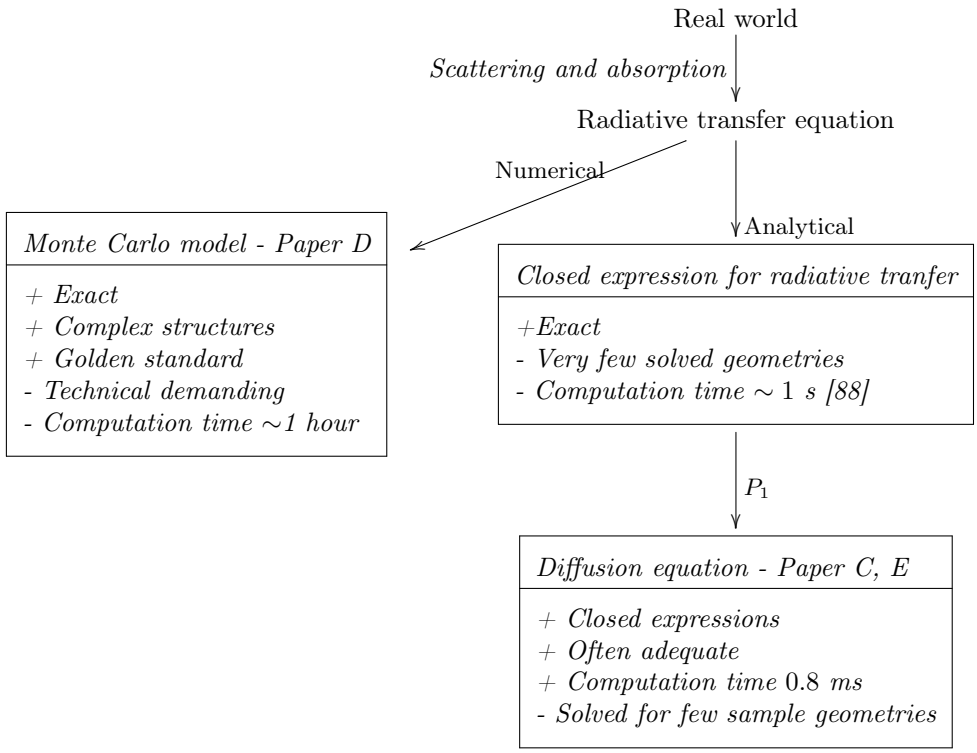

Figure 3.9: *Relation between physical based models*

The RTE describes the transport of neutral particles in a scattering and absorbing medium and is discussed in numerous text books [86, 87]. As it describes neutral particles, it also has some application in other scientific fields such as neutron scattering. The RTE has no general solution, but different approaches have been used to simplify it and to obtain analytical expressions or numerical solutions as with MC. Both approaches have been used through out the thesis and the relationship between their methods and the use is summarised in Figure 3.9.

Monte Carlo Models

A MC model is a numerical solution for the RTE. It can be used to solve the equation to an arbitrary precession [89]. The fundamental concept for MC

models is the tracing of multiple photon packages though a given scene and collecting the final photon density distribution on a sensor. This makes the framework somewhat general as it may be used to solve the RTE, even for light propagation though such complicated structures as the human head [90]. The main drawback of MC modelling is the requirement to tracing a large number of photons to obtain a low noise result. This makes it infeasible to deduce the optical properties from a given measurement by directly using MC models[91]. For this reason noise reduction techniques have been studied intensively and a summary of the state of the art is give by Zhu and Liu [92].

As the main drawback of MC modelling is the computation time, the methods are not often used for inverse modelling of the samples' optical properties directly. Instead, they are used for creating precomputed look-up tables of the reflectance profiles as presented by Thueler *et al.* [93]. In implementation by Thueler, the reflectance profiles were precomputed for a grid spanning three parameters: μ_s', μ_a, and a ratio of the single scattering phase function moments. For the work conducted in this Ph.D., a library of precomputed MC simulations was used for evaluation of optical properties in Paper D. The models was first presented by Alerstam *et al.* [94, 95], further details are available in the thesis[96]. The MC model was a continuation of the White Monte Carlo Light (WMCL) model developed by Wang *et al.* [97]. WMCL exploits two scale-invariant properties of the RTE. The simulation is performed without including absorption, and the distance propagated by each photon is stored. This is different to the approach by Thueler *et al.* [93], where only the final accumulated photon density distribution is stored. Although a larger data-base is required, since every photon package is stored, it allows for an arbitrary scaling of the absorption by adding the attenuation due to absorption as given by equation 3.1. Along the same lines, the implementation makes use of an invariance between the distance of propagation with the time duration and the refractive index of the sample. This makes the same MC library useable for different parameters of fibre separations, the refractive index of the sample, and the value of the reduced scattering coefficient. In the present work only the reduced scattering coefficient was analysed using a predefined grid, and the optimal absorption was deduced for each measurement. The final solution was the combination of reduced scattering and absorption which resulted in the minimum fit residual.

Diffusion approximation

The RTE may be solved by expanding the radiance in spherical coordinates, the so called P_n solution. This may, however be computationally intensive to solve and has only been solved for a few geometries such as the semi-infinite medium[88]. A more common approach has thus been to simplify the RTE by

only keeping the first two terms of the radiance expansion. By further assuming that the change in radiance is small, the following Diffusion Equation (DE) may be derived [67]

$$\nabla^2 L - \frac{\mu_a}{D} L = -\frac{S_0}{D} + 3\nabla \cdot S_1 \tag{3.8}$$

where S is a spherical harmonic and the subscript denotes its order. The assumption of a relatively small gradient in radiance is satisfied when absorption is significantly smaller than scattering. Throughout the Ph.D. project, solutions to the DE for a semi-infinite media have been used which were proposed by Farrell *et al.* [67] as may be seen in paper C, as well as the solution for a slab of medium by Martelli *et al.* [98] which was used in paper E.

Breakdown and Cross-talk

The use of diffusion approximations for the RTE is often investigated in the forward problem, displaying the difference between the reflectance profiles as in Figure 3.10(a). Here the dependency on the scattering phase function have been reported in multiple papers e.g. Wang and Jacque [99] and corrections have been proposed by Chen *et al.* [100] and Zemp [101]. The diffusion models are often only adequate far away from the source, and they break down at short distances or for samples with relatively high absorption and scattering asymmetry.
While these visual methods give some validation and interpretation of the models, they do not quantify how well the model quantifies the optical properties (the inverse problem). An illustration of this is given in Figure 3.10(b), where the optical properties deduced by both MC models and a diffusion model are presented. It is seen that the diffusion approximation deviates systematically, and mostly for high absorption values. This effect is often referred to as cross-talk, as it effectively couples the values deduced when applying a diffusion model.

The effect of cross-talk was could may be present in the deduced optical properties in paper C, where the presence of both milk fat and water gave absorption peaks. However, because the scattering coefficient was increased for the samples with high fat contents, absorption was reduced.
One approach to compensating for this cross-talk could be to precompute the perturbation from the diffusion models, and then compensate by the same amount when the optical properties have been computed for a given sample.

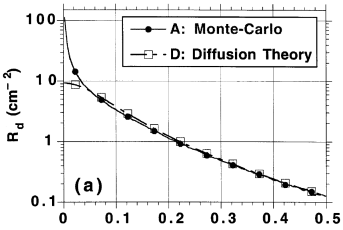

(a) Imperfections of the reflectance profiles as seen in the forward problem as presented by Wang and Jacque [99].

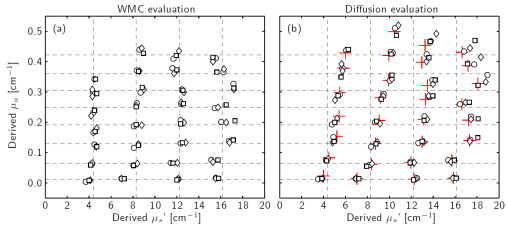

(b) Evaluated (inverse problem) optical properties on a set of optical phantoms using MC simulations (right) as opposed to a diffusion model (left) presented by Alerstam *et al.* [94].

Figure 3.10: *Illustration of the diffusion approximations breakdown. The effect is seen for anisotropic scattering in the forward problem 3.10(a) and the for the "cross talk" between scattering and absorption illustrated in the inverse problem 3.10(b)*

3.3 Solutions to light propagation

In this section the solution to light propagation for the SLS and PToF techniques is presented. It gives important intuition into how the optical properties, scattering and absorption, affect the measurements. This knowledge is used in a discussion of the strengths of the two techniques.

3.3.1 Photon Time-of-flight

The measurement principle for PToF spectroscopy is illustrated in Figure 1.1(b), a light pulse with a very short temporal width (~ 50 ps) is sent into the sample. The light emerging at another position on the sample is collected, and the PToF distribution is measured. Some photons take a short path and arrive early, some are scattered many times and arrive late. Because of the different propagation times, the temporal width of the emerging PToF distribution is broadened. For PToF the optical properties are deduced from the shape of the temporal distribution of the broadened light pulse which emerges from the medium. The solution to the diffusion equation for a semi-infinite medium is provided in a thesis by Svensson [102] and presented below

$$\Phi(r,t) = \frac{c_0}{n} \mathrm{E}_0 \left(\frac{\mu_\mathrm{s}'}{4\pi tc/n} \right)^{3/2} \exp\left[\frac{-3\mu_\mathrm{s}' r^2}{4tc/n} - \mu_\mathrm{a} tc/n \right]. \tag{3.9}$$

Here E_0 is a scaling coefficient which incorporates the light source intensity.

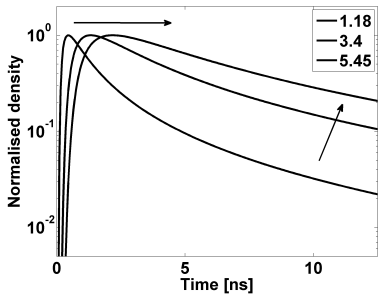

(a) Changes induced by scattering, values used are 5, 15 and 25 1/cm, absorption was zero.

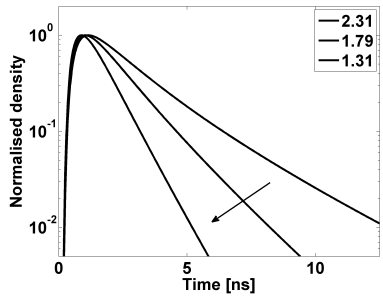

(b) Changes induced by absorption, values used are 0.01, 0.02 and 0.04 1/cm and scattering is 15 1/cm.

Figure 3.11: *Solution to the diffusion equation for a semi-infinite medium in TOF [102]. The fibre separation is* 1.5 *cm and the refractive index 1.347 (milk). The legends denote their respective FWHM [ns].*

Examples of the PToF distribution are provided in Figure 3.11(a) for different scattering levels and in Figure 3.11(b) for different absorption levels. These figures show that the two optical properties affect the PToF distribution in different ways. Increased scattering broadens the TOF distribution and delays the arrival time. Absorption on the other hand, mainly contracts the PToF distribution. The same may naturally be seen directly from Equation 3.9. This is a strength of PToF. For diffuse light, optical properties can be determined purely from the shape of the PToF distribution.

Though these effects are discussed for a semi-infinite media, the concept of how scattering and absorption influence the PToF distribution is the same for other measurement geometries. In Paper D the measurements were conducted with both source and detector fibre submerged in the samples, and in report E the measurements were conducted by transmission though a slab. For measurements in both of these geometries, the absorption most strongly affects the late-arriving photons. This is a consequence of the Lambert-Beer law, where the relevant distance is the path length of the photons, and not the distance between source and detector.
A note on the effect of the refractive index: all the optical properties are measured relative to the refractive index as seen from Equation 3.9.

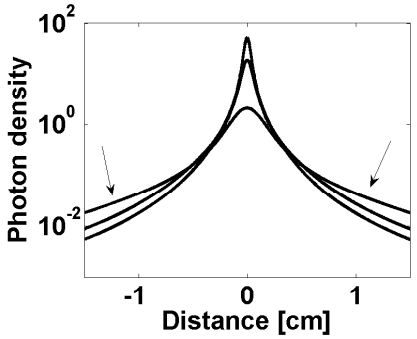

(a) Changes induced by scattering, values used are 5, 15 and 25 1/cm, absorption was zero.

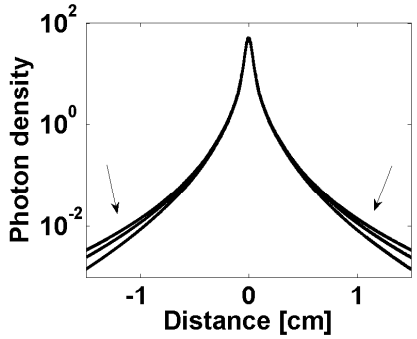

(b) Changes induced by absorption, values used are 0.01, 0.02 and 0.04 1/cm and scattering is 15 1/cm.

Figure 3.12: *Solutions to the diffusion equation for a semi infinite medium with SLS [67]. A refractive index of* 1.347 *is assumed.*

3.3.2 SLS - Orthogonal incidence

In comparison, an analytical solution to the diffusion equation has been derived by Farrell *et al.* [67] for a semi-infinite medium using SLS. Here, the light is incident orthogonal to the sample surface, and the solution to the diffusion equation is then given by:

$$Rr(r) = \frac{\mu_t'}{4\pi\mu_{\mathrm{s}}'}\left[\frac{1}{\mu_t'}\left(\mu_{\mathrm{eff}}+\frac{1}{r_1}\right)\frac{\exp\left(-\mu_{\mathrm{eff}}r_1\right)}{r_1^2}+\left(\frac{1}{\mu_t'}+\frac{4A}{3\mu_t'}\right)\left(\mu_{\mathrm{eff}}+\frac{1}{r_2}\right)\frac{\exp\left(-\mu_{\mathrm{eff}}r_2\right)}{r_2^2}\right] \tag{3.10}$$

where, $\mu_t' = (\mu_{\mathrm{s}}' + \mu_{\mathrm{a}})$ is the total interaction coefficient and μ_{eff} is the effective attenuation ($\mu_{\mathrm{eff}} = [3\mu_{\mathrm{a}}(\mu_{\mathrm{a}} + \mu_{\mathrm{s}}')]^{1/2}$). The coefficient "$A$" is a scaling of the contribution between the positive and negative point sources which ensures the boundary coefficients for the reflectance profile. It is thus determined by the refractive index. Finally,

$$r_1 = \left[\frac{1}{\mu_t'^2}+r^2\right]^{1/2} \quad \text{and} \qquad r_2 = \left[\left(\frac{1}{\mu_t'}+\frac{4A}{3\mu_t'}\right)^2+r^2\right]^{1/2} \tag{3.11}$$

are the distances to a set of point sources (positive and negative) which give rise to the light distribution. Examples of the solution are provided in Figure 3.12(a) for different scattering levels, and for different absorption levels in Figure 3.12(b).

The reflectance profiles presented in Figure 3.12, together with the closed expression in Equation 3.10, show that it is not possible to deduce the optical properties from the shape of the reflectance profile alone. The decay is measured in units of the effective attenuation which includes both scattering and absorption. To separate the two effects, it is necessary to perform measurements with the intensity calibrated. With knowledge of both the amplitude and the decay over distance, scattering and absorption may be quantified individually.

For continuous inspection in a production environment this will thus require control of the light source's power and, possibly, the transmission efficiency of the cover slip in front of the samples. Otherwise, the deduced optical parameters will vary over time simply because of the measurement technique. This technique has been applied on milk samples by Qin *et al.* [54].

The SLS measurements are however interesting from an application point of view, as they may be performed using a camera looking through a cover slip. This makes in-line inspection feasible without the risk of contamination by physical contact. Finally the detectors used for static light scattering are inexpensive compared to those used in PToF spectroscopy.

3.3.3 SLS - Oblique incidence

To circumvent the requirement for an absolute intensity measurement in SLS, Wang *et al.* [103] proposed the use of oblique incidence light to estimate the reduced scattering coefficient. The model was later expanded to include absorption by Lin *et al.* [84] and this approach has been used in Paper C. The advantage of OIR, compared to the original approach by Farrell *et al.* [67], is that the problematic absolute intensity measurements are replaced by a spatially-resolved measurement of both the diffused light and the profile close to the entry point. OIR has become an established technique, and has advanced the application of diffuse optical spectroscopy for clinical use [104, 105, 106, 107].

The measurement technique is illustrated in figure 3.13 (A) where the light beam is incident on the sample surface. The colour of the surface corresponds to the intensity of the diffuse reflection. The intensity is highest close to the entry point and decays as a function of distance. Due to the oblique incidence angle however, the decay is slower in the forward direction, making the reflectance profile skewed, as is illustrated in Figure 3.13 (B). This asymmetric shape enables a quantification of the light's mean free path in the sample. This is given by the distance between the symmetry point of the reflectance with high intensity (red) from that with low intensity (blue). The optical properties may be deduced by combining the symmetry shift (Δx) with the effective attenuation

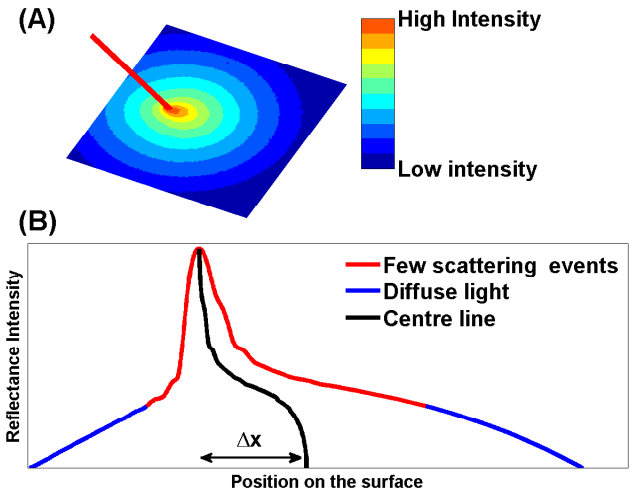

Figure 3.13: *Illustrations of OIR as given in Paper C.* ***(A)*** *A red light beam is obliquely incident on a sample surface. The surface is colour-code by the intensity of the diffuse reflectance.* ***(B)*** *Shows the reflectance intensity along a line though the entry point in the direction of incidence. The symmetry point of the reflectance profile shifts by a distance* Δx between high and low intensity light.

by the low intensity light (blue). The details of the measurement technique are provided in paper C.

3.4 Combining the benefits of time-resolved and static measurements

With an understanding ot the different optical interactions and measurement techniques, it is clear that the advantage of SLS measurements with OIR is not only that it circumvents the requirement for absolute intensity measurements. The need to spatially resolve the displacement (Δx in Figure 3.13), by measuring the light which has only scattered a few times, inherently enables quantification of both the speckle and phase function properties as well. These effects are only observable close to the beam entry point - within a distance of $\sim$ 2 MFP as discussed in the previous section. In this way, OIR could intrinsically support the different optical signals relevant for dairy inspection as discussed in section 2.2.2. Simultaneously, if performed with a camera as detector, it retains the

benefits of non-contact inspection and cheap detector technology of the static measurements. Lastly, the high resolution of modern CCD cameras enables quantification of a broad range of optical properties, as is demonstrated in paper C.

Chapter 4

Measurement design and analysis of data

Planning of the measurement campaigns and the subsequent data analysis has been important parts of the Ph.D.. The large amount of wavelengths which is used to characterization of the samples, complicates interpretation and validation of the results, and care must be taken to make sure that they are generalizable. For this reason, it is necessary to introduce some aspect of experimental design and multivariate data analysis. In this chapter, the different aspects of planning a measurement campaign, and validating and quantifying the results is described. The description is focused on how to handle the challenges posed when the number of measurements is smaller than the number of variables.

In the first section a short introduction to the considerations behind the different measurement campaigns is given. Following this, there is a discussion of the visualization of sample correlations, as well as methods for dimensionality reduction of before these visualizations. The third section is devoted to the construction of regression models. Two very different regression methods are described, Partial Least Square (PLS) regression which is a commonly used method and a newer method called The Elastic Net (EN) regression. The later is a new sparse regression methods, which has some interesting prospects in terms of variable selection. Finally, an outlook is given on how objective statistical quantifications of the most significant parameters can be used in broadband

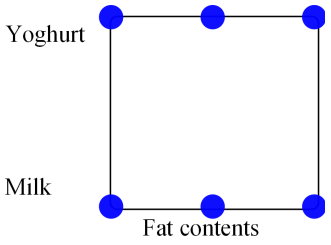

(a) 3^2 factorial, used in the Papers A, D and C.

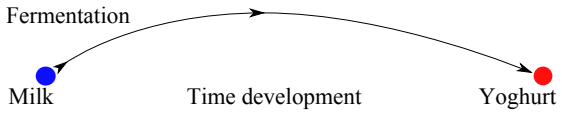

(b) Continuous inspection, performed in Paper B and in the comparative study in Chapter 9.

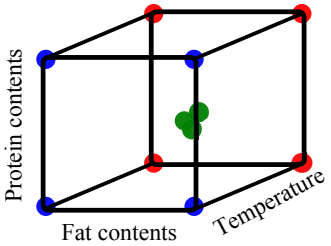

(c) 2^3 factorial study performed in Paper B.

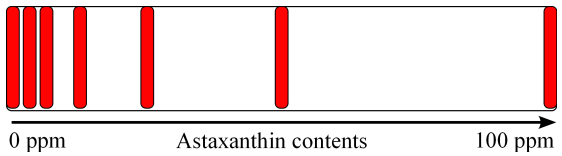

(d) Sensitivity analysis as used in Paper F.

Figure 4.1: *Visualization of the different designs of the measurement campaigns conducted in the Ph.D..*

characterization to drive the hardware development towards a faster and more focused industrial implementation.

4.1 Design of experiments

The collection of data is often expensive and time consuming. For this reason, the number of measurements becomes limited, and the experimental campaign must be designed to obtain an optimal amount of information within the constraints of resources. The measurement campaigns have therefore involved different experimental designs which are illustrated in Figure 4.1. Although often only discovered retrospectively, the measurement design sketches and limits the possible results of the scientific contributions, and must always be considered carefully. En introduction to experiment design is provided in [108].

The 3^2 factorial experiment design illustrated in Figure 4.1(a) is typically used for pre-studies of sensitivity and dynamic range for a given set of parameters. A small experimental design spanning a large variation for a given process, can

be used as pre-study for a larger and more focused experimental design. In it-self, the experimental design is typically to small too provide the necessary knowledge for regression models quantification of non-linear dependency between the variables which is developed in the other designs. For the present work, this experimental design was adopted for Paper A to investigate the instrument's sensitivity to different fat contents and structural properties. From this, the analysis technique was found to be suitable for the larger measurement campaign conducted in Paper B. The same measurement campaigns were performed routinely as part of the development of the SLS technique. The objective was to cover a range of milk and yoghurt products with a fat contents ranging from $0.5 - 3.5$ %, which spans the range of many milk gels. As part of this, a knowledge of the measurements' limitations and dynamic range for OIR developed. This lead to an expansion of the SLS imaging system's field of view, together with new analysis methods which made it possible to cover broad range of optical properties of the dairy samples. The final result is presented in Paper C and provided valuable knowledge on the measurement technique (OIR) for dairy inspection.

The continuous inspection of milk fermentation presented in Figure 4.1(b) is an example of a more demanding data collection process. The measurement campaign is time consuming, a single fermentation takes ~ 5 hours, and requires simultaneous access to rheology equipment. These measurements were conducted in Paper B in combination with the 2^3 factorial design presented in Figure 4.1(c). The 2^3 factorial study is a very compact way of getting information on the interactions between the changing factors. As seen from the illustration, each pair of corner points enables quantification of a linear dependency of a parameter. In addition to this, the diagonal through the centre point, enables quantification of non linearities. The predictive strength of the design is enhanced by the repetitive centre points, which allows for a quantification of the overall measurement precision. Ideally, the measurements of the centre points are closely clustered compared to the corner points. The reproducibility of the centre point thus provide a characteristic length scale for the measurement. The strength of the different interactions are quantified by Analysis of Variance (ANOVA) and Multivariate analysis of variance (MANOVA), which is outside the scope of the thesis.

Lastly, the measurement design illustrated in Figure 4.1(d) was used to obtain a broad dynamic range while retaining small concentration differences in the sample design. The manufacturing and subsequent evaluation of astaxanthin contents for different concentration levels, using HPLC, is expensive. Because of this, the number of different astaxanthin levels was limited. For the work presented in Paper F the manufacturing process favoured this form of scaling of the concentration differences during the manufacturing process. For the analysis however, it can introduce a bias as the model is more focused on accurate

prediction of low concentration values. The concentration was dimidiated in levels starting from 100 to 3.125 parts pr. million (ppm) lastly and a set of samples was included without any added astaxanthin.

4.2 Data exploration

When a measurement campaign has been conducted, exploration and validation of the collected data is commenced. One way of investigating the data is through a scatter plot of the measurements. An example of a scatter plot which visualises the correlation is presented in Figure 4.2(a). Here it is revealed that the measured reduced scattering and the absorption are correlated.

For higher dimensional data, such as the reflectance measurement in Paper F it is not possible to know in advance which axes are natural for the variance of the data set. To determine these axes, a number of statistical methods are available. The most commonly used method is Principal Component Analysis (PCA), which provides an orthogonal decomposition of the data, where the eigen vectors are sorted by amount of covered variance. An illustration of how PCA operates is presented in Figure 4.2(a) where the scatter plot in the rotated coordinate system is presented in 4.2(b). Here the multiple measurements and low dimensionality (2 variables) makes it easy to identify the variance components. An introduction to multivariate data analysis and PCA is provided in many textbooks. The description by Hastie *et al.* [109] is recommended as it also gives an application-oriented description, and discusses alternative decompositions

In Paper F the first few principal components are used to inspect the separation between classes. Because the groups of samples only differ by their astaxanthin concentration, it was comforting to see that the pellets were separated by the first few components. Furthermore the results presented in Figure 4.2(d) shows that PC2 and PC4 gave a separation ordered by the hierarchy of the concentration levels. This is a very good starting point for the construction of linear models.

PCA has been used for dimensionality reduction in Paper B, as there is no analytical expression for the time development of the SLS features during fermentation. So, to make a compression of the time developments of the optical signals, with 2^3+3 time resolved measurements, the signal was decomposed into the first three PCA components.

While PCA provides the most compact description of the data, the variance of

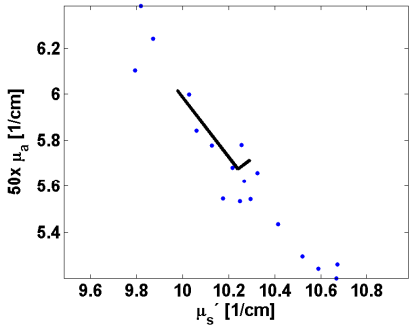

(a) Scatter plot of optical properties as measured with the SLS instrument, the black lines are the two principal components. $n = 19$, $p = 2$

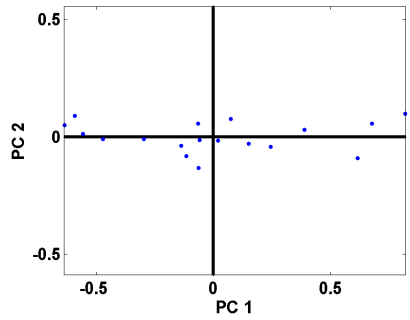

(b) Scatter plot of the data from Figure 4.2(a) in the rotated coordinate system determined by PCA. $n = 19$, $p = 2$

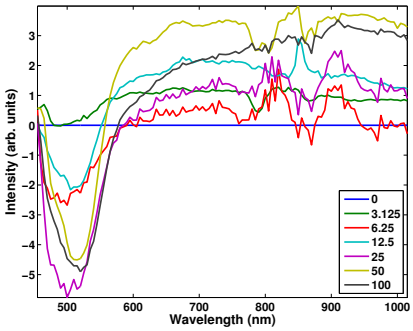

(c) Reprint of Figure F.8(b), in Paper F. The difference in mean reflection spectra from the concentration level of 0 ppm using the SuperK setup, $n = 70$, $p = 112$.

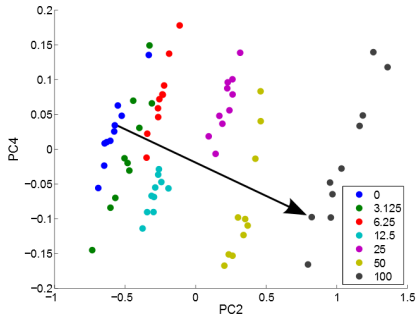

(d) Reprint of Figure F.9(b), in Paper F. Scatter plot of synthetic astaxanthin coating using PC2 and PC4 from a PCA on whole image samples using the SuperK, $n = 70$, $p = 112$. The black arrow indicates the direction of increased astaxanthin contents.

Figure 4.2: *Examples of PCA. A simple illustration of the principle on a 2D dataset in figure (a) and (b). Figure (c) and (d) shows the more complicated scenario from Paper F.*

interest may not be described by the first components. This is, in part, because PCA is an unsupervised method, meaning it does not use information on the response variable. The leads to two weaknesses of the method. Firstly, the principal components are influenced by the cardinality of the measured data. If the data set has a non-uniform distribution of samples, the weight of the components may shift accordingly. Secondly, the principal components may not pick up on a variance in the data which is correlated to the intended output. One way to overcome these limitation is by supervised methods, which use the correlation between the measurement data and the response variable.

4.3 Regression methods

The objective in Paper F was to investigate the predictability of astaxanthin contents from hyperspectral reflectance images. To accomplish this, several different regression models were constructed. based on features from the hyperspectral reflectance images. It is outside the scope of the thesis to cover all of these methods, but it is instructive to investigate the basis for constructing these models. This will entail considerations between data design and parameter extraction from the samples in a context relevant for broadband material characterization.

In Paper F, the focus was on linear regression models. The only change between samples, was the concentration of astaxanthin. In accordance to Lambert-Beer's law (Equation 3.1), the light absorption was assumed to be linear with astaxanthin concentration. Letting y denote the predicted concentration, the models may be formulated as

$$y = \mathbf{x}\boldsymbol{\beta} \tag{4.1}$$

where $\mathbf{x}$ is a vector with features deduced from the measurement, the length of the vector is the number of features deduced from each measurement (p). Thus the objective is to calculate the optimal value of $\boldsymbol{\beta}$ which is the coefficient vector, of length p. Each entry in $\boldsymbol{\beta}$ quantifies how significant the related variable is for the regression model. For the notation, a superscript on $\boldsymbol{\beta}$ refers to the coefficient vector for a specific model.
The regression models are built by having a number, (n) of measured samples with known astaxanthin contents; the known contents are combined in the vector $\mathbf{y}$ of length n. For these samples, the measured features are combined in the matrix $\mathbf{X}$ with n rows and p columns.
The most straight forward approach for a linear model is the Ordinary Least

Squares (OLS) solution in which the coefficient vector is given by

$$\boldsymbol{\beta}^{\mathrm{OLS}} = \underset{\boldsymbol{\beta}}{\operatorname{argmin}} \left(\|\mathbf{y} - \mathbf{X}\boldsymbol{\beta}^{\mathrm{OLS}}\|_2^2 \right) \tag{4.2}$$

$$\Rightarrow \boldsymbol{\beta}^{\mathrm{OLS}} = (\mathbf{X}^T\mathbf{X})^{-1}\mathbf{X}^T\mathbf{y}. \tag{4.3}$$

As part of the experimental design, it is evident that the number of measurements and concentration levels are smaller than the number of wavelengths. For these problems ($p > n$) the inverse of $\mathbf{X}$ does not exist, and some form of reduction of the measurement data is necessary. Increasing the number of measurements is one approach. However, knowing the difference in absorption spectra (Figure F.7(a)), it is evident that the spectrum of oil with added astaxanthin only differs from unadulterated fish oil in a few spectral regions. Because of this, the focus should be on finding the best lower dimensional space that would explain the variation in the response variable $\mathbf{y}$. Both of the following methods reduce the dimensionality of the initial measurement data, but in different ways.

4.3.1 Partial least square regression

As indicated by the black arrow in Figure 4.2(d), the scores of PC2 and PC4 can provide a monotonic ordering of the samples by their astaxanthin contents. Such an ordering is not present in the original wavelength data presented in Figure 4.2(c). This indicates that it is possible to create a linear model between the new "latent" variable and the response variable (astaxanthin contents). As discussed previously one way of creating this linear mapping, and possible dimensionality reduction, is using PCA[1]. PLS regression [109] works in a very similar way, but instead uses the correlation of variance from the measurements ($\mathbf{X}$) *and* the response ($\mathbf{y}$). Because of this, PLS may be more direct to pick up on the relevant variance in the measurements for predicting the response variable. Both PCA and PLS create a new, ordered orthogonal basis, but as has been explained, the ordering and direction of PLS includes information from the response variable. Though both methods may span all the variance in the data, only a few latent variables are mainted for modelling. By operating on a reduced dimensional space, PLS succeeds in obtaining more generalisable models and avoids overfitting. The number of dimensions for PLS is referred to as its latent components. The optimal number of latent components for a given dataset may be determined by comparing their prediction errors on a set of unseen data. For data campaigns which suffer from fewer measurements than variables, the number of test sets may be boosted by re-sampling the data. This

[1] If the linear regression model is created directly on the PCA components, as motivated in Figure 4.2(d), the technique is called PCA regression.

may be conducted using bootstrapping, or different forms of cross validation as performed in Paper F.

4.3.2 The elastic net

Another way to reduce dimensionality is by selecting only a few components of the original measurements' features for prediction. One way of doing this is by penalising the coefficient vector ($\boldsymbol{\beta}$) to only maintain few variables with a significant contribution. This approach is taken by EN[110], where $\boldsymbol{\beta}$ is given by the criteria

$$\boldsymbol{\beta}^{\mathrm{EN}} = \underset{\boldsymbol{\beta}}{\operatorname{argmin}} \left(\|\mathbf{y} - \mathbf{X}\boldsymbol{\beta}\|_2^2 + \lambda_2 \|\boldsymbol{\beta}\|_2^2 + \lambda_1 \|\boldsymbol{\beta}\|_1 \right) . \tag{4.4}$$

The EN contains two penalising terms, the l_2 norm which is inherited from Ridge regression, and the l_1 norm which is used in LASSO regression. Both of these form solutions which limit the number and weight of entries in the coefficients vector. They effectively work in different ways however. Ridge regression reduces the overall weight, and indirectly the contribution of correlated variables. In comparison LASSO term is more prevalent to set the weight of insignificant variables to zero. EN is a merger of the two and can produce both effects, but as it has more degrees of freedom it may require more training. For EN, the tuning coefficients λ_1 and λ_2 are decided upon similarly to the number of optimum variables in PLS.

4.4 Combining broadband characterisation and sparse quantification

The intent with the different measurement instruments (SLS, PToF and hyperspectral imaging) has been to develop broadband characterization platforms. However for an actual industrial implementation, measurement speed and instrument costs are important aspects. In this chapter, different considerations in design and evaluation of the measurement campaign have been discussed. The different approaches to quantification of the most important variables have been addressed, and an objective quantification of these can lead to cheaper and better characterizations for a specific production process.
By objectively quantifying the most significant features, such as wavelength or optical properties (phase function, speckle, scattering). Because some are completely omitted, as the coefficient value is zero, it may be used directly to optimize the instrument and data acquisition. If the only significant features

prove to be the phase function or the speckle properties, HDR imaging may be avoided and only a single significant intensity level on the camera needs to be captured. Similarly, data acquisition may be reduced by only capturing the most relevant wavelength. Lastly, the sparse models may also be used to alter the hardware design itself by focussing on single wavelength light sources or detectors dedicated to the property selected by the EN model.

In Paper B the significance of wavelength was investigated in a measurement campaign designed as a factorial study, and the wavelength significance was quantified by ANOVA and MANOVA.

For Paper F, it was evident that linear models could not be solved without some form of dimensionality reduction. Two regression methods have been discussed in this chapter. Of these the EN is advantageous in that it specifically sets the contribution of some variables to zero. This information can be used to optimize the instrument design by avoiding the acquisition of unimportant information. In comparison, PLS still relies on capturing all variables, and dimensionality reduction takes place only in the new transformed space.

Chapter 5

Instruments for broadband characterization

This chapter gives an introduction to the instruments used for material characterization throughout the PhD. As the majority of the instruments are centred around the use of supercontinuum light sources and AOTFs the first two sections are devoted to these topics. The wide tunability of the combined light source has provided an excellent tool for broadband characterization of material properties. Following this the different instruments which have been used are described.
The first instrument is the SLS platform developed at DTU Compute. The instrument has been used for the Papers A, B, C, [12], [13] and, [83]. This dissertation gives a through description on the instrument, its development of it have been a major part of this Ph.D. project. For this reason, the description is more extensive than those of the other measurement platforms. Following this, the PToF spectrometer at Lund University is described. The description covers the measurement principle of time-correlated counting which is used to measure the PToF distributions. The instrument was used for the Papers E, D, [11] and, [7]. Lastly, there is a presentation of the instrument for hyperspectral imaging using diffused laser light. instrument is present which was used in a comparative study for quantification of astaxanthin contents in fish feed in Paper F.

5.1 Supercontinuum generation

The application of supercontinuum light sources has been a consistent component of the Ph.D. project. The light source combines the following features, tight beam profile, short temporal pulses and a broad spectral profile, all in an easy to use instrument. The wide versatility of the supercontinuum light sources has been the key to the broad range of techniques which have been investigated throughout the Ph.D..
Supercontinuum generation refers to the significant spectral broadening which may be exhibited by light when interacting with a material. The first observations of supercontinuum generation were reported in the 1970s by Alfano and Shapiro[111]. The supercontinuum is generated due to higher order terms in the materials susceptibility, where the first order term is related to the material's refractive index. The form of the interaction was not covered in Chapter 3 as it is outside the scope of this thesis. The supercontinuum is generated by a combination of many optical phenomena, of which self-phase modulation and optical solitons are among the most exotic. However, one shared property of these phenomena is that they first become significant when the electric field is very strong, and for this reason, the effects are not seen under normal circumstances. Furthermore, the light must be confined in both space and time sufficient time to interact and create the broad spectrum. For most materials the process will terminate quickly due to the different propagation speed of the generated light. The propagation speed as a function of wavelength is called the material's dispersion, and describes the material's refractive index as a function of wavelength. For this reason, it was not until the development of Photonic Crystal Fibre (PCF)s in the late 1990's that the process could be controlled well enough. The first supercontinuum generation in PFCs was demonstrated by Ranka, Windeler and Stentz[112]. PCFs provide a high spatial confinement as the beam propagates in the fibre core ($\sim$ 5 μm) - a common feature for optical fibres. The advantage of PCFs is that the dispersion properties can be tailored so that the difference in propagation speed by the generated light is minimised. In this way, the light pulse intensity is kept high so the supercontinuum generation can evolve to form a broad spectral profile. The temporal overlap is furthermore ensured by the cross wavelength interaction which locks the propagation of red and blue shifted light. Although supercontinuum generation is complex, it is know sufficiently well to be modelled, and to create light sources with new properties as summarised by Thomsen *et al.* [113]. A review of developments in supercontinuum generation is provided by Dudley, Genty and Coen[114], who give additional details about the complex optical interactions.

The key steps for the creation of a supercontinuum light source are shown in Figure 5.1(a). The process is initiated by a fibre laser, typically operated at 40 or 80 MHz, referred to as the "seed". A light source with an upgraded "Pulse

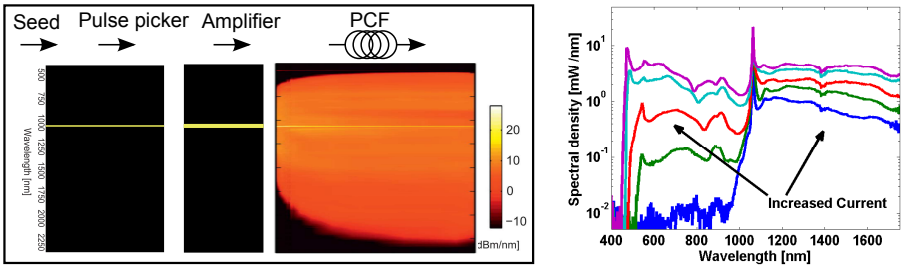

(a) Key components for super continuum generation. Starting with a low-power seed laser which is amplified before entering a PCF which generates the broad spectrum[115].

(b) Supercontinuum spectrum for different pump intensities.

Figure 5.1: *Supercontinuum generation*

Picker" ability for adjustment of the repetition rate was used for the technical report E. The pulse picker is positioned at this stage in the process due to the fairly low pulse power. Afterwards the light intensity is dramatically increased by all-fibre integrated amplification. The actual supercontinuum generation is only in the last few meters of optical fibre in the light source.
In Figure 5.1 two ways of observing the non-linear nature of supercontinuum generation are presented. The generation of the spectrum as a function of fibre distance is presented in the right hand part of Figure 5.1(a), reproduced from Møller *et al.* [115]. Here it is seen that the spectrum develops mostly in the start of the fibre and, in some sense, it converges or equilibrates. Similarly the spectrum may be investigated as a function of laser amplification (i.e. the current in the amplifier) as shown in Figure 5.1(b). Here it is seen that the spectral density changes in a non-linear way. For the present system, the pulse energy is at first pushed upwards towards the infra red, and then light strats being generated in the visible spectral range. Because the spectra changes non-linearly, the source power was kept constant in Paper F where absolute intensities in the recorded hyperspectral imaging was used for quantitative inspection. The measurement precession was instead increased by passively monitoring the intensity of the wavelength filtered output.

Even though the light generation is complex, is combined in a simple turn-key instrument, replacing bulky free space lasers such as optical parametric oscillators. For this reason the success of supercontinuum light sources is derived not only from their list of hardware specifications, but just as much from their ease of use. A number of companies provide commercial solutions, and the most versatile suppliers are NKT Photonics A/S (Birkerød, Denmark), Fianium (Southampton, United Kingdom) and Toptica (Munich, Germany). The

main application areas of the light sources are within the fields of optical confocal microscopy and optical coherent tomography where the broad spectral range is used.[1] Due to their short temporal width they are also used in fluorescence lifetime imaging, and in light detection and ranging (LIDAR).
When it comes to measurement within diffuse optical spectroscopy in particular, supercontinuum sources have been used previously for the classical double integrating sphere measurement technique as presented by Wang *et al.* [116] and for PToF spectroscopy by Swartling *et al.* [117].

5.2 Wavelength filtering and selection

For broadband material characterization the supercontinuum light source may find numerous applications, but as the light source creates a broad spectrum, some form of filtering is necessary to separate the different wavelength contributions. Wavelength filtering may be applied either between the sample and the light source, or between the sample and the detector. Throughout this Ph.D. the light source has been used with different AOTFs using a SuperK SELECT (NKT Photonics A/S, Birkerød, Denmark) which was positioned between the light source and the sample.

In this section the operating principle of the filtering units is presented first. Following this, the characterization and calibration of the AOTFs is described, which was important for the use and development of the SLS, PToF and hyperspectral imaging measurement techniques. Finally, two are section reserved to describe new investigations into extending the dynamic wavelength range and polarization direction of the combined filtering units and delivery system. Extension of the wavelength range is important for a successful implementation of the measurement platforms as it extends the wavelength range beyond the instruments specification. The direction of the filtered light's polarization is important because it affects the phase function properties, as is described in Section 3.1.3.

The most widely used alternative to AOTF is filtering by dispersive optics such as prisms or gratings; an example of this mounted on the detector side of the sample is given by Johnston and Lehmann[118]. The advantage of filtering the source is typically a reduction of the total power to which the sample is exposed.

[1] www.nktphotonics.com/supercontinuum_publications

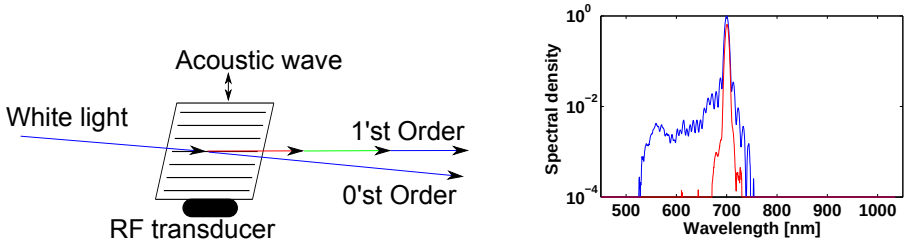

(a) Concept of AOTF filtering, the first order diffracted light is collected by an optical fiber (the FDS).

(b) Spectra recorded for the AOTF filter box with and without a FDS

Figure 5.2: *Principle and effect of AOTF filtering.*

5.2.1 AOTF filtering principle

The wavelength filtering of an AOTF relies upon Bragg diffraction, an effect which arises in materials with a periodic structured. The discovery of this effect led to W. L. Bragg being awarded the Noble Prize in Physics in 1915, because it enabled measurement of crystal lattice spacings. As the name suggests, an AOTF imposes an acoustic wave onto the material. The properties of the combined lattice structure from the crystal together with the acoustic wave was theoretically described as early as in 1922 by Brillouin [119]. However, generating the stable and persistent waves is not trivial. It was not until the development of piezoelectric transducers that the acoustic properties could be controlled well enough to widespread use of acousto-optical crystals. A review of the technology is given by Gupta[120] describing crystal types, operation, and the wavelength range covered by different materials. A general text book introduction is provided by Bass[121]. Today acousto-optical components are used for wavelength filters, beam deflectors, intensity switches and wavelength modulators.[122, 123]

The acousto-optical filter is illustrated in Figure 5.2(a). The incoming white light beam enters the crystal, where it is diffracted by the superimposed crystal and acoustic periodicities. The great advantage of this filtering principle is that the direction of the first order diffraction is largely wavelength independent.[124] The diffracted light is collected by an optical fibre; this setup is referred to as the FDS, which collect the light and redirects it to the point of measurement. Because the light sent to the sample is filtered without any need for mechanical movement, the AOTF provides a filter which is rapid. The diffraction efficiency of the AOTFs is typically $\sim$ 90 % of the output polarization making it an effective filtering process. The combination of wavelength independent geometry

and high filtering efficiency have also lead to the development of hyperspectral imaging based on acousto optical filtering[55, 56, 57]. The primary limitation of this approach is the relatively low numerical aperture imposed by the active area of the AOTF.

A transmission spectrum of an AOTF filter is presented in Figure 5.2(b) with and without coupling into the FDS. From Figure 5.2(b) it is seen that spectral purity is significantly improved by applying a spatial filter as part of the FDS. The spatial filter removes the side loops efficiently, and shrinks the Full Width at Half Maximum (FWHM) of the profile. This is accomplished while retaining a high filtering transmission of typically 75 % of the peak wavelength. A comparison of AOTF and prism-based filtering has recently been reported by Farina *et al.* [125]. The strength of the side-bands of the reported spectra suggests that a multimode fibre was used for coupling the beam from the AOTF, which results in an increase of both bandwidth and side lobes. This shows that a detailed knowledge of all aspects of the instrumentation is essential to make full use of the technology.

5.2.2 AOTF wavelength calibration

As has been mentioned, the filtering technique relies on piezoelectric transducers to create the acoustic wave. The transducer is driven by a Radio Frequency (RF) driver, typically a variable-frequency driver using voltage controlled oscillators or Direct Digital Synthesizer (DDS). The latter is commonly used for AOTFs as it enables multiple signals to be applied simultaneously, which transfers to multiple transmitted wavelength. The transmitted wavelength depends upon the frequency of the RF signal applied to the AOTF. This dependency is called the "tuning curve". The tuning curve is calibrated for each crystal, and after reconfiguring a crystal, the transmission wavelength can be varied a little by adjusting the angle between input beam and the crystal. A calibration is supplied at purchase, but as part of this Ph.D. involved exchanging crystals and carrying out field measurements, the calibration procedure was carried out on a routine basis. Because wavelength filtering takes place just after the light source, calibration may be performed simply by directing the output of the AOTF filtering unit into a spectrometer. A integrating sphere is typically used to collect the output, which provides ease of use and ensures low enough intensity levels to avoid damage to the spectrometer. The spectrometer is a USB 2000+ (XR1 grating, Ocean optics, Duiven, Netherlands) which covers the very broad spectral range from $200-1050$ nm. The bandwidth increases as a function of wavelength, but for these measurements only the peak intensity was of importance. The integrating sphere is a IS200 (Thorlabs, Göteborg, Sweden). By scanning the RF frequency of the DDS through the range covered by a particular

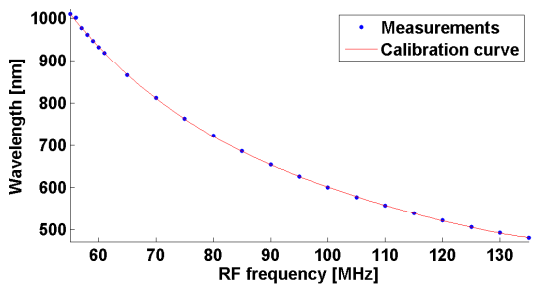

(a) Typical tuning curve for wavelength calibration.

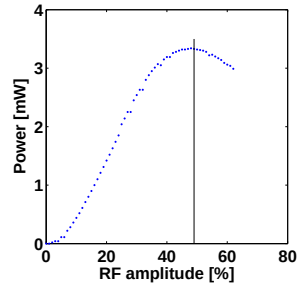

(b) Transmission power vs. RF amplitude.

Figure 5.3: *Typical characteristics for AOTF crystal wavelength and transmission power. This particular crystal was used for the Papers A,B, C and F.*

crystal and recording the corresponding spectra, the peak of the transmission is measured with respect to RF frequency. An example of such a calibration curve is given in Figure 5.3(a). The tuning cure is typically parametrised as a polynomial, and the coefficients are transferred to the measurement program.

While the RF frequency specifies the transmitted wavelength, the transmission efficiency of the AOTF is determined by the amplitude of the RF signal. This dependence is shown in Figure 5.3(b), which shows that there is an optimum RF amplitude for the transmission efficiency. This is a typical effect for AOTFs[126]. This value is also wavelength dependent, and a calibration is supplied at purchase. Unlike the tuning curve, the amplitude calibration is largely unchanged by adjustments to the crystal.

As part of the measurement routines for both the SLS and PToF spectrometer it has been necessary to adjust the power levels for the combined light source and filtering system. This may be done directly on the supercontinuum light source, although then, the wavelength variation is not linear, as was shown in Figure 5.1(b). A faster and more stable method has been to vary the RF amplitude instead. For this reason, measurement routines were developed which automatically adjusted the power level for the measurements. This was used in the Doctoral by Skytte [36], where the unattenuated illumination system caused overexposed images. This effect depended on the optical properties of the sample, as the detected intensity increases when scattering increases. For Paper F the power was adjusted at some wavelength ranges to simplify the measurement routine. By reducing the most intense wavelengths the entire spectrum was recorded for one exposure time of the camera and HDR imaging

was avoided. The intensity response of a mixed combination of pellets was investigated prior to the actual measurement campaign to ensure the diversity of the different samples could be resolved. For the PToF spectrometer it was necessary to operate with a significantly larger dynamic range of the attenuation level, for this reason the intensity was primarily adjusted using fibre coupled variable attenuators.

While different RF drivers may be used to perform the wavelength selection, the choice of RF driver may influence the optical signals' wavelength and power stability because of drift and jitter in the RF signal. Also, particularly for broadband material characterisation, the choice of RF generator is important for wavelength selection speed. This may affects the possibilities of the measurement. The acoustic waves have a rise/fall time which is under a microsecond, and so the selection speed is often limited by the control mechanism for the RF generator and not the acoustic wave itself. Throughout this Ph.D. the interaction with the RF generator has been via. software communications which typically have a response time of some milliseconds under an undedicated operating system as Windows 7. Procedures for validating the communications speed are essential for creating the final measurement platform and ensuring a high quality in the data produced. The different procedures have been a major task in the creation of measurement software for both the SLS platform at DTU and the PToF spectroscopy software created during my external stay.

5.2.3 Extending the tunable wavelength range of AOTFs

As part of the Ph.D. project, it was investigated whether the filtered wavelength could be extended beyond the instrument's specifications. The SuperK SELECT was originally designed to cover the range from $500 - 900$ nm and it is of general interest to determine the limits of the instrument. Particularly for the quantification of absorption in dairy products, it was of interest to also cover the absorption of fat below 500 nm and the water absorption peak at 970 nm, so as to investigate the accuracy of the absorption measurements in Paper D and C.
As discussed in the previous section, the supercontinuum light source generates a broad spectral range $\sim 455 - 2400$ nm and the range of wavelengths which may be selected is determined by the filtering unit (SuperK SELECT). In the filtering unit, the dynamic range of an AOTFs is typically one octave, where the limiting factor often is the dynamics of the piezoelectric traducers.[123] This may not a hard limit though, and in this subsection the results of driving the crystal outside its specification range are presented.

The crystal used for Paper C is specified for the wavelength range 500 nm -

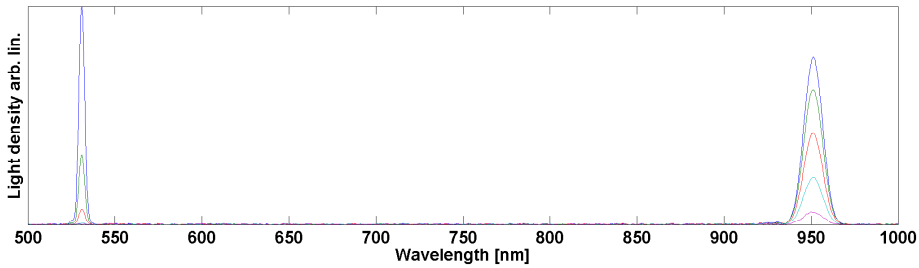

(a) Measured spectra at different RF ampltides, the power of the two peaks is given below.

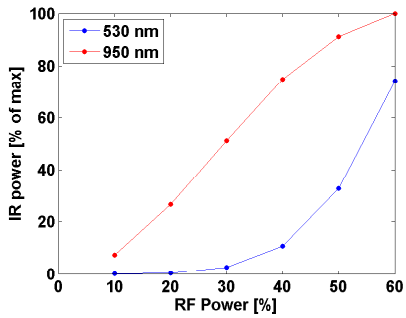

(b) Relative transmission efficiency of the intended (NIR) peak.

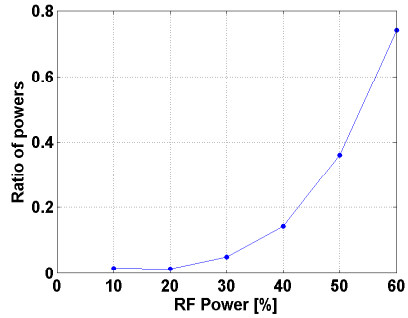

(c) Ratio of integrated peaks, showing that the unintended green contribution vaniches at low RF ampltides.

Figure 5.4: *Optical spectra taken while driving the AOTF crystal at* 950 *nm, where the specification limit is* 900 *nm.*

900 nm. An example of the transmission spectra for the crystal when operated outside the range covered by its specification is presented in Figure 5.4(a). In this case, a wavelength of 950 nm is intended. It is evident that an additional peak in the green part of the spectrum has appeared. When the wavelength was set below that covered by the specifications, no additional peak was present.
For the measurements presented in Figure 5.4(a), the RF amplitude was altered for each of the different coloured curves, and the power of the two peaks was calculated. The results are presented in Figure 5.4(b). From this it is seen that the two effect don't scale linearly as was seen from Figure 5.3(b), and more importantly that the unintended peak rises slower as a function of filter amplitude. Thus the RF amplitude may control the ratio between the two peaks, as seen from Figure 5.4(c). For the measurement present in Paper C the crystal was operated with a reduced amplitude of 25 %.

To investigate this further, the RF signal generation of the DDS was investigated

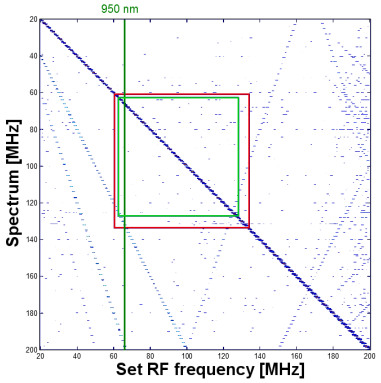

(a) Electrical characteristics of the DDS. The diagonal is the intended frequency. The background level has been made transparent.

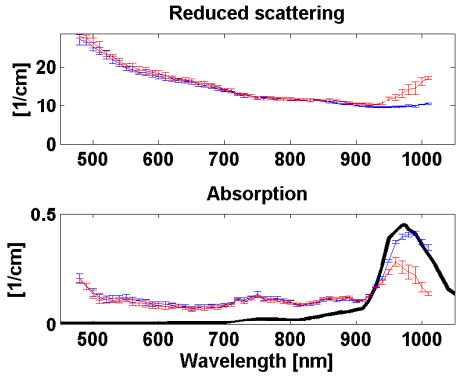

(b) With reduced RF amplitude

Figure 5.5: *Measured optical properties for semi skimmed milk, with different filtering powers applied to the AOTF crystal.*

with a spectrum analyser (8753ES, Agilent Technologies, California, USA). The frequency analyser measures the frequency components in a given RF signal by performing a hetrodyne detection. The measured frequencies are presented in Figure 5.5(a), the intended RF frequency is the high intensity diagonal. However it is also seen that some additional, weaker lines cross the image. As an overlay on the measured RF profiles, the frequency range given in the specification is marked as a green box. The red box illustrates the range used for Paper C. It can be seen that one of the unintended lines crosses the extended frequency range of the crystal used for Paper C.
These measurements suggest that the additional peak is not caused by the limited range of the piezoelectric transducer but arises from the electrical characteristics of the DDS. This effect is only present when the crystal is driven outside the range given by its specifications.

The effect of recording the optical properties using the maximum transmission RF amplitudes is presented in Figure 5.5(b) (red curve), it is seen that the reduced scattering exhibits an increase in the IR range beyond the range for which the crystal is specified. The error bars shows the standard deviation of six repeated measurements. Similarly, the measured absorption level is significantly below that of water, reported by Hale and Querry [127].
The optical properties of the same sample are shown again in Figure 5.5(b), but now with the RF amplitude reduced to 25 %. From this it is seen that the scattering level now falls continuously as a function of wavelength, while at the

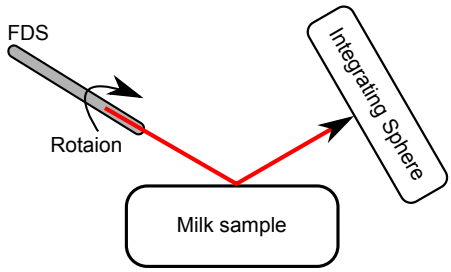

(a) Illustration of the measurements settings for investigation of the lights polarization direction.

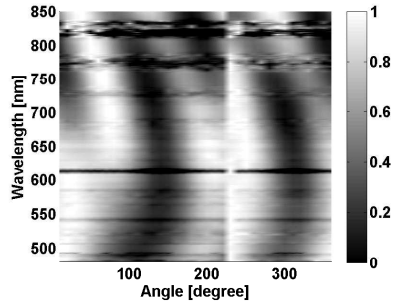

(b) Reflected intensity vs. FDS rotation angle measured with the setup in 5.6(a).

Figure 5.6: *Measurement of the polarisation direction for the AOTF filtered light after the FDS.*

same time the absorption level is now significantly raised, approaching the level of pure water in this spectral range.

With this knowledge, the RF amplitude was lowered for the measurements in Paper C to only 25 %, and the spectral range was extended to the 475 nm - 1020 nm. With this extended spectral range it was possible to the water absorption peak at $\sim$ 975 nm in the measurements, as well as absorption by fat below $\sim$ 500 nm.

5.2.4 Measurement of polarisation direction

The final consideration with the combined supercontinuum light source and AOTF filters is the polarization of the filtered light. The AOTF filter only diffracts one of the linear polarisation directions into the FDS. The FDS used for the SLS system is a non polarization maintaining VIS-nIR FDS (NKT Photonics A/S, Birkerød, Denmark). Although the fibre does not preserve the polarisation direction, it is preserved to some extent because the fibre is rather short (2m). For this reason, the polarization may be adjusted by simply rotating the fibre around its symmetry axis as is illustrated in Figure 5.6(a).

The direction of the light's polarization affects the SLS measurements in two ways. Firstly, the transmission into the samples is polarization-dependent, thus and this can be used to optimize the signal intensity on the CCD. This was discussed in relation to Figure 3.2(a). Secondly, the scattering phase function

is dependent on the polarization as was discussed for Figure 3.5(b).

To quantify the direction of the polarised light, the reflected intensity was measured as a function of both rotation angle and wavelength. An illustration of the experimental setup is presented in Figure 5.6(a). The filtered light was directed onto the sample in the same way as the SLS measurement is performed. The light reflected from the sample is collected by an integrating sphere, and sent to the USB 2000+ spectrometer. In this way, the wavelength dependence was recorded for different rotations of the FDS around its symmetry axis.

The relative transmission is displayed in Figure 5.6(b). Ideally, all wavelengths would have a minimum reflection for the same angular orientation of the FDS if the polarization direction were preserved. From Figure 5.6(b) it is seen that the angle showing the minimum transmission changes with wavelength, and it is not possible to create a single minimum for all wavelengths at once. The measurement also shows a number of blank wavelength intervals: however, this is a consequence of the measurement technique. It is not possible to transmit the full spectrum at once. To measure the effect at several wavelengths simultaneously, the AOTF is set to select eight wavelength. As described in the discussion of Figure 5.2(b) each selected wavelength only cause transmission in a narrow window around the centre wavelength. However, enough signal was present at in-between wavelengths to obtain the smooth results presented in Figure 5.6(b).

Because the direction of the polarization state is not preserved at the different wavelengths, the quantification of the phase function dependence has not yet been published. Polarization maintaining fibres are commercially available, and it will be of interest to implement such a fibre to extract additional information about the scattering phase function, and about the sample structural composition.

5.3 Static light scattering vision system

This section describes the combined instrument for performing static light scattering measurements. The development of this vision system for broadband material characterisation was specifically focussed on homogeneous samples of dairy products. As described in Chapter 2 this particular measurement technique was the initial motivation for the CIFQ project: the SLS instrument as a generalization of the commercially available Videometer SLS (Videometer A/S, Hørsholm , Denmark). The instrument has been used for the papers A, B , C [12, 83, 2, 13].

In the following sections, an overview of the instrument is given first. Second, the design considerations of the optical components are presented. This should make the ideas transferable to other wavelength ranges or applications. Then the measurement procedure is described, giving valuable information on the construction and use of the instrument. The data acquisition procedure is then presented, followed by a description of the measurement procedure, covering the steps for aligning the hardware components at construction, and how measurements are performed. Lastly, some examples of measurement results made with the instrument on dairy products are shown.

5.3.1 Outline of the instrument

An photograph of the SLS instrument is shown in Figure 5.7(a). Starting from the left, we see the monitor and computer used for instrument control and data analysis. Then comes the supercontinuum laser (SuperK Extreme EXW-12, NKT Photonics A/S, Birkerød, Denmark) followed by the filtering unit (SuperK SELECT, NKT Photonics A/S, Birkerød, Denmark). The filtering unit uses an AOTF and spectrally narrow fractions of the supercontinuum light can be freely selected in the range from 465 nm to 1030 nm, as has been described in the previous sections. The FDS (vis-NIR FDS, NKT Photonics A/S, Birkerød, Denmark) couples light from the filtering unit into the black measurement box on the far right of the image.

The measurement box holds the camera and sample as an isolated vision instrument. The configuration of the FDS, camera (AM-800GE, JAI, Miyazaki, Japan) and sample inside the box as is seen in figure 5.7(b). The sample is at the centre, with the light delivery fibre to the left and the imaging objective (LM50XC, Kowa Company Ltd., Nagoya, Japan) positioned above. The light is directed onto the sample at an oblique angle, and an image of the diffuse reflectance profile is captured. With this setup hyperspectral images such as were presented in Figure 3.7 are created. The SLS platform has been used for several field campaigns on dairy products, an image of the instrument setup for in-line measurement of the milk fermentation process is seen in Figure 5.7(c).

5.3.2 Optical design consideration

As was described in Section 3.2, the optical properties of the samples are expressed on different length scales. For this reason, appropriate design of the imaging systems is essential because it limits the range of samples which may

(a) Overview image of the SLS equipment.

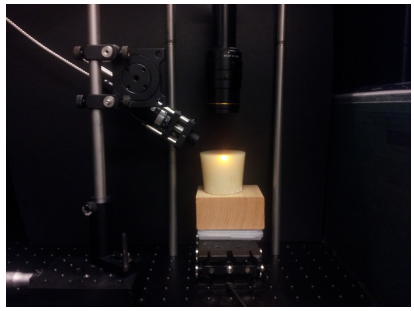

(b) Image of the measurement process conducted in a black enclosure for laboratory measurements

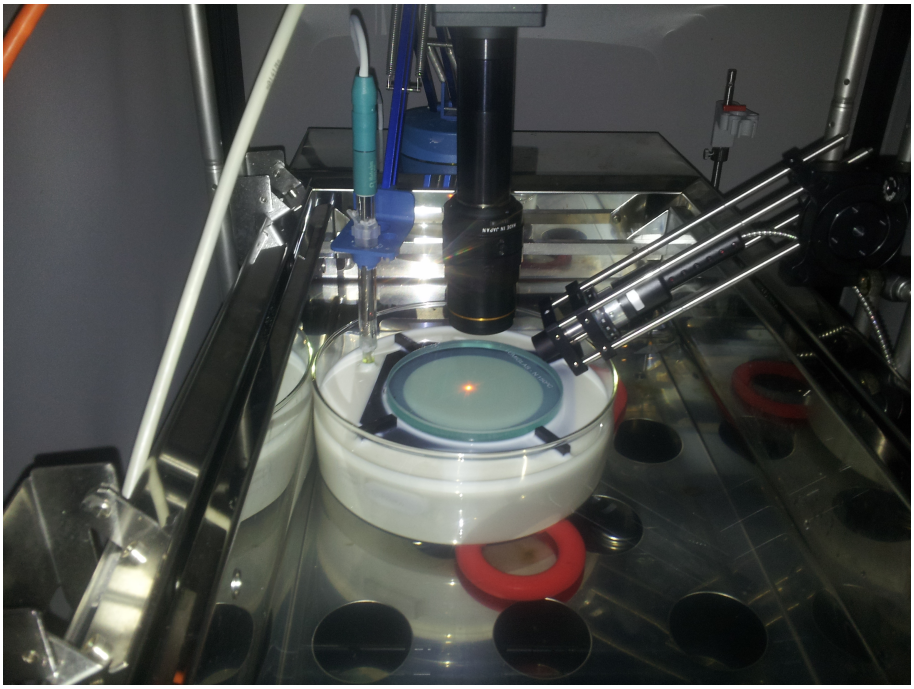

(c) Image of the measurement process during an in-line measurement of milk fermentation. The milk sample is located at the centre of the image, with the camera positioned above. The light delivery with the FDS is to the right and the pH probe to the left. All of this is placed in a temperature controlled water bath with a cover slip as would be used in an industrial production process. Measurement results are presented in section 9.2.

Figure 5.7: *Images of the SLS measurement platform*

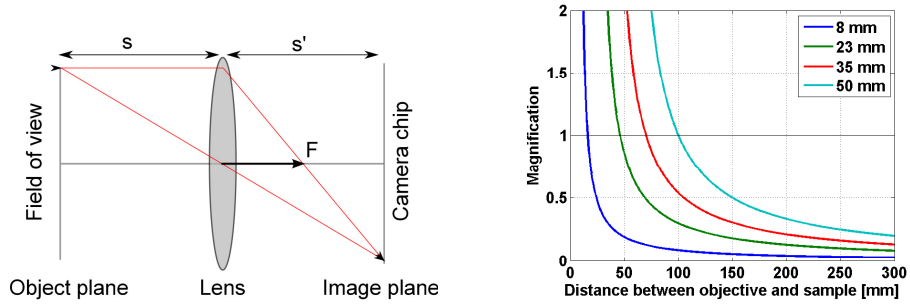

(a) Imaging by a thin lens, the lines are the parallelray and the chief ray.

(b) Magnification for commercially available pbjectives of different focal length.

Figure 5.8: *Considerations for design of the imaging system*

be inspected. This section describes the considerations taken into account in the final design of the SLS instrument.

Firstly, the instrument should allow measurements of samples which are **diverse** in terms of their optical properties. A range of dairy products from milk (0.5 $\%fat$) to yoghurt (3.5 $\%fat$) was chosen as the objective for these measurements; their industrial relevance was discussed in Chapter 2. To cover this broad range, high resolution industrial cameras (8 megapixel AM-800GE) were chosen.

Secondly, it is advantageous to **resolve single scattering effects**. This facilitates the measurement technique of OIR because the diffusion displacement is resolved. Simultaneously, this gives the opportunity to quantify both the speckle and phase function properties. Paper D reported the reduced scattering and absorption properties for the first time on milk and yoghurt products. With these results in mind, the expected diffusion displacement was calculated as a function of incidence angle, as was shown in Figure 3.2(b). The diffusion displacements are in the range of ~ 100 μm and upwards. To resolve this it was decided to design the imaging system with an image resolution of ~ 3.3 $\mu m/$, which for the present camera requires a magnification of ~ 1.8. This configuration was used in the paper C. This high magnification is probably at the limit of what may be accomplished without using a microscope.

Lastly, the instrumentation should have **industrial relevance**. The imaging objective should allow enough space between the front of the objective and the sample surface to hold a cover slip, which typically is ~ 10 mm thick. Along the same lines, there should be space for inserting the FDS with a proper focusing lens without obstructing the camera's view of the surface. An analysis of the

imaging process for an infinitely thin lens was performed to chose a proper imaging objective. The notation is summarised in Figure 5.8(a), introducing the distance to the object (S) and image plane (S') for a thin lens with focal length F. Following this notation, the image is in focus when the following criteria is satisfied

$$\frac{1}{S} + \frac{1}{S'} = \frac{1}{F} \quad , \quad M = \frac{S}{S'} \tag{5.1}$$

and M is the magnification for the configuration. The calculated magnification for typical values of effective focal length is presented in Figure 5.8. From these it is seen that long focal length lenses provides the longest working distance to the sample, and a $F = 50$ mm lens was feasible, hence the LM50XC from Kowa was chosen as one of the few high resolution lenses available for the large 4/3" chip size of the camera.

Image intensity corrections

The features extracted from the SLS images (phase function, speckle or by OIR) are all dependent on accurate quantification of the reflectance profiles without instrument perturbations. To accomplish this the IRF of both camera and imaging objective must be compensated for.

The first necessary correction to the image data is the spatially dependent camera readout noise. If this background signal is not subtracted during data acquisition it will cause undesired stitching artefacts between image regions with different exposure times.
This effect is constant, and may be measured while the instrument is being assembled, by capturing images with the imaging objective blocked. The noise has two contributions, an offset which may be adjusted, and a variance. The camera offset is set sufficiently high that the pixels produce positive values. The background intensity is different for each pixel, and one half of the CCD has a slightly higher noise level. Lastly, this background is affected by both the camera temperature and exposure time. For this reason, the calibration images are acquire after the camera have been turned on for some time, and the average value for 100 images is recorded for each exposure time in the HDR routine. The background images are subtracted from the captured images before scaling by the shutter time.

The second intensity correction is the spatially depended linear intensity scaling of the image called vignetting. This may be caused by both imaging objective and the camera chip. The objective can cause vignetting in two ways, either as a smooth scaling which is caused by non flat imaging onto the chip. The second

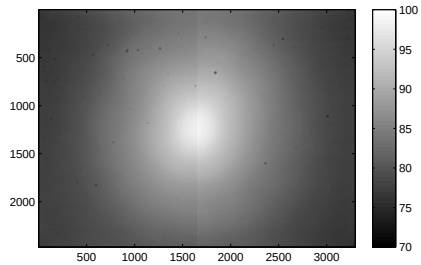

(a) Vignetting of the combined camera and imaging objective. Color map is in percent.

Figure 5.9: *Characteristics of the IRF for the camera and the imaging objective.*

is a physical block of the image field. This typically occur if the objective is not designed for the large chip size. Vignetting from the CCD chip arises because the detection efficiency is pixel depended. This can cause individual dead pixels or gradients in the image.
To quantify the vignetting of the SLS instrument the following procedure was used. An image of a flat white poster was acquired. The poster was positioned far behind the object plane and uniformly illuminated by the sun. An example of the vignetting transfer function is presented in Figure 5.9(a). From here it is seen that the vignetting has two contributions, one is an almost radial decreasing transmission profile which is caused by the imaging objective. The other contribution is again difference in sensitivity of the two parts that the chip is assembled from.

In this approach, in which the vignetting image is recorded by measuring light from an object far away, the light which enters the objective is fairly well described by a plane wave. However, the image-forming light during SLS measurements may not be well described by plane waves because the camera objective is positioned close to the sample when compared to the size of the entrance pupil. The vignetting correction may thus not be completely transferable to the SLS measurements. Alternative approaches have been proposed for microscope systems by both Bevilacqua *et al.* [128] and Leong *et al.* [129], though they still relying on a uniformly radiating subject. Lindberg *et al.* [82] proposed an alternative approach specifically for OIR which illuminates a homogeneous sample with a monitor from 4 directions. The sample was positioned in the actual instrument in contrast to our approach. I suspect there are still some improvements which can be made in this area. A last approach, is calculating the vignetting function by an actual numerical simulation of the entire process from tissue scattering to ray propagation through the imaging objective. These

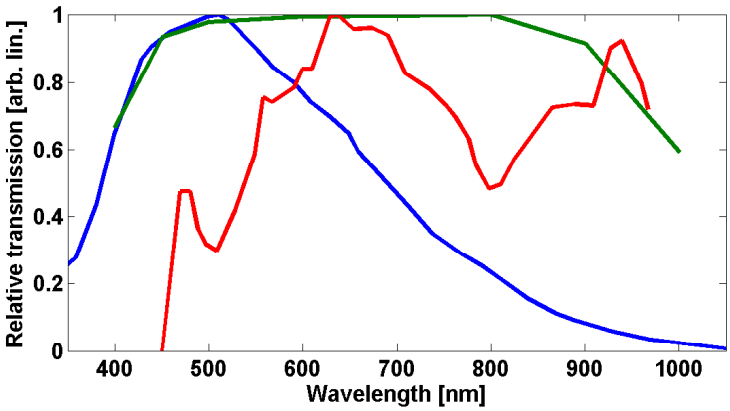

Figure 5.10: *Intensity response function for camera (Blue), bbjective (Green) and bombined illumination system (Red).*

options are available by commercially available optics analysis software such as Zemax® (Redmond, Washington, USA).

Wavelength range of the combined instrument

The wavelength range over which this instrument can be operated is given by the combined intensity transfer function of the different hardware components and the properties of the sample. The predefined wavelength dependencies of the instruments are depicted in Figure 5.10, which shows the slow decline of the silicon CCD chip in the NIR range. These intensity transfer functions are passive in the sense that they cause a linear scaling of the entire image during acquisition. The combined effect may be removed by performing a calibration against a standard, such as Spectralon® by LabSphere (North Sutton, New Hampshire, USA). However, the analysis techniques used in this work have specifically been focused on quantification of shapes rather than the absolute intensity response. Thus this normalization is not important for the work, though it effectively set a limit on the wavelength range of the instrument.

5.3.3 Data acquisition

The data acquisition routines are implemented as an extension to Videometer Lab (Videometer A/S, Lyngsø Allsé 3, 2970 Hørsholm , Denmark).

High dynamic range imaging

The SLS image data will by itself span multiple intensity decades, which makes it impossible to record with a single configuration of a CCD chip. The samples which exhibit a high degree og scattering also produce images which span the largest dynamic range of intensities. The peak intensity of the reflectance image increases with the amount of scattering, as does the effective attenuation of light away from the entry point of the beam. The ability to resolve the reflectance profile is essential for the analysing with the technique OIR. Similarly, in the work by Skytte *et al.* [12] and Sharifzadeh *et al.* [83] is makes it possible to quantify speckle and similar structural noise over the entire intensity range of the reflectance profiles. The intensity range spanned by yoghurt 3.5 % fat contents is an astonishing 65 dB on the camera! This huge span is cause by the combined intensity transfer functions of the light source, imaging objective, and camera chip together with the sample's optical properties.

To increase the dynamic range of the camera, images are captured using multiple exposure times and combined into a single High Dynamic Range (HDR) image for each wavelength. Today, the construction of HDR images has become a common application for smart phones where it compensates for the low quality CCD chips. There are multiple ways of combining the low dynamic range images, and a good textbook introduction is given in by Banterle *et al.* [130]. We apply a global image correction to each layer following the approach by Mann and Picard *et al.* [131] and Robertson *et al.* [132]. Both estimate a camera transfer function, and the final image is a combination of all the low dynamic range images. This approach is memory intensive, however, as it require all exposure times to be kept in memory simultaneously. For the present 8 mega pixels, at ~ 100 discrete wavelengths and floating point precision, is single exposure time takes up ~ 4 GB of memory. This could be reduced by capturing a single wavelength at a time. However, for the present instrumentation, this approach will entail a significantly longer data acquisition time, as changing the exposure time of the camera is time expensive. After changes of exposure time, the present instrumentation require acquisition of an additional to ensure the exposure was changed. Instead a hyperspectral "HDR filter image" is used during image acquisition, is illustrated in Figure 5.11 (**a**). The filter keeps track of which pixels were overexposed in the previous image layer and successively replaces the pixel values as the exposure time is reduced. At each layer the respective background noise from the pixel is subtracted and normalised to the exposure time. The method of generation is presented in Figure 5.11 (b), and a trace of intensity along a line of pixels is presented in Figure 5.11 showing a continuous profile across several decades of intensity.

The advantage of this approach is that the values at short exposure times don't

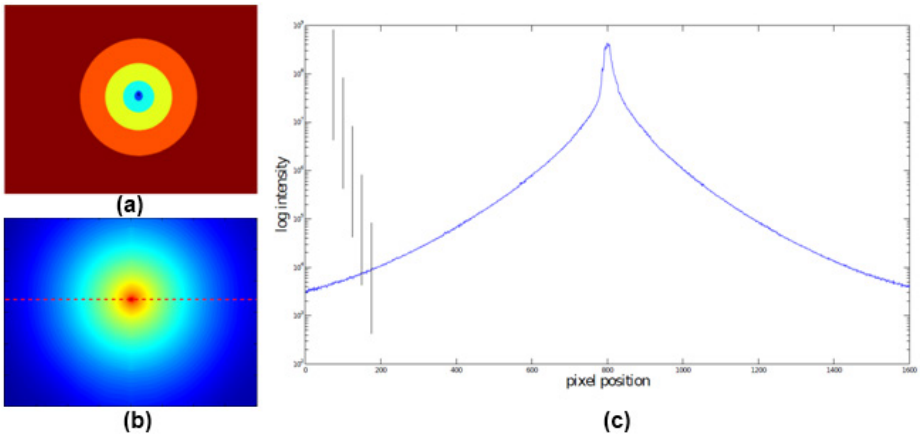

Figure 5.11: *Illustration of a HDR image construction of milk as reported in [15].* ***(a)*** *False color map in which each area uses the same exposure time.* ***(b)*** *Combined HDR image using the exposure times presented in* ***(a)****.* ***(c)*** *Reflectance values in a line across the image presented in* ***(b)****.*

accumulate noise from each of the stitching layers. It does, however, require a CCD chip with a linear intensity response. The technique is validated by the smooth shape of the reflectance profiles.

5.3.4 Measurement procedure

The measurement procedure has two stages. The first is the alignment of image field with the beam. This is carried out when the SLS instrument is under construction. The second is a height adjustment of the sample to ensure the camera is focused on the sample surface. An easy alignment procedure ensures high data quality, as it provides sharp and reproducible images.

Instrument assembly and alignment

During construction and assembly of the SLS platform, the first parameter to set is the incidence angle of the beam. This is done with an angular rotation stage. The specific angle is measured from images of the final setup, similar to that shown in Figure 5.7(b). To give a strong contrast between diffuse and single scattered reflectance, the light beam from the FDS is focused. This is performed with a 38 mm focal length achromatic lens (Edmund Optics Inc., Barrington,

(a) Image of the instrument during alignment of the camera and beam positions in the SLS instrument.

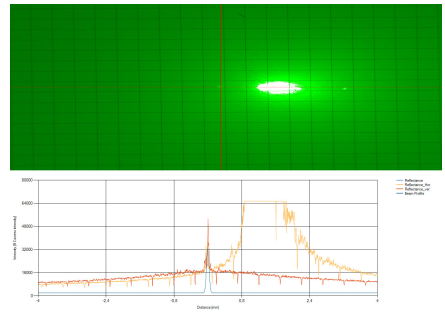

(b) Screen shoot of the alignment process from the userinterface. **Top** Camera image during alignment, **Bottom** image intensities along a line through the centre

Figure 5.12: *Illustration of the image calibration process, 5.12(a). Show the calibration target positioned upon a scattering object. 5.12(b) Shows the images of the calibration target as seen in the user interface during calibration.*

New Jersey, USA). The focal length is sufficiently long that the mounted optics may be positioned outside the imaging system's field of view. The achromatic nature of the lens reduces chromatic aberration which causes width of the beam waist and its location to be wavelength dependent. The lens is anti-reflection coated with the VIS-NIR coating from Edmund optics, covering the range from 400 nm to 1050 nm. If a smaller beam size were desired, a Newtonian telescope could be used for beam expansion prior to the focussing lens.

In the next stage, the optical beam is centred in the object plane of the imaging objective. To accomplish this the vertical position of the object plane must first be determined. This is done by focussing the imaging system on a calibration grid (R1L3S3p, Thorlabs, Gothenburg, Sweden). The distance between the grid and the imaging objective is adjusted using the lab jack seen in image 5.7(b). By shining the laser onto the sample, the grid is effectively illuminated from the back, as is seen in Figure 5.12(a). The optimum position is found by evaluating the contrast of the grid in the SLS images as seen from the user interface, Figure 5.12(b). In this way, the vertical alignment is ensured.
The overlap in the horizontal plane is accomplished by adjusting the combined XY-translation stages holding the FDS which may be seen at the bottom of image 5.7(b) bottom left. This can also be monitored from the user interface, where it is important to note that the largest intensity peak in the images is not from the glass surface. This arises from the sample the upon which the calibration grid is positioned. The true surface reflection is weaker and positioned in the centre of the image in Figure 5.12(b). The image presented in

5.12(b) is thus perfectly aligned. This procedure ensures an optimum alignment of the hardware. A further advantage of this approach is the ability to measure both the pixel size and lens distortion as a function of wavelength. This approach was first presented in Paper C.

Alignment during measurement

With the instrument pre-aligned as described, the only aliment during measurement is a vertical adjustment of the sample. This is necessary as samples do not necessary all have the same height. This last alignment process is therefore only necessary because the samples are not confined, which they would be in an industrial implementation. Due to the oblique incident beam, the sample surface is in focus when the SLS hot spot is centred similar to the alignment during construction with the calibration target. If the sample is position too low, the peak of the diffuse reflectance will shift towards the incidence direction of the beam, and vice versa if the sample is positioned to high. The lab jack is again adjusted until the reflectance is centred on the image.

5.3.5 Examples of measurement data

Examples of measurement data from the commercial dairy products in Paper C are presented in Figure 5.13. Each image is normalised to its maximum intensity to remove the differences in the intensity transfer function.

From Figure 5.13 it may be seen that the width of the profiles changes as a function of both fat content and wavelength. This is the most prominent differences between products, and is a result of the scattering properties.

Examples of the reflectance profile close to the entry point are presented in Figure 5.14, showing the difference in both phase function and speckle as the sample and wavelength are varied.
The shape difference is a recent discovery, and is addressed in the doctoral thesis by Skytte [36]. It is evident that significant changes occur as the wavelength varies, which may be related to the phase function properties previously addressed. For the current work, detailed measurements have shown that, unlike the reduced scattering properties, this change is not monotonic as a function of wavelength. However, as the scattering phase function is polarization dependent (see section 3.5(b)) and the light's polarisation direction for the present system is wavelength-dependent. The effect is currently not well enough controlled to form a solid conclusion. In future work, the elongation may be quantified by

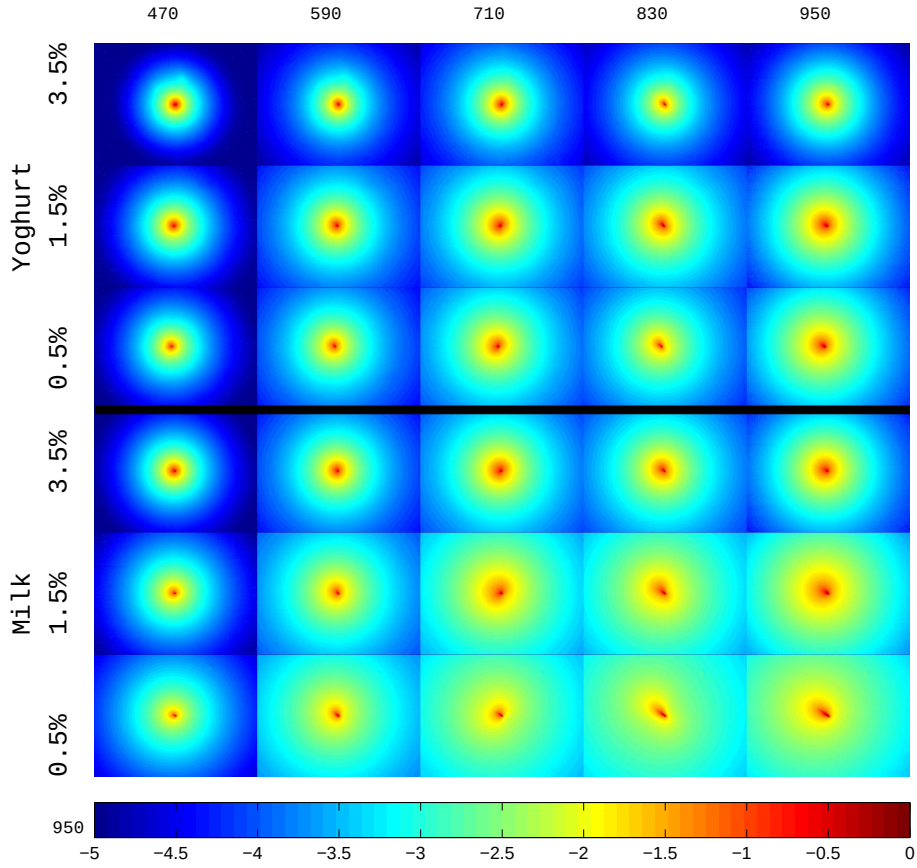

Figure 5.13: *Examples of diverse measurement results for different commercial dairy products presented in Paper C. Each row is from a single product, these are sorted by increasing fat contents with the highest at the top. Each column represents a given wavelength. The color map is a logarithmic scale and each individual image is normalised to the maximum intensity.*

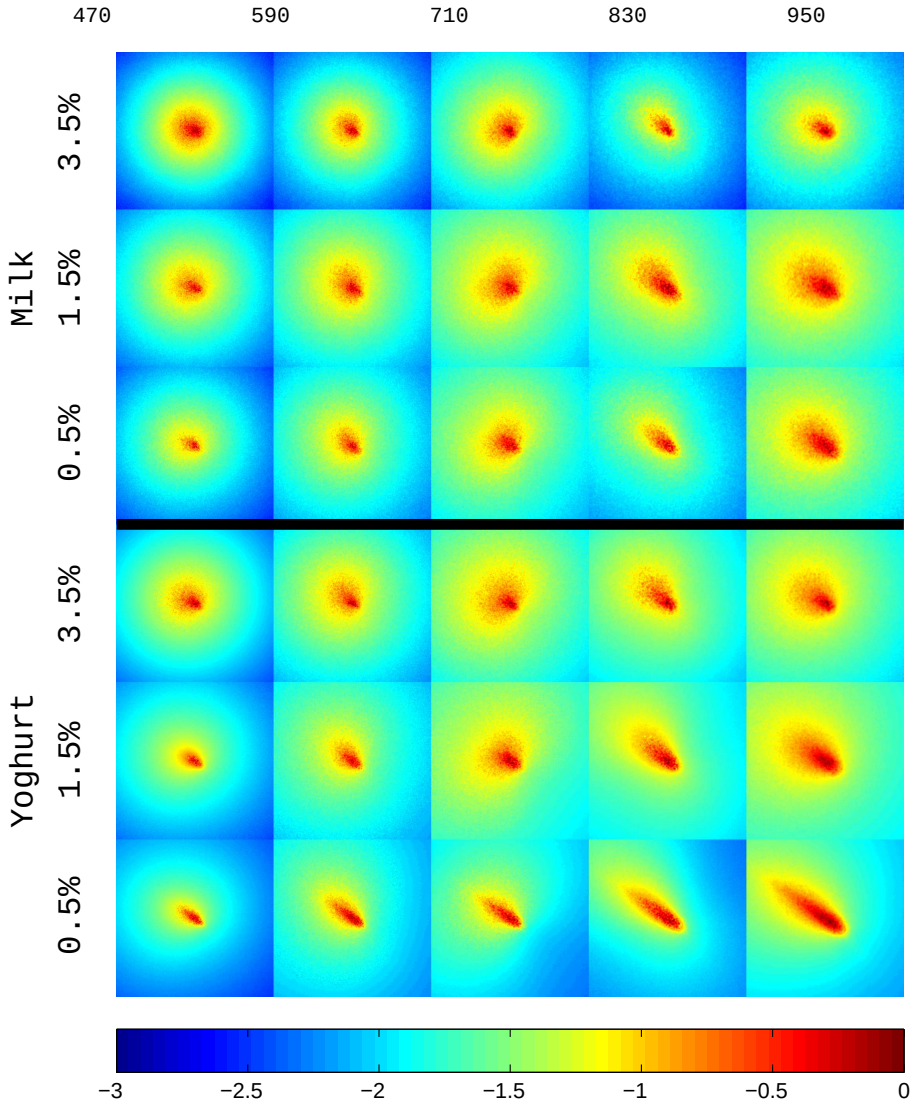

Figure 5.14: *Examples of the reflectance profile close to the entry point,* $[0.66 \times 0.66]$ *mm. The color map is a logarithmic scale and each individual image is normalised to the maximum intensity.*

statistical methods [36], or by physically-based models such as a phase function corrected diffusion model which has recently been presented[101]. Speckle properties have been addressed by Sara *et al.* [83].

5.4 Photon time-of-flight spectroscopy

This section describes the background for the work within PToF spectroscopy. Firstly an introduction to time resolved techniques is given. Following this, the technology used for Papers D, E, [7] and, [11] is described.
A photograph of the laboratory and instruments is given in Figure 5.15.

5.4.1 Introduction

PToF spectroscopy relies on resolving the temporal change a photon density wave undergoes when passing through a diffusive medium. The measured Time-of-Flight (ToF) distribution may then be inverse modelled using the methods presented in Chapter 3. Realising that the speed of light is $\sim 3{\cdot}10^8$ m/s the measurement technology is more extreme than the static light scattering previously discussed. Because of the high speed of light, the time-resolved measurements may be conducted though thick samples of media which only scatter lightly. Such measurements are typically performed using the frequency domain technique. Here a continuous wave light source is intensity modulated on the source side of the sample. The temporal profile of the outgoing diffusive wave from the sample is measured. The optical properties are deduced from the detected wave's amplitude reduction and phase change. A more detail description of the method is provide by Tromberg *et al.* [133]. The technology is largely used in diagnostics of breast cancer, where measurement though several centimetres of tissue is possible in the $650 - 1000$ nm wavelength range[134, 135].

The high propagation speed of light also enables measurement of highly scattering media, but over shorter distances. Here the broadening and delay of a *single* short light pulse is measured, and this way of working is called a time domain measurement. This is the approach taken in this Ph.D.. The technology has been used to a large extent for the investigation of pharmaceuticals[136] where the scattering properties are in the range $200 - 600$ 1/cm, although the technique has also been used for biomedical applications [137, 138].
To accomplish a high temporal resolution the following detectors are typically applied: photonmultiplier tubes, as in Svensson *et al.* [139]; SPADs, as in Patterson *et al.* [140]; or streak cameras, as were used by Abrahamsson et al.[141]. Of these, both SPADs and PMTs require on post-processing of their signals to accumulate the PToF distribution, and this is done by Time-Correlated Single Photon Counting (TCSPC). The streak camera uses an analog acquisition principle, where the PToF distribution is converted into an spatial distribution of an electric charge. The streak camera thus measures the PToF distribution without the need for additional counting circuits.

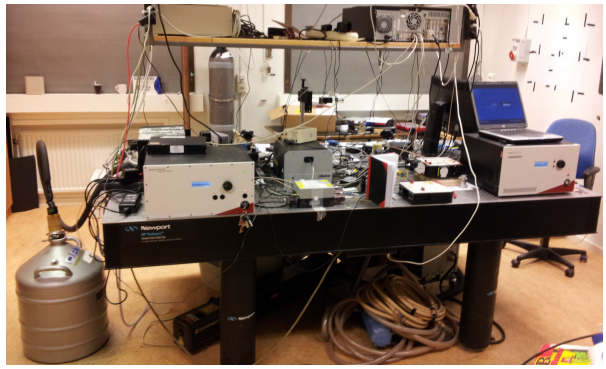

(a) Photograph of the PToF spectroscopy lab. Most of the table is occupied by the three supercontinuum sources present at the time, with their respective ATOF filtering units. A schematic presentation is given in Figure 5.16.

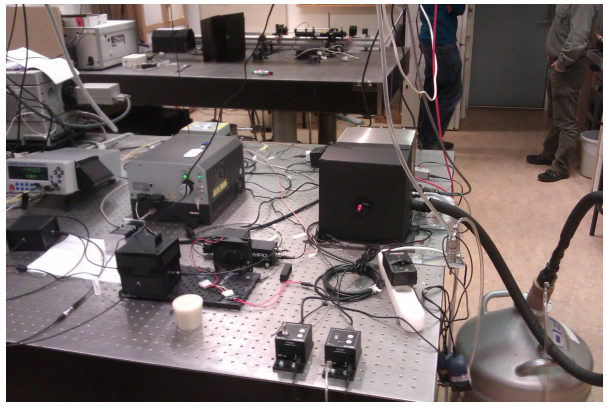

(b) Photo of the optical tables from the back. Here the detectors may be seen.

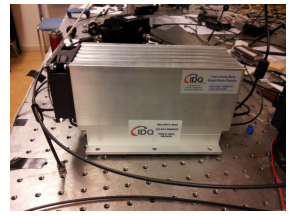

(c) Photo of the ID220 SPAD under investigation in Paper E.

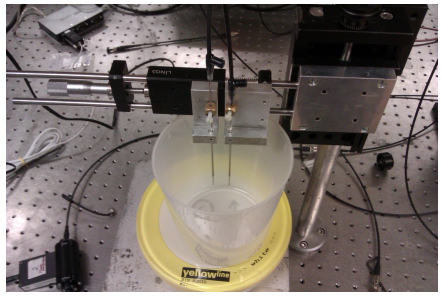

(d) Photo of the optical fibers befor submerging them in the dairy sample.

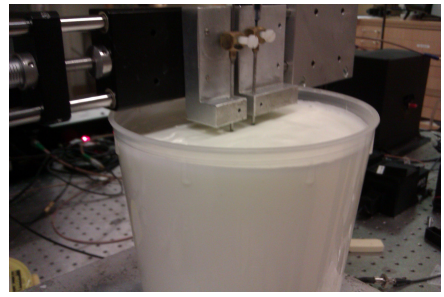

(e) Photo from the measurement campaign on dairy products showing dairy samples during measurement with PToF spectroscopy.

Figure 5.15: *Photographs of the PToF spectrometer at Lund University Department of Physics. The top images are of the laboratory and the bottom images taken during the measurement campaign on dairy products.*

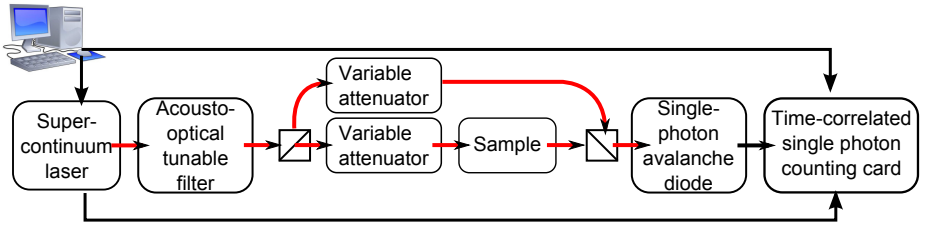

Figure 5.16: *Schematics of the instruments used in Paper D. A similar setup, but with different NIR detectors, was used for Papers E and [7].*

5.4.2 Outline of the instrument

A schematic of the PToF spectrometer is presented in Figure 5.16. The light pulses at the different stages of the experiment are illustrated in Figure 5.17. The instrument has previously been described in the doctoral theses by Abrahamsson [142], Svensson [102] and Alerstam [96], who developed the combined setup and data evaluation.

The supercontinuum light source and AOTF are used for generating a tunable source of light. The temporal profile of supercontinuum light generally has a banana-like shape as reported by Dudely *et al.* [143], this is illustrated on the left side of Figure 5.17. The entire light pulse has an extent of 700 ps. The AOTF effectively selects a narrow spectral part of the super continuum pulse, which also reduces the temporal width of the transmitted profile ($\sim$ 30 ps). The beam is separated into two components, and only one is sent to the sample. The other beam bypasses the sample and acts as a Time Reference (TR). This is used to compensate for temporal drift between the syncronisation pulse on the light source electronics and the actual optical output, this was also seen in Paper E. This enhances the measurement precision, as was demonstrated by Khoptyar *et al.* [136]. A further discussion and analysis of the instrument's performance is provided in the master thesis by Subash [144].

The temporal profiles of the TR and from the sample are illustrated in the centre of Figure 5.17. Because the TR pulse avoids the samples its shape is identical to the temporal IRF of the system. The time profile from the sample on the other hand is broadened, as was described in chapter 3. The combined signal from the TR and the sample is shown in the center panel of Figure 5.17. The fibre length for the TR signal is adjusted so it arrives $\sim$ 2 ns earlier at the SPAD than the signal from the sample.

The SPAD converts the arriving single photons into a macroscopic current. A

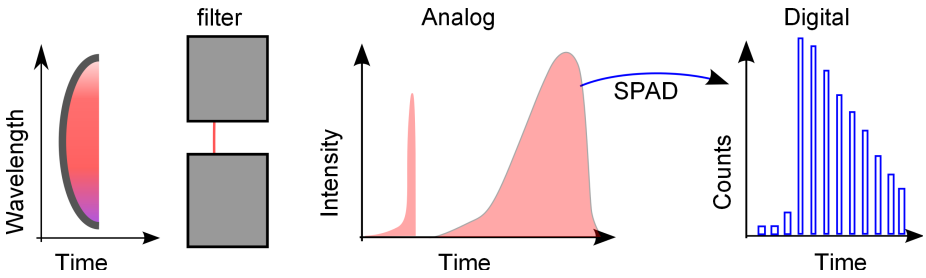

Figure 5.17: *Measurement principle of the PToF spectrometer. The PToF distribution is depicted at the different stages*

more detailed discussion of SPADs is provided in the introduction of Paper E. This current is used as source signal for a TCSPC card (SPC-130, Becker & Hickl, Berlin, Germany), where the electronic signal from the "seed pulse" from the light source is used as trigger.

The actual digitalization of the ToF distribution is complex and involves a pipeline of events starting with Constant Fraction Discriminator (CFD), Time-to-Amplitude Converter (TAC), and, lastly an Analog-to-Digital Converter (ADC) before the actual time span is calculated. The details are provided in the "handbook" by Becker[145]. At each of these stages of the detection process the dynamic range and thresholds can be adjusted, and it is therefore vital to check the performance after changing detectors or cables in the setup. Miss adjustments can cause noisy measurements, or multi-peak or broadened pulses in the recorded ToF distributions.

The laser operates with a repetition rate of 80 MHz with the exception of the work in Paper E, and only one detection process is possible for each light pulse. When the SPAD detects a photon, the device needs to quench the electronic avalanche and re-arm, thus it experiences a "deadtime" before it may detect again. Similarly, the principle of TCSPC requires a new trigger signal from the source. If the measured ToF distribution is to reflect the true photon density distribution, it is further required that the detection is independent of the proceeding pulse shape. This is only accomplished when the detection probability is less than one per. cycle, and this requires very low light intensities. In summary, the maximum count rate is thus limited by the cycle time of the source, and, potentially the total dead time of the detector. A short dead time is desirable as it increases the allowable count rate. The quantification of the systematic changes induced by operating at too high a count rate was the topic for Paper E.

Finally, to accomplish these low light intensities the setup is equipped with

variable attenuators on each of the possible beam paths. As part of the Ph.D. software for the combined instrument was created to provide a systematic and more rapid data acquisition. As a side note, the process of automating the instrumentation requires a detailed knowledge of the individual components' operation, this was the starting point for doing the work on extended range spectroscopy presented in Paper E.

5.4.3 Examples of measurement data

Examples of the measurement data from the commercial dairy products in Psaper D is presented in Figure 5.18. Each image is normalised to its maximum intensity to remove the different of the intensity transfer function of the combined instrument.

The measurement consist of the two signals, the first pulse is a TR pulse the second is the pulse broadened by the sample. Each measurement shows the overall time shift as a function of wavelength due to the temporal shape of the supercontinuum pulse. The ToF distribution at the top, for each sample, has the broadest profile due to the wavelength dependence of the scattering. The measurement precession is in part given by the contrast between the FWHM of the pulse broadened by sample and the pure IRF of the detector and source. For the present measurement, it is seen that the change in width from the

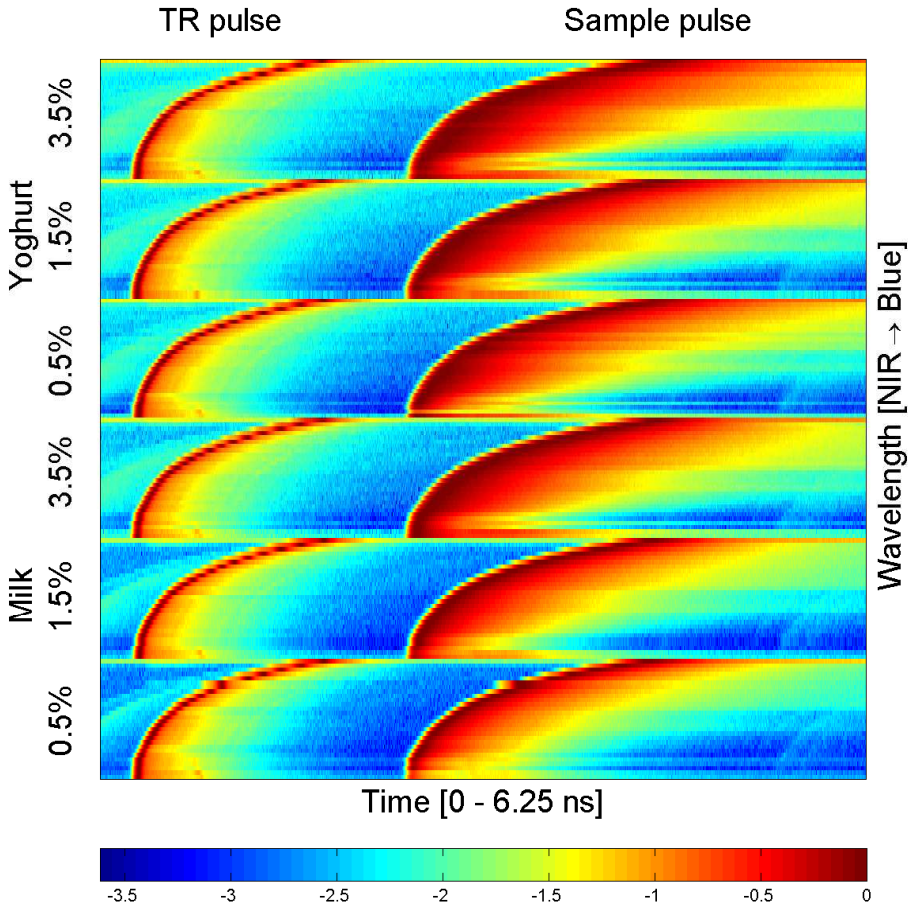

Figure 5.18: *Examples of the spectrogram images of the PToF for the different dairy products. Colormap is a logarithmic scale and each individual ToF distribution is normalised to the maximum count.*

5.5 Hyperspectral camera

The last technique used for broadband material characterisation used full field illumination. For this, lasers light is diffused to create an apparently smooth illumination of a square area rather then the spot illumination used for SLS measurements. This instrument used for this work was constructed and developed at DTU and was used for Paper F.
In this section an overview of the apparatus is first provided, along with the motivation for creating this novel new instrument. Subsequently, examples of images acquired with this setup are presented, quantifying the smoothness of the instrument's illumination. Lastly some of the considerations involved in calibration of the instrument's intensity response function are given, and as well as discussion of the power normalization technique.

The idea for the instrument was inspired by imaging systems which use AOTF filtering on the camera side to construct hyperspectral images, such as in Paper [55, 56, 57]. However, a simpler way to acquire the hyperspectral information would be to position the wavelength filtering on the light source side of the sample. This made the instrument resemble the SLS instrument, and so much of the software could be re-used directly. The remaining work was concerned with the hardware needed tp provide smooth illumination and to control the light source power. The aim of the instrument design was to combine the hyperspectral performance of the AOTF filters with illumination of a larger area, as used in hyperspectral imaging.

5.5.1 Overview

A schematic of the full field setup close to the sample is shown in Figure 5.19(a). The full field instrument uses the supercontinuum source and AOTF filtering unit to provide a tunable wavelength illumination like the previous systems. However, rather than making use of the tight beam profile, the beam is instead expanded by a lens (LC1715, −50.0 mm focal length, Thorlabs, Sweden). This creates a large Gaussian beam which illuminates a diffuser (ED1-C20-MD, Thorlabs, Sweden). The diffuser has a micro engineered structure and has a high light transmission, despite broadening the light and forming a square shape more suited for the imaging process.

An photograph of the equipment is shown in Figure 5.19(b). A Petri dish with fish feed pellets is positioned in front of the vision system together with the National Institute of Standards and Technology (NIST) calibration standard (SRS-02-020, Labsphere, New Hampshire, USA).

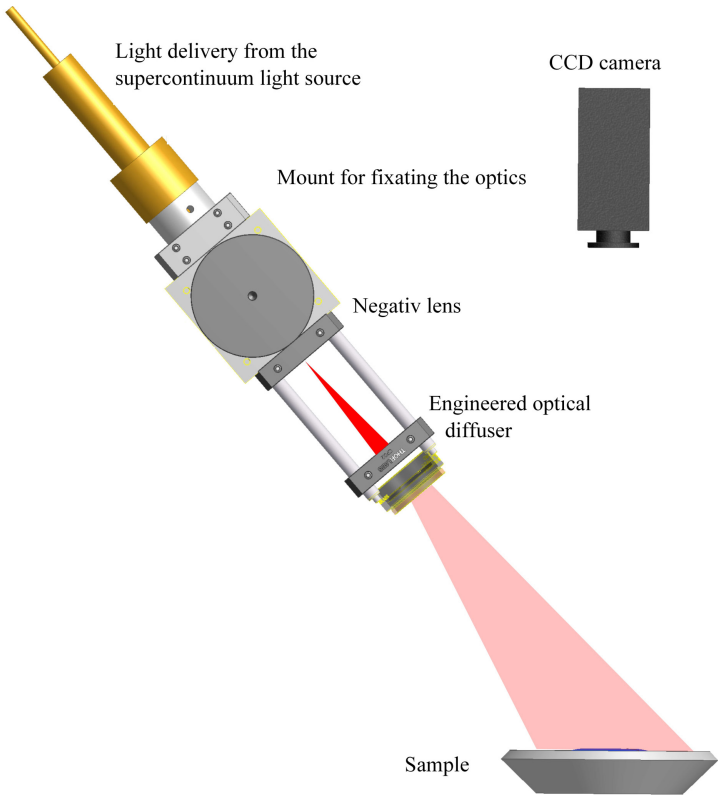

(a) Illustration of the instrument configuration, showing the light delivery fiber and the beam expansion optics, consisting of a lens, and an engineered optical diffuser. The camera is mounted above the illuminated sample.

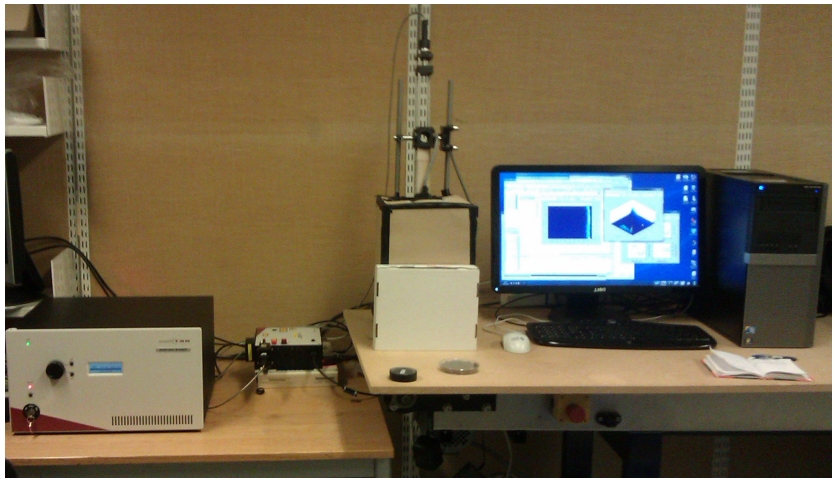

(b) Image of the equipment for full field illumination measurements. From left to right: the supercontinuum source and filtering unit, the enclosed vision system, and the computer for data collection.

Figure 5.19: *Illustration and photo of the equipment for hyperspectral imaging.*

5.5.2 Image quality

As the instrument aims to combine a classical vision system with hyperspectral resolution some compromises may be necessary. One of these is the smoothness of the illumination. To quantify this smoothness images of a calibration target for reflectance was taken. This section reports how these effects may be quantified.
Images of the NIST calibration target is shown in the top row of Figure 5.20. From this it evident that there are some high frequency intensity variations, these arise from the microstructure of the diffuser. These fluctuations makes segmentation of the pellets harder, as is seen from the comparison of segmentation results in Figure F.6(b) relative to the segmentation on the images with the Videometer Lab in Figure F.5(b). The histogram of the intensity distribution within the NIST puck should ideally be a delta distribution, with all pixels having the same value. The measured histogram is shown as red lines in the graphs in the bottom row of Figure 5.20. Inspection of both the raw images and the intensity distributions show that the strength of the high frequency components reduces as a function of wavelength.
The width of this distribution should be seen in relation to the span covered by the investigated samples. To investigate this, images of a Petri dish with a mixed combination of fish feed pellets were taken, and example images are seen in the second row of 5.20. From these images it is apparent that the full dynamic range of the light reflected from the pellets i recorded. The smaller brighter pellets stand out clearly between the darker, larger pellets. The pixel intensity distribution is again analysed using histograms, which are shown in the bottom row of Figure 5.20.

Another advantage of taking hyperspectral images of the calibration target is the ability to calculate the transfer function of the combined imaging and illumination system into NIST-traceable radiometric units. Using this method, the pseudo RGB images presented in figure F.11(f) were created. From this is also evident that the pellets are fairly dark, with less than 10 % of the light undergoing diffuse reflection. Secondly it enables a quantification of the illuminations fields homogeneity of the illumination field. Ideally the histogram should be a delta function, with all pixels having the same value. However the diffuser can cause some high frequency spatial noise which broadens the distribution. A broad instrument response function makes the prediction of astaxanthin in Paper F less accurate.

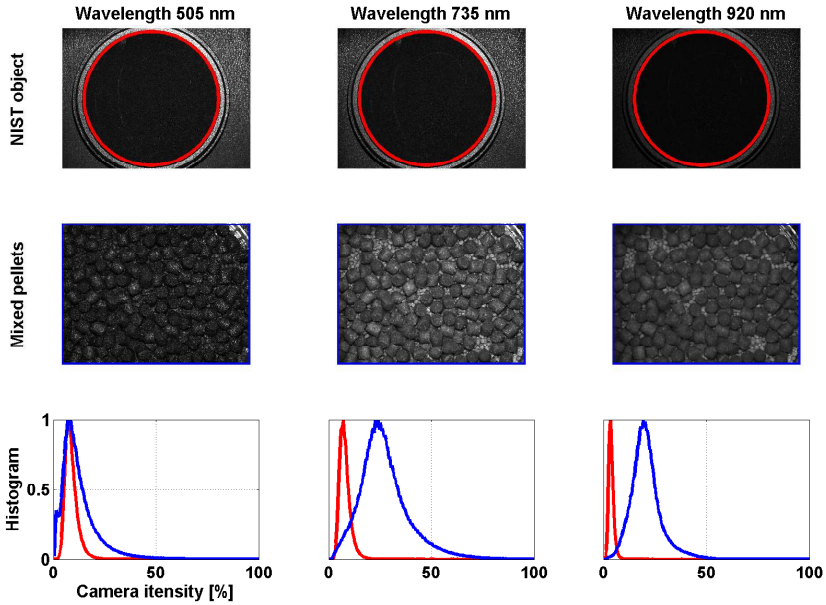

Figure 5.20: *Investigation of the illustration fields smoothness for the hyperspectral imaging system, examples at three wavelength is shown.* ***Top row*** *shows images of a NIST reflectance standard.* ***Middle row*** *shows images of the mixed fish feed samples, the color scale is the same for all images, spanning zero to saturation of the camera.* ***Bottom row****: shows histograms of the intensity distributions for the region of interest in each image.*

5.5.3 Calibration of instrument intensity response function

Another aspect of instrument design are the different variable factors which ensure that the image intensities are well resolved by the camera. For the Videometer Lab these procedures are automated, but for the SuperK system this had to be implemented.
The adjustable parameters which determine the recorded intensity are first, the camera's field of view; second, the light source power; and third, the camera integration time. The field of view was somewhat dictated by the applications, and the present 4.5×3.4 cm was found to be a decent compromise, although of course, it is not a hard limit. With this determined, only the integration time and source power were adjustable. It was possible to use HDR image acquisition technique developed for the SLS system to ensure that all pixels were accurately measured. The exposure time should be long enough to detect the low intensity

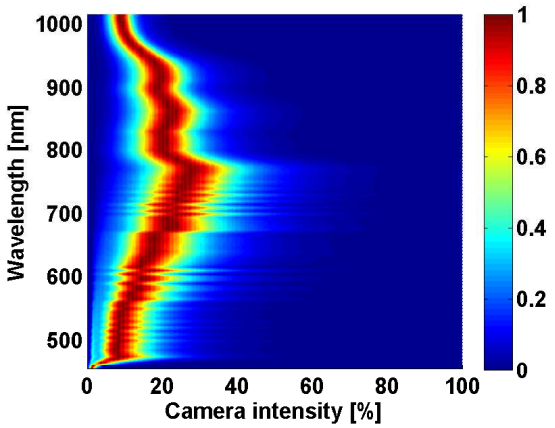

Figure 5.21: *Normalised distribution of pixel intensity distributions for the different wavelength by images of the mixed fish feed pellets. Visualizations such as this were used to adjust the filtering power and integration time of the camera. This is the final calibration result.*

signals at the longest and shortest wavelengths. In some wavelength ranges, the intensities drop as a result of the intensity transfer functions discussed in Figure 5.10. However, capturing images at multiple different exposure time was unnecessary as the individual wavelength had a fairly low dynamic range of reflectance intensities. For this reason, the power was instead adjusted to make all reflectance signals fit into the same exposure time. The intensities was adjusted by reducing the RF amplitude of the AOTF filter on the most intense wavelengths. Here, the histograms of the pixel intensity distributions from images of mixed fish-feed were inspected again. The histograms may be combined as a function of wavelength as is shown in Figure 5.21. Increasing the exposure time would scale all distribution linearly towards higher levels, the RF amplitude was reduced on individual wavelengths to make the measurements span the same intensity range. Figure 5.21 shows the final histogram after power adjustment. The final image acquisition time was 3.6 min including time for placing new samples into the instrument.

5.5.4 Improved intensity control

The last comment on the instrument design and implementation concerns improving the power normalization of the image data. As the image feature used to predict the astaxanthin content is the average pixel intensity of a segmented area, it was evident that prediction would be improved by obtaining a detailed

knowledge of the illumination power. As noted during the description of AOTF's (section 5.2), it is desirable adjust the power on the AOTF rather than the laser as it provides a fast feedback mechanism. To accomplished this two different approaches were considered: the first was *active* feedback to the AOTF which would use the RF amplitude to improve power stability. The second approach was a *passive* monitor on the filtered wavelength intensity which was then used to normalise the measurements. This last approach was implemented as it has a minimum turnaround time. The filtering power is not iteratively adjusted as would occur in active feedback. By coincidence, this option to monitor the output power became available in the second generation of supercontinuum sources, and it was therefore used during the measurement campaign.

Part II

Summary of scientific contributions

In this part, the scientific contribution made by each of the papers in the Appendix is summarised. The summaries are compiled together into chapters dedicated to each of the techniques, SLS, PToF and hyperspectral imaging. Each chapter provides a reference to the description of the theoretical background and an associated description of the instrument. Following this, the contents of the individual papers are briefly described by presenting the motivation, instrument development, measurement campaign and results.

Because many different approaches have been taken in quantifying the structural properties of dairy products, a discussion specifically for this application is provided in Chapter 9.

Finally Chapter 10 gives a combined summary on the accomplishments and perspectives on the Ph.D..

Chapter 6

Scientific contribution based on SLS

This chapter gives a summary on the research conducted within the scientific field of SLS. The research has been centred on camera-based inspection of the diffuse reflectance of the tight light beam from a sample. The theoretical background for the light-matter interactions which may be quantified with this technology were described in Chapter 3. For this inspection method, a measurement platform has been designed, constructed, characterised and developed. The final form of the measurement platform is presented in Section 5.3. In parallel with the development of the hardware, image analysis, and interpretations of the optical properties correlate with the given samples have been reported in several papers and conference contributions.

6.1 Supercontinuum Light sources for Hyperspectral Subsurface Laser Scattering - Paper A

In Paper A the use of AOTF-filtered supercontinuum light for SLS inspection was reported for the first time. The image magnification were low with an image resolution of ~ 18.5 μm/pixel and the reflectance profiles was recorded in the

wavelength range from $480 - 900$ nm. Measurements were performed on commercially available dairy products to investigate the discrimination of chemical constituents (fat contents) of milk and cream and of structural properties comparing milk and yoghurt. To quantify the atom-light interaction, the reflectance profiles were analysed using a statistical model (loglog). The measurements showed a high reproducibility of slope and offset of the loglog distribution sensitive to both the chemical and structural differences.

6.2 Monitoring Optical Changes during Milk Acidification using Hyperspectral Diffuse Reflectance Images - Paper B

Following the successful characterization of commercial products, the SLS technique was applied to on-line inspection of the milk fermentation process on a laboratory scale. As part of the instrumental development, the imaging objective was exchanged to obtain an image resolution of ~ 3.2 μm/pixel. The beam's spot size was reduced accordingly. Data acquisition routines were developed to include HDR imaging of the reflectance profiles. The measurement campaign investigated the impact of structural changes by monitoring the fermentation process continuously. Temporal developments were set in relation to three different parameters of the production process. The campaign was performed as a factorial study, varying both fat and protein contents, along with the fermentation temperature.
The diffuse reflectance images showed a number of new interesting features between the start and end state of the milk fermentations. This included changes in the shape and the speckle pattern close to the entry point. The speckle characteristics have been used in contributions [12] and [83]. However, as the dominant change during fermentation was a shrinkage of the profiles, this was again quantified using the loglog model. The time development of the deduced optical properties was compared to the time development of the rheological properties. Here it was found, for the first time, that the instrument observed changes prior to the those detected by conventional rheology measurements. The temporal development of the optical properties was decomposed using PCA and the sensitivity for the factorial parameters was quantified using MANOVA. This was performed over different wavelength intervals, and it was found that all parts of the spectrum showed clear effects related to both fat contents and temperature. These two factors also had the largest impact on the rheological development. The effects of the protein content were only seen for wavelength in the blue wavelengths range and were similar to that of rheology.

6.3 Non-invasive assessment of dairy products using spatially resolved diffuse reflectance spectroscopy - Paper C

In this last paper on SLS, commercially available dairy samples were investigated with the more advanced inspection technique OIR. The motivation was to deduce the reduced scattering and absorption coefficients which provide physically interpretable quantification of the atom-light interaction, but with an instrument which would be suitable for in-line inspection.

The camera and imaging objective were exchanged to increase the field of view, while retaining a high spatial resolution. This enables characterization of a broader range of optical properties which is necessary for characterization of the milk fermentation process [4]. A simple calibration technique was presented capable of quantifying image distortion for point illuminations systems as used by both Farrell *et al.* [67] and Wang *et al.* [103]. Previous proposed methods only deduce an average pixel size, the new approach added both wavelength dependence and quantification of lens aberrations.

The literature have reported a list of challenges for camera based OIR which have been addressed in various ways. As part of the scientific contribution, the previously proposed methods for camera based OIR were investigated. The methods did not generalise well to the given measurement of dairy samples. Thus new methods were developed, combining the benefits of previous proposals. For estimation of the entry point, a method was developed which avoided over shooting along the line of incidence. This effect was evident from the image data using the previous method and caused increased scattering and reduced absorption. For estimation of the diffusion centre, a method was proposed which made better use of the CCD chip by only using a single line along the diagonal for estimation of the diffusion. Lastly a previously reported dependence on fit range was quantified and reported systematically.

With these necessary improvements of the measurement method, discrimination of the structural properties during fermentation was investigated. The measurements showed a clear distinction between products with different fat contents and structure (milk/yoghurt). Simultaneously, it was found that with the extended spectral range of the AOTF, both water absorption in the NIR and fat absorption in the sub 500 nm as were present.

Chapter 7

Scientific contribution in PToF spectroscopy

PToF spectroscopy is an advanced measurement technique capable of quantifying the different light-matter interactions from scattering and absorption with low correlation. The theoretical background for the technique is presented in Section 3.3.

The instrument for PToF spectroscopy was a combination of the light sources and filtering units supplied by CIFQ and NKT with the PToF spectrometer at the Department of Physics, Lund University. The systems were integrated, and measurement software combining control of all the hardware components was developed to automatize the data acquisition. The instrument and measurement technology are presented in Section 5.4 and have been used for Paper D, and the technical report E which is included in the thesis. Lastly, the instrument was used in the work presented by Kamran *et al.* [7].

7.1 Spectral characterizations of dairy products using photon time-of-flight spectroscopy - Paper D

In Paper D PToF spectroscopy was used for investigation of the reduced scattering and absorption coefficients of commercially available milk and yoghurt products. The paper reported the feasibility of measuring the PToF distribution through the samples in the wavelength range from $500 - 1030$ nm. To deduced the optical properties, an inverse modelling of the PToT distribution was performed with a library of pre-calculated MC models. The measured reduced scattering coefficients increased with respect to fat content, and a similarly large change was seen between milk and yoghurt products. Here, the latter indicated that the reduced scattering properties could provide a clear quantification of the structural properties during fermentation of milk to yoghurt, which was the first time this had been reported. Concerning the absorption coefficient, the work showed that the spectrum was in good agreement with that of water. This indicated that the fat absorption peaks are weak for the present wavelength range.

7.2 Evaluation of the ID220 single photon avalanche diode for extended the spectral range of photon time-of-flight spectroscopy - Paper E

Following the work on dairy products, efforts were made to extended the spectral range of measurements towards the NIR ($900 - 1700$ nm) by integrating the ID220 SPAD. Recent publication on PToF spectroscopy [146] has shown nonlinearities in the deduce optical properties by using NIR SPADs. To investigate the validity of the measured PToF distributions for the ID220, two aspects of the instrument response function was investigated and reported in the technical report E. Here, an analysis technique for quantification of the detector response function was reported for both the temporal shift and the width of the recorded PToF distribution. These are relevant quantities for PTOF spectroscopy as the shape of the PToF distribution alone is used to deduce the optical properties. The measurements showed the instrumental response of the detector was an influence, which is undesirable: the detector perturbs the shape of the PToF distribution. The significans of this effect was also investigated for PToF spectroscopy, here especially absorption in particular systematically changed as a function of count rate. Lastly, it was demonstrated that the measurement per-

turbations was reduced by operating the light source with a reduced repetition rate.

Chapter 8

Scientific contribution within hyperspectral imaging

During this Ph.D. project a hyperspectral imaging system was constructed by merging the high wavelength resolution of the AOTF-filtered supercontinuum light with the spatial resolution of a camera. This would operate as a hyperspectral imaging system for quantification of surface chemistry of solid samples. The details of the instrument design were described in chapter 5.5.

8.1 Instrument development

To accomplish this task, the circular laser beam was expanded by a negative focal length lens and modified into a homogeneous square-like illumination by a commercially available micro engineered optical diffuser. In this way a $\sim 4.5 \times 3.4$ cm area of a sample was illuminated with a desired wavelength in the range from $455 - 1015$ nm. Images was captured with a monochrome CCD camera. The smoothness of the illumination field were investigated on a NIST calibration target and a mixed set of fish feed pellets which demonstrated that the instrument

could distinguish the different pellets. For improving the measurement precision of the images, a light power level and camera pre-calibration procedure was investigated. This ensured that the dynamic range of recorded intensities from the samples could be covered by the instrument. Lastly, to enhance the measurement precision, a feedback system for monitoring the laser light power was implemented.

8.2 Hyperspectral imaging based on diffused laser light for prediction of astaxanthin coating concentration - Paper F

The supercontinuum based hyperspectral imaging system was used in Paper F, as part of a comparative study of the capabilities of spectral imaging systems when imaging the surface chemistry fish feed. Here, a measurement campaign was designed for predicting the astaxanthin contents in the pellets and the performance of two imaging instruments was reported. Astaxanthin is a necessary additive to the fish feed as it ensures a proper color in the fish, which is important for consumer's perception its quality.
To accomplish this, the contents were predicted using different statistical methods based upon supervised learning. It was found, that the supercontinuum based laser system could accomplish a Standard Error of Prediction (SEP) of only 3.7 ppm, which was similar to the results obtained by the same approach for the multispectral vision system Videometer Lab. Lastly, the prediction models were based on a spare regression technique, EN, for the purpose of identifying the optimum wavelength for the inspection process. The spectral bands in the visible part of the spectrum $\sim$ 450 - 650 nm were found to be the most important. These results are in good agreement the with the reflectance measurement performed on pure and astaxanthin added fish oil.

Chapter 9

Discussion of methods for in-line monitoring of milk fermentation

In this Ph.D. different measurement techniques have been used for inspection of dairy products with the purpose of quantifying optical changes induced by the fermentation process. As outlined previously in Figure 1.3 the scientific work has been performed using the two measurement techniques SLS and PToF. The measurements taken using the SLS platform have further differed in how they were analysed, the diffuse reflectance having been quantified by both a statistical and a physical interpretation of the light propagation. In this chapter, the results of the scientific contributions are compared and discussed. The first section compares the measurement techniques, while the following section focuses on present and future analysis methods. In the final section, a discussion of the future prospects for this measurement technology is given.

9.1 Comparison of measurement techniques - PToF and SLS

PToF spectroscopy is an established technique for measuring the optical properties of scattering media. Its theoretical background is described in Section 3.3. The technique allows a strong discrimination between scattering and absorption properties. This discrimination was further enhanced by evaluating the optical properties with the advanced inverse modelling of MC models. MC models are a gold standard, and provide the most accurate assessment of the optical properties because the reduce cross-talk (see Section 3.2.1). The combination of PToF spectroscopy and evaluation by inverse MC models thus provides a state of the art tool for quantitative spectroscopy of scattering samples. These results were presented in Paper D.
The experimental results show that for the dairy samples and the wavelength range studied, absorption is significantly less of a factor than the reduced scattering properties, which facilitates the application of diffusion models to the inverse modelling. With this knowledge, the measurement technique OIR was implemented for the SLS instrument. The dynamic range of the instrument was expanded to match the broad dynamic range of the dairy products. Building upon this, the equivalent optical properties of similar commercial dairy products were presented in Paper C.
Because it is possible to describe light propagation as a diffusion process, the evaluation time is shortened considerably, which is an important aspect for in-line and real time measurements. For the PToF measurements, the data evaluation takes a few minutes for each wavelength, assuming that good start criteria exist. In comparison, the evaluation time for the diffusion fit is less than half a second, even for an unoptimized implementation in Matlab 2012®.

9.1.1 Evaluating optical properties with physically interpretable models

A comparison of the results from the two types of measurements is given in Figure 9.1. Only mean values are presented. The SLS data is coloured blue, and PToF results are in black. In absorption measurements graphs, the spectrum of from Hale and Querry [127], i also show as reference colored red. It is important to understand that a perfect overlap should not be expected. The samples were purchased a year apart, and differences and occur due to production variation. Also, the yoghurt with the highest fat content was of a different type, both in terms of its fat content and fermentation culture, so these are not exactly comparable.

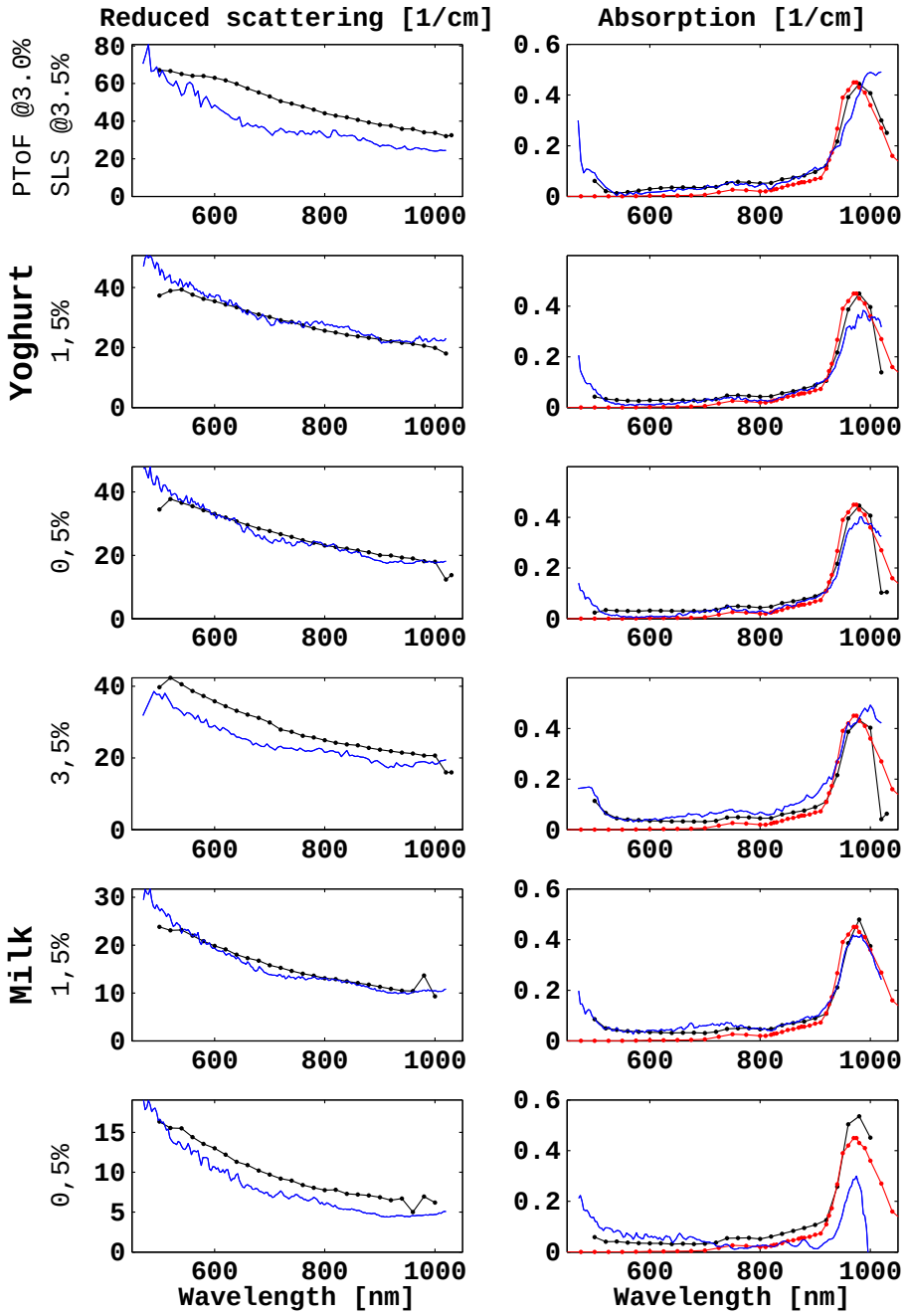

Figure 9.1: *Direct comparison of measurement results for dairy products. The black line was obtained with the PToF spectroscopy presented in Paper D. The blue lines are measurements results with SLS presented in Paper C. The red line is absorption by water [127].*

For both instruments, the wavelength dependence for the measured reduced scattering coefficients are in good agreement with an approximation from Lorenz-Mie theory (Equation C.10). Furthermore, both techniques have observed distinctive changes in the reduced scattering properties between milk and yoghurt of the same fat content. This is promising for future process inspection.
The high fat content PToF measurements of both milk and yoghurt show a slightly lower scattering level than for the SLS measurements. Using the current instrumentation for PToF spectroscopy, the highest scattering coefficient may experience some truncation. The measurement series for both milk and yoghurt at 1.5 % fat show an almost perfect overlap, which is unexpected given the probable product variations. For the samples with 0.5 % fat content, the yoghurt samples again show an almost perfect overlap both in terms of their amplitude and wavelength dependence. For the milk sample, the estimated reduced scattering is generally lower.

Concerning the measured absorption coefficients, their wavelength development shows a relatively low variation in the mean values for the SLS measurements. This is expected, since repeated measurements reduce the variation. Both measurement techniques show an absorption peak in the short, blue wavelength range, which previously has been associated with fatty acids [147, 65]. The extended wavelength range used with the SLS measurements confirms the presence of the peak, which was barely covered by the original PToF measurements. Both techniques show the presence of water. The SLS measurement does however show more variation between the milk and fermented milk states than is seen in the PToF spectroscopy results. This is probably an effect of crosstalk (Section 3.2.1), and solutions have been suggested for correction of the scattering phase function dependence [101] and absorption [88]. It will be of great interest to investigate these approaches in future work.

9.1.2 Additional prospects for the measurement techniques

Another important aspect of the two measurement techniques is their ability to provide additional information on the samples, further to the reduced scattering and absorption described in the previous section. This may be seen by examining the characteristics of the raw measurement data from the two instruments. Examples of the SLS measurements are compiled in Figures 5.13-5.14 and likewise for PToF in Figure 5.18. From these images it is evident that the reflectance measurements obtained with the SLS technique, when designed for the evaluation of optical properties by OIR, indeed do show effects caused by the phase function and by speckle. In this way, camera based inspection naturally facilitates the quantification of additional optical properties not detected by the present PToF measurement. However, this does not rule out the possibility of

including phase function effects in PToF measurements by making adjustments to that technique [148, 149].

9.1.3 Industrial applicability

The final aspect of the two measurement techniques which is considered is their applicability for in-line process inspection. Photographs of the two instruments during measurements are shown in Figure 5.7 and Figure 5.15 for the SLS platform and PToF spectrometer respectively. Inspection with the SLS platform is already suitable for in-line measurements, as the instrument has been tested in on-line scenarios, working through a cover slip. In comparison, the PToF measurement at present time rely on very controlled measurement settings. The invers modelling rely on a known fibre to fibre distance, and both flow in the sample or vibration from external equipment may perturb this.
Another important issue is the cost of the instrumentation: the dominant difference between the two techniques in this regard is the detector. For the SLS technique, the development of vision technology and commercial RGB cameras has pushed the technology very far, providing high quality sensors with respect to noise, resolution and dynamic intensity range. In comparison, the time-resolved measurement technique relies on more advanced detection schemes, mainly using TCSPC and extremely fast detectors (SPAD, and PMT). Because of this, SLS measurement appear to be more viable for future in-line inspections systems.

9.2 Comparison of physical and statistical models

For the present work, the diffuse reflectance profiles captured with the SLS platform have been quantified using two numerical methods. The statistically based loglog model used in Paper A, and OIR, which is based on a physical interpretation of the light scattering process. The wavelength dependencies of the slope coefficient and the reduced scattering coefficient for the respective models have been evaluated for commercially available dairy products, and are shown in Figure 9.2. Similarly, the optical properties have been measured in a measurements series following the fermentation of milk, and the results are shown in Figure 9.3. The results from OIR are further analysed using the approximation from Lorenz-Mie theory presented in Equation C.10. The milk fermentation was performed on Ultra-high Temperature Treatment (UHT) milk (1.5 % fat) by GDL and conducted in settings simulating an in-line production

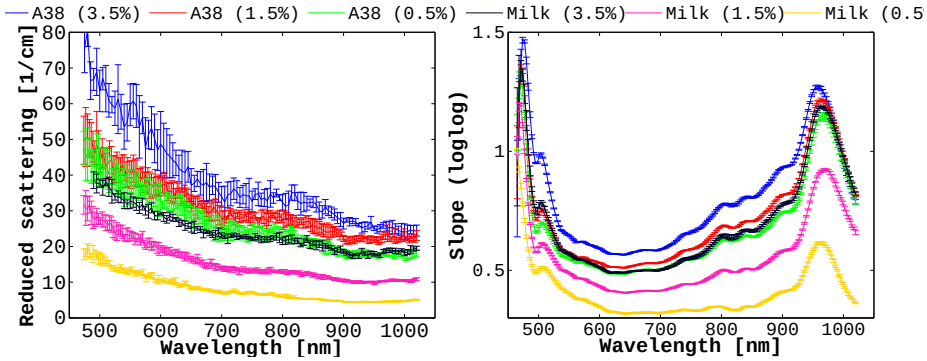

Figure 9.2: *Optical properties evaluated by physical and statistical models of the SLS measurement on the dairy products from Publication C.*

process - see the photograph shown in Figure 5.7(c). The measurement series spanned the wavelength range from 480−920 nm with 23 individual wavelengths.

From this, it is evident that the measurement precision of the slope coefficient for the loglog model is higher than for the reduced scattering properties evaluated by OIR. The biggest noise contribution in the present OIR analysis is the quantification of the diffusion displacement, specifically the quantification of the diffusion centre. So, even though the statistical model does not provide physically interpretable properties, it does provide a low variance estimate of the optical properties. At the present time, the strength of the physically based model may therefore not lie so much in the precision of the measurements as in their interpret-ability. This is more evident in the milk fermentation measurements shown in Figure 9.3. From this it is seen that the wavelength decay of the scattering properties changes significantly, while the amplitude is largely unchanged. Because the measurement can be interpreted further by the approximation shown in Equation C.10 the measurement noise is also reduced. At the present time, no such method is proposed which focus on particle size from the cross wavelength variation of the loglog slope coefficient.

Future analysis methods

While the low noise of the loglog model's slope coefficient is encouraging, the slope coefficient quantifies the combined light attenuation. This may also be measured by simple light attenuation measurements e.g. with fibre probes, as discussed in Section 2.2.2. For this reason, the future development of the technique should focus on statistical models which can combine the benefits of

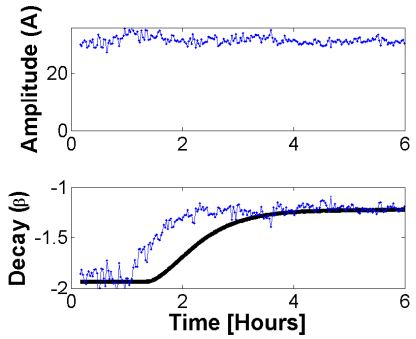

(a) Evaluated amplitude of the reduced scattering coefficient and spectral decay, quantified by Equation C.10. The black curve shows measurements of viscosity by rheology, scaled to fit the numerical values of the spectral decay (β).

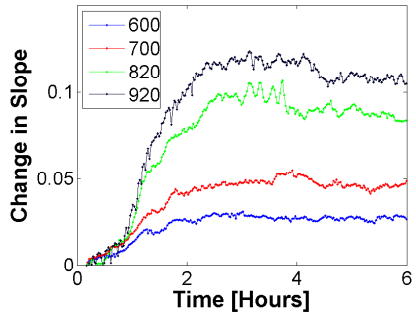

(b) Slope coefficient dedueced by the statistical loglog model. The legend referrers to the respective wavelength.

Figure 9.3: *Evaluated optical properties by physical and statistical models for an acidification of UHT milk (*1.5% *fat) by GDL. A photograph taken before the measurement series is shown in Figure 5.7(c).*

robust statistical quantification, and on relating these to physically based optical properties. The total attenuation measurement is more easily accomplished by total transmission or reflection sensors. In addition, it will be advantageous to pursue this in the NIR measurement range, where the necessity of decoupling scattering and absorption properties is more significant, and so the benefits of an independent quantification are more valueable. This is true in the NIR wavelength range because the reduced scattering coefficient continues to fall at longer wavelengths. The literature reports a number of examples of how such hybrid models may be accomplished, by training statistical models with physically based simulations. To some extent OIR may be seen as such a hybrid, as presented by Lin [84], where a set of MC models are used to find a simplified expression for the optical properties. Similar approaches have been used by Kazuya *et al.* [150] for separating μ_a and μ_s' and similarly Menon *et al.* [151] for g and μ_s. Another approach is the use of neural networks, which have been trained on features of the reflectance profiles from MC simulations to provide a fast and accurate estimation of the optical properties of scattering media by Jäger *et al.* [152].

9.3 Future SLS measurement technology

The work conducted throughout the Ph.D. enables some consideration of future measurement platforms. The work has focused on accomplishing a separation of the scattering and absorption properties using only a single line of reflectance values. The line was extracted though the entry point of the oblique incident beam, and the properties were evaluated by OIR. Because only a single line is used, the measurement platform may be adapted in two ways. The first, is by performing the image acquisition using spectrograph camera, as was performed by Qin and Lu [153]. In this way, the full wavelength dependence of the scattering and absorption may be deduced from single images, which makes data acquisition significantly faster. Another option is to continue with wavelength filtering at the source, and instead measure the reflectance profiles with a line scan camera. This will make the measurements faster and cheaper. The latter may be very important for realising an instrument in the NIR wavelength range, as the sensors are less mature than the silicon-based detectors. The wavelength regime covered by commercial systems is typically based on indium gallium arsenide (InGaAs).

In terms of wavelength range, the visible and near-visible range (< 1200 nm) spans a dip in the absorption spectrum of water [127]. As water is the main constituent for many dairy products, it is advantageous to focus on the quantification of light scattering properties within this absorption dip. At the same time,as mentioned above, the detector technology for these wavelengths is considerably more mature. Thus, the present wavelength range $\sim 465 - 1020$ nm provides a good "window" for obtaining high quality measurements focused on scattering properties rather than absorption. Furthermore, as is seen in Figure 9.3(a), the optical changes induced by the fermentation process may mostly be observed in the wavelength dependency (decay) and not in the amplitude of the scattering properties. With this in mind, the results in Figure 9.2 show that the largest wavelength dependence is exhibited towards the visible range, while the change in slope reduces in the NIR range. Therefore, the shorter wavelength range is better for discriminating between structures.
However, working in the NIR region may also provide benefits. First, from the perspective of a robust industrial implementation. The reduced scattering properties continue to fall in the NIR wavelength range, making the penetration depth larger. It follow that a smaller magnification is necessary to resolve the diffusion displacement. This may be important for in-line measurements as high magnification imaging is affected more by vibration from surrounding pumps mounted on the production line. Similarly, the reflected light represents the optical properties of a large volume, and is therefore less sensitive to local perturbations. In production environments, these may be lumps, air bubbles, or a fat layer covering the surface of the cover slip.

Another advantage is the inclusion of both absorption and scattering, where absorption at the present wavelength range is unchanged by the fermentation process. Wavelength specific changes have been reported for example in milk coagulation by Saputra *et al.* [31] in the wavelength range $1100 - 2500$ nm. The techniques studied in the present thesis may prove advantageous compared to those using total attenuation, as it gives a quantification of each effect independently. In this way, structural changes could be characterised by the direct effect on the light scattering and the indirect effect of the products' chemical composition.

Chapter 10

Conclusion

In this thesis different instruments and analysis techniques have been investigated for optical broadband characterisation of samples relevant to industrial production processes. The Ph.D. has focused on development of the measurement techniques, and work is presented on measuring the structural differences between milk and yoghurt, and quantifying levels of the fish feed additive astaxanthin. The work has been centred around the great versatility of AOTF filtering of supercontinuum generated light, which has allowed the work to encompass very different measurement techniques. This combination of filter and light source accomplishes a broad spectral wavelength range, with pulsed light with a short temporal profile, and with fast wavelength selection - features which have made it possible to contribute to the measurement techniques SLS, PToF spectroscopy, and hyperspectral imaging.

The most significant contribution of the Ph.D. is the platform constructed for SLS measurements, and the associated data analysis techniques based on OIR. The objective of the instrument design was to enable imaging that resolves different optical interactions between light and matter. The instrument is constructed to match the characteristic length scales for the atom-light interaction of milk and yoghurt products in the visible to near infra red wavelength range. These interactions are expressed in the recorded HDR images: as a decay of the reflectance profile caused by scattering and absorption; as structured high frequency noise from speckle; and, finally as an elongation of the reflectance pro-

files due to a preferred light scattering directionality. The instrument further enables measurements over a broad wavelength range, and is thus a versatile tool for broadband optical characterization. The intent with the platform is to enable research into the types of optical interactions which are the most significant for a given problem, and further, to resolve their wavelength dependence. The thesis discusses design considerations, making the knowledge transferable to other applications and wavelength ranges. The different optical interactions are all used for commercially available dairy inspection techniques, and are typically operated at a single wavelength. Thus the present instrument may be seen as a generalization of existing measurement technologies.
For analysis of diffuse reflectance images, the thesis contributes with an implementation of OIR for camera based non-invasive inspection. The deduction of physically based optical properties may provide a more clear characterization of a sample by distinguishing between the effects of particle concentration and particle size distribution. This has been investigated in an on-line measurement of the milk fermentation process, where the dominant optical change was the decay of the reduced scattering coefficient. The physical models clearly show this to be a change which is only related to the particle size distribution. It was demonstrated that the measurements could be conducted through a cover slip, which is necessary for any industrial implementation. In addition, the extracted physically based optical properties showed sensitivity to changes taking place earlier in the fermentation process than those detected by classical rheology measurements.

PToF spectroscopy is an established technique for quantifying the absorption and reduced scattering properties of light scattering samples. The measurement technique was applied to commercially available dairy products, and the results showed, for the first time, that the scattering properties changes significantly by the fermentation process. This was quantified and reported for the wavelength range from $500 - 1030$ nm (D). The results therefore demonstrate that PToF spectroscopy can provide important insights into the optical properties, and this information was subsequently used to design the more industrially applicable SLS platform. Concerning instrument development within PToF spectroscopy, efforts was made to extend the wavelength range by integrating a NIR SPAD for measurements up to 1700 nm. However, at the present stage the measurement technology is too sensitive to instrumental settings to provide conclusive results (E). In summary, two contributions have been presented in the thesis within the field of PToF spectroscopy, one on the application of the technology and one on the challenges for future instruments.

Summarising the future prospects for in-line inspection of structural properties in dairy production, the camera based SLS inspection appears most promising. The technique has used non-contact measurements to demonstrate distinctive changes in the deduced optical properties over the visible to near infrared range.

The most distinctive differences are observed by a broadband characterization, but do not necessarily need high wavelength resolution. Here physically based modelling could distinguish between the change in concentration of the scattering particles and their effective size. Future work should therefore focus on improving the measurement precision, and on investigating the novel optical properties using changes in speckle and scattering phase function dependencies.

For the development of hyperspectral imaging, a new instrument was constructed based on the supercontinuum and filtering units previously applied to SLS measurements. The building of the instrument and the development of relevant methods to quantify its performance are presented in this thesis. The hyperspectral imaging system was used in an industrially relevant measurement campaign presented in Paper F. Hyperspectral images were used to construct chemometric models, using multiple different regression methods, for quantification of astaxanthin in fish feed pellets. The results showed astaxanthin contents could be measured with a SEP of 3.7 ppm, which is a smaller variation than was obtained using standard HPLC techniques. The results are therefore promising, as the first proof-of-principle measurements with using this technique.

The development of broadband optical inspection techniques in the industry is driven by the continued desire for cost reduction and quality improvements. With the measurement platform created in this thesis, the foundation for versatile sample characterization is provided, which demonstrates the potential for applying optical inspection techniques for optimizing food production. Hereby, many of the problems associated with in-line inspection are solved. In turn this enables research into both instrument design and data analysis methods, with the ultimate aim of creating sensitive and cost efficient inspection systems.

Appendix A

Supercontinuum Light sources for Hyperspectral Subsurface Laser Scattering

Otto Højager Attermann Nielsen[1], Anders Lindbjerg Dahl[1], Rasmus Larsen[1], Flemming Møller[2], Frederik Donbæk Nielsen[3], Carsten Lilholt. Thomsen[3], Henrik Aanæs[1] & Jens Michael Carstensen[1]
[1] DTU Informatics, Technical University of Denmark
[2] DANISCO A/S
[3] NKT Photonics A/S

Published, Article in Proceedings of Scandinavia Conference on Image Analysis 2011 as part of the section "Application for Food Inspection"

abstract

A materials structural and chemical composition influences its optical scattering properties. In this paper we investigate the use of subsurface laser scattering (SLS) for inferring structural and chemical information of food products. We

have constructed a computer vision system based on a supercontinuum laser light source and anAOTF to provide a collimated light source, which can be tuned to any wavelength in the range from 480 to 900 nm. We present the newly developed hyperspectral vision system together with a proof-of-principle study of its ability to discriminate between dairy products with either similar chemical or structural composition. The combined vision system is a new way for industrial food inspection allowing non-intrusive online process inspection of parameters that is hard with existing technology.

Introduction

The properties of a suspended materials or colloids are affected by the particle size distribution. Knowledge about particle size distribution is especially relevant for many products in the food industry, for example fat and protein particles suspended in water. The size and density distribution of particles influences parameters such as "mouth feel" and shelf life, which are important quality parameters in the food industry. In this paper we address the problem of inferring information about particle size distribution based on subsurface laser scattering (SLS). The subsurface scattering of light is affected by both the chemical and structural composition of a material [68]. Based on these properties we have designed a vision system consisting of a hyperspectral laser and a CCD camera for measuring subsurface scattering. We provide a proof-of-principle for inferring information about particle size distribution demonstrated on a number of dairy products. This system allows an opportunity for effective online monitoring of food products as well as real time process inspection, based on a non-intrusive system.

Other methods exist for measuring parameters affected by particle size distribution, for example rheology based on a measurement of the consistency and flow of the food product [154]. Another approach is based on measuring the scattering of a water diluted sample [155]. However the water dilution can alter the particle composition of the food product. A vision system avoids the intrusive nature of these methods yet being fast and objective.

Many vision based techniques have been developed for industrial food inspection, and especially multispectral and hyperspectral methods have been successful [42, 156, 157]. The present system is based on a supercontinuum lightsource, filtered by and AOTF and light delivered through a single mode fiber. Together with a camera, as illustrated in Figure A.1, the setup becomes a highly flexible vision system. Our setup follows the work of [158], where an SLS-system[1] devised

[1] `http://www.videometer.com/products/products.html`

with laser diodes is demonstrated. In their work SLS-features are correlated with the composition of milk and rheology of yoghurt. Our system is extended with multiple wavelengths.

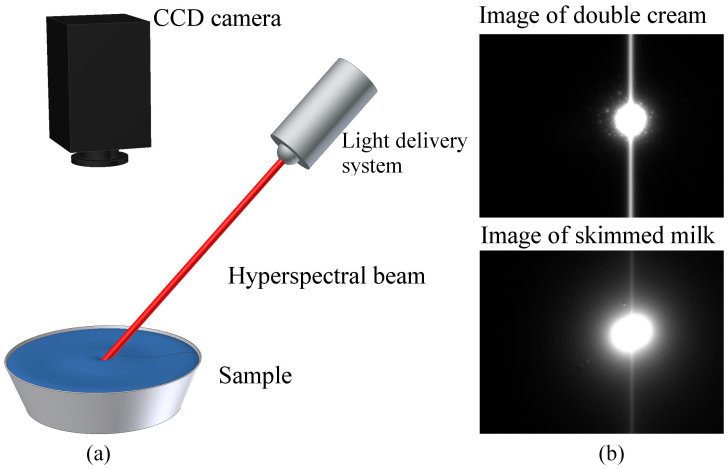

Figure A.1: **(a)** Illustration of our hyperspectral vision system for probing a samples SLS properties. **(b)** Image examples of the SLS properties of two diary products measured at 630 nm. Both structural and chemical properties affect the appearance of the laser spot.

Hyperspectral imaging was originally developed for geology and mining based on remote sensing [159, 160] and many hyperspectral analysis techniques have been developed from these problems like spectral unmixing. But hyperspectral imaging has many other useful applications including food analysis where these techniques is widely employed in both research and industry [161, 162, 157].

Hyperspectral images can be acquired by point scanning, line scanning, area scanning and single shot acquisition [157]. In the point and line scanning the acquisition device or the sample, needs to be moved to obtain a hyperspectral image, which potentially is a source of error [161, 163]. In the area scanning, multiple exposures are acquired from the same geometry, whereas the single shot acquires the full hyperspectral information at one exposure. Single shot has clear advantages for speed and robustness, but hyperspectral single shot technology is still under development and not ready for industrial inspection [164]. The narrow spectrum for hyperspectral images are typically obtained by filtering in front of the imaging device [157], whereas we perform light filtering based on an AOTF allowing a precise control of the wavelength. In this setup we take advantage of the stable geometry with a fixed camera. The tradeoff is the need for multiple exposures – one at each wavelength. Our aim is to construct a

setup where a few relevant wavelengths can be identified and subsequently used for constructing an industrial inspection system.

A very simple approach for obtaining hyperspectral images is to use a filter wheel [165], but this is restricted to a limited number of spectral bands. Tunable filters has a clear advantage in providing a flexible control of the wavelengths, but until now the use of tunable filters for food inspection has been limited [157, 166]. There are some examples tunable filters for quality control of food including the estimation of fruit firmness in [167] and rot of mandarins in [168] based on a LCTF (liquid crystal tunable filter). The LCTF is placed in front of the camera lens to filter the light into the camera, in contrast to our setup where the light source is filtered. The LCTF technology is capable of covering a similar spectral range as the AOTF. We have chosen the AOTF because it is appropriate with the laser beam setup that we employ.

The main contributions of this paper are:

1. A SLS computer vision setup based on a CCD camera and a hyperspectral laser obtained with an AOTF in front of a supercontinuum laser.

2. A proof-of-principle that particle size distribution can be inferred from the SLS measurements.

3. A platform for future development of hyperspectral SLS.

In the following section we will provide details of the vision system and describe how we extract relevant features. After that we show our experimental validation, and finally we discuss the obtained results.

Method

The purpose of the SLS technique is to correlate the observed image response with material properties of the measured samples. This involves design choices for the vision setup, extraction of relevant features and statistical analysis of the robustness of the measurements.

Table A.1: Hardware used in the SLS vision system.

System	Device
Supercontinuum light source	SuperK Power from NKT Photonics
AOTF	SpectraK Dual from NKT Photonics
Camera	Grasshopper CCD camera from Point Grey

Vision system

The hyperspectral analysis is based on images acquired from the vision system shown in Figure A.1 and A.2. The system components are described in Table A.1. The systems ability to perform hyperspectral imaging is imposed by changing the wavelength of the illumination light. The illumination system is based on a supercontinuum white light laser producing a quasi continues output in the range from 470 nm to 2400 nm. The output is delivered in a microstructured optical fiber to an AOTF for spectral filtering of the beam. Currently the spectral filtering is supported in the range from 480 nm - 850 nm with a spectral width growing linearly from 3.5 nm to 14 nm. The final beam power output of the combined system varies as a function of wavelength from around 0.4 to 2.5 mW, but the output is very stable over time. The AOTF is controlled by a direct digital synthesizer (DDS) which enables a fast computer controlled frequency change up to 10 times per second with an accuracy of 0.1 nm.

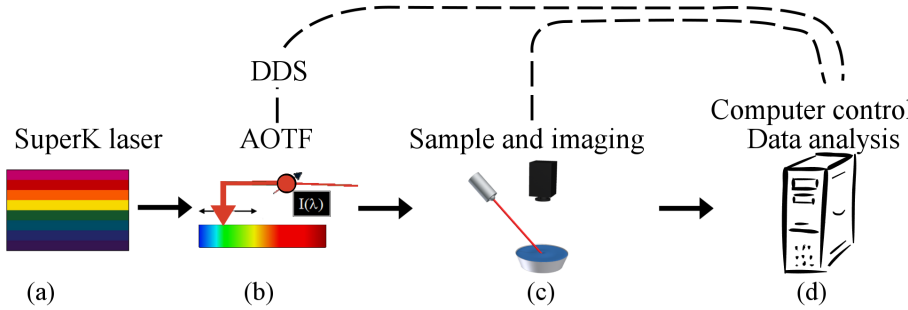

Figure A.2: Schematic illustration of the system interfaces and the scheme for generating the hyperspectral illumination system. The supercontinuum laser (a) delivers white collimated light to the AOTF, which is controlled by the DDS (b). A focused laser beam is illuminating the sample and an image is captured with a normal CCD camera (c). The entire setup is computer controlled (d).

The scattering distribution monitored from the sample will be a convolution of the scattering profile with the beams profile on the surface. Therefore, it is preferred to have a small simple beam profile. The final light delivery from the

AOTF to the food sample is performed using a LMA-5 photonic-crystal fiber. The beam is collimated after the fiber using a 5 mm focal length lens. Simultaneously the scattering center for the hyperspectral visions system remains fixed because the LMA-5 fiber support light delivery in the full spectral range covered by the AOTF.

The scattering profile is imaged using a 16 bit CCD camera with a spatial resolution of 1600×1200 pixels. The current camera connection reduces the frame rate to 4 Hz, resulting in a total acquisition time of about 3 min for a hyperspectral characterization of a sample with images from 480 nm to 850 nm with a spectral resolution of 5 nm.

Characterization of SLS features

The images are characterized by analysing a single profile through the scattering distribution. We have adopted a model from [32] to characterize the distributions, based on taking the logarithm to the distribution and fitted with a linear curve. An example of the data analysis is presented in Figure A.3.

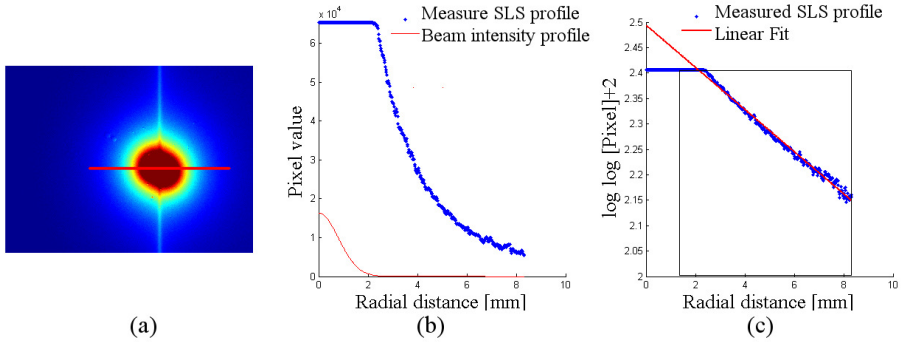

Figure A.3: Illustration of the data produced with the new vision system and the data analysis from the loglog model. (**a**) An image of the SLS profile in whole milk, the red trace is used in the analysis of the scattering profile (red pixels have is high intensities and blue have low). (**b**) Intensity through the scattering profile together with the beam profile. (**c**) loglog model for the scattering profile together with the linear fit. The black box indicate the range of data for the analysis.

The image from Figure A.3 (**a**) shows a typical example of the scattering profile. It is vaguely elongated along the vertical-axis due to the beam being non orthogonal to the samples surface. In addition the images are suffering from a vertical

smearing because of the heavy overexposure of the center pixels. An example of a scattering profile used and the loglog analysis of the image is presented in Figure A.3. The scattering profile shows two different regimes previously presented by [169]. The interval closest to the scattering center is dominated by single scattering or diffuse reflection. In this regime the resulting scattering profile is almost proportional to the beam profile projected on the samples surface. Light rays in this part of the image have not undergone multiple scattering and do not give much information on the samples properties. The scattering pattern, which exceeds the size of the beam width, have undergone multiple scattering events and can to some extend be modeled as a diffusion process. In this range, the data with higher intensity than the background noise of the camera is fitted with a linear slope. The trace analyzed with this method results in two parameters, a slope and an offset. The offset of the loglog curve, which represents the amplitude of the SLS profile at the image center, is very system dependent. It may be possible to make the value independent of the system by calibrating the signal strength on the CCD camera. The slope of the loglog curve describes the rate of descend and is therefore a combination of the scattering properties of the sample and its absorption spectrum. A high value of the loglog slope corresponds to a narrow scattering profile.

This form of characterization will be referred to as the loglog model. It only makes use of a limited amount of image information close to the scattering centre. The loglog model is not motivated by a physical understanding of the scattering process, but it gives a robust method that previously has been shown to correlate well with the structure of the sample [32].

Reproducibility

The measurements are performed by first filling up a measuring cup to a specific height, then conduct a measurement. This procedure has two major uncertainty elements, the reproducibility of characterizing the same sample, which is a combined effect of the vision system, and a simpler uncertainty element in the way the sample and cup is positioned in the vision system. The beam is not perfectly collimated so the spot size of the laser beam may vary as a function of the samples height in the cup. A variation of the samples height will also change the size of the scattering profile measured by the camera, which is focused to fixed depth below the camera.

To estimate the vision systems robustness against variations in the characterization of a given sample, the same sample was depicted four times and analyzed with the loglog model as shown in Figure A.4. The resulting average values and standard deviation is presented in Figure A.4(a). Similarly the reproducibility

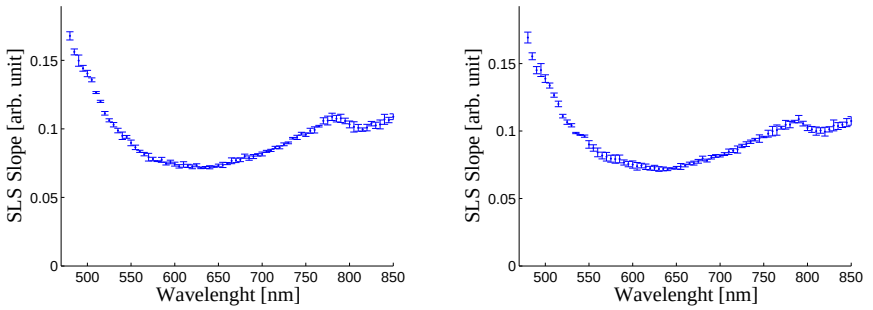

(a) Measurement of the same sample repeated four times.

(b) Measurement of the whole procedure repeated four times.

Figure A.4: Average value and standard deviation showing the loglog slope of the scattering distribution in four measurements on the same sample of whole milk as a function of the spectral band. The figures are almost identical because whole milk is measured in both experiments – the difference is that the same milk sample was measured four times in (a) whereas four different samples were used in (b).

of the measurements procedure was estimated by performing the parameters of the same product four times. The whole milk was poured into the measurement cup and analyzed with the vision system, and the results are presented in Figure A.4(b). The standard deviation of the sample characterization is generally much smaller than both the amplitude and the range spanned by the slope of the full spectrum that have been analyzed.

Experiments

Here we present the results of experiments that demonstrate the vision systems capabilities of discriminating chemical and structural variation. These measurements are the first presentation of hyperspectral characterization of the SLS properties of a material. As a proof-of-principle study a set of commercially available diary product where measured and characterized using the loglog model.

Chemical composition

The first three measurements focus on products with different chemical contents. We have chosen cream products with different fat percentage to be characterized using the SLS vision system. The different fat contents will affect the scattering profile because it increases the number of scattering centers in the sample, and thus the slope and offset of the profile. The measured profiles are presented in Figure A.5 showing a generally increasing slope as a function of the fat contents.

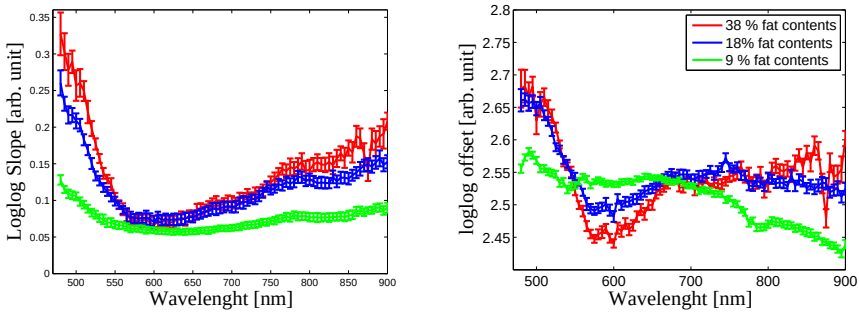

(a) Slope parameter

(b) Offset parameter

Figure A.5: Experiment showing the hyperspectral response for cream products differing by fat content. The fat content is especially distinguishable for low and high wavelengths for the slope parameter, whereas there is also information in the mid rage of the offset parameter.

The measurements of the scattering slope using the loglog model indicate that the largest discriminative power is found at the long and short wavelengths. The slope curves collapse in the spectral range from $\sim$ 530 nm to $\sim$ 700 nm. It is seen that the changes in the slope occurs on a length scale of one hundred nanometer in this spectral range. With the new hyperspectral vision system we are able to verify this trend. However the offset still discriminates between the samples in this interval.

Structural variation

Another important parameter, that we intend to measure is the particle sizes of different components in the sample. As a first indication of this, the SLS properties of reduced fat milk was performed on conventional milk and a organic product. These products have different particle size distributions due to

the homogenization of the conventional milk, which reduces the particle size. Consequently the conventional milk has a higher density of scattering centers, but with a smaller average size. The resulting SLS response is presented in Figure A.6.

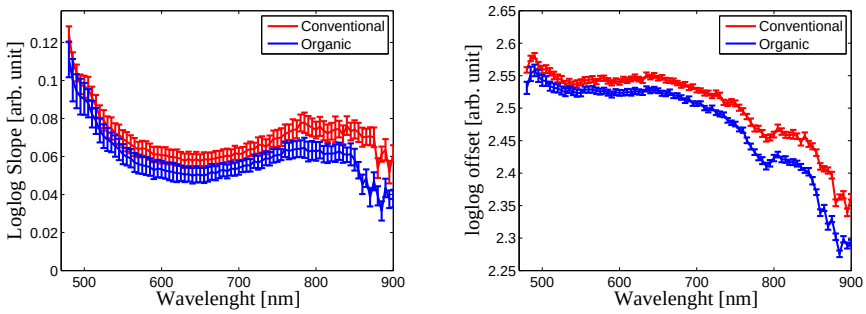

(a) Slope parameter

(b) Offset parameter

Figure A.6: Experiment showing the hyperspectral response for reduced fat milk differing by particle size and distribution. The organic product is unhomogenized whereas the conventional is homogenized. The homogenization process alters the size and distribution of the fat particles. Note that the difference is primarily a scale change of the SLS parameters.

The gain of hyperspectral analysis is small, but from the analysis we can choose the most discriminative wavelengths. This allows a simple but powerful method for discriminating between these products that only differ by homogenization process.

To illustrate the diversity of samples that can be examined using the new hyperspectral SLS vision system, the scattering profiles of a high particle density cream is compared to the scattering profile of fat reduced milk and yoghurt. The measured profiles are presented in Figure A.7(a).

Discussion

We have demonstrated hyperspectral SLS on a number of samples and shown that we can uniquely characterize a sample using SLS parameters. Repeated studies show that the parameters only vary slightly when the data acquisition is performed several times, indicating that the system is stable over time. This is very encouraging in relation to industrial inspection of food products based

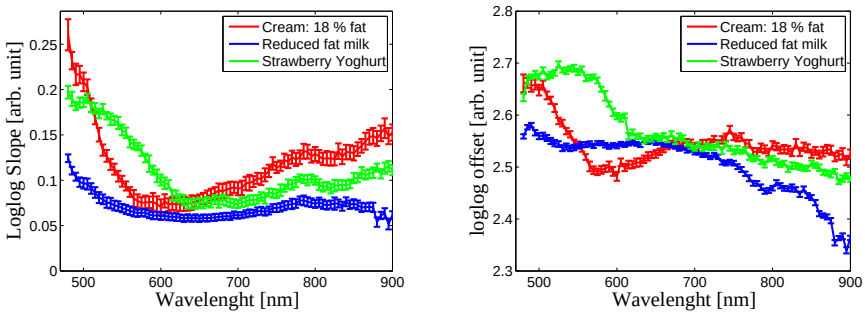

(a) Slope parameter (b) Offset parameter

Figure A.7: Experiment showing the hyperspectral response for a diverse collection of products. This illustrates the large amount of information in hyperspectral SLS measurements.

on this technique.

We chose to demonstrate the hyperspectral SLS on dairy products because they contain suspended particles causing the subsurface scattering. Also a large variety of dairy products are easily available making it a good choice for demonstrating the SLS system. But the SLS technique can be used for measuring many other products – especially biological samples have subsurface scattering, making the technique widely applicable to a range of food products including meat and vegetables.

We measure a parameter based on the logarithm of the measured pixel intensity taken twice ($log(log(I))$, where I is the image intensity), which is adopted from [32]. Empirical studies have shown that this map becomes linear, which allows a characterization based on two parameters – the slope and the intercept of the profile. The simplicity of this approach is very attractive, because it has shown to be robust and it is easy to measure. The only problem is the parameters dependence of the system, and to overcome this we need to include a calibration procedure in a future system. Further research should address the parameters characterizing a sample. One interesting application would be to directly infer particle size and distribution and another would be to measure refractive properties.

Results are reported for a single profile, so at the moment we are not utilizing the information in the entire image. A consequence is that image noise is influencing the measurements, as seen from the error bars in the graphs shown in Figure A.5, A.6 and A.7. We could utilize more of the image to obtain higher signal to

noise ratios, for example by sampling more profiles or employing a 2D model.

The characterization is based on measurements of the subsurface scattering, so we would like to optimize the system to capture as much information about the subsurface scattering as possible. The parameters governing the measurements include the beam power and profile of the laser and the exposure time of the camera. A large proportion of the light reflected close to the center of the beam is a result of single scattering or diffuse reflection. Optimally the beam profile should be as small as possible, so our relatively large profile can make the result less precise.

The beam power and exposure time have similar effect, and a large power or long exposure results in a large saturation of the depicted laser spot. This gives a high signal to noise ratio, but at the cost of information at low intensities. Low beam power or exposure will provide this information, but with lower signal to noise ratio. This tradeoff between illumination and exposure time can be accounted for by using high dynamic range, where an image is composed of multiple exposures to obtain high signal to noise ratio in both the low and high intensity range. In this paper we chose a single exposure, and despite this we were able to distinguish small differences like homogenized vs. non-homogenized milk.

Many of the samples are distinguishable at one wavelength, but it is important to note that this is not known in advance. Consequently our SLS system allows us to select the wavelengths with highest discriminative power, and can this way aid in constructing an optimal food inspection system, for example based on less expensive hardware like laser diodes. As a result the reconfigurable nature of the SLS system has great potential in explorative food analysis, but also in more general material characterization.

Conclusion

We have addressed the problem of inferring properties of a material from measurements of subsurface light scattering. Our contributions are (*i*) a hyperspectral SLS (subsurface laser scattering) vision system, (*ii*) a procedure for characterizing the measured samples, and (*iii*) an experimental analysis of a number of dairy products. This explorative analysis shows a proof-of-principle of our hyperspectral SLS system for food characterization, and acts as a platform for future development.

Acknowledgements

This work was financed by the Centre for Imaging Food Quality project which is funded by the Danish Council for Strategic Research (contract no 09-067039) within the Program Commission on Health, Food and Welfare.

Appendix B

Monitoring Optical Changes during Milk Acidification Using Hyperspectral Diffuse Reflectance Images

Jacob L. Skytte[a], Otto H. A. Nielsen[a,b], Ulf Andersen[c], Flemming Møller[d], Jens M. Carstensen[a], Anders B. Dahl[a], Rasmus Larsen[a]

[a] *DTU Compute, Department of Applied Mathematics and Computer Science, Technical University of Denmark, Matematiktorvet, Building 322, DK-2800 Kgs. Lyngby, Denmark*
[b] *NKT Photonics A/S, Blokken 84, DK-3460 Birkerød, Denmark*
[c] *Arla Strategic Innovation Centre, Rørdrumvej 2, DK-8220 Brabrand, Denmark*
[d] *DuPont, Edwin Rahrs Vej 38, DK-8220 Brabrand, Denmark*
[e] *DTU Photonics, Technical University of Denmark, Ørsteds Plads, Building 343, DK-2800 Kgs. Lyngby, Denmark*

Abstract

A novel hyperspectral (480-1030nm) laser imaging system is used to monitor the optical changes during a milk acidification process. Images of diffuse reflectance are captured remotely using a tuneable laser and CCD camera, and differences in the response images between base milks and corresponding gels elucidate several interesting features. In this paper one of these features is quantified using a simple and noise resistant quantification scheme inspired by conventional light interaction models. The generalisability of the feature is investigated through a factorial design in which fat content, protein content and the fermentation temperature is changed systematically. The acidification is initialised using glucono-δ-lactone (GDL), and conventional oscillatory rheology is used to validate the gel development. Through analysis of variance the extracted image feature shows significant effects from fat and temperature throughout all wavelengths. Additionally a significant effect for protein is only seen at lower wavelengths (480-540nm).

Introduction

Simple in-line monitoring techniques for food manufacture can aid in production of high quality products with low variability. Food quality relates to factors like appearance, taste, and texture that are important for consumer acceptance, as well as chemical and microbiological composition that hold information about nutrition and food safety. For decades there has been an interest in optical methods for measuring food quality parameters, especially methods based on non-contact designs, as these methods are well-suited for monitoring fragile systems and for in-line implementation in factory settings. In this paper we investigate the potential for using hyperspectral images of lights diffuse reflectance to monitor the gelation process in dairy production. The images are captured using a novel hyperspectral vision system, which is a generalisation of the commercially available product, VideometerSLS (*Videometer A/S, Hørsholm, Denmark*).

Milk gelation is a central process in the production of many products including yogurts and cheeses. These milk gels are formed by lowering the pH value of the milk, which ultimately leads to destabilization and aggregation of the suspended casein micelles. Hereby a gel network is formed by the casein. The structure formed through the gelation process is important for the consumers experience of the final yoghurt or cheese Bourne*et al.* [170]. Creaminess and viscosity are key factors for product quality and closely linked to the gel structure[171]. To optimize the product quality a control mechanism of the gel formation is

required, here a reliable monitoring system plays a key role.

The structural properties of the final gel can rely on a plethora of different parameters. Milk standardization, homogenization [172], pre-heat treatment [173] and incubation temperatures [174] are parameters that can be controlled [20]. With a precise tool to monitor the structure development these parameters can be adjusted to account for uncontrollable parameter like the natural variations in the raw milk [175].

Milk gelation is obtained by lowering the pH in the milk, and it is common to measure the temporal pH development. This is important to ensure that the product has the correct acidity, but the development of pH is not uniquely related to the structure development. Two gelation processes might have the same temporal pH development, but result in products with different viscosity or creaminess [22].

It is well known that the optical properties change throughout a milk gelation process, and these optical changes have been investigated intensively. Many methods have been suggested, which are primarily based on near infrared (NIR) transmission and reflectance [176]. Especially diffuse reflectance measurements using optical probes have been investigated to a great extent. A system for estimating the optimal cutting time during cheese making was presented by Payne *et al.* [27]. This system has also been investigated for a variety of different product types as well as other application areas in the milk gelation process, and multiple application studies have been published [177].

Menzzenga *et al.* [178] pays special interest to dynamic light scattering (DLS) and diffusing wave spectroscopy (DWS). These methods illuminate scattering media using a coherent laser beam. By observing the fluctuations in scattering intensity (speckle), which is caused by Brownian motion of the scattering particles, information about the size and dynamics of the particles can be derived. This can be estimated on the basis of the temporal autocorrelation function of the observed fluctuations. While DLS deals with single scattering events, DWS is an extension of DLS that deals with multiple scattering and is more suited for real world applications [179].

Despite the abundance of optical methods, only few in-line systems are commercially available for monitoring milk coagulation [180, 181, 176]. This can partly be explained by the hostile process conditions where plant vibrations and strict requirements for the implementation exist. The optical methods needs to be performed in situ, should not interfere in the production, and has to meet dairy hygiene standards. Light transmission, light reflectance, and DWS (both transmission and backscattering), have all been used for in-line measurements [176, 181].

A well-documented light reflectance system is the CoAguLite (*Reflectronics, 3009 Montavesta Road, Lexington, KY 40502, USA*), which measures light reflectance ratios using optical probes. During milk coagulation it records a sigmoidal behaviour from which the time of gelation and the optimal cutting time for cheese can be predicted [182]. This particular system is installed by welding optical probes into the side of a cheese vat. While this is well-suited for large scale production, it can be uneconomical for small scale production where smaller (and perhaps several different) cheese vats are used [183].

In this paper we investigate the potential of using a hyperspectral diffuse reflectance imaging system as a tool for in-line milk gel assessment. Measurements are made by shining a tuneable laser (480-1030nm) into the sample and a CCD camera capturing an image of the spatial distribution of the diffuse reflection. Directly compared to CoAguLite, the system is also based on light reflectance, but offers increased flexibility in both system setup and analysis of data. Data can be collected non-invasively which should alleviate in-line implementation. The system was introduced by Nielse *et al.* [1, 15], and has similarities to backscattering DWS. However, the signal output and subsequent analysis is significantly different. While DWS is based on measuring particle dynamics our measurements are influenced by the changes in the absorption and scattering properties.

We study the temporal changes in the hyperspectral diffuse reflectance images in different milk gelation processes. Protein content, fat content, and fermentation temperature are changed systematically in a factorial design to investigate the generalisability of the method. The images are quantified and through analysis of variance significance effects are determined across different wavelengths. The gelation processes are validated using small-amplitude oscillatory rheology, which can provide information about the rheological properties continuously throughout the acidification process.

Material and Methods

Experimental Design

The purpose of the experiment was to investigate the generalisability of the diffuse reflectance images towards three common process parameters: protein content, fermentation temperature, and fat content. These three factors were varied systematically at two levels, resulting in a full single replicated 2^3 factorial experimental design. Additionally, three replicates were added as centre

Table B.1: Factors and target levels for the 2^3 factorial experiment (plus three centre points) used for testing the generalizability of the diffuse reflectance images.

		Target factor levels		
Factor	Code	Low	Centre	High
Protein content [%]	P	3.4	3.7	4.0
Temperature [°C]	T	27.5	32.5	37.5
Fat content [%]	F	1.5	2.5	3.5

points to the design. Centre points can be used to estimate the mean squared error (MSE) of the experiment from the centre points alone, and to investigate for quadratic factor effects [184]. Additionally the centre points provided enough degrees of freedom to check for significance in all first and second order interactions in the experimental design.

The factor levels were chosen to ensure reasonable differences between the different gelation developments while still being relevant in the scope of commercial products. The absolute value of the fat content was ensured using commercially available UHT milk with two levels of fat; semi-skimmed (1.5%) and whole-milk (3.5%). The protein content was increased by adding 1.67% (w/w) skimmed milk powder (SMP), which results in an increase in protein content from 3.4% to 4.0%. The temperature spanned 27.5°C to 37.5°C and was controlled using water baths. The factorial design is summarised in Table B.1.

For each of the nine different process compositions, the acidification was performed by adding 2% (w/w) glucono-δ-lactone (GDL), as it is a reproducible model system for milk gelation as opposed to bacteria cultures [185]. Each sample in the experimental design was a 5.5-hour-long series of diffuse reflectance images (taken every 6 minutes) and rheological measurements (taken every 2.5 minutes). First measurement were made three minutes after GDL addition. The time points for image acquisition were recorded, and linear interpolation was used to obtain time correspondence between the 11 measurement series.

For the remainder of this article, the capital letters (P, T, and F for protein content, temperature, and fat content respectively) in sample names denote a high factor level, while absence of capital letters denote a low factor level. The centre points will be referred to as "centre".

Milk Sample Preparation

The milk was kept at room temperature in its commercial packaging, until it was used. In preparation of the experiments, each milk sample (500ml) was initially heated for an hour in a water bath at the target temperature. It was then taken out of the water bath and the SMP was immediately dissolved (if required) in the sample using a magnetic stirrer. Hereafter GDL was added and the sample was stirred for three minutes. Three aliquots were taken from the sample. Two 200ml aliquots in open glass containers were placed back in the water bath, one for capturing diffuse reflectance images, and one for temperature measurements. One 20ml aliquot was used for rheology measurements. All experiments were carried out during a one-and-a-half-week period.

Milk Temperature Control

For temperature control, a shaking water bath (*SW2* $\pm 0.2^{\circ}C$, *Julabo Labortechnik GmbH, Seelback, Germany*) was used. The shaking function was turned off to avoid any vibrations, which would cause shifts in the sample height and interfere with the image acquisition. Using a temperature probe (*Tes-1380 Temperature Meter* $\pm 0.5^{\circ}C$, *TES Electrical Electronic Corp., Taipei, Taiwan*) it was found that the general temperature was between 0.1 to $0.5^{\circ}C$ lower than the target factor levels. As the milk was prepared outside the water bath the temperature dropped a few degrees before it was put back into the temperature-controlled environment.

Hyperspectral Diffuse Reflectance Images

An example of a diffuse reflectance image is shown in Figure B.2. The images are formed using a system following that of [1, 15]. A schematic view of the system set-up is shown in Figure B.1. The set-up is based on a super continuum light source (*SuperK Extreme, NKT Photonics, Birkerød, Denmark*), filtered by an acousto-optic tunable filter (*SuperK Select, NKT Photonics, Birkerød, Denmark*), and the combined system produces a collimated light beam, in the range 480-1030nm, at high spectral resolution. For each wavelength the laser is shined into the milk sample from the top down at an oblique incident angle (45°), and a CCD camera (*Grasshopper CCD Cam, Point Grey Research Inc., Richmond, Canada*) with a spatial resolution of 1200×1600 pixels, captures an high dynamic range (HDR) image of the diffuse reflectance.

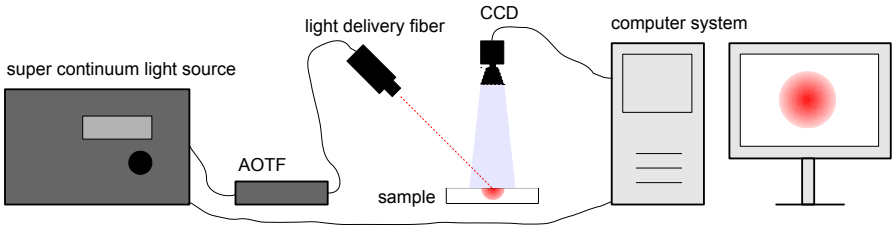

Figure B.1: A schematic view of the hyperspectral vision system. Additionally two lenses were installed, one in front of the laser beam and one in front of the camera.

Additional to the system shown, a biconvex lens (focal length: 100mm) was installed in front of the light beam. This focussed the light to a Gaussian (*transverse electromagnetic mode*$_{00}$) beam waist of 150μm. In front of the CCD a zoom lens (*23FM50L, Tamron Co. Ltd., Saitama, Japan*) was installed with a 6.5cm spacer, which yielded a spatial pixel size of 3.2μm in the object plane. The vision system was installed around the water bath (see Section B), and the entire set-up was shielded from background light.

Both the output power of the light source and quantum efficiency of the CCD chip are wavelength dependent. For this reason we make a pre-calibration of the output power and the exposure times in the HDR algorithm, to ensure that no pixel become overexposed for short exposure times, and that an adequate signal is available for the longest exposure time. The calibration is performed on a highly scattering medium that represent the final state of the fermented milk. For these measurements whole milk was used. The camera was set to minimum exposure time and the light source power was reduced until no pixels were saturated. Using this reduced power the maximum shutter time is set high enough to produce low noise pixel intensities far from the light entry point. A compromise was made on maximum exposure time, to avoid too long acquisition times. Thus, some averaging is performed when quantifying the images (see Section B).

The wavelengths were sampled in 10nm steps, which resulted in 56 different spectral samples at every time point. With a consistent acquisition time just under six minutes, approximately 60 data points were acquired throughout the 5.5-hour-long acidification process.

Parameter Extraction

Milk products are highly scattering media and following diffusion theory, the area close to the beam centre is dominated by a single or few scattering events. These events take place close to the sample surface, and do not give much information about subsurface sample properties. Further away from the beam centre, multiple scattering events begin to dominate. Here light has entered the sample and been scattered multiple times before leaving the sample again (diffuse reflectance). The appearance of this part is therefore dependent on the optical properties of a larger volume of the sample, which relates to particle sizes and volume concentration – this is where we extract the slope parameter. For simplicity we have only considered a single image feature which models the rate of light decay far away from the point of incidence. This parameter was presented by Carstensen [32] and is being used in a commercially available product (*Videometer A/S, Hørsholm, Denmark*).

The parameter is the slope of a double logarithmic transformed profile, $\log(\log(I+2))$, where I is the pixel intensities. The profile is sampled orthogonally to the incident direction of the laser through the intensity peak. This profile is symmetric and we average the two sides. To reduce the noise further we use the average of an 11-pixel-wide band. A linear model is fitted to the latter half of the profile, i.e. the part of the profile far (400 pixels, i.e. 1.3mm) from the beam centre, which reduces the parameterisation to a slope and an intercept. The parameter extraction is visualised in Figure B.2. Both parameters hold information about the samples scattering properties and its absorption spectrum. However, the intercept parameter is also highly dependent on the amplitude of the measured signal. Thus, the slope parameter should be better suited to follow the optical changes during milk gelation.

This parameterisation can be seen as a simplification of the work by e.g. [67, 103]. Their work is based on physical models where they utilise the diffusion approximation to estimate the absorption and reduced scattering coefficients. Our approach is a more statistical way of quantifying the light diffusion. The double logarithmic transformation combined with the linear model can be seen as a compromise between resistance towards noise and suppressing information.

Small Amplitude Oscillatory Rheology

Acidified milks are weak gel networks, thus easily damaged by deformation. In order to continuously measure on a single sample, small amplitude oscillatory rheology (SAOR) can be used. In SAOR a small sinusoidal deformation is

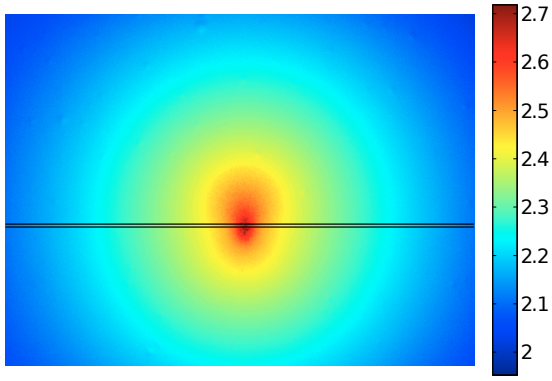

(a) Horizontal band

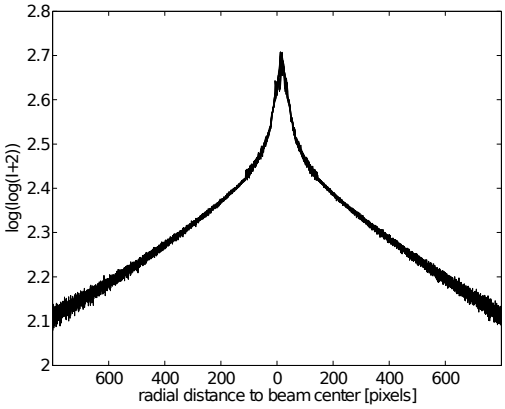

(b) Intensity profiles

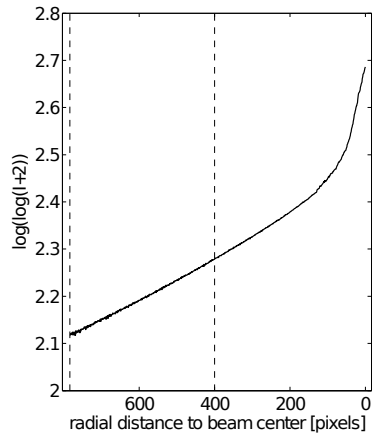

(c) Slope parameter from final profile

Figure B.2: Extraction of the slope parameter from a double logarithmic transformed diffuse reflectance image of whole milk at 900nm. In (a) a horizontal band of profiles is extracted from the image, and the corresponding intensity profiles can be seen in (b). (c) shows the final profile after averaging over all profiles in the band, as well as across the profile centre. The dashed lines indicate the interval where the linear model is fitted, and the slope parameter is extracted.

applied, in which small deformation is defined as a relative deformation, which does not disrupt the development of the network structure ([20]). Acidified milks are viscoelastic, meaning that they express both ideal elastic and ideal viscous behavior. These behaviors can be described by the storage (elastic)

modulus (G'), which is the amount of energy stored per deformation cycle, and the loss (viscous) modulus (G''), which is the amount of energy lost as dissipation per deformation. Only the storage modulus (G') is reported when the rheological measurements are presented. Typically, during milk fermentation the storage modulus has a zero baseline until the point where casein micelles starts to aggregate (referred to as the gelation point), after which a sigmoidal behaviour can be observed [20].

In this experiment a 20ml sample was used in the rheometer (*Stresstech HR* with temperature cell $\pm 0.1^{\circ}C$, *Reologica Instruments AB, Lund, Sweden*) with a double gap concentric cylinder measuring system.

Analysis of variance

Analysis of Variance (ANOVA) was used to determine the significant factors when considering the slope parameter or the rheology measurements as the response variable. Significance of main effects, as well as all possible interactions were investigated. Some slight modifications were made to the standard ANOVA. The mean squared error (MSE) was estimated from the centre points and the presence of quadratic effects was also included in the analysis. Also, a slightly different approach to hypothesis testing was used as the degrees of freedom in the experiment were limited. Here, the mean squares and degrees of freedom of a factor are pooled with the error, if the p-value of the corresponding F statistic is larger than 0.25. A sequential approach to the pooling is used, starting with the higher order interactions. Thus, the error can be estimated with more degrees of freedom. These modifications to the ordinary ANOVA are suggested by Montgomery [184].

As each acidification process is a temporal series of measurements, it is necessary to find a scalar representation for the ANOVA. Two approaches were used. The first was to record the amplitude of the signal at fixed time points, and the time points at 10, 25, 50, 75, 90, and 100% of the total time were used. The second approach utilised Principal Component Analysis (PCA) of entire signals, in which principal scores are used to make a scalar presentation of the process. To investigate the variation explained by the principal components, the approach presented by Cootes *et al.* [186] can be used. Here the mean signal is calculated, and all signals are centred around it. A PCA is performed on the centred signals, and the loading vectors, scaled by their eigenvalues, are added to/subtracted from the mean shape. In this way we can investigate the variation described by each principal component.

Multivariate analysis of variance

Multivariate analysis of variance (MANOVA) was also considered. MANOVA is a generalisation of ANOVA, where multiple responses can be tested simultaneously, and linear combinations of the response variable are considered when determining factor and interaction significance. MANOVA requires more degrees of freedom, thus with this experiment we are limited to two dependent variables, if we wish to retain all factor effects from the previous ANOVA tests. The first and second principal scores are chosen as dependent variables, and Pillais trace is used as an approximation to the F statistic [187]. MSE calculations from centre points, and pooling of MSE and factors with a p-value, as described in Section B, was also used for the MANOVA.

Results

Hyperspectral Diffuse Reflectance Images

Examples of diffuse reflectance images are presented in Figure B.3. Most of the appearance of these images can be encoded by a parametric model based on the refractive index, scattering, absorption and phase function [169]. To show the effect of the milk acidification directly in the image data, an early and late image in the time series is combined and separated by a black line. The images are presented for two different samples at three wavelengths.

For all measurements, the light attenuation is stronger by the final fermented product, as can be seen by the faster decaying signal, which corresponds to an increase in either scattering or absorption. This is remarkable, the chemical composition is the same throughout the acidification process, and yet the optical signals change significantly. This have recently been verified by Nielsen *et al.* [4] where it is shown that the primarily optical difference between milk and fermented milk products is in the reduced scattering coefficient.

The elongation is caused the oblique incidence angle of the light. The specific shape is arising by a combination of the light penetration depth, which is used by Wang and Jacque[103], and the shape of the phase function of single light scattering. As a general trend, the penetration depth increases as a function of wavelength. This makes the shape more elongated. However, it is evident that the elongation also is different between the samples with high fat or protein, where the later is more elongated across all wavelength. The shape of the elongation is also complex, for the start point of the high protein samples at

500nm the light is forming a narrow fan-shaped shape profile rather than a simple ellipsoid. Thus it is clear that more information about the scattering process is available than what is covered by the parameterisation in Section B.

Additionally, the images also show differences in an underlying interference pattern, which is mostly visible close to the point of incident, and is stronger in the fully fermented samples. The effect is present over the whole image, and have been utilised in [83] to distinguish milk and yogurt products with coinciding optical properties.

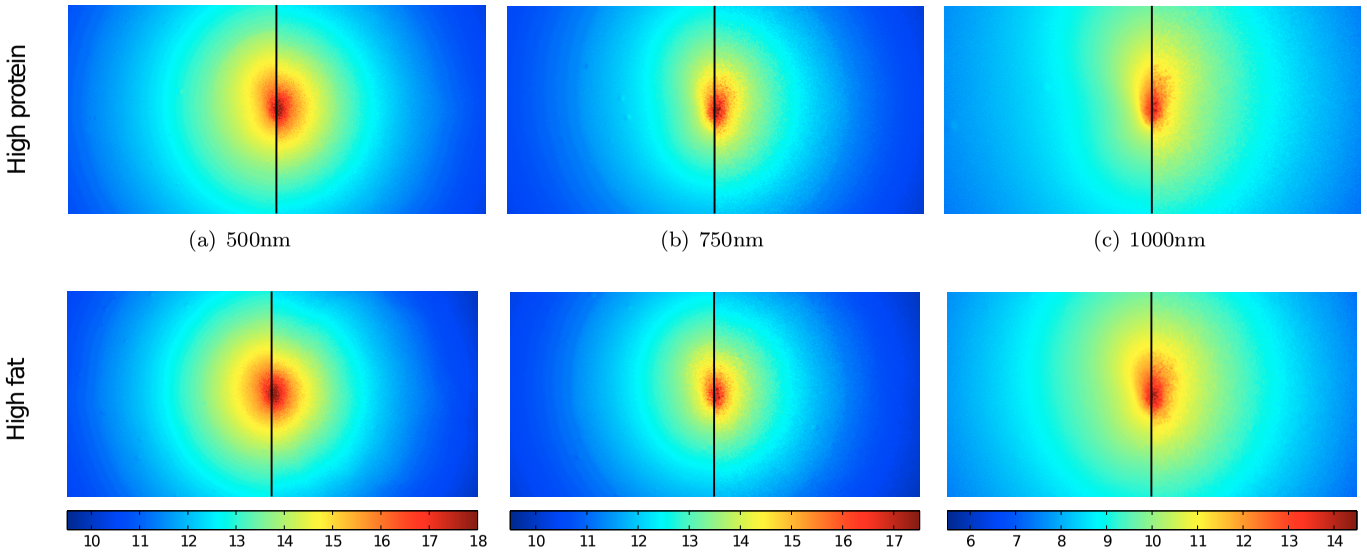

(a) 500nm (b) 750nm (c) 1000nm

(d) 500nm (e) 750nm (f) 1000nm

Figure B.3: False colour images of the double logarithmic transformed system responses for two extrema in the experimental design at different wavelengths. Red corresponds to high pixel intensity and blue corresponds to low pixel intensity, and the scale of the colour map is the same across wavelengths. The left hand side of each image shows the response from the milk base, and the right hand side shows the system response late in the fermentation process. The laser is shone in from the bottom of the images.

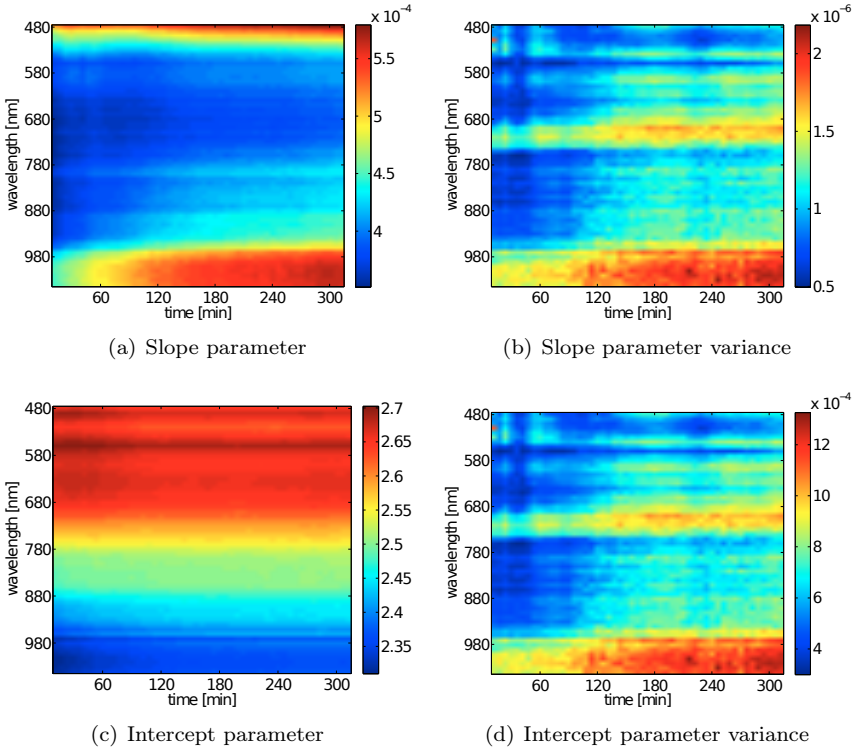

(a) Slope parameter

(b) Slope parameter variance

(c) Intercept parameter

(d) Intercept parameter variance

Figure B.4: Parameter and variance estimates for a centre point sample. (a) and (c) shows the parameter estimates for the slope and the intercept parameter respectively and (b) and (d) shows the corresponding variance estimates of the parameters.

Parameter Extraction

The intercept and slope parameter were extracted from the diffuse reflectance images for each time point (61 in total) and wavelength (56 in total). Figure B.4 shows the estimated parameters and their corresponding variance for a centre point in the factorial experiment.

The low numerical value of the parameter variance for both the slope and intercept, combined with the smooth development of the parameters themselves, validates the applied linear model. However, the slope parameter shows clearer dynamics across time when compared to the intercept parameter. For the sake of simplicity we will only consider the slope parameter for further analysis.

Looking at the outer regions of the wavelength interval, there is a tendency towards steeper slope parameter estimates. This was the general behaviour seen throughout all experiments. Also, from Figure B.4(b) it can be seen that parameter variance is higher in two major regions. This pattern was repeated throughout all the experiments. One region is in the near-infrared area, where the low quantum efficiency of the CCD cameras results in a lower signal-to-noise ratio, and thereby larger model errors. The other region is around 700nm late in the acidification process, which is because the transformed profile starts to show more curvature inside the fitting interval. The slope parameter, averaged over three different wavelength intervals is shown alongside the rheology measurements in Figure B.5.

Small Amplitude Oscillatory Rheology

The rheological measurements seen in Figure B.5. According to Lucey and Singh[188] and Sodini *et al.* [189] an increase in total solids content (protein and/or fat) increase the final gel strength (storage modulus). Following Phadungath [190] higher temperature generally increases the speed of the acidification, and lowers the final gel strength level, as a response to the increased rearrangement of the casein particles. While the increased temperature results in earlier gelation points as seen in Figure B.5, the final gel strength after 5.5 hours is also generally larger. While this contradicts Phadungath [190], Anema [191] notes that inconsistencies regarding this matter exist in the literature. These inconsistencies are attributed differences in the measuring conditions. Additionally, Anema [191] presents more general results on the matter, which corresponds well to our observed values.

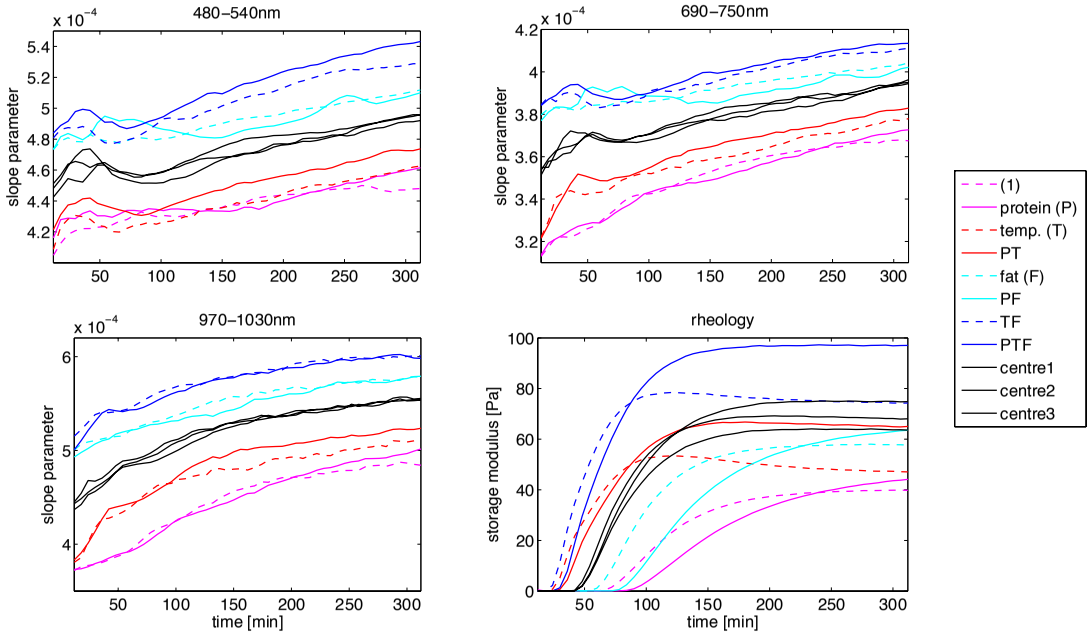

Figure B.5: The slope parameter averaged in three different wavelength interval and the rheology measurements as a function of time. Samples are coded by capital letters. A capital letter denotes a high level of that particular factor, and an absence of a capital letter denotes a low level of the factor. For sample (1) all factor levels are low. "centre" denotes the centre points.

Analysis of Variance

ANOVA was both performed at different time points in the measurement time series, and on the entire time series projected into one dimension, and thereby suitable for ANOVA. For the sub-space projected measurements Figure B.6 exemplifies the variation explained by the first three principal components for the slope parameter (averaged over all wavelengths) and the rheology measurements.

For the slope parameter in the lowest wavelength interval the first principal component (PC1) describes the amplitude of the signal and both PC2 and PC3 seem to cover the temporal location and amplitude of the bump located early in the process. Looking at individual spectral bands the same observation were made, however PC2 shows more pronounced effects of the bump for the lower wavelengths c.f. Figure B.5. For the rheology measurements, both PC1 and PC2 seem to incorporate the signal amplitude, steepness after the gelation point, and the overall shape of the signal, whereas PC3 was harder to interpret. In case of both slope parameter and rheology the two first components accounted for more than 95% of the total variation. It should be noted that the PCAs were applied separately for the different response variables. This means that we cannot be sure that all data is transformed in the exact same manner.

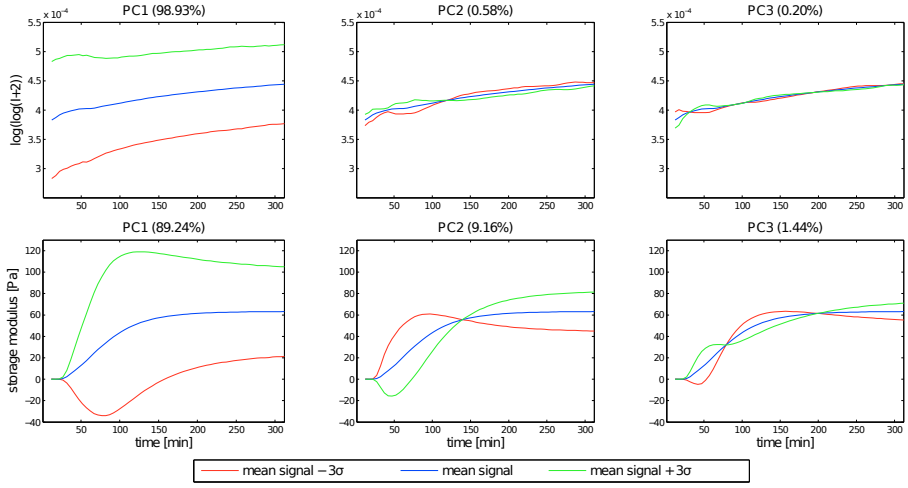

Figure B.6: The interpretation of the 1st, 2nd, and 3rd Principal Components (PC) scores used in the Analysis of Variance (ANOVA) analysis. The top row shows for the slope parameter (averaged over all wavelengths) and the bottom row shows for the rheology. The shown percentages denotes the amount of variance explained by each PC.

In order to also incorporate the hyperspectral information of the slope parameter, the overall wavelength interval was uniformly divided into eight subintervals. Within these subintervals the slope parameter was averaged. Thus, in total, we effectively have 6+3 different scalar representations of the 8+1 response variables, that is a total of 81 ANOVA tests had to be performed.

Rather than presenting conventional ANOVA tables, the p-values are presented in Figure B.7. The p-values clearly show that both temperature and fat level have significant impact on both rheology and the averaged slope parameter for all wavelengths. Protein only has an effect on rheology and the averaged slope parameter in the lowest wavelength interval. Additionally, the slope parameter seems to be more sensitive to factor interactions as well as quadratic effects. These tendencies mostly appear at higher wavelengths.

Looking at the amplitudes for the rheology measurements after 10% of the total time, it can be seen that all factors are significant. This is due to the period before the gelation point in the milk acidification process, where no signal is measured for most of the experiments. Thus the centre points coincide and result in a MSE close to zero, which causes all factors to be significant. Similar trends can be observed for some slope parameter ANOVAs (550-610, 690-750, and 760-820nm). As these occur as abrupt changes compared to the neighbouring ANOVA tests, this might as well be due to nearly coinciding centre point measurements.

Multivariate Analysis of Variance

The MANOVA was performed on PC1 and PC2, as they accounted for more than 95% of the variance for both the slope parameter and the rheology. The results are presented in Figure B.8, and they resemble the ANOVA tests. Both fat and temperature are significant for the slope parameter and the rheology measurements, while protein is significant for the rheology measurements and the slope parameter in the 480-540nm interval. Again interactions and quadratic effects seem more prominent for the slope parameter.

Discussion

The raw image data presented in Figure B.3 show significant variation between the initial and the end states of the milk gels. This is a strong motivation for further processing of the image data. In this work we consider linear modelling of

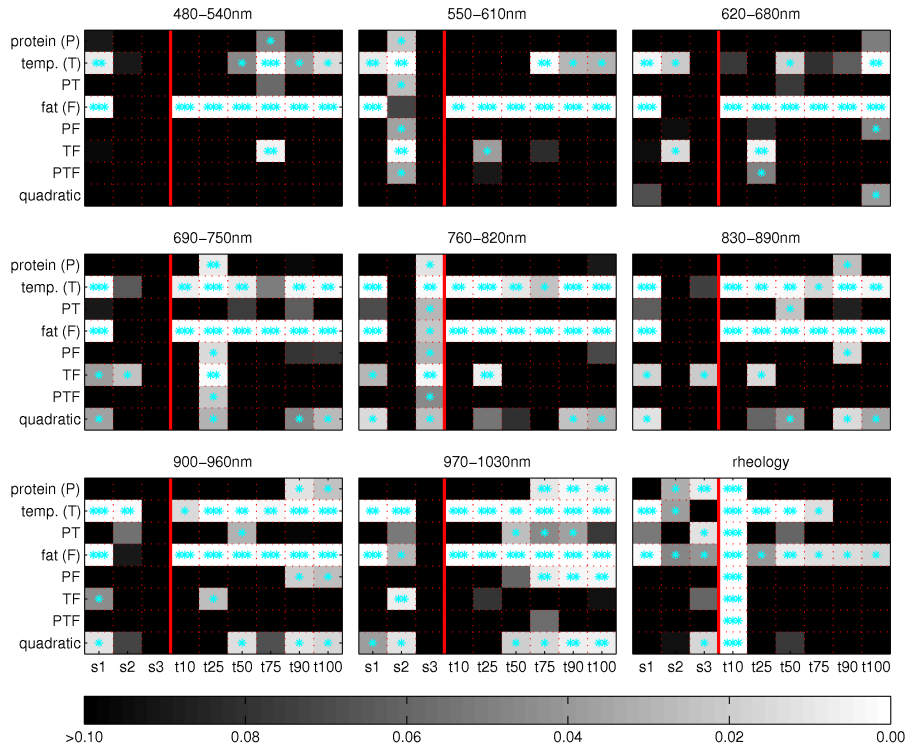

Figure B.7: Summary of the p-values in the ANOVA tests. The first eight images show the results for the averaged slope parameter in the eight different wavelength intervals, and the last image is the results for the rheology measurements. Each column in an image is one ANOVA test. {s1,s2,s3} are the principal scores and {t10,t25,t50,t75,t90,t100} are the slope parameter amplitudes recorded at 10, 25, 50, 75, 90, and 100% of the total time. Level of significance is denoted by asterisks ($*** \; p < 0.001$, $** \; p < 0.01$, $* \; p < 0.05$).

double logarithmic transformed diffuse reflectance profiles, but it is evident from the image that other features can also be considered. Nevertheless, the linear model provides a good description of the diffused light far from the entrance point, and specifically the slope parameter show significant changes in dynamics. Furthermore, the estimated variance of the slope coefficient was small compared to both the temporal changes during the milk fermentation and between the different sample composition. This motivates it as a robust model for inspection of the diffuse reflectance images.

Through ANOVA and MANOVA we saw that all chosen factors were significant for the rheology. This was also the case for the slope parameter. However,

protein content was only found significant at the lower wavelengths. Factor interactions were not predominant in either rheology or slope parameter, but quadratic effects were found to be significant for the slope parameter at the higher wavelengths. However, due to the small experimental design it is not possible to determine the source of the quadratic effects. This shows that the slope parameter was seemingly affected by both the structure development and the chemical composition of the milks. Figure B.5 also illustrates how the low wavelengths differentiate protein levels better, with the exception of samples F and PF. In general it seems harder to distinguish between protein levels in samples with a high level of fat. This is consistent with the literature as casein micelles are known to generally scatter less light than the fat globules [192].

As previously mentioned the slope parameter models the light decay rate, which depends on the total attenuation. Thus, increasing either scattering or absorption properties will increase the decay of light and thereby increase the slope parameter. Scattering is inversely proportional to wavelength [87]. However, Figure B.4(a) only shows a monotonous decrease in the slope parameter from 480 to 780nm hereafter it starts to increase again. A possible explanation is based on the water absorption spectra [193], where a small absorption peak is located between 700 and 800nm and a more dominant peak is located between 900 and 1030nm. This corresponds well to the observed behaviour of the slope parameter.

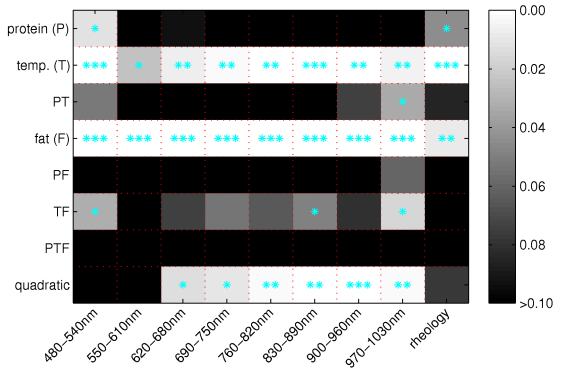

Figure B.8: Summary of the p-values in the MANOVA tests. Each column is a MANOVA test. The first eight columns are the results for the slope parameter averaged in different wavelength intervals, and the last column is the results for rheology measurements. The dependent variables are the first and second principal scores. Level of significance is denoted by asterisks ($***$ $p < 0.001$, $**$ $p < 0.01$, $*$ $p < 0.05$).

It is clear that the rheology measurements and the slope parameter describe two different developments in the milk acidification process. Contrary to the rheology measurements, the slope parameter shows a clear signal before the gelation point (the point where the casein micelles starts to aggregate), which has been observed before using optical methods [194, 195]. Furthermore, the slope parameter has a clear ordering of the different acidification processes early on, especially when looking at the processes with different fat levels and temperature levels. However, the protein effect is clearly weak for the slope parameter. In terms of wavelength dependency the signal in the interval 480-540nm shows a clear bump in the beginning of the process, which is not present at the higher wavelengths. Especially at 970-1030nm the initial steepness of the signal seem to correspond to the fermentation temperature. The steepest initial signals are seen at high temperatures and may relate to the faster gelation processes, which are also seen for the rheology in Section B.

Also, an early ordering of the acidification processes was found when looking at the slope parameter. The ordering is kept throughout the entire acidification process and corresponds well to the final levels of G' of the rheology measurements. Lastly, the slope parameter shows a clear signal development before the gelation point. Alexander and Dalgleish [194, 195] also observed this phenomenon using DWS. They suggested this was due to changes in the so-called structure factor, i.e. changes to the positional correlation of the casein micelles. This may be further emphasised by a wavelength-dependent "bump", that can be found near the gelation point at lower wavelengths seen in Figure B.5. The bump is most pronounced at the lower wavelengths, which might be explained by the size of the casein micelles (50nm to 600nm [21]). If the positional correlation of the micelles changes, it manifests itself in changes of the scattering properties for light at the lower wavelengths as casein mainly contribute as Rayleigh scatterers[87].

The analysis in this paper suggests that use of hyperspectral information can be beneficial for the use of diffuse reflectance images. Apart from the light-delivery system, the system described in Section B consists of basic components. Thus, if all necessary information (to a given problem) can be expressed by a combination of few wavelengths (or bands of wavelengths), the light source may be replaced by laser diodes. This will allow significant shorter acquisition times and more cost-efficient vision systems. This, of course, leads to the task of determining an optimal subset of wavelengths, which will be prioritised when larger data sets are acquired.

Conclusion

The use of hyperspectral diffuse reflectance images has provided some encouraging results for monitoring optical changes during milk acidification. The images data of the milk fermentation process show that it has a high sensitivity to both the structure formed during the fermentation process, but also the contents of both protein and fat level. A single feature from the diffuse reflectance images, the slope parameter, was found to be reproducible and enabled us to differentiate between different milk acidification processes. Some wavelength dependency was observed, in which protein content was only distinguishable at lower wavelengths. This wavelength dependency will be investigated further in the future, as it can be a key element in designing specialised multispectral vision systems. The experiment presented in this paper is limited in scope and acts as a screening of the generalisation abilities of the presented vision system. While protein, temperature, and fat were included in the experiment, these are only a few of the parameters that have been reported to influence the structure development. So it would be obvious to include other process parameters, as well as starter cultures, in addition to GDL in future experiments. Also, different quantification methods for the diffuse reflectance images will be investigated. Further, we believe the method is very applicable for diffusive media in general, and coupling the flexibility of the system set-up and data that can be recorded remotely, it may be suited for both at-line and in-line implementations.

Acknowledgements

We would like to thank The National Food Institute, Technical University of Denmark, for providing laboratory space and time during the course of our experiments. This work was (in part) financed by the Centre for Imaging Food Quality project, which is funded by the Danish Council for Strategic Research (contract no 09-067039) within the Programme Commission on Health, Food and welfare.

Appendix C

Non-invasive Assessment of Dairy Products Using Spatially Resolved Diffuse Reflectance Spectroscopy

Otto H. A. Abildgaard,[a] **Faisal Kamran,**[b] **Jacob Lercke Skytte,**[a] **Anders Bjorholm Dahl,**[a] **Frederik Donbæk Nielsen,**[c] **Carsten Lilholt Thomsen,**[c] **Peter Eskil Andersen,**[b] **Rasmus Larsen,**[a] **Jeppe Revall Frisvad**[a]

[a] Department of Applied Mathematics and Computer Science, Technical University of Denmark. 2800 Kgs. Lyngby, Denmark.

[b] Department of Photonics Engineering, Technical University of Denmark, 4000 Roskilde, Denmark.

[c] NKT Photonics A/S. Blokken 84. 3460 Birkerød, Denmark.

Submitted, Applied Spectroscopy, 2014.

Abstract

The quality of a dairy product is largely determined by its microstructure which also affects its optical properties. In this way, an assessment of the optical properties during production may be part of a feedback system for ensuring the quality of the production process. In this paper, we investigate the use of a camera based measurement technology which allows quantification of both the reduced scattering coefficient and absorption coefficient. We base our measurements on hyperspectral images of diffuse reflectance in the wavelength range of 470 **nm -** 1020 **nm. We measure the optical properties of commercial available milk and yoghurt products with three different levels of fat content which constitute a relevant range of products at a dairy plant. The measured reduced scattering properties of the samples are presented, and show a clear discrimination between levels of fat contents as well as fermentation. Our measurement technique and method of analysis is thus suitable for a rapid, non-contact and non-invasive inspection that can deduce physically interpretable properties. Because the measurements are performed without the need for sample extraction and dilution the inspection technology is suitable for inline inspection during production of milk gels, for example.**

Index Headings: **Oblique incidence; Diffuse reflectance; Absorption; Reduced scattering; Milk; Yoghurt; Fermentation; Non-invasive; Dairy.**

INTRODUCTION

Monitoring microstructures in food and beverages is a key to enhancing manufacturing process flexibility and efficiency, while also improving the quality and safety of the products.[24, 196] For yoghurt products, the microstructure, as defined by Bijnen et al.,[24] is a central component in consumers' perception of mouthfeel and thus their acceptance of the product.[25] The microstructure is formed from an aggregation of protein during the fermentation process.[23] It is known that reduced scattering properties,[4] scattering phase function[72] and the speckle characteristics[195, 83, 12] are affected by the microstructure. Inspection tools which quantify any of these effects may therefore reduce manufacturing costs and improve product quality.[197, 16]

The reduced scattering properties can be calculated from steady-state diffuse reflectance measurements as demonstrated by Farrell et al.[67] This enables

C.1	Low dynamic intensity range of the captured images.[82, 200]
C.2	Estimating the entry point.[82, 200]
C.3	Laser speckle.[82]
C.4	Estimating the diffusion centre.[82, 200]
C.5	Image size calibration.[200]
C.6	Image vignetting.[82]
C.7	Fitting the diffusion model.[200, 84]

Table C.1: Challenges in the use of camera-based OIR measurement reported in the literature.

measurement of the reduced scattering and absorption properties. However, this requires measurement of absolute intensities which is infeasible for in-line measurements.[167] To solve this problem, the technique has been modified by Wang and Jacques[103] into oblique incidence reflectometry (OIR). The requirement of absolute intensities is avoided by instead resolving both single and multiple scattering of the light. The drawback of using OIR is that the range of optical properties which can be inspected, is limited directly by the finite spatial resolution and the field of view of the detector system. This limits the ability to resolve optically dense or dilute media.

OIR has mainly been used for inspection of tissues, which span a relatively small range of optical properties.[84, 198, 106, 107] Tissue measurements are obtained using a fibre probe. Such probes are convenient for measuring the skin properties of live subjects, but also limited to the small range of optical properties of skin. To make the measurement of a milk fermentation process more feasible, we must cover a wider range of optical properties.[4] This is most feasible with camera-based measurements which has a much higher spatial resolution, typically a few thousand detectors along the diagonal of a modern charged coupled device (CCD) in comparison to 12 for fibre probes.[107] The original OIR technique[103] was camera-based and demonstrated the potential of the technique for measuring the reduced scattering μ_s'. Measurement of the absorption coefficient μ_a and the spectral dependencies was not introduced until after the shift to systems based on fibre probes.[84, 199] Some work has been done in camera-based OIR,[82, 200] where the challenges summarised in Table I were identified. We refer to these using the markers **C.1** to **C.7**.

Our objective in this paper is to demonstrate an inspection tool for quantifying the reduced scattering properties as well as the absorption properties of

dairy products suitable for in-line process inspection. To ensure industrial relevance, our inspection tool is applied to commercial available milk and yoghurt products with three different levels of fat content. In comparison to previous camera-based instruments for measuring OIR, ours provide spectrally resolved measurements. We describe how the challenges listed above occur in our measurement method and how they are solved. We handle the challenges in a sample independent manner, so that they are directly transferable to other applications. Finally, the reduced scattering properties that we measure show a clear distinction between fermented and commercial milk which is promising for future in-line inspection of the milk fermentation process.

Related work

The measurement principle of OIR is illustrated in Figure C.1. In Figure C.1 (a), the light beam is obliquely incident on the sample surface. Inside the sample the light is scattered in different directions, and some emerge from the surface as diffuse reflectance. The highest intensity is closest to the entry point, and the intensity declines further away. Most of the reflectance can be described as two components, and this is illustrated in Figure C.1 (b). Here, a profile of the reflectance values is illustrated; the line goes through the entry point in the direction of the incident beam. The first component (red) is most intense. This is a region where light has only experienced a few scattering events. The second component (blue) is the low-intensity contribution far from the entry point. This is the region where the reflectance may be described by a diffusion process. Because light enters the sample at an oblique angle the reflectance profile is elongated, more light is emitted from the forward direction. This is seen from the so-called centre line between the two sides of the reflectance profile, marked by a black line in Figure C.1 (b). The centre line is the geometrical centre of the reflectance profile for different intensity levels. At high intensities, the line is located at the entry point, and at low intensities the line is shifted forward towards a new location. The displacement of the two symmetry points for the reflectance profile is denoted Δx.

In OIR the relation between Δx and the light transport diffusion coefficient D is modelled as follows:[84]

$$D = \frac{\Delta \mathrm{x}}{3 \sin \theta_t} = \frac{n \Delta \mathrm{x}}{3 \sin \theta_i} \ , \tag{C.1}$$

where θ_t is the angle of refraction, and this depends on the angle of incidence θ_i and the relative index of refraction n as specified by the law of refraction (Snell's

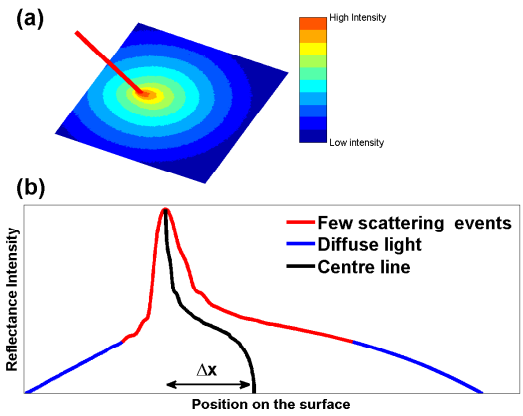

Figure C.1: Illustration of measurement principle in OIR. **(a)** Illustrates reflectance intensity from a sample's surface illuminated by a laser beam (red line). **(b)** Illustration of the reflectance from the sample along the entry direction and through the entry point. The profile is asymmetric and shifts by a distance Δx from top to bottom.

law). The relative index of refraction is $n = n_{\text{sample}}/n_{\text{ambient}}$. In the present work, the surrounding medium is air ($n_{\text{ambient}} = 1$) and the refractive index of milk is assumed to be 1.347.[201] D may also be related to the transport mean free path (mfp') as $3D \approx 1\text{mfp}'$, which gives the simple interpretation that light on average travels this distance into the sample before being scattered.[84]

It has been found, by comparison with Monte Carlo models,[84] that the diffusion coefficient can be expressed as

$$D \approx \frac{1}{3(\mu_{\text{s}}' + 0.35\,\mu_{\text{a}})} \quad . \tag{C.2}$$

Here μ_{s}' and μ_{a} are the reduced scattering coefficient and the absorption coefficients respectively, and this provides the first parametrisation of the optical properties. Equation C.2 can be considered a simplification of the expression for D reported by Ripoll et al.[85]

The light becomes diffuse as we move away from the point of entry. Therefore, the light is modelled using a displaced diffusion dipole as illustrated in Figure C.2. We use the expression by Farrellet al.[67] but now with the dipole (the positive and negative point sources) shifted horizontally by the distance Δx and shifted toward the sample surface according to the modified expression for D. The diffuse reflectance at a point $\mathbf{r} = (x, y, z = 0)$ on the surface then

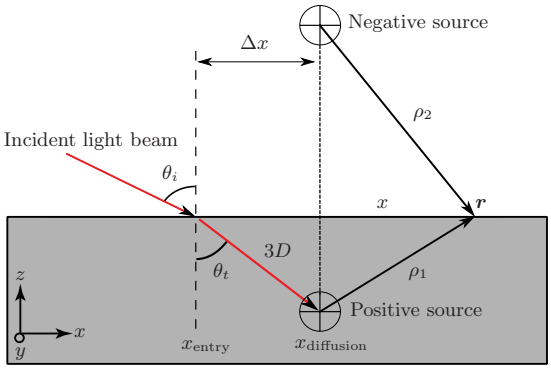

Figure C.2: Schematic presentation of OIR. The incoming light is refracted at the sample surface. The model describes the emergent intensity of light at the point **r** as a sum of contributions from a positive and a negative point source at distances ρ_1 and ρ_2. The two point sources are shifted horizontally by a distance Δx from the entry point of the light.

becomes[84]

$$\mathrm{R}(\mathbf{r}) = 3D\left(\mu_{\mathrm{eff}}\rho_1 + 1\right)\frac{e^{-\rho_1\mu_{\mathrm{eff}}}}{4\pi\rho_1^3} + \left(3D + 4AD\right)\left(\mu_{\mathrm{eff}}\rho_2 + 1\right)\frac{e^{-\rho_2\mu_{\mathrm{eff}}}}{4\pi\rho_2^3} \quad , \tag{C.3}$$

where ρ_1 and ρ_2 are the distances from the positive source and the negative source to the location **r** on the sample surface, μ_{eff} is the effective transport coefficient. These sources are positioned at vertical distances of $z_1 = 3D\cos\theta_{\mathrm{t}}$ and $z_2 = z_1 + 4AD$. The parameter A corrects the position of the negative source to account for internal reflection from the boundary back into the sample. It is approximated by[67]

$$\mathrm{A} = \frac{1+F}{1-F} \tag{C.4}$$

$$F = 0.0636\,n + 0.668 + 0.710\,n^{-1} - 1.440\,n^{-2} \quad . \tag{C.5}$$

To measure the optical properties, we first find the diffusion coefficient D by estimating the distance between the entry point and the diffusion centre (Equation C.1). We insert D in Eq. C.3 and find μ_{eff} by a nonlinear least squares fit of the equation to measured data. Combining this, the optical properties may

be deduced[84]:

$$\mu_{\mathrm{a}} = D{\mu_{\mathrm{eff}}}^2 \tag{C.6}$$

$$\mu'_{\mathrm{s}} = (3D)^{-1} - 0.35\mu_{\mathrm{a}} \ . \tag{C.7}$$

The technique thus imposes two criteria on the detection in relation to the optical properties of the sample

1. The reflectance profile must be resolved with sufficiently high resolution to expose the horizontal shift Δx.
2. The field of view must be sufficiently wide such that the light becomes diffuse enough to match the diffusion expression (C.3).

The range of optical properties that can be quantified robustly are therefore dependent on the detector system. One important aspect of the data collection is therefore that the reflectance profiles are completely resolved without saturated pixels. To accomplish this, together with a low noise measurement of the diffused light, the original implementation used two images of the reflectance. One images was taken with a neutral density filter to avoid saturation of the pixels close to the entry point. This had the undesirable side effect of shifting the position of the beam on the sample surface, which caused a systematic measurement error. Sun et al.[200] used only one image with no filter applied to the source. This limits the range of the optical properties which can be measured, as highly scattering samples may saturate the CCD and low scattering causes a low with noise.

With an image of the reflectance profile recorded, the calculation the of the light's entry point has been handled in different ways. In the original OIR technique,[103] the entry point is identified as the pixel of highest intensity. The pixel with highest intensity may however be a noisy estimate, especially in the presence of speckle which arises in narrow bandwidth systems. To improve the measurement precision, Sun et al.[200] used a weighted centre of mass of all pixels above the average intensity. Lindbergh et al.[82] used the most intense pixel, but after a convolution with a Gaussian filter. To reduce noise even further, the average value of five repetitive measurements was used.

Similarly, different approaches have been taken for calculation of the diffusion centre. It was originally estimated as the position at which the centre line for the reflectance profile converged,[103] see illustration in Figure C.1 (b). For each point in the reflectance profile, the corresponding position on the other side is calculated by linear interpolation on a logarithmic scale of two points with the

closets intensities above and below. The centre of the two positions, on opposite sides of the entry point, is added to the reflectance line. In this way, the centre line gives an estimation of the reflectance centre at different intensity levels of the profile. The diffusion centre is at the location where the centre line converges. However, camera based data requires a smoothing of this otherwise noisy profile. To improve the estimate of the diffusion centre, Sun et al.[200] used an iterative method. The location of the diffusion centre was moved as well as the region of the image for which the diffusion fit was evaluated. Both were sequentially updated until a minimum change in the deduced optical properties was reached. The diffusion centre was calculated as the symmetry point for the reflectance profiles of two intervals positioned symmetrically around the previous diffusion centre. This iterative approach involves an additional nested loop for deducing the optical properties, and is thus slow. Lindbergh et al.[82] computed a number of threshold-filtered images, where the thresholds were different percentages of the maximum intensity. The diffusion centre was calculated as the evenly weighted centre of mass for the pixel above the threshold. The intensity levels are only used if the light is sufficiently diffuse. This was quantified by the ratio of two second order moments for pixels above the threshold. Working on the entire images with iterative or multiple thresholds is time expensive, and scales with the camera resolution to the power of two.

METHOD

In this section we describe our suggested solutions to the challenges of camera-based OIR (see the list of challenges in Table I).

Camera intensity range (C.1). To fully resolve the profiles we use high dynamic range imaging.[202] This means that we take several images of different exposure times and combine them into a single high dynamic range (HDR) image. We use the procedure described by Nielsen et al.[15] To ensure a linear response of the pixel value from the light intensity, the most intense pixels are interpreted as saturated. The actual value in these pixels is instead measured at a shorter exposure time using the HDR imaging.

Entry point and laser speckle (C.2 and C.3). To obtain an accurate estimate, we deduce a temporary centre position as the median coordinate of pixels above 40% of the maximum image intensity. Subsequently, we extract the reflectance profile along the direction of incidence for analysis. The angle of the horizontal axis in the image plane with the direction of incidence is measured during the assembly of the instrument, and the line is marked with black in Figure C.3. Reflectance values along this line and the most intense pixel is the

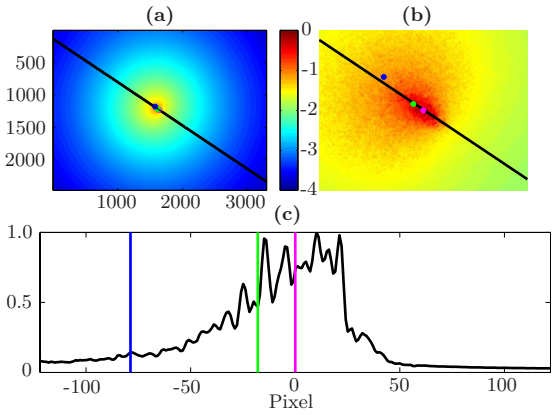

Figure C.3: The centre estimation and line extracted from a HDR image of Arla Lærkevang® 1.5% fat at 750 nm. Intensity is normalised and the colormap uses a logarithmic scale. **(a)** HDR image, the blue marker is the centre determined with the method by Sun et al.,[200] and the green shows the results of using the method by Lindbergh et al.[82] The black line is the extracted line we use for estimation of the entry point marked with magenta. **(b)** Zoom in on the beams entry point in **(a)**. **(c)** The extracted reflectance profile together with the projected entry points from **(b)**.

entry point. To reduce the noise of this estimate further, we use the average position over all wavelengths.

Estimating the diffusion centre (C.4). As in the work of Linet al.[84] we use a single profile in the image rather than processing the entire image. However, due to the noise properties of the CCD, we found that it is necessary to extend Lin's work so that we can handle non-monotonously decreasing data. To obtain a high accuracy estimate of the diffusion centre, we capture the overall development of the centre line using a regularized quadratic spline. Splines are advantageous as they do not enforce a specific shape of centre lines as opposed to a closed expression. The regularisation ensures robustness against noise in the image data. Finally, due to the quadratic nature, its derivatives are smooth, which is ideal for estimating the convergence of the profiles towards the location of the diffusion centre. We calculate the diffusion centre as the position of the spline at which its derivative as function of intensity is zero. If the derivative is zero in more than one position, the one of the highest image intensity is chosen.

Examples of calculated centre lines as a function of intensity depth are presented in Figure C.4 (a) each together with its associated spline marked with black. Considering that the centre lines consist of roughly 3.5 thousand points, the

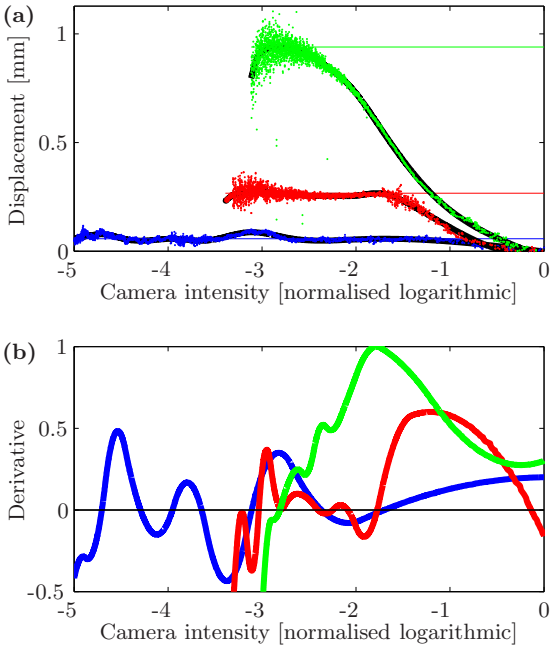

Figure C.4: *Calculation of diffusion centres for Arla A38® 3.5% at 500 nm (blue), Arla Lærkevang® 1.5% at 970 nm (red) and Arla Lærkevang® 0.5% at 970 nm (green).* ***(a)*** *The measured diffusion centre lines presented as dots and a spline presented as the black line through each. The position of the diffusion centre is marked as a vertical line.* ***(b)*** *The normalised derivative of the spline from the centre lines, these are used to calculate the convergence of the lines*

development as a function of intensity is fairly well defined. The derivative of the splines used for estimating the convergence is seen in Figure C.4 (b). The diffusion centre is evaluated as the point at which the derivative of the spline first crosses zero. At lower intensity values, the centre line may be more subject to experimental factors such as sample roughness and unintended tilt between surface normal and camera axis.

CCD pixel calibration and vignetting (C.5 and C.6). As OIR relies on intensity and shape it is essential to characterise both lens distortion and vignetting. To quantify lens distortion, we place a calibration grid on top of a homogeneous scattering sample. The light beam illuminates the sample similar to a measurement. The diffuse reflectance effectively provides a background illumination of the grid as seen in Figure C.5 (a). The image of the grid was enhanced by removing the smooth and diffuse part of the reflectance profile. This is done using a local noise normalization and dynamic range reduction of the image. From this the grid is annotated manually and the distance between points was fitted with a linear model. An example of the fit residual is presented in Figure C.5 (b). This procedure is carried out at 480 nm, 650 nm and 970 nm. From this, it was found that the image distortion is less than two pixels across the entire field of view, which causes changes significantly below the measurement precession. Therefore we do not need any additional correction for lens distortion. The chromatic aberration, causing a wavelength-dependant image magnification, is quantified as less than 1%.

This approach is advantageous as it provides hyper spectral information and enables quantification of not only average pixel size but also possible image distortion.

To quantify the vignetting of the imaging system, an image is captured of a white paper poster smoothly illuminated by sunlight. The poster was positioned at a distance of around 1.5 meters from the lens so that it was completely out of focus. This measurement shows a drop of transmission through the lens to about 80 % toward the peripheral parts of the image. Traces of the vignetting signal are presented in Figure C.5 (c). It is used to correct all images captured to measure optical properties.

Fitting the diffusion model (C.7). The last unanswered question for the evaluation of the fit is the area excluded around the entry point and diffusion centre. The reflected light in this area is interpreted as being insufficiently diffuse to be described by the diffusion equation. As noted by Lin et al.[84] an advantage of OIR is that the area may be quantified in units of the mfp', calculated from Δx (see Figure C.2). Lin et al.[84] reports that the measured optical properties for low scattering samples are especially sensitive to this excluded area, and they used an area with a radius of 1.5 mfp'. Their work was based on fibre probes,

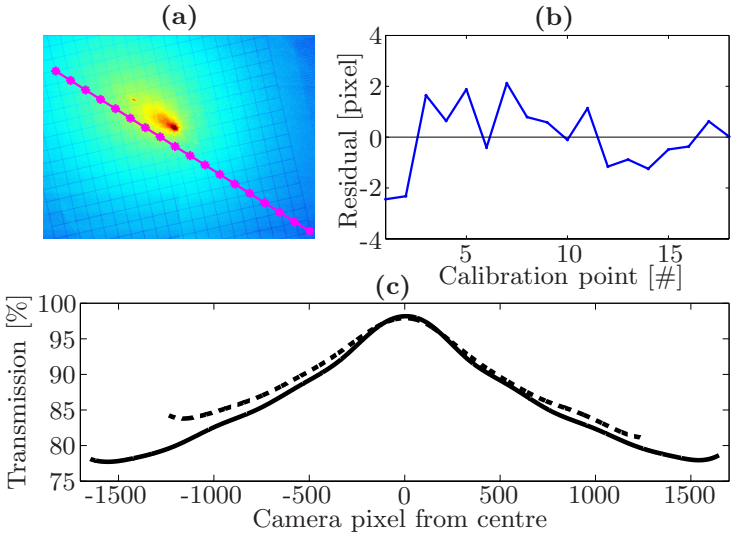

Figure C.5: **(a)** Image of the calibration grid on a logarithmic scale. **(b)** Residual in pixel distance from the model. **(c)** Vignetting along the two camera axes through the centre.

which limited the possibility of a more general analysis. We have the means to do this due to the high spatial resolution of our camera-based instrumentation. The analysis is important in two regards:

K.I	The previously suggested value may not be optimal
K.II	How does the width of the excluded region affect the deduced optical properties?

Table C.2: Objectives off investigating the data selection, previously refereed to as the foot print of the model.[101]

We exclude the part of the reflectance profile which is too close to either the entry point or diffusion centre to be modelled as a diffusion process. This requirement is quantified in the following criterion:

$$\max\left(|x - x_{\text{Entry}}|, |x - x_{\text{Diffusion}}|\right) < \left(\kappa \cdot \text{mfp'} + 1.5 \cdot \omega_{\text{beam}}\right) \tag{C.8}$$

Here, x is a point along the line extracted from the image data as seen in Figure C.3. The beam waist is denoted by ω_{beam}, and κ is the number of mfp', which

is excluded and quantifies the width of the reflectance profiles not described by the diffusion approximation.

Measurement of the effective attenuation. The second parameter used for determining the optical properties is the effective attenuation (μ_{eff}), which is deduced from the shape of the diffused light by Eq. C.3. The implementation by Lin et al.[203] report a minimization of the following expression, though without the beam convolution

$$\chi = \frac{1}{N}\sum_{n=1}^{N}\left(\frac{\int_{3\cdot w_{\text{beam}}}^{-3\cdot w_{\text{beam}}} \mathrm{R}(x_n - x)dx - y_n}{y_n}\right)^2. \tag{C.9}$$

Here N denotes the number of points along the line of incidence, marked in black in Figure C.3, which fulfil the criterion (C.8). R denotes the diffuse reflectance intensity calculated by Eq. C.3, and is evaluated in position x_n. The integral over x is a convolution due to the finite beam size with waist w_{beam}. Lastly y_n denotes intensity at a given pixel. Using this expression, each pixel only contributes with an error relative to the magnitude of the intensity. The two optimal values are determined by minimization using the Levenberg-Marquardt algorithm.

Interpretation of optical properties. For the reduced scattering coefficients, the wavelength dependence is fitted with an approximation derived from Lorenz-Mie theory and presented by Graaff et al.[78] We do this by fitting the model

$$\mu_s' = \mathrm{A}\lambda^{-\beta} \tag{C.10}$$

Here λ is the wavelength in nm, A and β are fitted coefficients. The fitted amplitude coefficient A indicates the concentration of the scatterers and their scattering cross-section, and the decay rate β reflects the size parameter of the scatterers. In this way, wavelength resolved measurements of the reduced scattering coefficients enable discrimination between an increase in scattering particles density (A) from their size (β).

For the wavelength dependence of the absorption coefficients, we refer to the spectrum of water reported by Hale and Querry[127] and for milk fat reported by Michalski et al.[65]

MATERIALS

Hyperspectral imaging system. Figure C.6 illustrates our instrument for OIR measurements. The instrument is based on acousto optical filtering of a

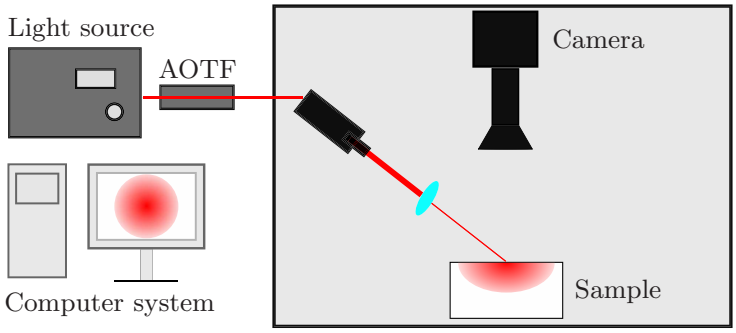

Figure C.6: Illustration of our diffuse reflectance instrument. The supercontinuum laser generates a broad spectral light profile and the specific wavelengths transmitted are selected using an acousto optical filter (AOTF). The beam, is focused onto the sample using an achromat. Images are captured of the light refletance profile by a CCD camera mounted above the sample.

broadband supercontinuum light source (SuperK Extreme EXW-12, NKT Photonics A/S, Birkerød, Denmark). The supercontinuum light source generates a beam throughout the spectral range from 450 nm to 2400 nm and for the present work, the acousto optical filter (SuperK SELECT, NKT Photonics A/S, Birkerød, Denmark) was equipped with a crystal that enables wavelength selection in the spectral range from 475 nm - 1020 nm. The optical bandwidth changes linearly from around 3.5 nm to roughly 16 nm. To accomplish this broad spectral range, the filtering amplitude is lowered in the wavelength range above 900 nm. The acousto optically filtered light is coupled into a fibre delivery system (VIS-nIR FDS, NKT Photonics A/S, Birkerød, Denmark). The combined instrument produces a collimated single mode beam with a tunable wavelength which is ideal for OIR.

The FDS provides a collimated beam, and the beam size is reduced further using a lens. To keep the lens and its mounting equipment outside the camera field of view, the beam is focus on the sample surface using a 38 mm focal length achromatic lens (Edmund Optics Inc., Barrington, New Jersey, USA). The waist of the beam is wavelength-dependent and grows from approximately 120 μm at 480 nm to 200 μm at 1000 nm; this includes the effect of the angular projection. The incidence angle of the beam is $\theta_i = 52°$, which was found as a compromise between increasing the diffusion displacement (Equation C.1) while keeping the projected beam small and having transmission into the sample. A more detailed considerations for incidence angle and polarizations direction is provided by Abildgaard.[204]

Images of the reflectance profiles are captured using a 12-bit CCD camera (AM-

800GE, JAI, Miyazaki, Japan) with a pixel resolution of 3296 × 2472. The imaging objective is a 50 mm focal length lens (LM50XC, Kowa Company Ltd., Nagoya, Japan), mounted to provide an image with a resolution of 3.2 μm per pixel of the sample surface. The shutter on the objective was set to F7 and magnification to 2. To calibrate the imaging system we used a calibration grid (R1L3S3p , Thorlabs, Gothenburg, Sweden).

Dairy samples. We evaluate the measurement technique based on a series of dairy products. This series contains commercially available milk and yoghurt with three different fat levels. The names of the products and key informations on their composition are presented in Table C.3. All products were purchased during December 2013 in Copenhagen, Denmark. The yoghurt products are fermented with the bacteria culture L. *acidophilus*. The milk and yoghurt products have very different structural properties, because the casein protein in yoghurts contain a gel network rather than being suspended individual micelles. The chemical composition in terms of fat and protein contents is largely unchanged, especially for the 1.5% products where the difference only is caused in the microstructure of the protein gel.

Products name	**Fat**		**Protein**	
	(g / 100g)	**Mode (μm)**	**(g / 100g)**	**Mode (μm)**
Arla Lærkevang® Sødmælk	3.5	0.99	3.5	0.046
Arla Lærkevang® Letmælk	1.5	0.99	3.5	0.046
Arla Lærkevang® Minimælk	0.5	0.99	3.5	0.052
Arla A38® naturel 3.5%	3.5		3.5	
Arla A38® naturel 1.5%	1.5		4	
Arla A38® naturel 0.5%	0.5		4.5	

Table C.3: Product information for the dairy products. The size parameters are typical values and measured by a Mastersizer 3000 (Malvern, United Kingdom) evaluated with a refractive index of 1.529**, the instrument does not support multiple constituents as is the case for milk. The corresponding values are not available on fermented milks as the necessary sample dilution destroys the gel network.[20]**

By inspecting the samples presented in Table C.3 the instrument sensitivity is evaluated as the discrimination between the deduced optical properties of similar milk and yoghurt products. The measurement precision of all dairy products was quantified as the standard deviation between five repetitive measurements. To further investigate the correlation between the deduced scattering and absorption coefficient, the optical properties of Arla Lærkevang® 1.5% fat was measured 19 times and deduced using a value of $\kappa = 2$. The measurement series was performed with only 11 spectral bands.

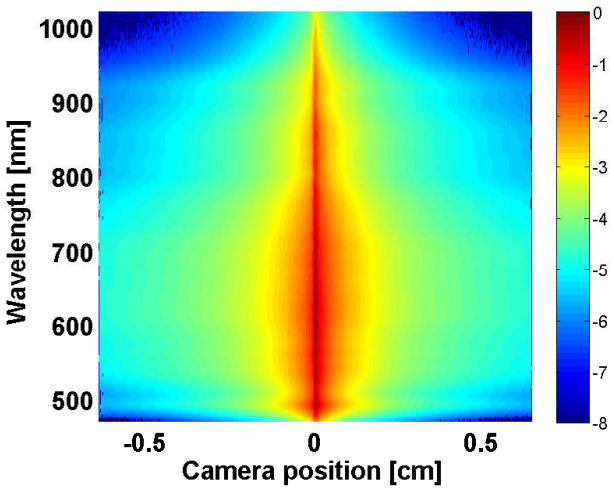

Figure C.7: Combined spectrograph image of the reflectance profiles for Arla A38® naturel 3.5%. Colormap shows the reflectance intensity on 10 base logarithmic scale.

RESULTS

Hyperspectral imaging system (C.1). An example HDR image is presented in Figure C.3 (a) which shows a smoothly changing profile across regions acquired with different exposure times. The HDR technique has previously been presented.[15] Lindbergh et al.[82] use a similar approach, but instead calibrate the response function to obtain HDR reflectance images. The data acquisition time is 1.9 seconds per wavelength for an HDR image. Since we deduce the optical properties from a line through the image, the entire hyperspectral information used to estimate the optical properties may be illustrated as a spectrograph image, see Figure C.7. The image data is normalised to the most intense pixel over the entire spectrum. Spectrograph images may be used to assess the dynamic of the instrument, where it is seen that the signal is preserved throughout the entire spectrum. It also shows that the dynamic range of intensities for this dairy product spans 80 dB. The broad dynamic range can not be covered by any CCD chip and the measurements are only possible due to the HDR procedure.

Estimating the entry point (C.2 and C.3). For the present instrument and samples the speckle structure seen in Figure C.3 surrounds the entry point. The entry points estimated with the methods proposed Lindberg et al.[84] and Sun et al.[200] are presented in Figure C.3 together with the result of our method.

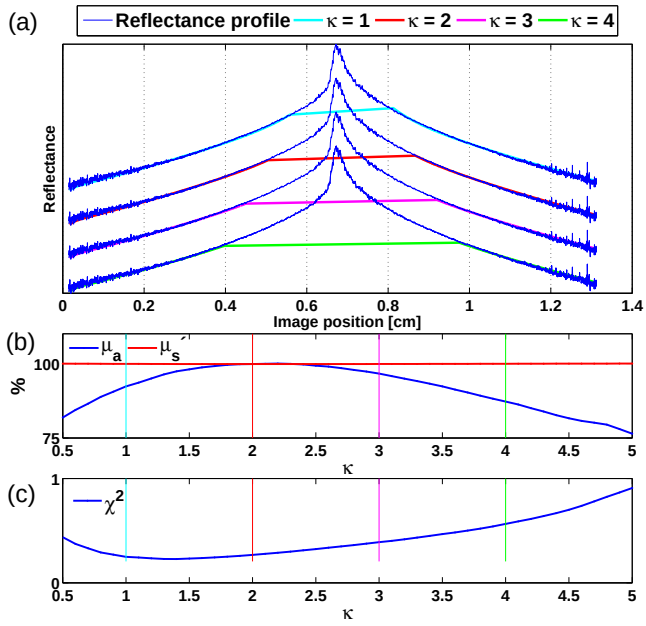

Figure C.8: Example of how the foot print affects the fit for Arla A38® naturel 0.5% at 970 nm. **(a)** Examples of the fitted profiles in colour. **(b)** Deduced absorption coefficient (red) and reduced scattering (blue). **(c)** Fit residuals.

It is evident that previous proposed methods overshoot along the incidence direction and is a general effect on our measurements of dairy products. This is because the previously proposed methods rely on estimating the centres of symmetric distributions. This causes an underestimation of Δx and leads to an overestimation of the scattering coefficient and underestimation of the absorption coefficient.

Fitting the diffusion model (C.7). It has previously been reported that the deduced optical properties depend on the range of the fit interval.[84] To investigate the significance of this effect on the dairy samples, we quantify the deduced optical properties and the fit residual when altering the width of the excluded data during the fit to Eq. C.9. The value of κ is varied in the range $0.5 - 5$ and the effect on both the deduced optical properties and fit residual is investigated. An example is presented in Figure C.8.

Measurement reproducibility. A scatter plot of the deduced optical properties is presented in Figure C.9 for a single wavelength.

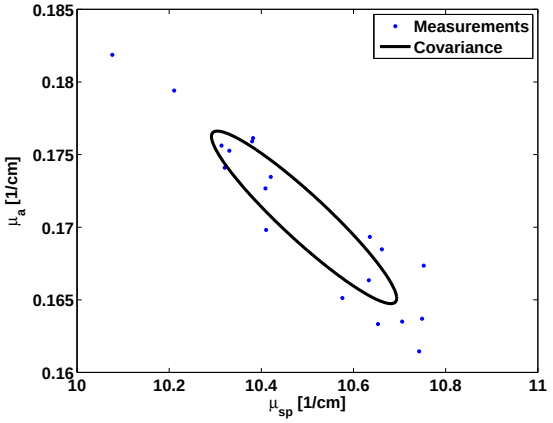

Figure C.9: Scatterplot of the estimated optical properties of 19 repetitive measurements of milk 1.5 % fat at 930 nm, the ellipsoid shows the circle span by the eigenvalue decomposition of the data's covariance.

Spectra for dairy samples. To investigate the performance of the combined instrument and analysis technique in characterising the optical properties of dairy products, we measure the optical properties of the samples in Table C.3. The resulting curve fits for some of the most diverse reflectance profiles of the dairy products are presented in Figure C.10, together with their respective fits. This gives an impression of how well the data is modelled with the proposed measurement technique. Measurement of all products was repeated 5 times, and the mean and standard deviation of the deduced optical properties are summarised in Figure C.11. We continue to use $\kappa = 2$.

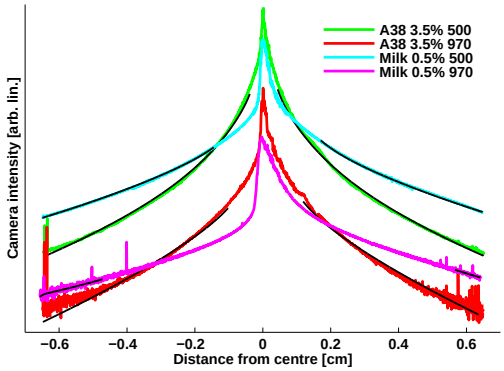

Figure C.10: Examples of reflectance profiles and their fitted effective attenuation (black lines).

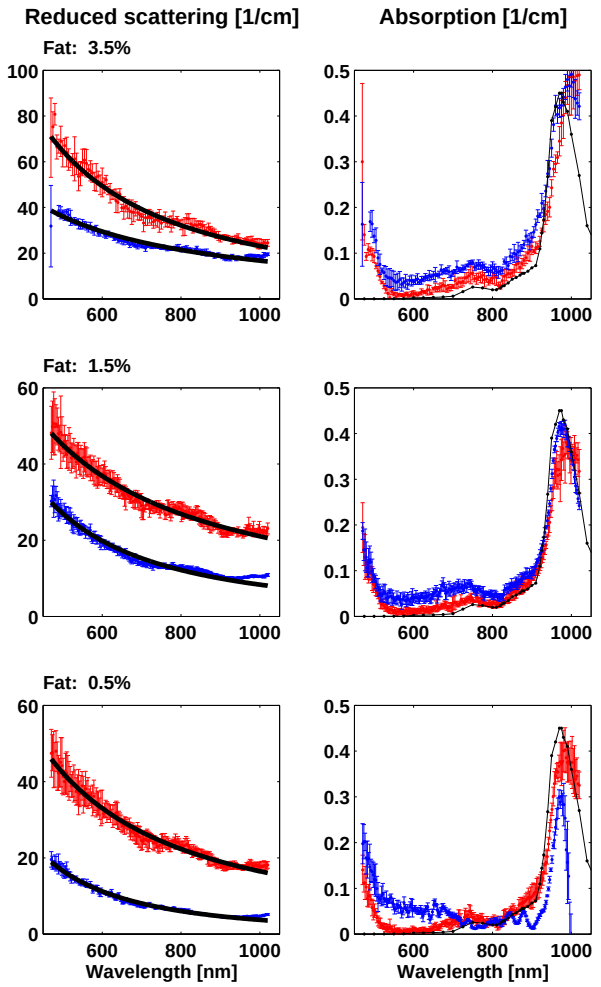

Figure C.11: Measured optical properties for dairy products with 5 repetitive measurements showing the standard deviation at each wavelength. Red data is for fermented milk products, blue is for milk. For the reduced scattering coefficients, the black lines are fit to Eq. C.10. For the absorption measurements, the black line is the absorption of water.[127]

DISCUSSION

Hyperspectral imaging system (C.1). Our measurement procedure satisfies two important properties for an in-line inspection system. The measurement can be obtained through a cover slip, thus compatible with the hygiene requirements in dairy production. Another important aspect of the measurement technique is that the optical properties are measured in reflection mode, as opposed to transmission, which allows inspection of large volumes such as milk fermentation tanks. Furthermore, to the best of our knowledge, our instrument has the broadest spectral and spatial range presented so far in diffuse reflectance spectroscopy.[54, 82, 84]

With respect to data acquisition, the data acquisition at present time is 1.9 seconds per wavelengths, but may be reduced as the same shutter times are used for all wavelength and samples. From the spectrograph images as presented in Figure C.7 it is evident that some of the long exposure shutter time for the wavelength range $550 - 900$ nm could be skipped as the signal for these is stronger. The short shutter time may be omitted for spectra in the blue and NIR range. Similarly the long shutter times could be omitted in the $500-800$ nm range. The measurement technique may also be carried out using an imaging spectrograph as conducted by Lin et al.[54] and Garcia-Uribe et al.[198] In this way, the wavelength filtering is performed on the source side, avoiding the repetitive image acquisition with different wavelengths. Such a system can provide the full spectrogram image such as presented in Figure C.7 in a single HDR image. Finally, the image may be used to identify absorption bands from the raw data directly. Absorption gives contraction of the reflectance profile over a short wavelength range, in Figure C.7 an absorption band is present from around 950 nm and upwards. In comparison, the scattering causes a slow monotonous decay.

Estimating the entry point (C.2 and C.3). The speckle pattern shifts the location of the most intense pixel in two directions of the images, centred on the entry point. For the present measurement, the location of the most intense pixel shifts around by approximately 15 pixels. Previous methods for reducing the effects of the speckle rely on a symmetric shape of the reflectance and overshoot in the present data, see Figure C.3 (c). This may in part be visible in our measurements because we investigate images of reflectance with such divers optical properties or because the milk samples are highly forward scattering. In any case, our method only searches for the most intense pixel along the line of incidence which reduces noise. Still, using the most intense point along this line is an estimation with high variance which is further reduced by averaging across wavelength. In this way, we obtain an unbiased estimate of the entry point in comparison to previous work.

Estimating the diffusion centre (C.4). By determining the diffusion centre from a single line of reflectance values instead of the entire image we gain two advantages. Firstly, it increases the range of optical properties which may be estimated. For samples with little scattering and absorption the asymmetric area of the reflectance is larger and 2D methods rely on convergence of the asymmetry within the image. The methods are thus limited by the field of view along the shortest side of the image. This limit was acknowledged by Lindbergh et al.[82] who excluded samples due to lack of dynamic range. The 1D method further extends the range, because the measurements may be conducted with the line of incidence along the diagonal of the image, which increases the number of pixels along the line. Secondly, the computation speed is significantly faster and scales better with the camera resolution.

Fit and foot print of the diffusion model (C.5 - C.6). The fit residual for a camera calibration presented in Figure C.5 (b) clearly shows that the image distortion is not causing systematic dependence of the optical properties on the fit region presented in Figure C.8. Nevertheless, a high precision method which we demonstrate for spectral characterization of the lens distortion is a necessary validation. Concerning the image vignetting, this effect is normalised after the images are captured. Nevertheless, the effect may be reduced by replacing the existing lens with a more expensive telecentric lens.

Fitting the diffusion model (C.7). With respect to fitting the diffusion model from Eq. C.3 to the reflectance measurements, a disagreement has been reported by Chitchian and Fried.[205] This disagreement is not experienced on the measurements of the dairy samples, which exhibit a good visual agreement for different values of κ as shown in Figure C.8 and for the most diverse dairy products in Figure C.10.

Concerning the fit range of the diffusion model, it has previously been reported that the optical properties depend on this.[84, 200] As stated in **K.I** Table C.2, it is of interest to investigate whether a proper value for κ may be deduced. The visual agreement between fit and selected data from our results does not, however give clear indication of which value to choose; this is seen from the example in Figure C.8. All values of κ seem to give a decent description of the data. Thus, we continue to investigate the dependence of κ as described in **K.II** Table C.2. The results show that the dependence on κ is not trivial. As seen from the example presented in Figure C.8 the deduced absorption and fit residual do not converge at large values of κ. Neither does a single value of κ exist at which the fit residual is minimised and absorption maximized, this might otherwise be a criterion for finding an optimal value of κ.

As seen from Figure C.8 (b), the deduced absorption coefficient depends on the region where the data is fitted. The deduced absorption changes smoothly, and

reaches maximum at $\kappa = 2.2$. The reduced scattering on the other hand is largely unchanged. Concerning the fit residual, the corresponding dependences on κ is presented in Figure C.8 (C). It is noteworthy that the minimum fit error occurs at $\kappa = 1.4$, which is different from where the absorption peaks. These effects have been investigated across wavelength and sample. In general it was found that the reduced scattering coefficient is independent of κ, as seen on Figure C.8. The deduced absorption coefficient does, however, depend on κ, but does not in general have a maximum.

One reason for these dependencies on the fit region is the analytical expression (Equation C.3) which is known to break down in two regimes: highly anisotropic scattering phase function[99, 206] and high absorption.[87] Recently, corrections have been proposed to include phase function dependencies by Zemp.[101] In addition, an improved analytical solution to the radiative transfer equation for a semi-infinite medium has recently been proposed by Liemert et al.[88] These two approaches may individually reduce the coupling between the optical properties. A combination of these approaches may provide a more general and adequate numerical model that describes the optical properties.

A final remark on the dependence on fit range (κ) is that the specific value mainly influences the absorption coefficient which is important when the measurements are used for chemometric evaluation of the sample constituent. For the purpose of quantifying the reduced scattering coefficient, and hence the particle size distribution which are change during milk fermentation, the specific value of κ is not essential.

Measurement reproducibility. The results are presented in Figure C.9. Here it is seen that the noise contribution in scattering and absorption is highly correlated. The correlation coefficient is -0.94, which indicates high correlation. We believe that the systematic variations are largely induced through the estimation of the diffusion displacement. This error then propagates on through the curve fitting procedure, where the estimated effective attenuation compensates for the error in mean free path estimation. This strong correlation between the optical properties is commonly recognised.[86, 87] The results suggests, that the method can become a high precision method for estimation of the optical properties if the source of error in mean free path estimation can be reduced further.

Spectra for dairy products. Firstly, the fit results presented in Figure C.10 demonstrate the fit performance for the investigated dairy products. These results show a fairly good characterisation of the reflectance profiles across both the diverse milk and yoghurt samples and the wavelength range from blue to NIR. However, it is evident that the amount of data to fit the diffusion model with milk 0.5 % is somewhat limited.

The measured reduced scattering coefficient, shown in Figure C.11, increases as a function of fat contents. This is as expected since fat particles are the main cause for scattering. Similar results have been reported for other measurement techniques.[54, 4]

Concerning the discrimination of the structural difference between milk and fermented milk products, the evaluated optical properties of the dairy samples are compared directly in Figure C.11. From this, it is seen that the reduced scattering properties provide a clear distinction between the two products. Furthermore, it is seen that the values are in agreement with the approximate development derived from Lorenz-Mie theory and previously reported by Nielsen et al.[4] The measurement precision of the fermented products is in general lower than the milk products, this is due to their deflation and slightly curved surface.

The measured absorption spectra, three peaks are present throughout all the measurements. The first peak is around 520 nm and has previously been reported for milk fat,[65] the presence of a weak peak at 750 nm and a stronger peak at 970 nm have previously been observed for water.[127] In general, the results show a reduction of the measured absorption for the fermented products. This effect may be a result of the scattering phase function of the samples. This induces a cross-talk between the absorption and scattering properties. We believe the improved models for radiative transfer by Liemert et al.[88] or phasefunction corrected diffusion by Zemp[101] may be a solution. Lastly, with respect to the range of optical properties which may be covered, it is seen that the limited field of view for the present system reduces the absorption estimate for the Arla Lærkevang® Minimælk 0.5 % fat.

CONCLUSION

The development of new optical characterization techniques is of great interest for the dairy industry. In the present work, a camera based instrument for quantifying the optical properties of milk and fermented milk has been demonstrated. Measurements are performed by only quantifying light reflection from the sample surface, this makes it feasible for in-line measurements, despite large sample volume as in a milk fermentation tank. In addition, the technique enables a non-contact and non-invasive measurement, which is important for avoiding contamination and accomplishing an automated measurement system.

The instrument covers the broad spectral range from 470 nm - 1020 nm and thus covers the absorption bands of both milk fat and water together with the reduced scattering properties of the samples. The optical properties of com-

mercially available milk and fermented milk has been reported and show strong capabilities of discriminating between initial and final state of fermented milk products by their reduced scattering coefficient. Simultaneously, the absorption coefficient clearly marks the presence of both fat and water but also a correlation to the scattering levels.

As future work, the in-line measurement of these optical properties during milk fermentation will be a high priority. In addition, we would like to continue the development of measurement precision using more advanced models for the reflectance profile. These can improve the instrument's suitability for material inspection in general.

Acknowledgements

This work was financed by the Centre for Imaging Food Quality project which is funded by the Danish Council for Strategic Research (contract no 09-067039) within the Program Commission on Health, Food and Welfare.

Appendix D

Spectral characterizations of dairy products using photon time-of-flight spectroscopy.

Otto Højager Attermann Nielsen[a], **Arman A. Subash,**[b] **Frederik D. Nielsen,**[c] **Jacob L. Skytte,**[a] **Stefan Andersson-Engels**[b] **and, Dmitry Khoptyar**[b]

[a] Department of Applied Mathematics and Computer Science, Technical University of Denmark. 2800 Kgs. Lyngby, Denmark.

[b] Department of Physics, Lund University, PO Box 118, SE-221 00 Lund, Sweden

[c] NKT Photonics A/S. Blokken 84. 3460 Birkerød, Denmark.

Published, Journal of Near Infrared Spectroscopy, 2013.

Abstract

In this paper, we present, for the first time, the absorption and reduced scattering spectra of commercially available milk and yoghurt products, obtained using photon-time-of-flight spectroscopy. The ability of this technique to separate the contributions from absorption and scattering in the sample provides important information on the chemical composition and micro-structural properties, which are not available with the traditional techniques used in dairy production. The instrument operates in the spectral range from 500 nm to 1030 nm. The reduced scattering coefficient varies from 5 cm^{-1} for milk with 0.1% fat in the near infrared range, to 60 cm^{-1} for yoghurt with 3.0% fat in the green wavelength regime. The absorption is within the range of 0.05–0.5 cm^{-1}, with only small variation in the absolute value between products. Our results show that the reduced scattering clearly distinguishes milk and yoghurt with the same fat content and can offer a reliable way of monitoring structural formation during milk fermentation.

Introduction

A great challenge in dairy production is to ensure products of consistently high quality, despite natural variations in the raw milk. It is thus of interest to monitor parameters in the production process that can be used to control production. This has led to the development of a broad range of techniques for online monitoring that probe the chemical and/or structural properties of a sample. In the milk fermentation process, it is necessary to know when the gelation point and curd–cut time occur[26] for production of yoghurt or cheese and this present work is focused on milk and yoghurt products. For a comprehensive review of inspection techniques, the reader is referred to Lucey.[180] Of the techniques available, optical inspection has the advantage of being non-destructive. The optical methods used in the dairy industry are usually based on diffusing wave spectroscopy and dynamic light scattering and provide information on the average particle size of a sample.[195] Alternatively, the total amount of reflected light is measured, either at a single wavelength as by CoAguLite (Tetra Pak, Switzerland) in Fagan et al.[17] or over a broader spectral range as reviewed by Mateo et al.[30] The instruments do not measure the curd–cut time or when the gelation point occurs directly but, for a given product, the signal may be correlated to the occurrence of these events. MilkoScan (Foss, Denmark) is the de facto standard for off-line characterisation of milk constituents and employs

Fouriertransformed infrared spectroscopy to measure the absorption of a small sample. For particle sizing, the MasterSizer 3000 (Malvern, United Kingdom) may be used. This instrument is based on single particle diffraction and thus requires dilution of the samples, which changes the particle size distribution of dairy samples.

The required temporal resolution for industrial inspection is application dependent with no specific value given in the literature. For yoghurt production, the process evolves continuously over 5 hours.[180] For estimation of cheese curd time an accuracy of less than 100 s has been accomplished, and an accuracy of less than 60 s is desired as presented by Callaghan et al.[26]

We propose the use of diffuse optical spectroscopy (DOS) measured utilising photon time-of-flight (PToF) spectroscopy to characterise dairy products by measuring their absorption and reduced scattering coefficients. The reduced scattering coefficient characterises the combination of scattering and the scattering anisotropy (here defined as the average cosine of the scattering angle of single scattering events). An introduction to DOS is given in Martelli et al.[87] In general, biological samples exhibit more scattering than absorption in the visible (vis)-NIR region, which is often considered a problem.[207] This may be overcome by analysing small amounts of the sample, which may not be representative, or by using a long wavelength instrument that may be more expensive and less sensitive. The method proposed here decouples scattering and absorption in the measurement, hence giving more information from the sample. This allows the use of cheaper silicon-based detectors such as those used by Kalinin et al.[207] Being able to measure both absorption and scattering properties possesses several advantages. First, it may be possible to measure more subtle changes in absorption, as presented by Abrahamsson et al.[208] Second, the information obtained can be useful when designing a simpler instrument.[207, 209] The method can be used to obtain the particle size distribution from the reduced scattering spectra, as used by Hajihashemi and Jiang.[76] Finally, the technique is suitable for online monitoring, as it does not require sample extraction and dilution.

The double integrating spheres technique, as described in Pickering et al.[210], is the original technique for DOS and takes measurements of both integrated transmission and reflectance to quantify scattering and absorption. This technique has also been implemented for broadband characterisation by Saeys et al.[211] The double integrating spheres technique is robust, as it does not make assumptions on the light propagation in the sample; however, it is not easily adapted for online applications, as it requires very thin samples (< 1 mm). To overcome this, more advanced techniques have been developed to achieve measurement procedures suitable for online sensing. A spatially resolved measurement of a reflectance profile is the most frequently used technique for DOS today.[67, 212]

The technique requires an absolute intensity measurement, which may not be feasible for industrial applications. A variation in the technique that solves this is oblique incidence reflectrometry as proposed by Lin et al.[84], which requires an estimate of spatial displacements in the reflectance profile. For highly scattering media, such as fermented milk/cheese, this distance becomes very short and may be hard to determine. Another alternative technique, suitable for heterogeneous samples, is frequency domain imaging.[213, 214] This enables spatial information to be obtained on the optical properties together with high penetration depth; however, this technique

has a lower spatial resolution. The final technique for DOS is PToF spectroscopy, which are temporal measurements in the time domain.[136, 215] An in-depth discussion of the two latter techniques is given in Sullivan et al.[214] The optical properties of a sample investigated using PToF spectroscopy are deduced by modelling the temporal broadening of a light pulse when passing through the sample. This temporal broadening is largely due to scattering, which delays the arrival of photons at the detector, due to a prolonged path length within the sample. The scattering will influence the delay of the photons and thus be prominent primarily in the rise-time of the PToF distribution. An important feature of PToF spectroscopy is that the temporal broadening and delay due to scattering can be measured very accurately. The absorption property of a sample affects the tail end of the PToF distribution most, which is a consequence of these photons having travelled the longest distance in the sample. The optical properties of the sample can thus be deduced from the shape of the PToF distribution and an absolute intensity measurement is not required for semi-infinite homogeneous media. The spectral range in which PToF instruments can be operated is limited by the sensitivity and speed of the detectors available; the longest wavelength is presently 1700 nm, demonstrated by Bargigia et al.[146] The detectors used are photon multiplier tubes as in Svensson et al.,[139] single photon avalanche diodes (SPAD) used by Patterson et al.[140] or streak cameras used by Abrahamsson et al.[141].

Materials and methods

PToF spectrometer

A schematic of the PToF spectrometer is presented in Figure D.1**(b)**. A short light pulse is emitted by an optical fibre acting as a source, which is sent into the sample. The scattered light is collected by another optical fibre that guides the light to a detector. Measurements can be carried out in direct transmission

mode, where the optical fibres are aligned facing each other, or in reflection mode, where the fibres are parallel to each other, facing in the same direction. In the measurements described here, the fibres were aligned parallel, 4.31 mm apart, as shown in Figure D.1**(b)**, and submerged 35 mm into the sample, as shown in Figure D.1**(c)**. The short fibre separation was found to be a compromise between the ability to measure the full PToF distribution for highly scattering measurements, while still resolving the average temporal delay of the photons for the low scattering measurements.

A broadband supercontinuum laser, SuperK Extreme EXW-12 (NKT Photonics A/S, Birkerød, Denmark), was used to generate short light pulses. This was combined with a SuperK SELECT and a vis-NIR Fibre Delivery System (both from NKT Photonics A/S, Denmark). The SuperK SELECT performs spectral filtering using an acoustooptical tuneable filter a spectrally narrow fractions of the

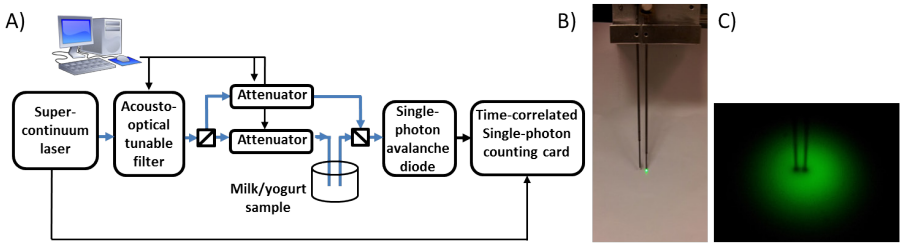

Figure D.1: ***(a)*** *Schematic of the photon time-of-flight set-up. The blue arrows illustrate optical paths and the black arrows communication.* ***(b)*** *Image of the optical fibres with green light emitted from the source fibre.* ***(c)*** *Image showing the fibres submerged in a milk sample. (A colour version of this figure can be found in the on-line version of this paper.)*

supercontinuum light can be freely selected in the range from 500 nm to 1030 nm. The optical bandwidth changes linearly from ~ 3.5 nm at 500 nm to 16 nm at 1030 nm. The light was coupled to a custom-made gradient index multimode fibre (400 μm/640 μm core/cladding diameter, Leoni Fibre Optics, Neuhaus-Schierschnitz, Germany). The use of gradient index multimode fibres increases the sensitivity of the instruments by reducing the intermodal dispersion of the light pulses. A time reference is generated by sampling a small fraction of the input beam, by using a set of beamsplitters. This increases measurement precision, as is shown in Khoptyar et al.[136] The PToF spectrometer is based on the time-correlated single photon counting (TCSPC) technique. TCSPC requires a low light intensity, so that only a single photon is detected for each pulse from the light source. The light intensity was attenuated using fibre-

coupled attenuators (DD-100, OZ Optics Ltd, Ottawa, Canada) and detected with a single photon avalanche diode detector (PD-050-CTC, Micro Photon Devices, Milan, Italy). To construct the PToF distribution, a time-correlated single-photon-counting card (SPC-130, Becker & Hickl, Berlin, Germany) was used to measure the time interval between the light source trigger pulse and the pulse from the detector.

Data evaluation

The optical properties of the samples were deduced from the PToF distribution with MATLAB, using a Levenberg–Marquardt fitting algorithm on a precalculated White Monte-Carlo simulation database previously demonstrated in Alerstram et al.[95, 94] The light pulses exhibit additional broadening due to the finite response time of the detector and residual fibre dispersion; this is referred to as the instrument response function (IRF).[145] The IRF is wavelength dependent and the combined effect of the IRF is measured by replacing the sample with a piece of double-sided, black-printed office paper.[139] The finite IRF was taken into account during data evaluation by convolving it with the Monte Carlo model. The combined full width half maximum of the IRF is $\sim$ 30ps. The Monte-Carlo model assumed a scattering anisotropy of 0.7,

where values from 0.93 for low fat milk with blue light to 0.68 for whole milk are presented in the literature.[216] A refractive index of 1.347 is also assumed for data evaluation.[217] To quantify the accuracy of the deduced optical properties, repetitive measurements were conducted using Intralipid (Fresenius Kabi, Uppsala, Sweden) as the scattering component in a water mixture. Intralipid is a commercially available fat emulsion often used in the literature for validation of DOS instruments.[218] The accuracy of our measurements was better than 10%. The main error source was attributed to positioning of the fibre, which was carried out using a micrometre stage.

Dairy products

Dairy products were chosen to investigate the capabilities of the instrument in two different scenarios. Three types of milk and three types of yoghurt were investigated. They were all fresh standard products from Arla Foods in Denmark, bought in September 2012. The milk was homogenised and pasteurised. The most essential parameters of the products are presented in Table D.1. The first of the two studied scenarios was an explorative study to assess which products can be evaluated robustly so products with different fat content were used for

both milk and yoghurt. Fat is the main cause for scattering in dairy products and should show significant changes between samples.

Product name	**Fat content** (g 100 g^{-1})	**Protein content** (g 100 g^{-1})	**Fermentation culture**
Arla Lærkevang Minimælk	0.5	3.5	
Arla Lærkevang Letmælk	1.5	3.5	
Arla Lærkevang Sødmælk	3.5	3.5	
Arla A38 naturel 0.5%	0.5	4.5	L. *Acidophilus*
Arla A38 naturel 1.5%	1.5	4.0	L. *Acidophilus*
Arla KO mild yoghurt Naturell	3.0	3.3	L. *Acidophilus* and S. *Thermophilus*

Table D.1: Product information on dairy products.

A second scenario was carried out to investigate how well the structural formation could be quantified. The yoghurts were all stirred yoghurts and chosen to match the fat content of the milk samples. Thus, the main difference between milk and yoghurt variants was in the structure formed by the fermentation, not the chemical composition of the products. In the production of yoghurt, lactic acid bacteria are commonly used to ferment lactose into lactic acid, which gradually lowers the pH of the milk. This eventually leads to destabilisation of the suspended protein structures and aggregation into a protein network or gel. The structural properties of the gel can be affected by process parameters such as the type of bacteria cultures and the fermentation temperature. Water and fat become embedded within the gel. A more detailed description on yoghurt production is given by Lee and Lucy.[20]

Results and discussion

Evaluation of the optical properties

The sample data were recorded for a duration of 25 s and attenuation was adjusted to provide a count rate of the SPAD of 50 kHz. The total data acquisition time was roughly 1.6 min for each wavelength and includes changing the wavelength, readjusting attenuation and collecting the PToF distribution. Examples of the recorded PToF distributions are presented in Figure 2. Each profile consists of two peaks. The first is the time reference pulse as described in the section on PToF spectrometers, which is independent of the sample, and the second is the pulse broadened by the sample. The part of the profile above

20 % of the maximum count was fitted with the Monte-Carlo model to ensure a robust fit.

From Figure D.2, it can be seen how the PToF distribution becomes broader as the fat content of the milk is increased to 3.5 % and even further for the yoghurt with 3.0 %fat. The background level also increased with the increasing fat content, eventually limiting the part of the profile that could be evaluated. The background level is partly due to photons that persist as diffuse light until the next pulse from the light source arrives at the sample. One way to overcome this is to reduce the repetition rate of the light source from where it is currently set at 80 MHz; however, this technique is presently not implemented in the light source. Signals stretching beyond 12.5 ns are thus a repetitive copy of the measured profiles for the current experimental set-up.

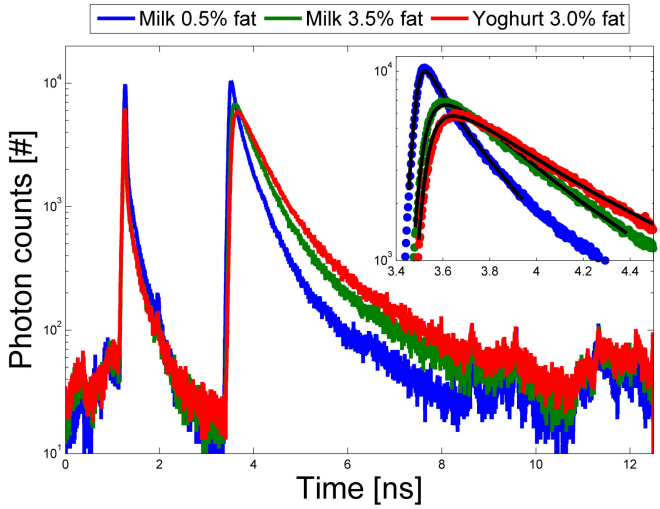

Figure D.2: Examples of measured PToF distributions for milk and yoghurt, the black lines are fitted Monte-Carlo models.

The range of optical properties which may be adequately evaluated can be tuned by changing the separation between fibres. Decreasing the separation will allow the measurement of larger scattering coefficients. Reduced scattering coefficients up to ~ 450 cm^{-1} are routinely measured with this method, using transmission measurements.[141]

The combined spectral response from a sample can be visualised as in Figure D.1, where two changes are seen as a function of wavelength. First, it is evident that there is an overall shift in the position of both the time reference signal and the

pulse from the sample. This is an intrinsic property of the light source. Second, the sample pulse exhibits a continuous change, becoming thinner as wavelength increases. From these images, the effect of wavelength specific absorption can be seen directly as perturbation of the otherwise continuously changing profiles. The effect is best seen in the wavelength range from 940 nm to 980 nm, where the distribution is narrower due to the increased absorption.

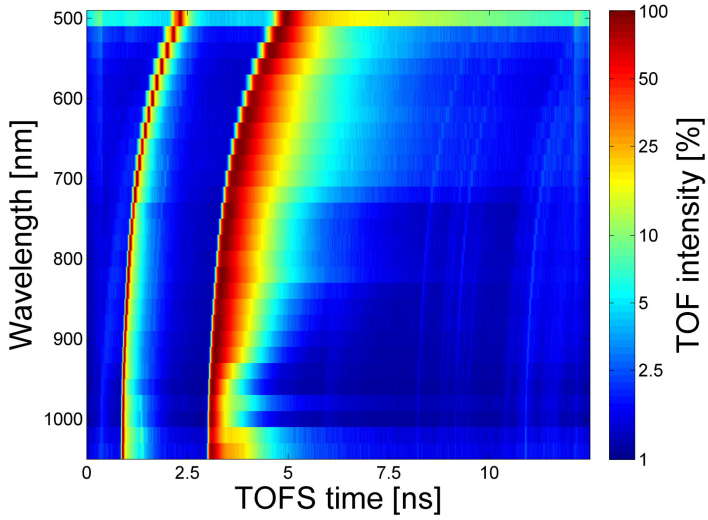

Figure D.3: Combined wavelength scan of PToF distributions of Arla Lærkevang Sødmælk (3.5 %fat).

Analysis of fat content

The optical properties of milk and yoghurt with different fat content are presented in Figure D.4 and Figure D.5, respectively. The errors bars are deduced from the accuracy obtained by repetitive measurements of Intralipid. The samples were characterised with a spectral resolution of 20 nm between measurements. Scattering dominates over absorption for both milk and yoghurt in this spectral range. The scattering amplitude increases with the fat content for both milk and yoghurt and each product is clearly separated. The reduced scattering coefficient was further analysed by fitting the model $\mu_s' = A\left(\frac{\lambda}{\lambda_0}\right)^b$, which is an approximation of the Mie theory presented in Graaff et al.[78]. Here, μ_s' is the reduced scattering coefficient, λ is the wavelength in nm, λ_0 is set to a wavelength of 500 nm and A and β are fitted coefficients. The obtained values

of the fitted coefficients are presented in Table D.2.
For both milk and yoghurt samples, the reduced scattering behaves as expected from Mie-theory, with a minor deviation at the edges of the spectrum. We consider this a validation of the measurements.
The fitted amplitude coefficient (A), indicating the concentration of the scatters, increased as a function of fat content and the decay rate (β) reflecting the size parameter of the scatters, decreased between the versions of yoghurt and milk with the same fat content.

Product name	A	β
Arla Lærkevang Sødmælk	44.4 ± 0.5	-1.19 ± 0.03
Arla Lærkevang Letmælk	25.7 ± 0.2	-1.42 ± 0.03
Arla Lærkevang Minimælk	17.2 ± 0.4	-1.65 ± 0.07
Arla KO mild yoghurt Naturell	58.6 ± 0.5	-0.82 ± 0.03
Arla A38 naturel 1.5%	42.9 ± 0.4	-1.08 ± 0.03
Arla A38 naturel 0.5%	41.0 ± 0.3	-1.19 ± 0.02

Table D.2: Fit coefficients from the expected Mie approximation to the reduced scattering coefficients.

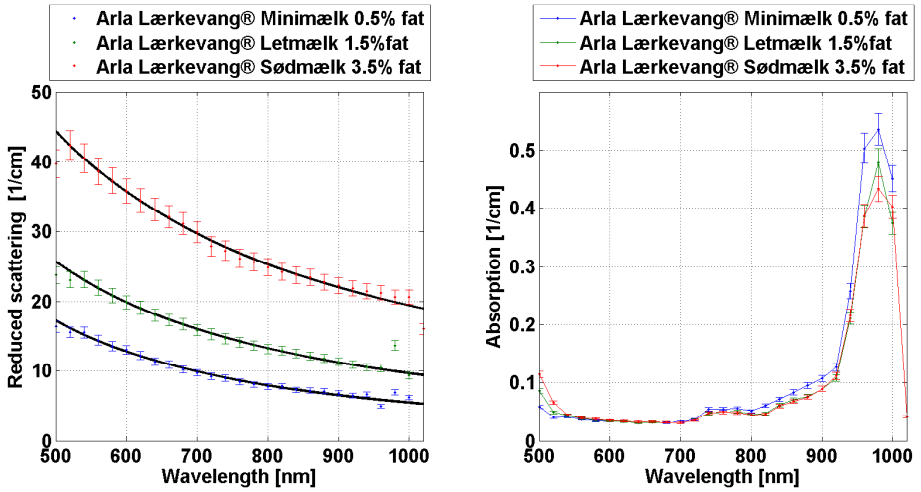

Figure D.4: Optical properties of milk with different fat content: (left) reduced scattering coefficient (right) absorption coefficient. The reduced scattering coefficient was fitted with an approximation from the Mie theory (black curve).

The absorption spectrum is a sum of the concentration of the chemical constituents multiplied by their wavelength specific absorption coefficient. The absorption spectra for both milk and yoghurt products show broad water absorption peaks at 970 nm and 750 nm, as previously summarised by Palmer and

Williams.[219] The absorption at these peaks varies slightly between samples. The ratio of the water absorption peaks found in our present study was also similar to the ratio reported previously, where the 970 nm peak was significantly stronger than the peak at 750 nm. The measurements of milk with very low scattering levels show an increase in absorption; this is an artefact of the data evaluation technique due to crosstalk between the optical properties. The optical properties are harder to evaluate due to the very short PToF distributions in the NIR range with the present fibre configuration, see Figure D.3. We suspect that the offset in absorption by approximately 0.03 cm^{-1} reflects the finite dynamic range of optical properties that may be deduced adequately. Compared to the high numerical value of the reduced scattering for Arla KO mild yoghurt Naturell in the blue regime ($\sim$ 60 cm^{-1}), the absorption outside the water peaks was small. With the present measurements, we cannot conclude whether the absorption coefficients change linearly in proportion to the fat content, but will investigate it in future studies. The lack of absorption peaks related to the fat content of samples suggests that the strength of the absorption bands presented by Tsenkova et al.,[61] combined with the relatively low mass percentage of the milk fat, gives rise to a total absorption below 0.03 cm^{-1}. The dominance of scattering in milk for this wavelength regime was reported by Qin and Lu,[54] but the absolute values were different. The coefficients reported by Qin and Lu resulted in more linear scaling with fat content for both scattering and absorption. The difference in absolute value is, in part, due to the difference in samples. A number of causes for measurement variations between DOS instruments and techniques were reported by Pifferi et al.,[220] whereas we note that the results by Qin and Lu[54] rely on a diffusion approximation which is known to cause deviation[86] compared to Monte Carlo models. The effect was quantified for our instrument according to Alerstram et al.[95]

Analysis of fermented milk products

As mentioned above in the section on dairy products, there are significant changes in structure during fermentation as the protein network forms a gel. This leads to signifi cant changes in optical properties, despite the fact that the chemical composition is essentially unchanged. The measured spectra from Figure D.4 and Figure D.5 were combined (Figure D.6) for direct comparison of milk and yoghurt with the same fat content. From this, it is concluded that scattering is increased significantly by fermented products and a clear distinction between fermented and unfermented products is observed for both fat levels. This is despite the small difference in their chemical constituent, as seen from Table D.1. The products differed slightly in protein content, which mostly contributed to the reduced scattering in the blue wavelength regime.[221] Proteins primarily exhibit Rayleigh scattering due to their small size, so we suspect that

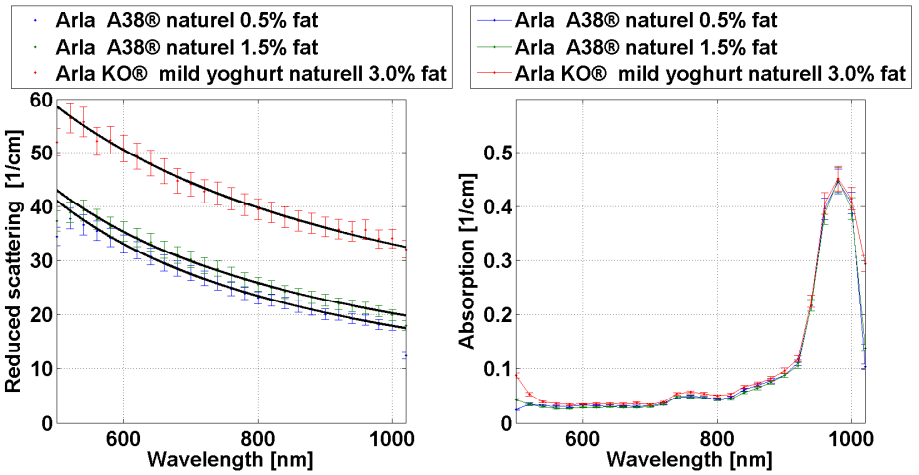

Figure D.5: Optical properties of yoghurt with different fat content: (left) reduced scattering coefficient (right) absorption coefficient. The reduced scattering coefficient was fitted with an approximation from the Mie theory (black curve).

the changed reduced scattering is due to changes in the samples structure induced by the protein gel. We did not measure a significant change in absorption between the milk and the yoghurt. From this combined picture, we conclude that the scattering coefficient changes drastically and will likely be a more sensitive parameter to monitor during the fermentation process rather than the absorption coefficient.

Conclusions

PToF spectroscopy has been investigated as an analysis technique for milk and yoghurt products. The technique enables independent monitoring of absorption and reduced scattering spectra in dairy products. These spectra are related to key quality parameters such as chemical composition and particle size distribution. In the studies presented, it was possible to quantify the absorption and reduced scattering coefficients for commercially available milk and fermented milk products. The reduced scattering coefficient showed significant and systematic changes, whereas the measured absorption coefficient had only minor changes between products. The PToF spectroscopy measurements were found to be highly sensitive to the structural composition in terms of both fat content and, more importantly, the micro-structure of the fermented products, which

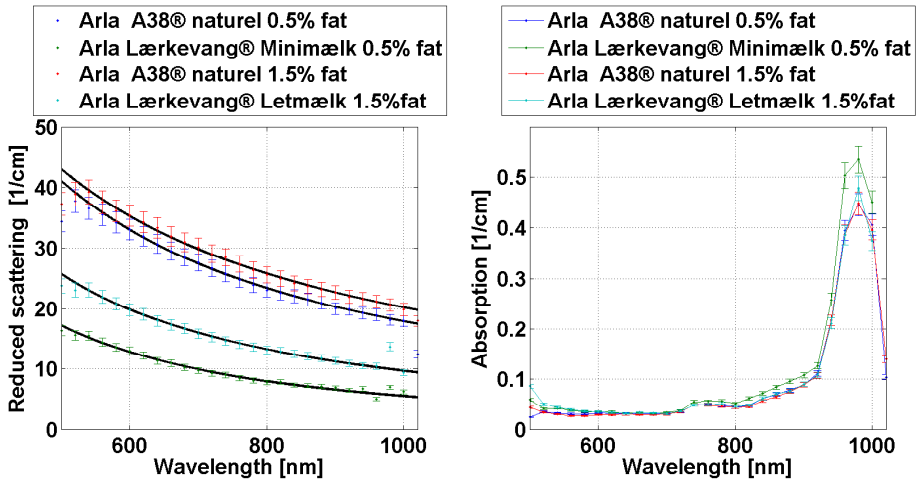

Figure D.6: Comparison of the reduced scattering and absorption coefficients for milk and yoghurt with the same fat contents.

may provide a new approach for the characterisation of dairy product structure.

The data acquisition speed of the present instrument may not be feasible for online inspection of the milk to yoghurt fermentation process. However, the spectral properties presented demonstrated that the most significant changes occur in the scattering coefficient, which may be recorded at lower spectral resolution and thus have a shorter acquisition time. For an industrial realisation, a multiplexing of wavelengths on the same recording, as presented by Re et al.,[222] may further reduced acquisition time. PToF spectroscopy has enabled further insight into the optical properties of dairy products which, in turn, form a basis for developing new milk analysis methods and improved sensors for online dairy process monitoring.

Future work may involve extending the spectral range of the instrument which, in turn, would increase the dynamic range of the particle size distribution which is investigated. An example of estimating the particle size distribution from reduced scattering spectra was presented by O'Sullivan et al.[214] This should be combined with detailed studies of milk optical properties during fermentation.

Acknowledgements

This work was (in part) financed by the Centre for Imaging Food Quality project which is funded by the Danish Council for Strategic Research (contract no 09-067039) within the Programme Commission on Health, Food and Welfare. D. Khoptyar gratefully acknowledges AstraZeneca for financial support.

Appendix E

Evaluation of the ID220 single photon avalanche diode for extended spectral range of photon time-of-flight spectroscopy

Otto Højager Attermann Nielsen[a], Frederik Donbæk Nielsen[b], Carsten Lilholt Thomsen[b], Stefan Andersson-Engels[c] and Dmitry Khoptyar[c]
[a] Department of Applied Mathematics and Computer Science, Technical University of Denmark. 2800 Kgs. Lyngby, Denmark.
[b] NKT Photonics A/S. Blokken 84. 3460 Birkerød, Denmark.
[c] Department of Physics, Lund University, PO Box 118, SE-221 00 Lund, Sweden

DTU Compute Technical Report-2014-06

Abstract

This paper describe the performance of the ID220 single photon avalanche diode for single photon counting, and investigates its performance for photon time-of-flight (PToF) spectroscopy. At first this report will serve as a summary to the group for PToF spectroscopy at the Department of Physics, Lund University (Sweden) together with ID Quantique Inc. (Genève, Switzerland). As such, the report does not give an introduction to PToF spectroscopy, which may be found om the Doctoral on the topic [96, 102, 142]. The report focuses on a description of the detectors ability to measure the PToF distribution of infrared light.

First, a motivation for using the ID220 for measuring PToF distribution is given, followed by a brief description of the experimental setup in which the detector was characterized. Following this, the quantification of delay using cross correlation between PToF distributions is described. This allows the changes in delay and shape to be characterized. A technique for reducing measurement artefacts by lowering the repetition rate of the light source is also investigated. Lastly, the applicability of the detector for PTOF spectroscopy is discussed and conclusions drawn about its suitability for this application.

Version History

Version	Date	Change revision
1.0	15 / 7 / 2013	First summary of measurements
1.1	20 / 10 / 2013	Updated results section
1.2	11 / 1 / 2014	Included description of single photon avalanche diodes.

Introduction

The aim of this work is to investigate the suitability of a newly available single photon avalanche diode (SPAD) for near infrared PTOF spectroscopy. The use of such detectors has recently been reported by Pifferi et al.[223], however not all properties of these detectors have been addressed. In this report we focus on how the detector performance can be quantified using interpretable features

(width and arrival time) which are important for any quantitative analysis of PTOF distributions. The characterization is first performed independently of our specific application, and as such it provides a general approach for SPAD characterization and an objective basis for identifying improvements to the devices.

The instrument has been investigated for PToF spectroscopy, a technique that allows deduction of the scattering and absorption properties of a material simultaneously. Using Lorenz-Mie theory, the scattering coefficients can be used to quantify a sample's structural composition in terms of particle size and shape distributions [224, 225, 226]. The absorption coefficient gives information on the sample's chemical constituents, because absorption arises from specific electronic and rotational-vibrational transitions in its atoms or molecules [60] A general introduction to the field of diffuseoptical spectroscopy is given by Martelli et al.[87]. The advantage of PToF spectroscopy is its ability to deduce optical properties without knowledge of the source power of the illumination. Instead, the change a short light pulse exhibits when passing through the sample is analyzed. The sample will delay the PToF together with broadening its temporal profile. Thus it is essential that the temporal delay of the pulses is measured with high accuracy and in an unbiased way. Similarly, the temporal width of the PToF distribution is influenced mainly by absorption, for measurements of which it is critical that the width be measured adequately.

The ID220 detector has been investigated as a replacement for a photon multiplier tube (PMT), that up until now has been used for the wavelength regime 900 - 1400 nm. PMT's require cooling by liquid nitrogen, operate at very high voltages, and are, in general, bulky. The advantage of using a solid state detector would be an extended spectral range, where measurements up to 1700 nm have been demonstrated [227], and the same range is covered by the ID200. The combined PToF spectroscopy setup would also benefit from a significantly to use, which would allow measurements in clinical facilities or during production in industry.

An illustration of the structure of a SPAD is shown in Figure E.1(a). An introduction to the detector technology is given by Fishburn and Charbon [229]. In principle, the diode is a p-n junction operated in reverse bias, with the bias set to a level above the breakdown voltage. This form of operation is often referred to as the "Geiger mode". In this mode, the multiplication region can induce new cascades due to both electrons and holes. The cycle which the detector undergoes in a detection process is illustrated in Figure E.1(b). The starting mode is an "armed" state ot the lower right where the diode's voltage is set to a voltage exceeding the breakdown voltage. From here the detection of a photon causes an avalanche current in the diode, which is stopped by the "quenching" process. From here the voltage is reset and the cycle may repeat.

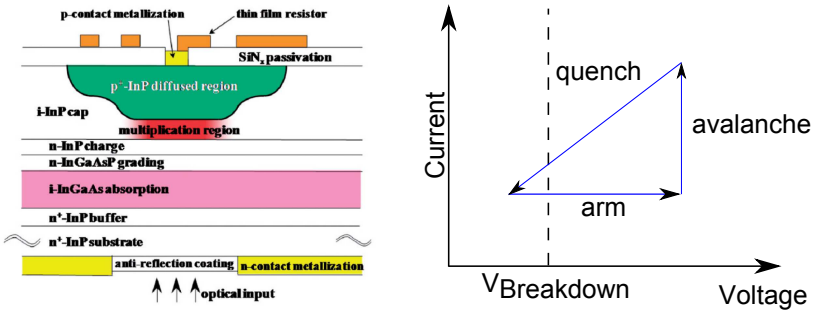

(a) Structure of a SPAD as reported by Lunghi [228]

(b) Changes in SPAD voltage and current for a detection cycle

Figure E.1: Illustration of the structure of an SPAD and the principle of its operation.

One of the limitations of the SPAD technology is afterpulsing of the detectors, which causes additional artificial detections when measuring the PToF distribution. These arise due to trapped electron-hole pairs which causes new avalanches after an actual detection event, hence the term after-pulsing. A physical interpretation of afterpulsing in SPAD detectors are given by Itzler et al.[230]. Suggestions for reducing afterpulsing while maintaining a high count rate are given in [231, 232, 227] which all employ gating of the detector signal to avoid artifacts. The ID220 uses a passive quenching technique, to reduce the non-linearity of the detector. The afterpulsing properties of the ID220 in particular have been investigated specifically in references [233, 228], but without investigating the pulse shape characteristics.
We present a characterization technique for the combined instrument, quantifying measurement perturbations independent of the source of error - whether afterpulsing, quenching or waveform generation.

Equipment and data acquisition

To quantify the instrument's performance with respect to estimation of both temporal delay and the width of the light pulses, it was combined with an instrument for PToF spectroscopy at NKT Photonics A/S (Birkerød, Denmark) in collaboration with Lund Photon time-of-flight spectroscopy laboratory. An illustration of the PToF spectrometer is presented in Figure E.2.

The PToF spectrometer uses a supercontinuum light source (SuperK Extreme

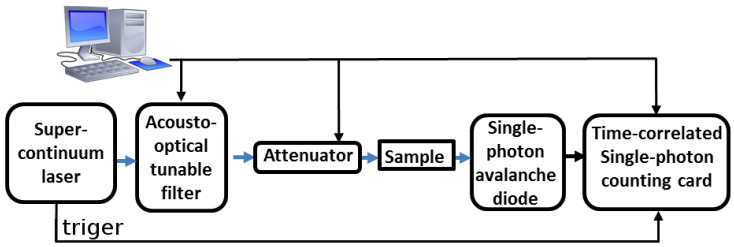

Figure E.2: A schematic of the photon time-of-flight spectrometer. The black lines are electronic signals, and blue are optical.

EXB-4). The laser operates at a repetition rate of 80 MHz, but a built-in pulse picker feature allows a selectable repetition rate in an interval between 2 - 80 MHz for the present source. The supercontinuum light is spectrally filtered using an acousto optical tunable filter (AOTF) with a SuperK SELECT (NKT Photonics - Birkerød Denmark). The system provide a temporally narrow laser pulse which can be tuned in the spectral range from approximately 400 nm - 2000 nm. The light pulses, filtered by the AOTF are delivered by a fiber based delivery system (LMA-10 NKT Photonics) and propagate afterwards in gradient-index fibers with a 400 μm core (Leoni Fiber Optics, Germany). To obtain sufficiently low intensity levels to permit single photon counting, we perform an adjustable attenuation of the pulse intensity by a fibre coupled attenuator (DD-100, OZ Optics, Canada). These attenuators are integrated into the measurement routines that are used for data acquisition. The laser intensity is reduced by positioning either a sample for a thin piece of paper in the optical path as when operated for PToF spectroscopy. This also has the effect of exiting all the optical modes of the GRIN fibre. The light pulses are afterwards sent to the ID220 detector. To construct a PToF distribution the detector output is wired to a time correlated single photon count (TCSPC) module (SPC-130EM - Becker & Heckl - Germany). The seed pulse from the super continuum light source is used as a time reference for the TCSPC card.

The installation of the detector is as described in the application note [234], a 12 dB attenuation is used between TCP card and the ID220 however. The TCP card settings for constant fraction discriminator level and range were adjusted to avoid a double peak structure and similar artifacts during data acquisition. Unless otherwise noted, all measurements of the PToF distributions were made over 32 seconds to ensure a decent signal to noise performance.

Dead time and Quantum efficiency

The ID220 has two adjustable parameters, the dead time after detection and the quantum efficiency (QEF), the effect of these was explored prior to the instrument characterization. The dead time can take integer values in the range 1 - 20 μs, and the QEF can be set to 10, 15 and 20 %. One of the key difference between InGaAs based SPADs and silicon based SPAD's is the necessity of long dead times after detection to avoid afterpulsing. The effect of setting dead time and QEF was quantified in terms of the dark count rate, and the results are presented in Figure E.3.

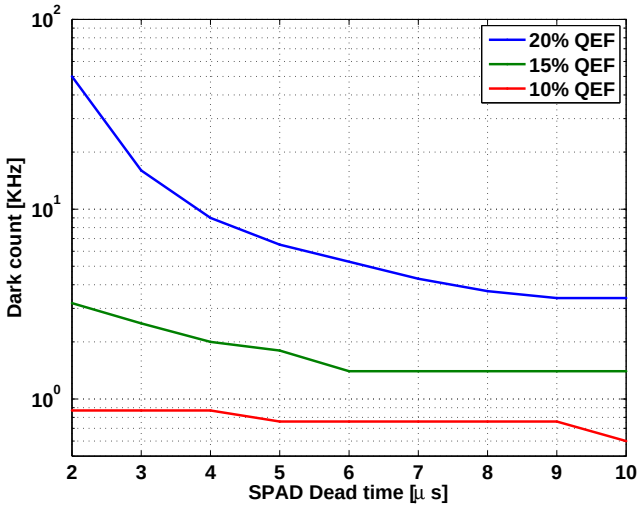

Figure E.3: Measured dark counts as a function of dead time for different quantum efficiencies of the ID220.

Similarly the detector response time is dependent on the QEF, the TWHM values are summarized in table E.1.

QEF [%]	20	15	10
FWHM [ps]	154	218	487

Table E.1: Instrument response function vs. quantum efficiency.

From these measurements it may be seen that an increase in the dead time significantly reduces the number of dark counts. Similarly the dark counts are reduced significantly by a low QEF value. The specific value of the dead time which is suitable for our application could not be determined from the

characteristics of the dark counts alone, beacause although an increase in dark count rate adds noise to the PToF distribution, it will also allow a higher count rate.

The measured instrument response time shows a significant increase when operating with a QEF of less than 20 %, as is seen from table E.1. For this reason, it was decided to operate the device with a QEF of 20 % to obtain the highest possible time resolution. The instrument response of the combined setup without the additional broadening of the detector is expected to be 40 *ps* based on measurements with a silicon SPAD.

Quantifying instrument linearities

An application-independent assessment of the linearity of the system is performed by measuring the change in pulse width and arrival time of the light pulse. The shape change is quantified by calculating the FWHM of the profile and the delay is quantified by measuring the change in arrival time. To measure the latter part with high accuracy, the cross-correlation of the profile is calculated with a reference pulse and the location of the peak position is extracted from the autocorrelation. In practice a third degree polynomial is fitted to the peak intensity part of the autocorrelation and the apex of this is used. An example of this technique and the analysis is presented in Figure E.4, the two signals which are compared are the two most extreme from the time series presented later in Figure E.5, with a separation of 92 ps. For each measurement series the absolute value of the delay is always relative, the signal with highest count rate is used because this has the best signal to noise.

The results show that visually a perfect overlap between the two profiles is achieved, and the shape of the cross correlation suggests that the noise in the estimation is very small.

Intrinsic fluctuation of the light source

To estimate precision and any possible intrinsic variation in the PToF distribution arising from the combined setup, the PToF distribution was recorded for ~ 70 hours, at 1510 nm, and the delay and FWHM were calculated. The results are presented in Figure E.5. The attenuation was fixed during measurement and a total count rate of 4.40 kHz $\pm$0.13 kHz with a detector dead time of 10 μs was used. The PToF distribution is recorded by triggering the clock on the TCP card by the first stage in the light generation process (the seed pulse). This

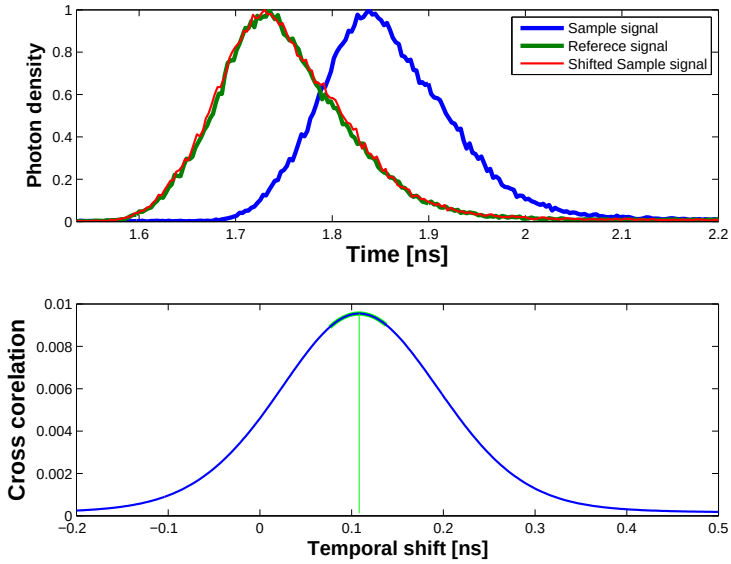

Figure E.4: Example of how the temporal delay is calculated. **Top:** Examples of photon time-of-flight distributions and their overlap after using their cross correlation to estimating the temporal shift. **Bottom:** Cross correlation of the two profiles together with the fitted polynomial at the center. The position of the peak is marked with a vertical green line.

signal pulse is thus not necessarily synchronized with the optical output of the laser.

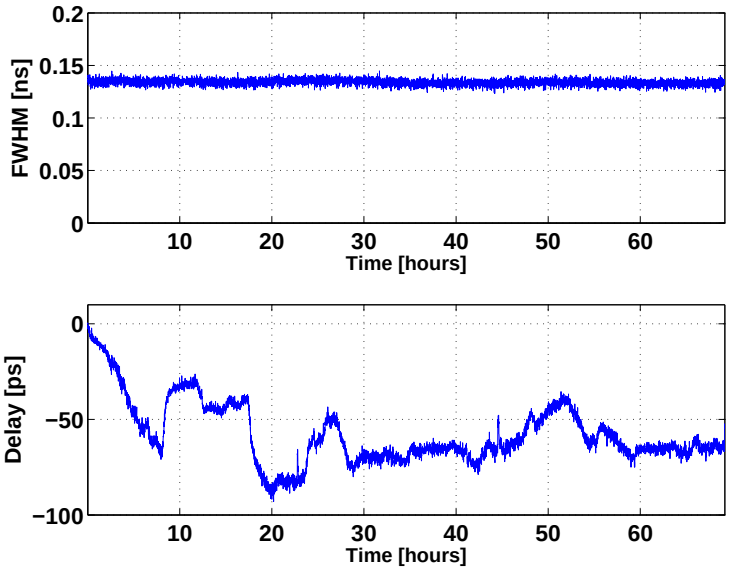

Figure E.5: Time stability of the light source. **Top:** Measured full width half maximum of the PToF distribution. **Bottom:** Measured delay compared to the start point.

The results show that the FWHM is very constant throughout the measurement. This shows that the temporal profile of the light pulse is unchanged during operation. The delay however varies a little over time, and is estimated with a precision of $\sim$ 5 ps as this is the variance on short time scales, the accuracy will depend on the ratio of signal to noise in the PToF distribution. For this reason repetitive measurements are performed during analysis later on to estimate precision at each measurement point. The variation on longer time scales is approximately $\sim$ 25 ps. This long term drift can be avoided by triggering on the actual output from the light source, but this is outside the scope of the present work.

The measurements serve as a validation of the analysis of both the light pulses arrival time and shape. Though only measured at a single wavelength, we suspect this to be a general result. The mechanism that drives the super continuum generation locks the average position of the different wavelengths in a well defined pattern [143]. Scatter plots, not shown here, of the correlation between the measured count rate and the delay and FWHM respectively revealed no correlation.

ID220 instrument response function

As explained previously it is imperative for PToF spectroscopy that the light pulse is characterized without artifacts. In single photon counting the count rate is arbitrary, but should be set low enough to avoid perturbation of the profile and the integration time should be sufficient to ensure a good signal to noise level. In this section we investigate how the delay and FWHM of the instrument change with count rate.

The PToF distribution of an optical phantom is presented in the left column of Figure E.6 for different count rates. The pulse width and delay relative to the lowest noise signal, measured at 95 kKHz is calculated and presented in the right column of Figure E.6. The optical phantom is composed by a combination of a pulverized BG36 bandpas filter and a expoxy plastic. The phantom is 1.9 mm thickness and was measured with a wavelength of 1000 nm. The detector was operated with a QEF of 20 % and a dead time of 10 μs.

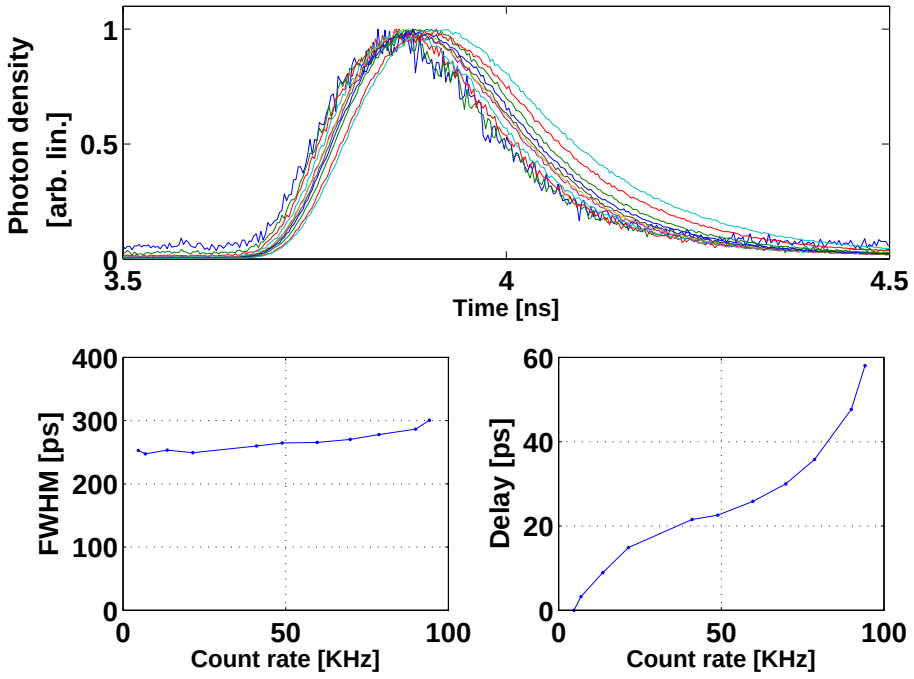

Figure E.6: ***Top*** *Normalized count rate for the PToF distribution of an optical phantom measured at different count rates.* ***Bottom*** *The measured FWHM of the profiles as a function of the repetition rate and the corresponding temporal delay.*

A first observation was that by setting the CFD values for the TCP card properly it is possible to measure PToF distributions without additional peaks appearing. Examples of detector-induced artifacts are summarized in Becker and Bergmann [235]. However, the raw measurement of the PToF profile clearly shows that the shape and position of the distribution changes systematically as the count rate is increased. This also shows that the advised count rate for measurements with the system[234] is too high for obtaining an unperturbed measurement of the PToF distribution. The change in FWHM and delay as a function of count rate shows that the detection of one photon is affected by the previous detection event. An increase in the FWHM can be seen as a reduced likelihood of detecting a photon in the start of the POTF distribution, imposed by the detector setup.

Effect of the light source repetition rate

In a similarly way, the instrument response was investigated as a function of repetition rate. The motivation is that reducing the repetition rate ensures that there is more time between detection events. When the TCP card registers an event on the detector signal, it will not become "armed" until it receives a trigger pulse from the source. Thus if the detector exhibits any afterpulsing effects in-between real detections, this will not affect a new measurement as the TCP card will not register the signal. This is the same effect that the detector is taking into account by using a dead time, and it is also the motivation for operating the SPAD in a gated mode. It was the hoped that a more well-controlled illumination could reduce the non-linearity of the detection which is seen in Figure above.

The measurement is performed on a piece of black paper, which causes a very low additional broadening of the time profile compared to the measurement on the optical phantom presented in Figure E.6. The PToF distribution becomes so short, that the detected broadening is given mainly by the detector, this measurement is often referred to as the instrument response function (IRF). The signal was measured at 1510 nm. For this reason, the IRF serves as a extreme measurement and is ideal for quantifying reductions of the measurement artifacts.

The measurements with different repetition rate require different cabling between the SPAD and TCP card to delay the pulses sufficiently to fit a fixed 12.5 ns window for the TCP card. The temporal width of this window is a standard in the laboratory, it matches the period of a laser with a 80 MHz repetition rate and therefore the PTFoF distributions also fits this window. For this reason the absolute position of the profiles on the card vary between mea-

surement with different repetition rate, though a fixed offset of $\sim$ 2.5 ns was used. To make the measurements comparable between repetition rates, the delay was shifted so all measurements were carried out relative to the value at 10 kHz measurement. The measured FWHM values and delays are shown in Figure E.7.

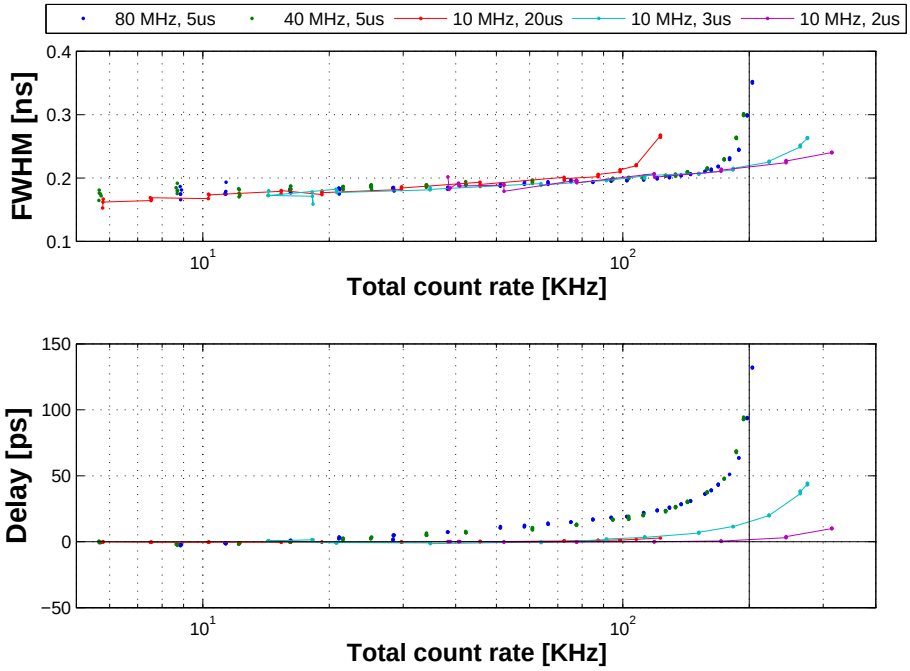

Figure E.7: *Instrument characteristics for different combinations of light source repetition rate and dead time, legend notes the repetition rate and dead time.* ***Top:*** *Absolute value for FWHM vs. count rate.* ***Bottom:*** *Measured delay relative to the 10 MHz value.*

From Figure E.7 it is seen that both the FWHM and the delay diverge towards higher values as the count rate is increased. The results show that the diverges is located around the saturation rate of the detector (defined as the inverse of the dead time). The FWHM value follows the same trend independently of repetition rate and dead time, except in the region close the divergence. Therefore, the only way to minimize this broadening is to reduce the total count rate. However, based on the current results, we do not see a stable regime as such. At the lowest repetition rate the change in signal level is comparable with the variance between measurements. A stable regime may be achieved at lower count rates with increased collection time to provide an adequate signal to noise level.

Concerning the delay time, we again measure a count rate dependent performance, suggesting that the detection is non-linear over the range of count rates we have investigated. The measurements show no significant change upon reducing the repetition rate from 80 MHz to 40 MHz, where the latter was used previously in the literature [223] for PToF spectroscopy. However when operated at 10 MHz, the change in the delay becomes significantly less as a function of the count rate. When combined with a short dead time of 2 - 3 μs, a stable regime is achieved for count rates less than $\sim$ 100 kHz. This shows that the detection artifacts are reduced by using this advanced feature of the light source.

Photon time-of-flight spectroscopy

To investigate the suitability of the detector for PToF spectroscopy the optical properties of an optical phantom were measured at 1510 nm as a function of count rate. The optical properties are deduced by modeling the temporal profile of the light that has passed though the sample with a analytical expression for diffused light through a finite material slab [98]. The analytical model is convolved with a measured instrument response to account for the temporal broadening of the combined setup. For the analytical model, a refractive index of 1.55 was assumed and the sample was 1.91 mm thick. Examples of the PToF distribution are shown in Figure E.8.

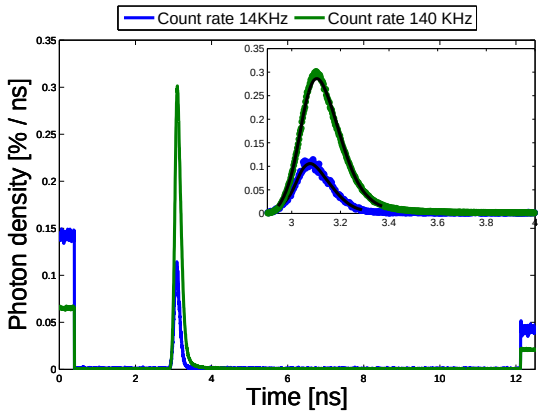

Figure E.8: *Example of PToF distributions for the BG36 phantom. The raw data is presented in the main plot, and the graph to the top right shows a zoom into the data with the fitted diffusion expression as black lines.*

From the raw data it is seen that the TOF distribution recorded with a high count rate is delayed, for both cases the model can fit the data, but the fit

results in different optical properties. This is a weakness of the technique: the optical properties are extracted, with decent fit to the profiles, but all the differences between the measurements is caused by the detector artifacts. Thus the evaluation of the PToF distribution itself does not give a way to quantify or validate the detector performance, it simply gives nice fit to the data with varying optical properties.

To quantify how the count rate affect the deduced optical properties the PToF distribution was measured, and the results are presented in Figure E.9. The corresponding reference values for both the delay and the FWHM are given in Figure E.10.

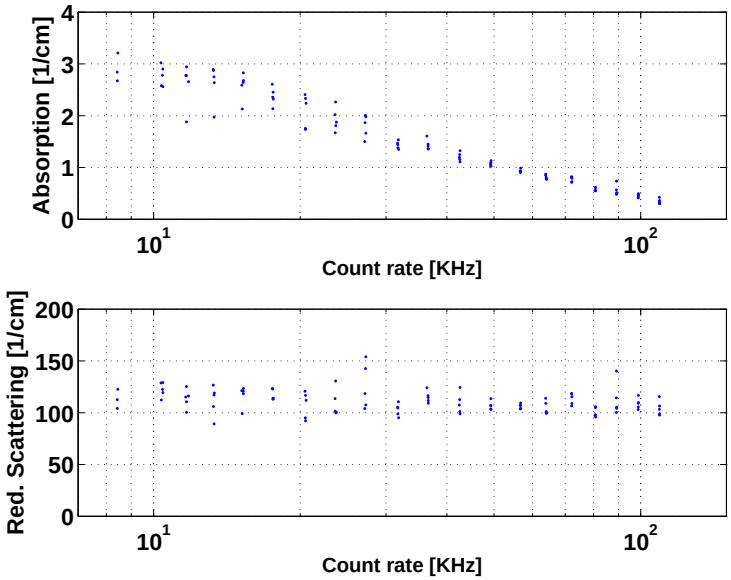

Figure E.9: *Deduced optical properties for a BG36 color glass phantom as a function of count rate,* ***Top:*** *Absorption* ***Bottom:*** *Reduced scattering*

The results show systematic decrease in the deduced absorption when the count rate is increased. For scattering, we see a relatively high variance throughout the measurement series, but no systematic change as a function of count rate. This is effectively a trade off between a high noisy value estimation at low count rates and low noise but biased value at higher count rates. The current results indicate that a stable regime has been accomplished at very low count rate, however the measurement exhibits significant noise and may be unsuitable for quantitative spectroscopy due to extensive measurement times to reduce noise.

The associated development of the delay and the FWHM are presented in Figure

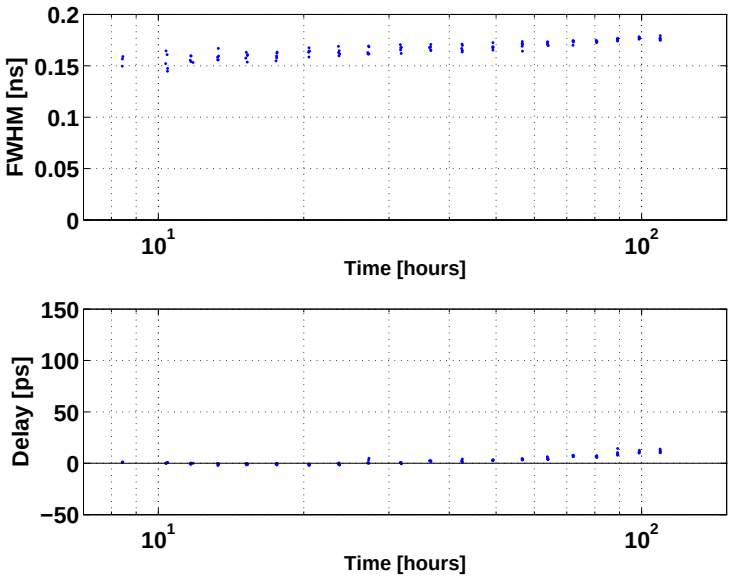

Figure E.10: *Pulse characteristics for the series of BG36 measurements presented in figure E.9.* ***Top:*** *full width half maximum* ***Bottom:*** *temporal delay.*

E.10. Both the delay and the FWHM changes when the count rate is increased. As was seen in Figure E.7, the change in FWHM is slow and almost linear, and similarly delay is almost constant at low count rates.

A better performance may be achieved by evaluating time of flight profiles on a longer time scale (longer than the 12.5 ns), which also require a reduced repetition rate of the source. The measurement accuracy is, in part, given as the ratio between the temporal width of the instrument response and the measured PToF from the sample. By measuring the temporal profiles on a longer time scale, the detector can be used with a lower QEF which causes a significant drop in the dark count rate of the device. This may provide a easier way for using the device in practice.

Conclusion

In this report we have demonstrated a technique for characterization of non-linearities in the response of SPADs for single photon counting in terms of delay and changes in temporal width. These features are useful from an application

point of view because they relate directly to the PToF signals that is used for analysis. Using the ID220 it was possible to make measurement of the PToF profile for both optical phantoms and measurement of the systems instrument response function. The results, presented in Figure E.6, suggest that the advised collection[1] rate of half the saturation rate (defined by the SPAD dead time) does not give a unbiased estimate of the PToF distribution.

By measuring changes in the instrument response function, it is demonstrated that some of the non-linearities may be minimized by reducing the repetition rate of the light source. Furthermore, it was found that reducing the dead time of the detector removed the systematic change in the pulse delay.

Based on an improved method of operation, with a low repetition rate and a short dead time, the detector was applied to PToF spectroscopy of tablets composed of BG36 color glass. The deduced optical properties are highly dependent on the count rate during the measurements, which is related to the systematic effects seen on the IRF. However, the results suggest that a stable regime, with high noise of the profiles, was accomplished with the present measurement settings.

In summary the field of single photon counting, and specifically PToF spectroscopy, can benefit from a simple commercially available solution for unbiased estimate of the PToF distribution in the NIR spectral range. We have quantified the detector performance, and demonstrated that artifacts can in part can be eliminated using a commercially available light sources with reduced repetition rate. However, the achieved performance is not sufficient for PToF spectroscopy yet.

The present work have focused on obtaining unperturbed measurements of the PToF distribution. However, it has not addressed how the profiles compared to those obtained with other detector technologies. Future studies may therefore include evaluation of the detectors in the spectral range around 1000 nm where both a PMTs and silicon based SPADs are available as benchmarking instruments.

Acknowledgement

This work was financed by the Centre for Imaging Food Quality project which is funded by the Danish Council for Strategic Research (contract no 09-067039) within the Program Commission on Health, Food and Welfare. ID Quantique

[1] Described in [234]

Inc. (Genève, Switzerland) is thanked for lending the ID220 for this first round of investigations. NKT Photonics A/S (Birkerød Denmark) is acknowledged for proving access to the advanced light source used in the measurement campaign.

Appendix F

Hyperspectral imaging based on diffused laser light for prediction of astaxanthin coating concentration

Martin Georg Ljungqvist[a], **Otto Højager Attermann Nielsen**[a], **Stina Frosch**[a], **Michael Engelbrecht Nielsen**[b], **Line Harder Clemmensen**[a], **Bjarne Kjær Ersbøll**[a]

[a] Department of Informatics and Mathematical Modelling, Technical University of Denmark. 2800 Kgs. Lyngby, Denmark.

[b] Division of Industrial Food Research, National Food Institute, Technical University of Denmark. 2800 Kgs. Lyngby, Denmark.

Published in Machine Vision and Applications 2013.

Abstract

We present a study on predicting the concentration level of synthetic astaxanthin in fish feed pellet coating using multi- and hyper-spectral image analysis. This was done in parallel using two different vision systems. A new instrument for hyper-spectral imaging, the SuperK set-up, using a super-continuum laser as the light source was introduced. Furthermore, a parallel study with the commercially available multi-spectral VideometerLab imaging system was performed. The SuperK set-up used 113 spectral bands (455-1015 nm), and the VideometerLab used 20 spectral bands (385-1050 nm). In order to predict the astaxanthin concentration from the spectral image data, the synthetic astaxanthin content in the pellets was measured with the established standard technique; high pressure liquid chromatography (HPLC). Regression analysis was done using partial least squares regression (PLSR) and the sparse regression method elastic net (EN). The ratio of standard error of prediction (RPD) is the ratio between the standard deviation of the reference values and the prediction error, and for both PLSR and EN both devices gave RPD values between 4 and 24, and with mean prediction error of 1.4-8.0 parts per million (ppm) of astaxanthin concentration. The results show that it is possible to predict the synthetic astaxanthin concentration in the coating well enough for quality control using both multi- and hyper-spectral image analysis, while the SuperK set-up performs with higher accuracy than the VideometerLab device for this particular problem. The spectral resolution made it possible to identify the most significant spectral regions for detection of astaxanthin. The results also imply that the presented methods can be used in general for quality inspection of various coating substances using similar coating methods.

Introduction

Astaxanthin is a naturally occurring carotenoid with a high antioxidant activity essential for growth and survival and it is important for the development of colour in salmonid fishes [236]. The primary use of astaxanthin within aquaculture is as a feed additive to ensure that farmed salmon and trout have similar appearance to their wild counterparts [237]. The colour appearance of fish products is important for customers as a quality indicator [37, 38, 39]. Astaxanthin is very expensive [238] and therefore optimisation of its use in fish feed production is of importance.

Synthetic astaxanthin is more easily available and costs slightly less than natural astaxanthin and is therefore used more often in industry. However, there is a

demand for natural astaxanthin for the organic salmonid fish market, where natural astaxanthin is mandatory.

Today, chemical measurement of astaxanthin is done by high pressure liquid chromatography (HPLC). HPLC is a well established technique for measuring synthetic astaxanthin content in fish oil. However, when measuring astaxanthin concentration in fish feed pellets, an additional step for extraction of the oil is necessary, and this is why measurements of astaxanthin from fish feed pellets are less accurate and more labour intensive.

An automatic vision system for at-line pigment quality control of astaxanthin coating concentration level would be of great benefit to the industry, in relation to both process control and process optimisation.

The aim of this study is to investigate the possibility of predicting the concentration level of synthetic astaxanthin coating on aquaculture feed pellets by spectral imaging. Since HPLC is used for measuring astaxanthin coating content in the industry, we used this as a reference method.

Spectral imaging is called multi-spectral when using a small number of spectral bands (e.g. less than about 50), and hyper-spectral when using a large number of spectral bands (e.g. hundreds).

Previous studies on feed pellet monitoring by spectral analysis include near infra-red (NIR) reflectance spectroscopy for classification of feed material and feed pellets by Fernández-Ahumada et al. (2010) [239], and predicting chemical information in pharmaceutical pellet core and coating using NIR imaging by Sabin et al. (2011) [240].

Previous work on multi- and hyper-spectral image analysis of astaxanthin coating by Ljungqvist et al. (2012) [241, 242] has shown promising results for screening of the concentration level. However, those studies did not use hyper-spectral imaging in the visual part of the spectrum. In [242] only the NIR range was analysed, and in [241] only 20 wavelengths were analysed in the visual and parts of the NIR range. Neither of them used chemical measurements for validation of the astaxanthin coating level.

For the previous work using the visual part of the spectrum [241], the spectral bands were located at predefined wavelengths due to instrument set-up, chosen without knowledge of the particular problem. The few spectral bands used may not be the ones that give the greatest ability to quantify the contents of astaxanthin. Thus a more detailed study is called for, and here we report the characteristics for a new imaging method based on diffused laser light with more spectral bands. The study is focused on the visual region of the electromagnetic

spectrum due to function of astaxanthin as a pigment.

Vision systems have previously been implemented for quantisation of chemical contents, and a number of light-source options exist. In this paper we present the use of a super-continuum light source for full-field illumination. The super-continuum laser, combined with an acousto-optical tunable filter (AOTF) provides a broadband tunable light source. This form of light source is often used for confocal microscopy [243], fluorescence lifetime imaging [244], and measurement of sub-surface laser scattering (SLS) [1, 15]; also known as diffuse reflectance. To apply the light-source for full-field illumination, the small beam from the AOTF box is simply expanded and made diffuse.

A parallel study with a commercially available multi-spectral system called VideometerLab was also performed. The performance of this device has been validated for similar surface chemistry applications [41, 42, 245, 246, 43, 44, 45, 46].

Since the hyper-spectral imaging device records more spectral bands than a multi-spectral device, it would give more detailed information for measuring the astaxanthin coating concentration.

The presented work thus investigates both the possibility of examining astaxanthin contents by hyper-spectral image analysis, and a comparison of the two modalities (multi- and hyper-spectral imaging) for astaxanthin prediction.

Materials and Methods

Material

The pellets used in this study were produced for the purpose of this experiment, and the recipe was based on normal commercial fish feed for salmonid fish. The pellets had the approximate production diameter of 4.5 mm, and were coated with fish oil.

An extruder machine was used for the pellet production. The feed material was extruded through a die plate with holes of a specific diameter which determined the diameter of the pellets. On the other side of the disk there was a set of rotating knives that cut the material into shorter, cylinder-shaped pellets.

The synthetic astaxanthin used was cold water dispersible (BASF SE, Ger-

many), and in total 7 different levels of synthetic astaxanthin concentration were added to the fish oil coating. The highest synthetic astaxanthin level in fish oil was 100 parts per million (ppm), and then the oil was diluted so that the concentration level became half of the original. This was repeated to achieve the 7 nominal levels of synthetic astaxanthin concentration in the fish oil coating, where the last level was 0 ppm, see Table F.1.

Fish oil in itself typically contains a small amount of natural astaxanthin, however this is assumed to be less than 1 ppm and is here referred to as a coating of 0 ppm concentration. Astaxanthin is commonly measured in ppm, and it is measured in mass so here ppm corresponds to mg/kg.

Between production and image acquisition the pellets were stored at 2° Celsius in a dark environment for two months. They were stored in plastic bags where the oxygen had been pumped out and the bags were filled with nitrogen to minimise the oxidation process and quality reduction during storage.

The spectral reflection of the pellets is a mix of the pellet compound (recipe) and the reflection of astaxanthin. The light captured by each pixel is thus assumed to be a linear combination of two main components; the pellet compound and the astaxanthin coating. Due to the production method, the coating is neither evenly distributed among the pellets, nor uniformly on each pellet.

In the extrusion process, parts of the astaxanthin coating will go inside the pellet, while we only measure reflection from the surface. However, the industry is interested in the total amount of astaxanthin in the pellets. Therefore, the surface reflection is assumed to be linearly related to the total amount of astaxanthin in the pellets.

It is assumed that most of the quantity of synthetic astaxanthin on each pellet can be estimated by measuring the coating surface of each pellet. For practical use, however, it is not interesting to estimate the quantity on each single pellet, but rather on a larger amount of pellets and calculate an ensemble average.

Equipment

SuperK

The hyper-spectral imaging system consists of four parts: light source, spectral filter, diffuse filter and camera. The illumination system is based on a SuperK Extreme (NKT Photonics A/S, Denmark) super-continuum white light laser

Table F.1: Data overview of the 7 pellet groups (nominal concentration levels) and the number of images taken (of different samples) with VideometerLab and SuperK respectively. Added synthetic astaxanthin to the fish oil coating in ppm.

	Synthetic Astaxanthin Concentration (ppm)						
Levels	0	3.125	6.25	12.5	25	50	100
	Number of images						
VideometerLab	30	30	30	30	30	30	30
SuperK	10	10	10	10	10	10	10

producing a quasi continuous output. The super-continuum light is filtered using a SuperK SELECT (NKT Photonics A/S, Denmark), where an AOTF is used for spectral filtering of the beam. The combined light source and filtering box provides a wavelength tunable laser beam delivered in a photonic crystal fibre (PCF) by a Fiber Delivery System (NKT Photonics A/S, Denmark). The combined system provides 0.5 - 6.5 mW.

In combination this system provides light in the visual and NIR region, ranging from 455 to 1015 nm. A step size of 5 nm was used as the spectral resolution, resulting in 113 spectral bands. The bandwidth grows linearly as a function of wavelength; at 500 nm it is 3.5 nm, at 900 nm it is 14 nm.

The spectrally filtered light from the Fiber Delivery System forms a Gaussian fundamental transverse electromagnetic (TEM_{00}) beam. This is transformed to illuminate a square area below the camera using an Engineered Diffuser (ED1-C20-MD, Thorlabs, Sweden). This diffusing method has a high power transmission onto the sample.

The illumination does not form a perfectly uniform intensity distribution; it produces a gradient due to the projection caused by the oblique incidence of the beam onto the camera field of view. It also produces a short distance intensity fluctuation. To minimise the latter effect, the Gaussian beam delivered after the AOTF box is expanded using a -50 mm focal length negative lens (LC1439, Thorlabs, Sweden). By illuminating the Engineered Diffuser, the short distance intensity fluctuations are minimised and become insignificant for this application.

Image capturing is done using a Grasshopper GRAS-20S4M grey-scale charge-coupled device (CCD) camera (Point Grey Research Inc., Canada), which uses a 12 bit analogue to digital converter (ADC) with a 16 bit output. The image

resolution is 1600 × 1200 pixels, with a pixel size of approximately 0.028 × 0.028 millimetres. For an overview of the SuperK set-up see Figure F.1(a).

VideometerLab

To compare the result of the SuperK set-up, the commercially available multi-spectral VideometerLab (Videometer A/S, Hørsholm, Denmark) was also used for image acquisition. It uses 20 wavelengths distributed over the ultra-violet A (UVA), visual and NIR region: 385, 430, 450, 470, 505, 565, 590, 630, 645, 660, 700, 850, 870, 890, 910, 920, 940, 950, 970, 1050 nm.

This system uses a Point Grey Scorpion SCOR-20SOM grey-scale CCD camera. The objects of interest are placed inside an integrating sphere (Ulbricht sphere) with uniform diffuse lighting from light sources placed around the rim of the sphere [247]. All light sources are light-emitting diodes (LED) except for 1050 nm, which is a diffused laser diode.

The curvature of the sphere and its matt-white coating ensure a uniform diffuse light so that specular effects are avoided and the amount of shadow is minimised. The device is calibrated radiometrically with a following light and exposure calibration according to the National Institute of Standards and Technology (NIST). The system is also geometrically calibrated to ensure pixel correspondence for all spectral bands [248]. For an overview of the VideometerLab set-up see Figure F.1(b).

VideometerLab has the advantage that the intensity is calibrated with respect to the sensitivity of the CCD and the intensity of the light sources, which means that the resulting reflection spectrum can be compared with e.g. a spectroscopy spectrum.

The image resolution is 1200 × 1200 pixels. In this situation one pixel represents approximately 0.072 × 0.072 millimetres. The Scorpion camera has a 12 bit ADC, and the system uses 8 bit data output from the camera. After calibration correction, the reflectance intensity is output at 32 bit precision.

Spectroscopy

In order to explore the spectral properties of astaxanthin further, and to assist in the interpretation of the spectral image results, a spectrometer was used in the visual and NIR range. Absorption spectra of synthetic astaxanthin in a solution

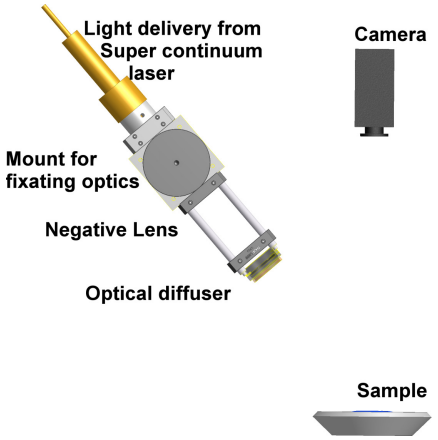

(a) Overview of the SuperK set-up showing the supercontinuum light delivery, negative lens, optical diffuser, camera, and sample position.

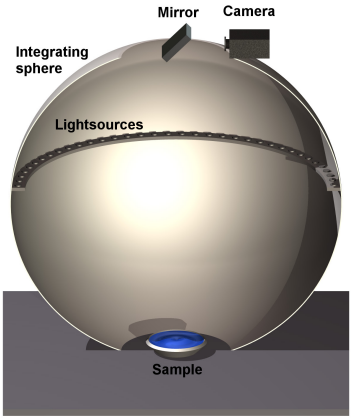

(b) The VideometerLab set-up showing a cross section of the integrating sphere, light sources, camera, and sample position.

Figure F.1: *Spectral imaging systems*

of fish oil along with plain fish oil were recorded using a NIRSystems 6500 absorption spectrometer (Foss NIRSystems Inc, USA) with a spectral resolution of 2 nm. The absorption spectra were transformed to reflection values using the standard relation $A = -\log(R)$, where A is the absorption values and R is the reflection values.

High Pressure Liquid Chromatography

In order to calibrate the hyper-spectral imaging prediction method, an HPLC analysis of the synthetic astaxanthin concentration in pellets was performed. By analysing samples from each concentration level we could estimate the average astaxanthin content in the pellets, which can be used to validate the nominal levels used in the production. In order to reduce the effect of the analysis method, we used two independent HPLC measurements from different parties.

The HPLC analysis was done at the National Food Institute, Division of Industrial Food Research at the Technical University of Denmark (Lyngby, Denmark) using an Agilent 1100 series HPLC (Agilent Technologies, Palo Alto, CA, USA), equipped with a UV diode array detector. The oil was extracted from the pellets using acetone and homogenised to a concentrate, which was analysed for synthetic astaxanthin content, according to the modified protocol of Bligh and

Dyer (1959) [249].

A fraction of the lipid extract was evaporated under nitrogen and redissolved in 2 mL of n-heptane before injection. Astaxanthin content was determined after injection of an aliquot (50 μL) of the n-heptane fraction into a LiChrosorb Si60-5 column (100 mm $\times$ 3 mm, 5 μm) equipped with a Cromsep Silica (S2) guard column (10 mm $\times$ 2 mm; Chrompack, Middelburg, The Netherlands) and eluted with a flow of 1.2 mL/min using n-heptane/acetone (86:14, v/v) and detection at 470 nm. Concentrations of astaxanthin were calculated using authentic standards from Dr. Ehrenstorfer GmbH (Augsburg, Germany).

Furthermore, HPLC analysis was also made at Eurofins A/S (Galten, Denmark), which is a commercial laboratory.

Image Acquisition

Images of petri dishes (plastic, diameter of 9 cm) filled with pellets were captured using both the SuperK set-up and the VideometerLab. For each concentration level, 10 images of different pellets were captured using both SuperK and VideometerLab, then an additional 20 images were captured with VideometerLab, see Table F.1. In total 70 SuperK pellet images and 210 VideometerLab pellet images were captured over two consecutive days.

The concentration level sequence was randomised, and samples were interleaved two at a time. The pellets were at normal room temperature during image acquisition.

A filled petri dish resembles the rapid inspection that the industry would desire for this application.

The pellet cluster inside the petri dish in each image was segmented from the light-grey background using a grey-scale threshold, using the band of 500 nm for the SuperK images and the band of 470 nm for the VideometerLab images. The threshold segmentation was complemented with the morphological methods erosion and dilation using a disk as structuring element [250]. Furthermore, the topmost layer of pellets was segmented to remove parts with less light, and in this way also avoid some of the granulometry information in the image. Since the SuperK images contained some specular reflections due to the direct lighting, the strongest specular effects were also removed by a threshold for both the VideometerLab and SuperK images.

The mean spectrum of the pixels in each segmented image was used as samples.

In this way the impact of the pattern from the diffuse filter used by the SuperK set-up was reduced and was assumed not to impact the results of the image analysis.

Standard red-green-blue (sRGB) colour image representations of the VideometerLab images for this paper were done by multi-spectral colour-mapping using penalised least square regression described in Dissing et al. (2010) [251]. Since the SuperK set-up is not calibrated towards the CCD, sensitivity standardised colour-mapping was not possible, instead non-standard RGB images were made in order to visualise the images.

Data Analysis

The number of samples is denoted n and the number of variables (the wavelengths) is denoted p. The stored data of n samples and p variables is denoted as matrix $\mathbf{X}$. The ground truth reference values (concentration level) are stored in vector $\mathbf{y}$ with length n. The predicted (estimated) value of $\mathbf{y}$ is denoted $\hat{\mathbf{y}}$.

For ground truth reference values, the nominal values in Table F.1 were used.

For the VideometerLab data p is 20 and n is 210. In order to compare the VideometerLab data with the SuperK data, the 70 images corresponding to the same petri dishes of pellets for both methods were used in the analyses; $n = 70$. For the SuperK data p is 113 and n is 70, this results in an ill-posed problem with more variables than observations ($p \gg n$).

Two different regression methods were used in order to estimate the concentration level of synthetic astaxanthin in the pellet coating. Both methods produce linear prediction models, but they calculate the models in different ways, as described below.

All image analyses and statistics were carried out using Matlab 7.9 (The Mathworks Inc., Natick, MA, USA).

Principal Component Analysis

The multivariate data from the images were analysed using principal component analysis (PCA) for exploratory purposes [252]. PCA is an unsupervised method, and the most optimal method with respect to maximising the variance in the data [109]. If the relation of interest contains large variations, then PCA

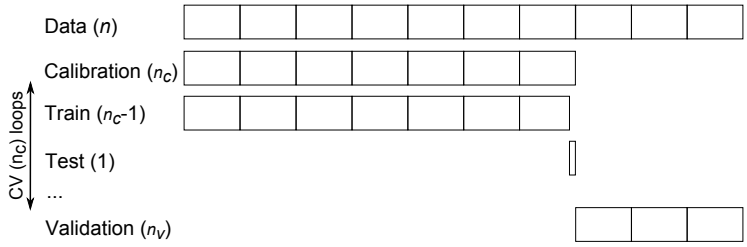

Figure F.2: *Schematic overview of the LOOCV used for calibration and validation of the prediction. The calibration set consists of n_c samples, and the validation set of n_v samples. One sample at a time is left out for test in the calibration step.*

is a good method for analysing the data. The pre-processing method, called standard normal variate (SNV) [253], was used, followed by PCA. SNV is performed by subtracting the mean from each sample, and normalising using the standard deviation (SD) of the sample spectrum.

Model Selection and Validation

In order to calibrate the statistical model parameters, a calibration set of 70% of the samples was used (n_c). Then the chosen model was validated on the remaining 30% of the samples (n_v). For the VideometerLab data with a total of 210 samples, $n_c = 147$ and $n_v = 63$, and for the VideometerLab data using 70 samples, $n_c = 49$ and $n_v = 21$. For the SuperK data with a total of 70 samples, $n_c = 49$ and $n_v = 21$.

The calibration and validation set was chosen randomly, but with all concentration levels present in both. The same corresponding samples for both devices were present in both the calibration and the validation set.

For parameter calibration two different methods were used in parallel. Firstly, the leave-one-out cross-validation (LOOCV) method was used on the calibration set, where each sample is used as validation once, see Figure F.2.

Secondly, what can be called a group-fold cross-validation (GFCV) was used both for parameter calibration and in order to investigate how the prediction generalises on unseen concentration levels. The GFCV was performed so that all samples with one concentration level, a group, was left out during training of the model, and then the left out group was used for prediction.

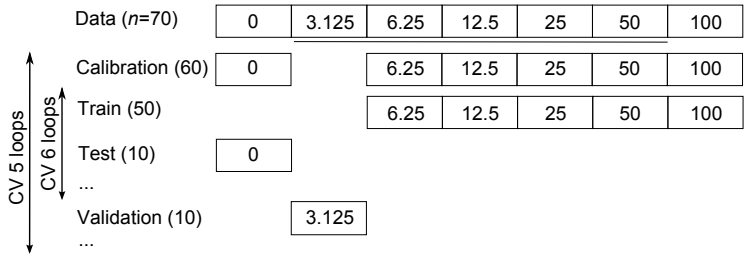

Figure F.3: *Schematic overview of the group oriented cross-validation GFCV for calibration and validation of the prediction. The GFCV is used both for calibration and for generalisation validation. The data contains 7 different concentration levels, groups, and the middle 5 of these are used for generalisation validation. Each group consists of 10 samples. Calibration is performed on 6 groups at a time. One group at a time is left out for validation. Synthetic astaxanthin concentration in ppm.*

Two nested GFCV:s were used, one for calibrating a PLSR model, and one for the final validation and generalisation. For every iteration a PLSR model was calibrated using GFCV on 6 levels, and then the validation was done on the left out level. For each iteration one of the 5 middle levels (3.125, 6.25, 12.5, 25, 50 ppm) were left out at a time in order to see how a model predicts on an unseen concentration level. The highest and lowest concentration levels were not used for the validation/generalisation part since we are not interested in extrapolation of the model. This procedure renders a result in terms of a pooled prediction error of the 5 group tests. For an overview of the GFCV scheme see Figure F.3.

Partial Least Squares Regression

The first method for analysing the concentration level was the partial least squares regression (PLSR) method [109, 254]. The data was mean centred, and the number of components to be used in the PLSR model was decided using LOOCV, and likewise GFCV, on the calibration set while minimising the mean of the residual sum of squares (RSS), see Equation F.1. A modified version of the 'one standard error rule' [109] for selection was used: The least number of components with RSS value inside the range of two SDs of the lowest value of RSS was selected.

For the VideometerLab data, the number of components (factors) n_f tested in the calibration step was varied from 1 to 20. For the SuperK data containing 113 variables and a calibration set of 49 samples; 47 was used as the maximum number of components tested.

The chosen value of n_f was used on the calibration set and the resulting prediction model was then validated on the validation set.

The coefficient of determination R^2 is a measure of how much variation is explained by the model and was calculated for the prediction of the validation set. R^2 is basically the ratio of the RSS and the total sum of squares (TSS), see Equation F.1.

$$R^2 = 1 - \frac{RSS}{TSS} = 1 - \frac{\sum_{n_v}(\mathbf{y} - \hat{\mathbf{y}})^2}{\sum_{n_v}(\mathbf{y} - \frac{1}{n_v}\sum_{n_v}\mathbf{y})^2}\,. \tag{F.1}$$

Furthermore, the ratio of the standard error of prediction and standard deviation (RPD) was calculated as a measure of how well the model predicts. The RPD is the ratio between the SD of the original data $\mathbf{y}$ (the reference values) and the standard error of prediction (SEP), see Equations F.2 and F.3.

$$SEP = RMSEP = \sqrt{\frac{1}{n_v}\sum_{n_v}(\mathbf{y} - \hat{\mathbf{y}})^2}\,. \tag{F.2}$$

$$RPD = \frac{SD}{SEP}\,. \tag{F.3}$$

The SEP is equal to the root mean square error of prediction (RMSEP). An RPD value of 1.0 means that the model cannot predict accurately, since this means that the mean error is equal to the SD of the reference values. An RPD value higher than 2.5 is considered satisfactory for screening, and values of 5–10 are adequate for quality control [255].

To further see what range of the spectrum is relevant for the prediction of astaxanthin concentration, we used interval PLS (iPLS) regression where the spectrum is divided into a number of regions and PLSR is performed on each region individually [256]. While the VideometerLab data has too few spectral bands for this method, we can investigate what parts of the SuperK spectrum give best prediction. We used 20 intervals and a PLSR model was calibrated for each of them.

Elastic Net Regression

In order to identify which wavelengths are of most interest, the elastic net (EN) was also used for regression analysis [110]. The EN is a sparse statistical method and performs variable selection while doing regression. In contrast to PLSR it does not use linear combinations of all variables, it uses only a few variables which are found important; non-zero coefficients. In this way EN excludes variables that do not contribute to the result and thus are potential noise.

EN tends to select variables that are correlated with each other, and this is suitable for spectral data with intrinsic correlation. This grouping effect would make the result suitable for an optical filter implementation.

EN needs two model parameters: λ_1 for the L_1 norm for determining the number of non-zero coefficients, and λ_2 for the Euclidean L_2 norm for regularisation. The regularisation is suitable for the ill-posed problem. The regression model consists of the variable weights (coefficients) in $\boldsymbol{\beta}^{en}$, see Equation F.4.

$$\beta_j^{en} = \underset{\beta_j}{\operatorname{argmin}} \left(\|\mathbf{y} - \mathbf{X}\beta_j\|_2^2 + \lambda_2 \|\beta_j\|_2^2 + \lambda_1 \|\beta_j\|_1 \right). \tag{F.4}$$

The estimated coefficients are then multiplied by $(1 + \lambda_2)$ to get the final EN solution.

The two parameters were selected using LOOCV on the calibration set. The λ_1 parameter steers the selection of variables and was calculated so that the number of selected variables was varied from 1 to 20. The λ_2 parameter was varied with 12 logarithmic steps from 10^{-7} to 10. The data matrix $\mathbf{X}$ was normalised, and the reference values $\mathbf{y}$ were centred, for each calculation of the EN.

RSS was used in order to find the optimal parameter set. If more than one combination of the number of selected variables and λ_2 was found to give the best calibration result, then the lowest number of selected variables and the highest value of λ_2 was used, giving the least complex model.

The implementation by Sjöstrand et al. (2012) [257] was used for calculations of the EN.

Results

SuperK Power Stabilisation

To estimate the acquisition reproducibility, the same sample was repeatedly imaged for ~ 11 hours, and the mean image intensity was measured. To compare across wavelengths, we report the variation relative to the mean intensity of the given wavelength; the ratio denoted as a percentage (%). The resulting SDs are presented in Figure F.4 showing the image acquisition reproducibility.

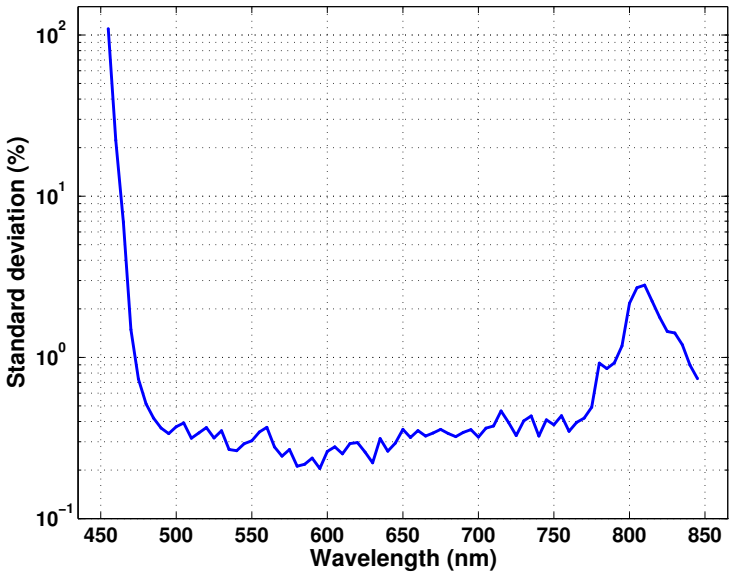

Figure F.4: *SuperK stability measurement. Standard deviation of the mean image intensities (%) of the power-normalised image data for each wavelength.*

Compared to the precision that is desired in estimating astaxanthin coating concentration (~ 1 %), we suspect that the wavelengths below 470 nm will be too noisy for modelling the concentration level. For the regression models this will automatically mean a reduced weighting for these bands.

Depending on which wavelength is chosen during modelling, and since we only apply linear models, the reported SD as a function of wavelength indicates the precision of ~ 0.3 % as a limit of the acquisition process itself.

Chemical Measurement

The results from the two independent HPLC measurements of the synthetic astaxanthin coating concentration both show lower values than the nominal values, and DTU shows lower values than Eurofins. However, both HPLC measurements are linear to the nominal values, see Table F.2, which means that the nominal values are valid as reference values for the regression.

Table F.2: HPLC measurement of the synthetic astaxanthin present in the pellets, carried out by two different parties. Added synthetic astaxanthin to the fish oil coating in ppm.

Nominal Values	HPLC DTU	HPLC Eurofins
0	0	0
3.125	1.90	3.07
6.25	4.36	5.88
12.5	9.56	11.6
25	19.44	24.8
50	42.64	49.3
100	90.46	95.1

Image Analysis

Background and dark sample parts were segmented out using threshold and morphological operations. Example results of a segmented VideometerLab image can be seen in Figures F.5(a) and F.5(b), as well as for SuperK in Figures F.6(a) and F.6(b). RGB versions of the captured images for all 7 concentration levels visualising the differences in pigment concentration can be seen in Figure F.11(e) for VideometerLab, and in Figure F.11(f) for the SuperK images.

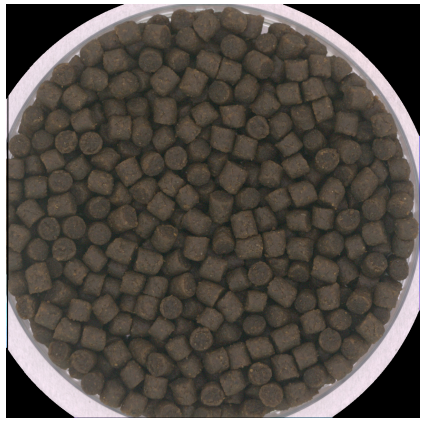

(a) SRGB representation of a VideometerLab image of pellets coated with synthetic astaxanthin of 50 ppm.

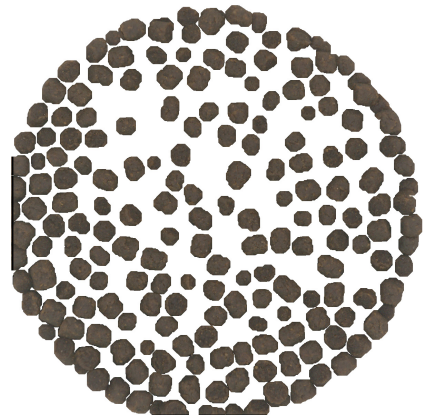

(b) SRGB representation of the segmented version of the VideometerLab image in Figure F.5(a), with pellets coated with synthetic astaxanthin of 50 ppm.

Figure F.5: *SRGB image from the Videometer Lab, with and without segmentation.*

(a) RGB representation of a SuperK image of pellets coated with synthetic astaxanthin of 50 ppm.

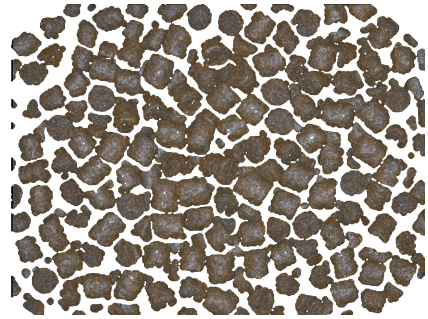

(b) RGB representation of the segmented version of the SuperK image in Figure F.6(a), with pellets coated with synthetic astaxanthin of 50 ppm.

Figure F.6: *SRGB image from the SuperK system, with and without segmentation.*

The spectrometer spectra of fish oil with added synthetic astaxanthin and plain fish oil are presented in Figure F.7(a), which shows that the largest separation is in the range of 490 – 610 nm.

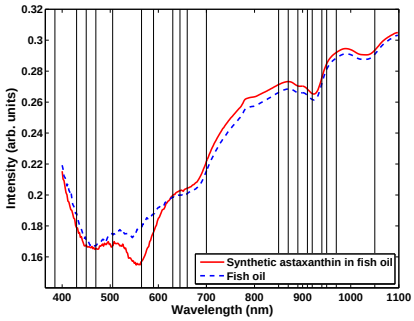

(a) Mean reflection spectra of synthetic astaxanthin coating in fish oil, as well as plain fish oil, using a spectrometer. No pellets were used here. The bands of the VideometerLab are marked by vertical lines.

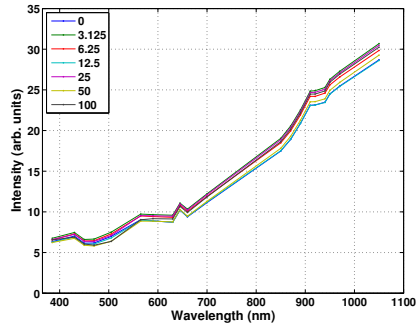

(b) Mean reflection spectra of the different concentration levels of synthetic astaxanthin in pellet coating, using image mean of the VideometerLab images, $n = 70$.

Figure F.7: *Absolute intensity measurements of astaxanthin contents by spectroscopy and from the Videometer Lab.*

Investigating the reflection spectra of the pellets coated with synthetic astaxanthin shows similar characteristics to the spectroscopy results of astaxanthin in fish oil, see Figure F.7(b). Looking at the difference of the concentration levels' reflection spectra in Figures F.8(a) and F.8(b) reveals that the largest difference between concentration levels is around 505 nm for the VideometerLab data, and between 500 and 520 nm for the SuperK data. This corresponds well with regions of difference in the reflection spectrum in Figure F.7(a).

From the explorative analysis of the concentration level of synthetic astaxanthin coating using PCA, score scatter plots using all combinations of PC1 to PC6 were investigated (results not shown). PC2 seems to describe the concentration scale well for the SuperK data, and PC2 in combination with PC3 for the VideometerLab data. However, both show some small overlap – mostly for the lower concentration levels, see Figures F.9(a) and F.9(b). This concludes that the variation between the concentration levels is the second largest variance in the image data (PC2), next after the total intensity variation (PC1), which corresponds well with the two spectra mentioned above.

Calibrating the PLSR model by LOOCV gives an optimum of 3 components for the VideometerLab data, and 7 components for the SuperK data, see Figure

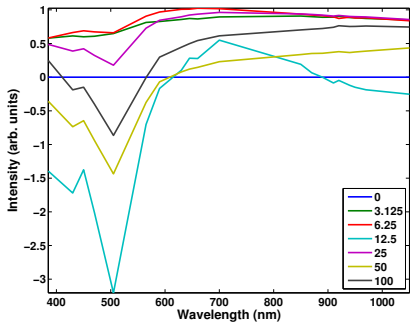

(a) Using the VideometerLab images, $n = 70$.

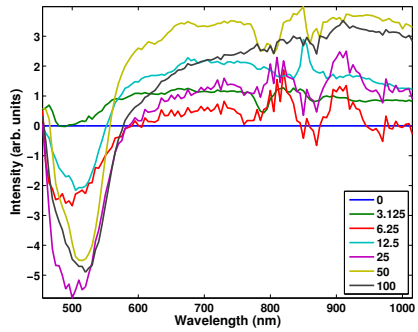

(b) Using the SuperK set-up, $n = 70$.

Figure F.8: *Measured spectral changes from the uncoated pellets by the two spectral imaging system. Both are normalised to their respective SD.*

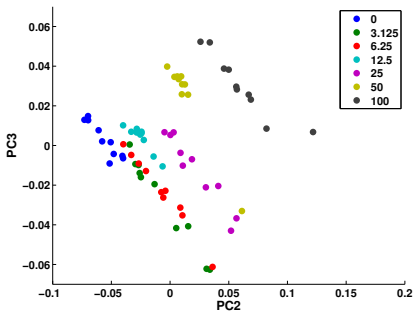

(a) Scatter plot of synthetic astaxanthin coating using PC2 and PC3 from a PCA on whole image samples using the VideometerLab, $n = 70$.

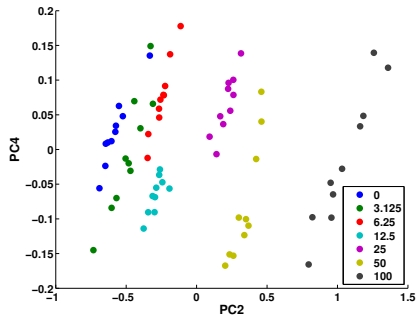

(b) Scatter plot of synthetic astaxanthin coating using PC2 and PC4 from a PCA on whole image samples using the SuperK, $n = 70$.

Figure F.9: *Scatter plot of the PCA scores of the image data from the two spectral imaging system.*

F.11(a). It also shows that the calibration error drops significantly around 3 components for both modalities.

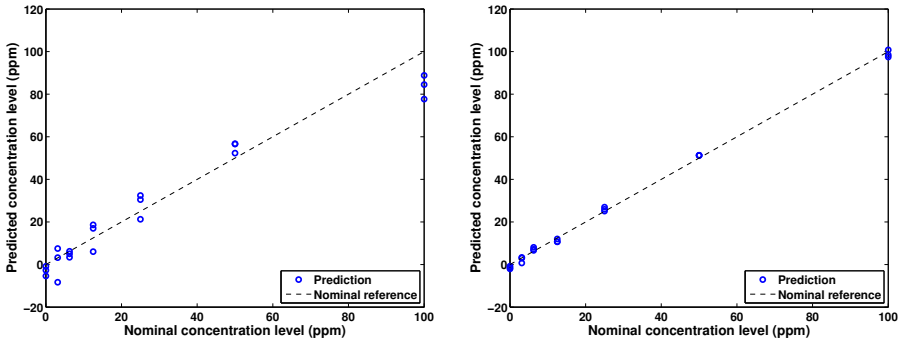

(a) From the VideometerLab, $n = 70$ and using 3 components.

(b) From the SuperK, $n = 70$ and using 7 components.

Figure F.10: *PLSR prediction of synthetic astaxanthin coating using LOOCV on image samples two spectral imaging system.*

Regression analysis of the synthetic astaxanthin coating concentration level using the whole images as samples shows good results. PLSR using LOOCV shows an R^2 value of prediction above 0.94 for VideometerLab and 0.99 for SuperK, see Table F.3, where VideometerLab uses 3 PLSR components and SuperK uses 7 PLSR components.The EN using LOOCV has R^2 around 0.97 for VideometerLab and 0.99 for SuperK, see Table F.3, where the VideometerLab data uses 8 non-zero coefficients, and the SuperK data uses 19 coefficients.

Table F.3: PLS and EN regression for synthetic astaxanthin coating concentration level prediction using LOOCV. PLS regression was also done using only the 16 bands that are in common for VideometerLab and SuperK. Synthetic astaxanthin concentration in ppm.

Device Samples (n)	Method	Comp. Coef.	R^2 Calibr.	R^2 Pred.	SEC Calibr.	SEP Pred.	RPD Pred.
VideometerLab							
210	PLS	3	0.9483	0.9479	7.6916	7.6180	9.1292
70	PLS	3	0.9598	0.9421	6.9785	8.0281	4.2588
210	EN	8	0.9729	0.9728	5.4904	5.5053	6.1094
70	EN	8	0.9853	0.9702	4.0426	5.7571	5.9387
SuperK							
70	PLS	7	0.9990	0.9982	1.1345	1.4278	23.9466
70	PLS	3	0.9788	0.9872	5.0698	3.7728	9.0622
70	EN	19	0.9989	0.9976	1.1093	1.6209	21.0926
VideometerLab-16							
70	PLS	2	0.8441	0.8432	13.5960	13.2122	2.5877
SuperK-16							
70	PLS	4	0.9850	0.9848	4.3091	4.1108	8.3170

For the VideometerLab data the RPD is between 4 and 9 for both PLSR and EN, while for the SuperK data the RPD value is almost 24 for PLSR and 21 for the EN. The mean prediction error is 7.6 ppm for VideometerLab using 210 samples, and 8.0 ppm when using 70 samples. For the SuperK data using 70 samples the mean prediction error is 1.4 ppm. The synthetic astaxanthin coating concentration prediction using PLSR and EN can be seen in Figures F.10(a) and F.10(b), and using EN in Figures F.12(a) and F.12(b), illustrating that the predicted levels correlate well with the nominal levels. For the SuperK data 3 PLSR components were also tested, resulting in an R^2 of 0.97, SEP of 3.8, and an RPD of 9, see Table F.3.

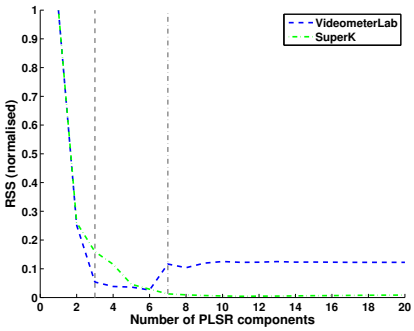

(a) PLSR calibration using LOOCV RSS, using the calibration data set of VideometerLab and SuperK respectively, $n_c = 49$, $n = 70$. Minimum of RSS with the least number of components within two SD was found at 3 components for VideometerLab, and at 7 components for SuperK. The first 20 components are shown for SuperK.

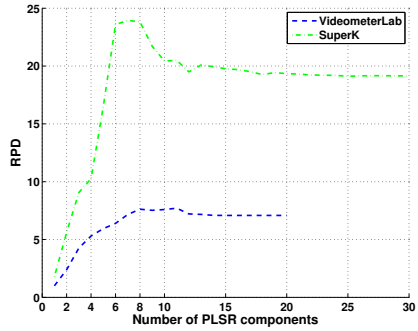

(b) RPD for different numbers of PLSR components. Using the calibration and validation data set of VideometerLab and SuperK respectively, $n = 70$. The first 30 components are shown for SuperK.

The RPD for different numbers of PLSR components can be seen in Figure F.11(b), where it shows that RPD above 5 is achieved for SuperK using only 2 components, and using 4 components for VideometerLab.

The PLSR components' weights show the contribution of different spectral regions to the model, and thus their significance. Similar to the difference from the grand mean, Figures F.8(a) and F.8(b), we rediscover the importance of the blue and green regime between 450 and 590 nm, but see distinctions also in the NIR measurements for the two instruments, see Figures F.13(a) and F.13(b). For the VideometerLab data the largest PLSR weights are at 385 nm and 505 nm, while for the SuperK data the largest PLSR weights are around 550 nm and around 860 nm. The importance of the visual range of the spectrum was confirmed by the iPLS regression of the SuperK data returning the lowest LOOCV calibration error around 545 – 575 nm, see Figure F.14.

The EN regression coefficients $\boldsymbol{\beta}_{en}$ that constitute the prediction model show similar results for both VideometerLab and SuperK data, see Figures F.15(a) and F.15(b). For the VideometerLab data the largest coefficient is at 565 nm, and the second largest at 505 nm. For the SuperK data the largest coefficient is at 550 nm. Both systems show similar clusters of spectral bands with high emphasis in the visual regime.

The results also show that using the 16 bands that are the same for both the VideometerLab and the SuperK set-up (470, 505, 565, 590, 630, 645, 660, 700,

Table F.4: Generalisation test with GFCV using PLS regression for synthetic astaxanthin coating concentration level prediction. The pooled SEP of GFCV is compared to the corresponding prediction error of LOOCV, where only the middle concentration levels (3.125, 6.25, 12.5, 25, 50 ppm) have been used for validation for both methods. The mean number of PLSR components used for GFCV is presented. Synthetic astaxanthin concentration in ppm.

Device	CV Type	Samples n	Comp. n_f	SEP Pred.
VideometerLab				
	LOOCV	70	3	5.4971
	GFCV	70	2	14.0364
SuperK				
	LOOCV	70	7	1.3240
	GFCV	70	1.6	9.5813

850, 870, 890, 910, 920, 940, 950, 970 nm) gives acceptable results for quality control with an RPD value of 2.6 for VideometerLab, and 8.3 for SuperK. The VideometerLab images got R^2 of 0.84 using 2 PLSR components, and the SuperK images got R^2 of 0.94 using 4 PLSR components, see Table F.3.

By leaving out one concentration level for validation using GFCV and PLSR, it was tested how the prediction performs on unseen concentration levels. Using LOOCV, all concentration levels have been used for calibration by leaving out one sample at a time, and for comparison with GFCV here 0 and 100 ppm have been left out when performing the validation. When using GFCV all concentration levels have been used for calibration while leaving out one concentration level at a time, and all concentration levels but 0 and 100 ppm have been used for validation, one at a time. We see that the pooled SEP of GFCV is larger than the corresponding SEP of LOOCV for both systems, as can be seen in Table F.4. For the VideometerLab using LOOCV, the SEP is 5.5, and for GFCV the pooled SEP is 14. For the SuperK data using LOOCV, the SEP is 1.3, and for GFCV the pooled SEP is 9.6.

Visualisation of the spatial distribution of synthetic astaxanthin coating on the pellets was done using the PLSR prediction result for VideometerLab and SuperK, and can be seen in Figures F.11(c) and F.11(d). Spectral images from the validation set and all different concentration levels have been projected using the PLSR components. This should only be seen as a visualisation, since the

PLSR models are calibrated on image mean values and then used for prediction on pixel values. The visualisations clearly show larger values for the higher concentration levels of synthetic astaxanthin.

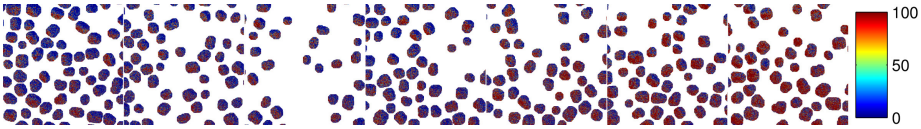

(c) Videomter Lab

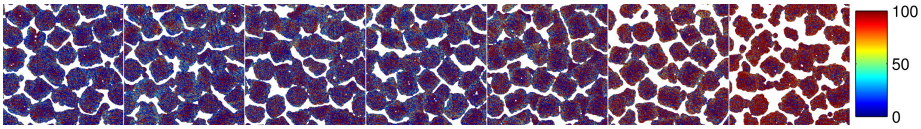

(d) SuperK system

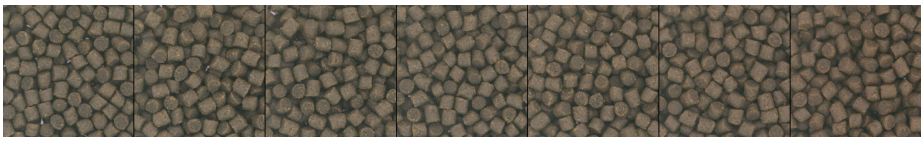

(e) Videomter Lab

(f) SuperK system

Figure F.11: ***a*** **-** ***b*** *Shows the projected images using the PLSR model, visualised using the jet colour map where 0 ppm astaxanthin is blue, and 100 ppm astaxanthin is shown as red. The images are taken from the validation set, cropped, clamped and masked. The pellets with different levels of synthetic astaxanthin coating concentration, from left to right: 0, 3.125, 6.25, 12.5, 25, 50, 100 ppm.* ***c*** **-** ***d*** *Shows a SRGB representation of cropped images of the pellets with 7 different levels of synthetic astaxanthin coating concentration. From left to right: 0, 3.125, 6.25, 12.5, 25, 50, 100 ppm.*

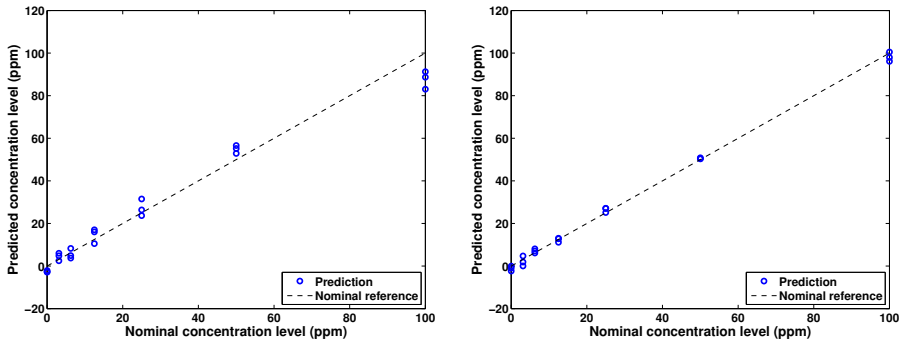

(a) From the VideometerLab, $n = 70$ and using 8 non-zero coefficients.

(b) From the SuperK, $n = 70$ and using 19 non-zero coefficients.

Figure F.12: *EN prediction of synthetic astaxanthin coating using LOOCV on image samples for the two spectral imaging systems.*

Discussion

The results from the multi-spectral VideometerLab and the hyper-spectral SuperK indicate that it is possible to predict synthetic astaxanthin coating on pellets.

The design has minimised the structure of the semi diffuse illumination used in the SuperK set-up so it visually becomes insignificant. It is evident that the presented technique using an Engineered Diffuser provides a sufficient trade-off between a smooth uniform illumination and high power transmission.

In addition, the SuperK system's image acquisition reproducibility was investigated. The results presented in Figure F.4 show low variation above 470 nm.

In industry it is desired to know the astaxanthin coating level with an accuracy of roughly 1 ppm, which corresponds to a sensitivity of 1% of the pixel intensity for the present study. For this reason it was satisfactory that the reproducibility SD of the power stabilised SuperK images taken over long acquisition times (11 hours) proved to be below 1%, see Figure F.4.

For each image acquisition, the two systems examined different numbers of pellets due to the difference of field of view. However, this difference was not significant since a large number of pellets were investigated in each image.

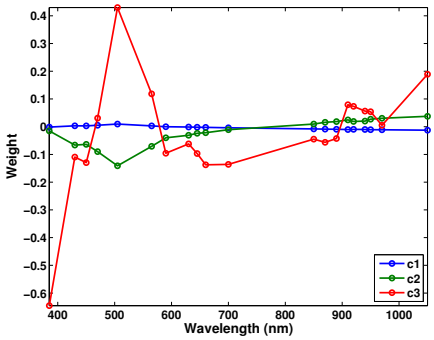

(a) From the VideometerLab, $n_c = 49$, $n = 70$. Calculated on the calibration set, showing the 3 PLSR components.

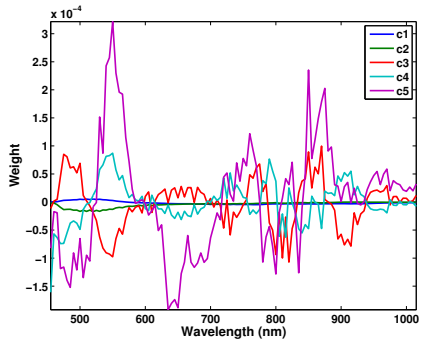

(b) From the SuperK, $n_c = 49$, $n = 70$. Calculated on the calibration set, here showing the first 5 of the total 7 PLSR components.

Figure F.13: *PLSR components for the prediction of synthetic astaxanthin coating concentration level using LOOCV on image samples for the two spectral imaging systems.*

Previous studies of astaxanthin [258, 259, 260] found absorbance peaks of astaxanthin of around 450 – 505 nm and secondary peaks of around 500 – 600 nm for various solvents, as well as at 870 nm. This corresponds with the spectrometer results seen in Figure F.7(a).

To continue the data exploration we have presented the spectral difference of the different synthetic astaxanthin coating concentration levels, seen in Figures F.8(a) and F.8(b). For both modalities the largest discrimination between data was present in the $\sim 500 - 550$ nm wavelength range. This is in good agreement with the difference in spectroscopy spectra, presented in Figure F.7(a), of fish oil with and without synthetic astaxanthin. Since astaxanthin is a pigment, it makes sense that the visual range of the spectrum is of importance in the results.

The two vision systems presented very similar characterisations of the samples. Spectral response from both systems shows a clear separation between concentration levels for the wavelengths of about 510 – 530 nm, and also along the entire spectrum. SuperK showed more distinction between the small concentration levels, which can be seen both in the difference spectra and the PCA plot, see Figures F.8(b) and F.9(b).

For concentration prediction, PLSR and EN models were trained on the data from each instrument and both systems were able to perform results suitable for industrial screening and quality inspection, as the high RPD values between

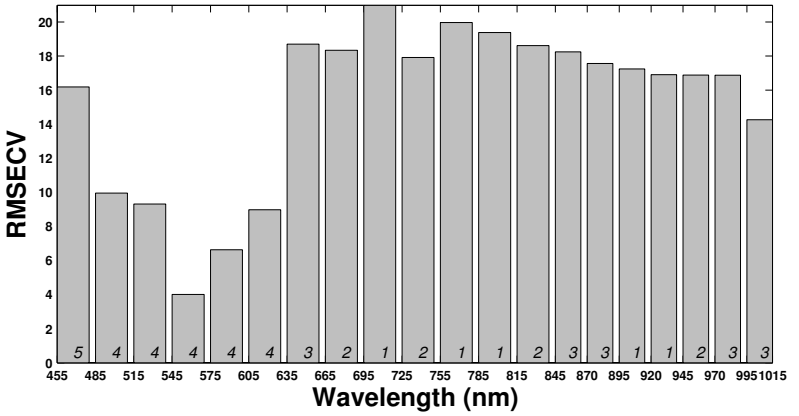

Figure F.14: *The iPLS regression calibration using LOOCV on SuperK images illustrating the error (RMSECV) of 20 different regions in the spectrum,* $n_c = 49$*,* $n = 70$*. The optimal number of PLSR components chosen for each interval is shown in italics.*

4 and 24 presented in Table F.3 indicate.

PLSR components 1 and 2 include a small amount of all spectral bands and these alone can explain a moderate part of the variance in the data corresponding to the reference values, see Figures F.13(a) and F.13(b). This could be interpreted such that the overall intensity in all spectral bands explains a part of the synthetic astaxanthin concentration level. However, this is not enough for quality control for the VideometerLab data with respect to RPD value, and just enough for quality control for the SuperK data, as can be seen in Figure F.11(b). This can be compared to the results in [43] where they found astaxanthin concentration in fish fillets to be strongly dependent on the overall pixel intensity in multi-spectral images, stated both for PC1 and PLSR component 1.

However, for astaxanthin in pellet coating it seems as if the concentration level has a more subtle dependency on pixel intensity, since the characteristics appear first in PC2, see Figures F.9(a) and F.9(b), and in PLSR component 2 and onwards, indicating that the concentration variance is a smaller portion of the data variance. This is common for variance of interest in image analysis [252]. In a previous study of astaxanthin coating, PC2 was also found to be of importance for detecting the presence of astaxanthin [46, 43]. Furthermore, for astaxanthin coating concentration prediction, PLSR component 2 and onwards showed considerable characteristics for prediction in [242] and component 3 and

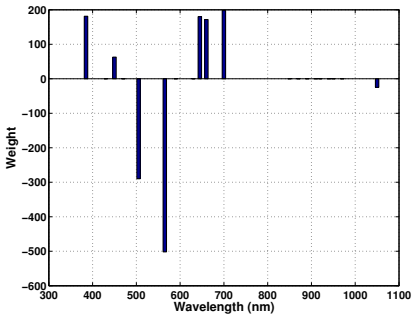

(a) From the VideometerLab, $n = 70$ and using 8 non-zero coefficients.

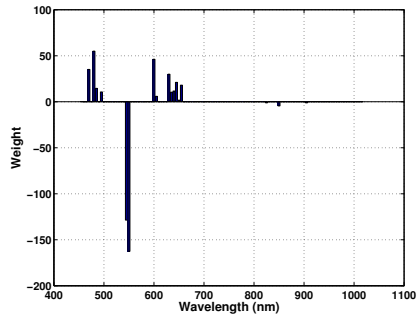

(b) From the SuperK, $n = 70$ and using 19 non-zero coefficients.

Figure F.15: *The coefficients in $\boldsymbol{\beta}_{en}$ from the prediction model of synthetic astaxanthin coating using EN regression with LOOCV on image samples for the two spectral imaging systems*

onwards in [241].

The RPD test shown in Figure F.11(b) illustrates that more than about 10 PLSR components do not improve the results, which is confirmed by Figure F.11(a). We therefore conclude that the regression problem for this data has a low complexity since 3 components suffice, though still with a considerable prediction error, and this is considerably improved by a few more components up to about 7 or 10 components.

The regression models show similar structures between VideometerLab and SuperK, both using PLS regression and EN regression. The PLS regression chose primarily two spectral regions for discriminating between the coating concentrations. The weight of the PLSR components and EN coefficients corresponds well with the variance seen in the spectral difference of the different astaxanthin levels shown in Figures F.8(a) and F.8(b). The weight of the PLSR coefficients also corresponds well with the primary absorbance peaks found of around 450 – 505 nm in previous studies of astaxanthin, and both PLSR and EN coefficients correspond well with the secondary absorption peaks of around 500 – 600 nm and 870 nm. This also corresponds to the spectroscopy results in Figure F.7(a).

Since the PLSR component weights are somewhat clustered to the above-mentioned regions, it makes sense to use these regions for making optical filters for an industrial inspection system. The weights of the EN coefficients are clustered in two main parts with opposite signs in the visual range for both modalities, which suggests that the prediction in future could be made using two optical filters.

Optical filters can make the equipment cheaper and faster for industrial quality inspection of astaxanthin. The optimum design of such filters can be estimated by using sparse methods such as EN or filter-focused methods [261, 242, 47].

For the EN results it can be seen that the RPD increases with the number of coefficients. While more coefficients in some cases can increase the result, it also enables EN to select different clusters of correlated variables.

To directly compare the performance of the two vision systems, the overlapping 16 bands from the two were used for prediction and the results are presented in Table F.3. The VideometerLab data show a prediction error of 13 ppm, while the SuperK have a prediction error of 4 ppm. This is too high for the industry and thus means that many spectral bands are important for a result with high accuracy for this particular prediction problem.

The SEP for the VideometerLab is about 5-8 ppm of synthetic astaxanthin concentration using PLSR and EN, and the SEP for SuperK with 3 PLSR components is about 3.7 ppm, which means that the error is larger than the smallest level of synthetic astaxanthin; 3.125 ppm. This means that the VideometerLab results are uncertain for this particular level; perhaps this is the limit of the used system. It can be noted that there is an overlap between the smallest astaxanthin concentration levels seen in the PCA plots in Figure F.9(a) and F.9(b).

Both PLSR and EN perform well for the prediction problem presented. However, the EN prediction model (coefficients) is more interpretable than the PLSR model (components); compare Figures F.13(a) and F.13(b) with Figures F.15(a) and F.15(b). While PLSR includes all spectral bands in several components in the prediction model, though weighted, EN selects just a few spectral bands which make the model easier to interpret and also makes it possible to use a low number of spectral bands.

For testing the generalisation of the PLSR prediction model, a validation scheme here called GFCV was used for leaving out one concentration level at a time for validation. This gives an indication on how the prediction behaves for unseen concentration levels. It is natural to expect a somewhat higher error in this case since the model has not been trained on all concentration levels. However, the generalisation result of GFCV is considered a more honest result than by using LOOCV. It is shown that the pooled prediction error of GFCV is much larger than the corresponding error of LOOCV for both systems, see Table F.4. The large difference in prediction error implies that the LOOCV scheme in combination with data with many variables compared to the number of samples, gives some over-fitting. This can also be assumed from the very optimistic results of both PLSR and EN for the SuperK data with 113 variables, compared to the

VideometerLab's 20 variables. The optimistic results by using LOOCV on all concentration levels are partly explained by the fact that the study contained only one production batch. It is clear that as the complexity of the reflection increases, the background may have very different contributions from different chemical compounds that all contribute in the surface reflection.

It is therefore concluded, that in order to make a robust and precise prediction model for synthetic astaxanthin coating concentration it is important to use all target concentration levels, and also that future work examines different production batches.

However, as mentioned previously, HPLC measurements of astaxanthin from fish feed pellets are less accurate than when measuring astaxanthin in oil. A clear difference could be seen in the two measurements of the pellets in Table F.2. Therefore, spectral imaging could be a good complement for screening of synthetic astaxanthin coating.

Conclusions

A new instrument for hyper-spectral imaging, the SuperK set-up, based on a spectral broad laser light source, was introduced together with a parallel study with the commercially available multi-spectral VideometerLab imaging system. We have shown that the new SuperK system can be used for chemical surface inspection using hyper-spectral image analysis.

The results show that it is possible to predict the synthetic astaxanthin concentration in the coating well enough for quality control using either multi- or hyper-spectral image analysis. Results also show that the SuperK set-up performs with higher accuracy than the VideometerLab for predicting the synthetic astaxanthin concentration in the pellets, while the VideometerLab performs well enough for quality control. The results were obtained by only measuring surface reflections, which in combination with the good results implies that the methods can be used in general for quality inspection of various coating substances using similar coating methods.

In addition, the higher spectral resolution of the SuperK system combined with sparse statistics for analysing the signals, made it possible to identify the most significant spectral regions for the particular detection of astaxanthin. This is of interest for a simple and robust commercial system.

Acknowledgements

The work presented has received funding from BioMar A/S and the EU under the Seventh Framework Programme FP7/2007-2013 under grant agreement number 214505.10. This work was in part financed by the Centre for Imaging Food Quality project which is funded by the Danish Council for Strategic Research (contract no 09-067039) within the Programme Commission on Health, Food and Welfare. The expert technical assistance of Heidi Olander Petersen is gratefully acknowledged.

Bibliography

[1] O. H. A. Nielsen, A. L. Dahl, R. Larsen, F. Møller, F. D. Nielsen, C. L. Thomsen, H. Aanæs, and J. M. Carstensen, "Supercontinuum light sources for hyperspectral subsurface laser scattering," *The Scandinavian Conference on Image Analysis - Proceedings*, pp. 327–337, 2011.

[2] J. L. Skytte, O. H. A. Nielsen, U. Andersen, F. Møller, J. M. Carstensen, A. B. Dahl, and R. Larsen, "Monitoring structure formation during milk acidification using hyperspectral diffuse reflectance images," *Submitted to Journal of Spectral Imaging*, 2014.

[3] O. H. A. Abildgaard, F. Kamran, A. L. Dahl, J. L. Skytte, F. D. Nielsen, C. L. Thomsen, P. E. Andersen, R. Larsen, and J. Frisvad, "Non-invasive assessment of dairy products using spatially resolved diffuse reflectance spectroscopy," *Submitted to Applied Spectroscopy*, vol. -, pp. –, 2014.

[4] O. H. A. Nielsen, A. A. Subash, F. D. Nielsen, A. B. Dahl, J. L. Skytte, S. Andersson-Engels, and D. Khoptyar, "Spectral characterisation of dairy products using photon time-of-flight spectroscopy," *Journal of Near Infrared Spectroscopy*, vol. 21, pp. 375–383, 2013.

[5] O. H. A. Nielsen, F. D. Nielsen, C. L. Thomsen, S. Anderson-Engels, and D. Khoptyar, "Evaluation of the id220 single photon avalanche diode for extended spectral range photon time of flight spectroscopy," tech. rep., Technical University of Denmark, 2014.

[6] M. G. Ljungqvist, O. H. A. Nielsen, S. Frosch, M. E. Nielsen, L. H. Clemmensen, and B. K. Ersboll, "Hyperspectral imaging based on diffused laser light for prediction of astaxanthin coating concentration," *Machine Vision and Applications*, vol. 25, no. 2, pp. 327–343, 2014.

[7] F. Kamran, O. H. A. Nielsen, A. Sparén, O. Svensson, J. Johansson, and S. Anderson-Engels, "Spectroscopic analysis of pharmaceuticals in the close NIR range using PToF spectroscopy," *Submitted: Applied Spectroscopy*, 2014.

[8] M. V. Kristensen, P. Ahrendt, T. B. Lindballe, O. H. A. Nielsen, A. P. Kylling, H. Karstoft, A. Imparato, L. Hosta-Rigau, B. Stadler, H. Stapelfeldt, and S. R. Keiding, "Motion analysis of optically trapped particles and cells using 2D Fourier analysis," *Optics Express*, vol. 20, no. 3, pp. 1953–1962, 2012.

[9] Y. Miroshnychenko, O. Nielsen, A. Thorsen, and M. Drewsen, "Profiling of micrometer-sized laser beams in restricted volumes," *Applied Optics*, vol. 51, no. 13, pp. 2341–2345, 2012.

[10] F. Kamran, O. Nielsen, S. Andersson-Engels, and D. Khoptyar, "Broadband photon time of flight spectroscopy: advanced spectroscopic analysis for ensuring safety and performance of pharmaceutical tablets," in *ACP/IPOC 2013*, Optical Society of America, 2013.

[11] D. Khoptyar, A. A. Subash, M. Saleem, O. H. A. Nielsen, and S. Andersson-Engels, "Wide-bandwidth photon time of flight spectroscopy for biomedical and pharmaceutical applications," in *NIR 2013 - 16th International Conference on Near Infrared Spectroscopy*, 2013.

[12] J. L. Skytte, O. H. A. Nielsen, U. Andersen, J. M. Carstensen, A. L. Dahl, R. Larsen, F. Møller, F. Kamran, and J. R. Frisvad, "Decomposition of diffuse reflectance images - features for monitoring structure in turbid media," *Proceedings of the InsideFood Symposium 2013*, 2013.

[13] J. Skytte, U. Andersen, F. Møller, O. Nielsen, J. Carstensen, A. Dahl, and R. Larsen, *Monitoring structure development in milk acidification using diffuse reflectance profiles.* University of Copenhagen, 2012.

[14] S. Sharifzadeh, J. Skytte, O. Nielsen, B. Ersboll, and L. Clemmensen, "Regression and sparse regression methods for viscosity estimation of acid milk from it's sls features," in *Systems, Signals and Image Processing (IWSSIP), 2012 19th International Conference on*, pp. 52–55, 2012.

[15] O. H. A. Nielsen, A. L. Dahl, R. Larsen, F. Møller, F. D. Nielsen, C. L. Thomsen, H. Aanæs, and J. M. Carstensen, "In depth analysis of food structures, hyperspectral subsurface laser scattering," in *Proceesings of Scandinavian Workshop on Imaging Food Quality, Ystad, Sweden*, pp. 27–32, 2011.

[16] C. Soukoulis, P. Panagiotidis, R. Koureli, and C. Tzia, "Industrial yogurt manufacture: Monitoring of fermentation process and improvement of final product quality," *Journal of Dairy Science*, vol. 90, pp. 2641–2654, 2007.

[17] C. Fagan, M. Castillo, C. O'Donnell, D. O'Callaghan, and F. Payne, "On-line prediction of cheese making indices using backscatter of near infrared light," *International Dairy Journal*, vol. 18, no. 2, pp. 120 – 128, 2008.

[18] F. Harte, L. Luedecke, B. Swanson, and G. V. Barbosa-Canovas, "Low-fat set yogurt made from milk subjected to combinations of high hydrostatic pressure and thermal processing," *Journal of Dairy Science*, vol. 86, no. PART 4, pp. 1074–1082, 2003.

[19] I. C. Torres, T. Janhoj, B. O. Mikkelsen, and R. Ipsen, "Effect of microparticulated whey protein with varying content of denatured protein on the rheological and sensory characteristics of low-fat yoghurt," *International Dairy Journal*, vol. 21, no. 9, pp. 645–655, 2011.

[20] W. J. Lee and J. A. Lucey, "Formation and physical properties of yoghurt," *Asian-Aust. J. Anim. Sci.*, vol. 23, no. 9, pp. 1127–1136, 2010.

[21] D. Horne and D. Dalgleish, "A photon correlation spectroscopy study of size distributions of casein micelle suspensions," *European Biophysics Journal*, vol. 11, no. 4, pp. 249–258, 1985.

[22] A. Haque, R. K. Richardson, and E. R. Morris, "Effect of fermentation temperature on the rheology of set and stirred yogurt," *Food Hydrocolloids*, vol. 15, no. NO 4-6, pp. 593–602, 2000.

[23] M. Auty, M. Fenelon, T. Guinee, C. Mullins, and D. Mulvihill, "Dynamic confocal scanning laser microscopy methods for studying milk protein gelation and cheese melting," *Scanning*, vol. 21, no. 5, pp. 299–304, 1999.

[24] F. G. C. Bijnen, H. van Aalst, P. Baillif, J. C. G. Blonk, D. Kersten, F. Kleinherenbrink, R. Lenke, and M. M. vander Stappen, "In-line structure measurement of food products," *Powder Technology*, vol. 124, no. 3, pp. 188–194, 2002.

[25] T. Janhøj, C. B. Petersen, M. B. Frøst, and R. Ipsen, "Sensory and rheological characterization of low-fat stirred yogurt," *Journal of Texture Studies*, vol. 37, no. 3, pp. 276–299, 2006.

[26] D. O'Callaghan, C. O'Donnell, and F. Payne, "On-line sensing techniques for coagulum setting in renneted milks," *Journal of Food Engineering*, vol. 43, no. 3, pp. 155 – 165, 2000.

[27] F. Payne, C. Hicks, P.-S. Shen, and Payne, "Predicting optimal cutting time of coagulating milk using diffuse reflectance," *Journal of Dairy Science*, vol. 76, no. 1, pp. 48 – 61, 1993.

[28] C. C. Fagan, M. Castillo, F. A. Payne, C. P. O'Donnell, M. Leedy, and D. J. O'Callaghan, "Novel online sensor technology for continuous monitoring of milk coagulation and whey separation in cheesemaking," *Journal of Agricultural and Food Chemistry*, vol. 55, no. 22, pp. 8836–8844, 2007.

[29] M. Castillo, J. Lucey, and F. Payne, "The effect of temperature and inoculum concentration on rheological and light scatter properties of milk coagulated by a combination of bacterial fermentation and chymosin. cottage cheese-type gels," *International Dairy Journal*, vol. 16, no. 2, pp. 131–146, 2006.

[30] M. J. Mateo, D. J. O'Callaghan, C. D. Everard, M. Castillo, F. A. Payne, and C. P. O'Donnell, "Evaluation of on-line optical sensing techniques for monitoring curd moisture content and solids in whey during syneresis," *Food Research International*, vol. 43, no. 1, pp. 177 – 182, 2010.

[31] D. Saputra, F. Payne, R. Lodder, and S. Shearer, "Selection of near-infrared wavelengths for monitoring milk coagulation using principal component analysis," *Transactions of the ASAE*, vol. 35, no. 5, pp. 1597–1605, 1992.

[32] J. M. Carstensen, F. Møller, and J. Frisvad, "Online monitoring of food processes using subsurface laser scattering," *Advances in process analytics and control technologies APACT*, pp. 5–7, 2009.

[33] M. Alexander, M. Corredig, and D. G. Dalgleish, "Diffusing wave spectroscopy of gelling food systems: The importance of the photon transport mean free path ($l*$) parameter," *Food Hydrocolloids*, vol. 20, pp. 325–331, March–May 2006.

[34] M. Renan, V. Arnoult-Delest, D. Paquet, G. Brule, and M.-H. Famelart, "Changes in the rheological properties of stirred acid milk gels as induced by the acidification procedure," *Dairy Science and Technology*, vol. 88, no. 3, pp. 341–353, 2008.

[35] F. Møller, R. Larsen, and J. M. Carstensen, *Imaging Food Quality.* PhD thesis, Technical University of Denmark, Department of Informatics and Mathematical Modeling, 2013.

[36] J. L. Skytte, *2D Static Light Scattering for Dairy Based Applications.* PhD thesis, Technical University of Denmark, 2014.

[37] T. R. Gormley, "A note on consumer preference of smoked salmon colour.," *Irish Journal of Agricultural and Food Research*, vol. 31, no. 2, pp. 199–202, 1992.

[38] J. Ostrander, C. Martinsen, J. Liston, and J. McCullough, "Sensory testing of pen-reared salmon and trout.," *Journal of Food Science*, vol. 41, no. 2, pp. 386–390, 1976.

[39] S. Sigurgisladottir, C. Parrish, S. Lall, and R. Ackman, "Effects of feeding natural tocopherols and astaxanthin on atlantic salmon (salmo salar) fillet quality," *Food Research International*, vol. 27, no. 1, pp. 23–32, 1994.

[40] M. A. Ritenour, J. Qin, X. Zhao, and T. F. Burks, "Effect of fruit harvest time on citrus canker detection using hyperspectral reflectance imaging," *Sensing and Instrumentation for Food Quality and Safety*, vol. 4, no. 3, pp. 126–135, 2010.

[41] L. Clemmensen and B. Ersbøll, *Data analysis in high-dimensional sparse spaces*. PhD thesis, DTU Informatics and Mathematical Modelling, 2010.

[42] L. H. Clemmensen, M. E. Hansen, J. C. Frisvad, and B. K. Ersbøll, "A method for comparison of growth media in objective identification of penicillium based on multi-spectral imaging," *Journal of Microbiological Methods*, vol. 69, no. 2, pp. 249–255, 2007.

[43] B. S. Dissing, M. E. Nielsen, B. K. Ersbøll, and S. Frosch, "Multispectral imaging for determination of astaxanthin concentration in salmonids," *PLoS One*, vol. 6, no. 5, p. Article No.: e19032, 2011.

[44] D. D. Gomez, L. H. Clemmensen, B. K. Ersbøll, and J. M. Carstensen, "Precise acquisition and unsupervised segmentation of multi-spectral images," *Computer Vision and Image Understanding*, vol. 106, no. 2-3, pp. 183–193, 2007.

[45] M. E. Hansen, B. K. Ersbøll, J. M. Carstensen, and A. A. Nielsen, "Estimation of critical parameters in concrete production using multispectral vision technology," *Lecture Notes in Computer Science*, pp. 1228–1237, 2005.

[46] M. G. Ljungqvist, B. S. Dissing, M. E. Nielsen, B. K. Ersbøll, L. H. Clemmensen, and S. Frosch, "Classification of astaxanthin colouration of salmonid fish using spectral imaging and tricolour measurement," Technical Report 08, Technical University of Denmark, Informatics, 2012.

[47] S. Nakauchi, K. Nishino, and T. Yamashita, "Selection of optimal combinations of band-pass filters for ice detection by hyperspectral imaging," *Optics Express*, vol. 20, no. 2, pp. 986–1000, 2012.

[48] J. M. Eichenholz and J. Dougherty, "Ultracompact fully integrated megapixel multispectral imager," *Integrated Optics: Devices, Materials, and Technologies XIII*, vol. 7218, pp. –, 2009.

[49] G. Themelis, J. S. Yoo, and V. Ntziachristos, "Multispectral imaging using multiple-bandpass filters," *Optics Letters*, vol. 33, no. 9, pp. 1023–1025, 2008.

[50] A. Merdasa, M. Brydegaard, S. Svanberg, and J. T. Zoueu, "Staining-free malaria diagnostics by multispectral and multimodality light-emitting-diode microscopy," *Journal of Biomedical Optics*, vol. 18, no. 3, pp. 036002–036002, 2013.

[51] M. E. Gehm, M. S. Kim, C. Fernandez, and D. J. Brady, "High-throughput, multiplexed pushbroom hyperspectral microscopy," *Optics Express*, vol. 16, no. 15, pp. 11032–11043, 2008.

[52] M. Arngren, P. W. Hansen, B. Eriksen, J. Larsen, and R. Larsen, "Analysis of pre-germinated barley using hyperspectral image analysis," tech. rep., Technical University of Denmark, 2011.

[53] N. Haala, D. Fritsch, D. Stallimann, and M. Cramer, "On the performance of digital airborne pushbroom cameras for photogrammetric data processing - a case study," in *Int'l Archives of Photogrammetry and Remote Sensing*, pp. 324–331, 2000.

[54] J. Qin, R. Lus, and Qin, "Measurement of the absorption and scattering properties of turbid liquid foods using hyperspectral imaging," *Applied Spectroscopy*, vol. 61, pp. 388–396, Apr 2007.

[55] S. C. Gebhart, D. L. Stokes, T. Vo-Dinh, and A. Mahadevan-Jansen, "Instrumentation considerations in spectral imaging for tissue demarcation: comparing three methods of spectral resolution," *Proceedings of SPIE*, vol. 5694, pp. 41–52, 2005.

[56] J. Katrasnik, F. Pernus, and B. Likar, "Illumination system characterization for hyperspectral imaging," *Proceedings of SPIE*, vol. 7891, p. 7891 0T, 2011.

[57] F. Pernuš, M. Bürmen, and B. Likar, "Spectral characterization of near-infrared acousto-optic tunable filter (aotf) hyperspectral imaging systems using standard calibration materials," *Applied Spectroscopy*, vol. 65, no. 4, pp. 393–401, 2011.

[58] S. N. Jha, "Near infrared spectroscopy," *Nondestructive Evaluation of Food Quality: Theory and Practice*, pp. 141–212, 2010.

[59] B. G. Osborne, "Near-infrared spectroscopy in food analysis," *Encyclopedia of Analytical Chemistry*, 1986. Encyclopedia of Analytical Chemistry Edited by Robert A. Meyers. Ó John Wiley & Sons Ltd, Chichester. ISBN 0471 97670 9.

[60] B. H. Bransden and C. J. Joachain, *Physics of Atoms and Molecules*. Pearson Education Limited, 2003.

[61] R. Tsenkova, S. Atanassova, K. Toyoda, Y. Ozaki, K. Itoh, and T. Fearn, "Near-infrared spectroscopy for dairy management: Measurement of unhomogenized milk composition," *Journal of dairy science*, vol. 82, pp. 2344–2351, November 1999.

[62] G. Bittante and A. Cecchinato, "Genetic analysis of the Fourier-transform infrared spectra of bovine milk with emphasis on individual wavelengths related to specific chemical bonds," *Journal of Dairy Science*, vol. 96, no. 9, pp. 5991 – 6006, 2013.

[63] L. Xu, S.-M. Yan, C.-B. Cai, Z.-J. Wang, and X.-P. Yu, "The feasibility of using near-infrared spectroscopy and chemometrics for untargeted detection of protein adulteration in yogurt: Removing unwanted variations in pure yogurt," *Journal of Analytical Methods in Chemistry*, p. 9, 2013.

[64] M. G. Ljungqvist, *Multivariate image analysis for quality inspection in fish feed production*. IMM-PHD-2012, Technical University of Denmark, 2012.

[65] M.-C. Michalski, V. Briard, and F. Michel, "Optical parameters of milk fat globules for laser light scattering measurements," *Le Lait*, vol. 81, no. 6, pp. 787–796, 2001.

[66] M. I. Mishchenko, "Gustav Mie and the fundamental concept of electromagnetic scattering by particles: A perspective," *Journal of Quantitative Spectroscopy and Radiative Transfer*, vol. 110, no. 16-16, p. 1210, 2009.

[67] T. J. Farrell, M. S. Patterson, and B. Wilson, "A diffusion theory model of spatially resolved, steady-state diffuse reflectance for the noninvasive determination of tissue optical properties in vivo," *Medical Physics*, vol. 19, no. 4, pp. 879–888, 1992.

[68] H. W. Jensen, S. R. Marschner, M. Levoy, and P. Hanrahan, "A practical model for subsurface light transport," in *Proceedings of the 28th annual conference on Computer graphics and interactive techniques*, SIGGRAPH '01, (New York, NY, USA), pp. 511–518, ACM, 2001.

[69] L. G. Henyey and J. L. Greenstein, "Diffuse radiation in the galaxy," *Astrophysical Journal*, vol. 93, pp. 70–83, 1941.

[70] J. R. Frisvad, N. J. Christensen, and H. W. Jensen, "Computing the scattering properties of participating media using Lorenz-Mie theory," *ACM Transactions on Graphics (Proceedings of ACM SIGGRAPH 2007)*, vol. 26, p. Article 60, July 2007.

[71] B. D. Cameron, Y. Li, and A. Nezhuvingal, "Determination of optical scattering properties in turbid media using Mueller matrix imaging," *Journal of Biomedical Optics*, vol. 11, no. 5, pp. 054031–054031–8, 2006.

[72] B. M. Agrawal and M. Mengüç, "Forward and inverse analysis of single and multiple scattering of collimated radiation in an axisymmetric system," *International Journal of Heat and Mass Transfer*, vol. 34, no. 3, pp. 633 – 647, 1991.

[73] G. Iadarola, C. Forestiere, L. D. Negro, F. Villone, and G. Miano, "GPU-accelerated T-matrix algorithm for light-scattering simulations," *Journal of Computational Physics*, vol. 231, no. 17, pp. 5640 – 5652, 2012.

[74] B. S. Meland, *An investigation into particle shape effects on the light scattering properties of mineral dust aerosol.* PhD thesis, University of Iowa, 2011.

[75] F. Bevilacqua and C. Depeursinge, "Monte Carlo study of diffuse reflectance at source-detector separations close to one transport mean free path," *Journal of the Optical Society of America A*, 1999.

[76] M. R. Hajihashemi and H. Jiang, "An inverse light scattering technique for morphological characterization of irregular particles based on the Gaussian-random-sphere model," *Journal of the Optical Society of America A*, vol. 29, pp. 1124–1131, Jun 2012.

[77] C. Li, S. R. Grobmyer, N. Massol, X. Liang, Q. Zhang, L. Chen, L. L. Fajardo, and H. Jiang, "Noninvasive in vivo tomographic optical imaging of cellular morphology in the breast: Possible convergence of microscopic pathology and macroscopic radiology," *Medical Physics*, vol. 35, no. 6, pp. 2493–2501, 2008.

[78] R. Graaff, J. G. Aarnoudse, J. R. Zijp, P. M. A. Sloot, F. F. M. de Mul, J. Greve, and M. H. Koelink, "Reduced light-scattering properties for mixtures of spherical particles: a simple approximation derived from mie calculations," *Applied Optics*, vol. 31, pp. 1370–1376, Apr 1992.

[79] X. Wang, B. W. Pogue, S. Jiang, H. Dehghani, X. Song, S. Srinivasan, B. A. Brooksby, K. D. Paulsen, C. Kogel, S. P. Poplack, and W. A. Wells, "Image reconstruction of effective Mie scattering parameters of breast tissue in vivo with near-infrared tomography," *Journal of Biomedical Optics*, vol. 11, no. 4, pp. 1–13, 2006.

[80] D. Gillespie, "The mathematics of Brownian motion and Johnson noise," *American Journal of Physics*, vol. 64, no. 3, pp. 225–240, 1996.

[81] J. Pope and B. CHU, "A laser light scattering study on molecular weight distribution of linear polyethylene," *Macromolecules*, vol. 17, no. 12, pp. 2633–2640, 1984.

[82] T. Lindbergh, M. Larsson, I. Fredriksson, and T. Strömberg, "Reduced scattering coefficient determination by non-contact oblique angle illumination: methodological considerations," *Proceedings of SPIE, Optical Interactions with Tissue and Cells XVIII*, vol. 6435, pp. 64350I–64350I–12, 2007.

[83] S. Sharifzadeh, J. Skytte, L. Clemmensen, and B. Ersboll, "DCT-based characterization of milk products using diffuse reflectance images," in *The 18th International Conference on Digital Signal Processing (DSP)*, pp. 1–6, July 2013.

[84] S.-P. Lin, L. Wang, S. L. Jacques, and F. K. Tittel, "Measurement of tissue optical properties by the use of oblique-incidence optical fiber reflectometry," *Applied Optics*, vol. 36, pp. 136–143, Jan 1997.

[85] J. Ripoll, D. Yessayan, G. Zacharakis, and V. Ntziachristos, "Experimental determination of photon propagation in highly absorbing and scattering media," *Journal of the Optical Society of America A*, vol. 22, pp. 546–551, March 2005.

[86] L. V. Wang and H.-I. Wu, *Biomedical Optics: Principles and Imaging.* Wiley, 2007.

[87] F. Martelli, S. Del Bianco, A. Ismaelli, and G. Zaccanti, *Light propagation through biological tissue and other diffusive media: theory, solutions, and software.* SPIE Press Bellingham, 2010.

[88] A. Liemert and A. Kienle, "Exact and efficient solution of the radiative transport equation for the semi-infinite medium," *Scientific Reports*, vol. 3, pp. 1–7, 2013.

[89] Flock, Patterson, Wilson, and Wyman, "Monte carlo modeling of light propagation in highly scattering tissues. i. model predictions and comparison with diffusion theory," *IEEE Transactions on Biomedical Engineering*, vol. 36, no. 12, pp. 1162–1168, 1989.

[90] A. T. Eggebrecht, H. Dehghani, J. P. Culver, and Y. Zhan, "Image quality analysis of high-density diffuse optical tomography incorporating a subject-specific head model," *Frontiers in Neuroenergetics*, vol. 4, no. MAY, pp. –, 2012.

[91] A. Garcia-Üribe, *Non-Invasice Optical Detection of Epithelial Cancer using Oblique Incidence Diffuse Reflectance Spectroscopy.* PhD thesis, Texas A&M University, 2009.

[92] Q. Liu and C. Zhu, "Review of Monte Carlo modeling of light transport in tissues," *Journal of Biomedical Optics*, vol. 18, no. 5, pp. –, 2013.

[93] P. Thueler, I. Charvet, F. Bevilacqua, M. S. Ghislain, G. Ory, P. Marquet, P. Meda, B. Vermeulen, and C. Depeursinge, "In vivo endoscopic tissue diagnostics based on spectroscopic absorption, scattering, and phase function properties," *Journal of Biomedical Optics*, vol. 8, no. 3, pp. 495–503, 2003.

[94] E. Alerstam, S. Andersson-Engels, and T. Svensson, "Improved accuracy in time-resolved diffuse reflectance spectroscopy," *Optics Express*, vol. 16, pp. 10440–10454, Jul 2008.

[95] E. Alerstam, S. Andersson-Engels, and T. Svensson, "White Monte Carlo for time-resolved photon migration," *Journal of Biomedical Optics*, vol. 13, no. 4, pp. 041304–041304–10, 2008.

[96] E. Alerstam, *Optical spectroscopy of turbid media: time-domain measurements and accelerated Monte Carlo modelling*. PhD thesis, Lund University, 2011.

[97] L. Wang, S. Jacques, and L. Zheng, "MCML - Monte-Carlo modeling of light transport in multilayered tissues," *Computer Methods and Programs in Biomedicine*, vol. 47, no. 2, pp. 131–146, 1995.

[98] F. Martelli, D. Contini, A. Taddeucci, and G. Zaccanti, "Photon migration through a turbid slab described by a model based on diffusion approximation. ii. comparison with Monte Carlo results," *Applied Optics*, vol. 36, pp. 4600–4612, Jul 1997.

[99] L. V. Wang and S. L. Jacques, "Source of error in calculation of optical diffuse reflectance from turbid media using diffusion theory," *Computer Methods and Programs in Biomedicine*, vol. 61, no. 3, pp. 163 – 170, 2000.

[100] Y. Chen, L. Cao, and L. Sun, "Asymmetric diffusion model for oblique-incidence reflectometry," *Chinese Optics Letters*, vol. 9, p. 101701, Oct 2011.

[101] R. J. Zemp, "Phase-function corrected diffusion model for diffuse reflectance of a pencil beam obliquely incident on a semi-infinite turbid medium," *Journal of Biomedical Optics*, vol. 18, no. 6, pp. 067005–067005, 2013.

[102] T. Svensson, *Pharmaceutical and Biomedical Applications of Spectroscopy in the Photon Migration Regime*. PhD thesis, Lund University, 2008.

[103] L. Wang and S. L. Jacques, "Use of a laser beam with an oblique angle of incidence to measure the reduced scattering coefficient of a turbid medium," *Applied Optics*, vol. 34, pp. 2362–2366, May 1995.

[104] K.-B. Sung and H.-H. Chen, "Enhancing the sensitivity to scattering coefficient of the epithelium in a two-layered tissue model by oblique optical fibers: Monte Carlo study," *Journal of Biomedical Optics*, vol. 17, no. 10, pp. 107003–107003, 2012.

[105] J. C. Ranasinghesagara and R. J. Zemp, "Combined photoacoustic and oblique-incidence diffuse reflectance system for quantitative photoacoustic imaging in turbid media," *Journal of Biomedical Optics*, vol. 15, no. 4, pp. 046016–046016–5, 2010.

[106] A. Garcia-Üribe, K. Balareddy, J. Zou, and L. Wang, "Micromachined fiber optical sensor for in vivo measurement of optical properties of human skin," *IEEE Sensors Journal*, vol. 8, no. 10, pp. 1698–1703, 2008.

[107] A. Garcia-Üribe, E. B. Smith, J. Zou, M. Duvic, V. Prieto, and L. V. Wang, "In-vivo characterization of optical properties of pigmented skin lesions including melanoma using oblique incidence diffuse reflectance spectrometry," *Journal of Biomedical Optics*, vol. 16, no. 2, pp. 020501–020501–3, 2011.

[108] D. C. Montgomery, *Design and analysis of experiments*. Wiley. com, 2006.

[109] T. Hastie, R. Tibshirani, and J. Friedman, *The Elements of Statistical Learning: Data Mining, Inference, and Prediction*. Springer, 2nd ed., February 2009.

[110] H. Zou and T. Hastie, "Regularization and variable selection via the elastic net," *Journal of the Royal Statistical Society Series B - Statistical Methodology*, vol. 67, pp. 301–320, 2005.

[111] Alfano and Shapiro, "Emission in the region 4000 to 7000 å via four-photon coupling in glass," *Physical Review Letters*, vol. 24, no. 11, pp. 584–587, 1970.

[112] J. Ranka, R. Windeler, and A. Stentz, "Visible continuum generation in air-silica microstructure optical fibers with anomalous dispersion at 800 nm," *Optics Letters*, vol. 25, no. 1, pp. 25–27, 2000.

[113] C. L. Thomsen, F. D. Nielsen, J. Johansen, C. Pedersen, P. M. Moselund, C. Larsen, O. Bang, U. Mœller, S. T. Sœrensen, and O. Bang, "New horizons for supercontinuum light sources: From uv to mid-ir," *Proceedings of SPIE - the International Society for Optical Engineering*, vol. 8637, p. 86370T, 2013.

[114] J. M. Dudley, G. Genty, and S. Coen, "Supercontinuum generation in photonic crystal fiber," *Reviews of Modern Physics*, vol. 78, no. 4, pp. 1135–1184, 2006.

[115] U. Møller, S. T. Sorensen, C. Larsen, P. M. Moselund, C. Jakobsen, J. Johansen, C. L. Thomsen, and O. Bang, "Optimum PCF tapers for blue-enhanced supercontinuum sources," *Optical Fiber Technology*, vol. 18, no. 5, pp. 304–314, 2012.

[116] L. Wang, S. Sharma, B. Aernouts, H. Ramon, and W. Saeys, "Supercontinuum laser based double-integrating-sphere system for measuring optical properties of highly dense turbid media in the 1300 - 2350 nm region with high sensitivity," *Proceedings of the SPIE - the International Society for Optical Engineering*, vol. 8427, p. 84273B, 2012.

[117] J. Swartling, A. Bassi, C. D'Andrea, A. Pifferi, A. Torricelli, and R. Cubeddu, "Dynamic time-resolved diffuse spectroscopy based on supercontinuum light pulses," *Applied Optics*, vol. 44, no. 22, pp. 4684–4692, 2005.

[118] P. S. Johnston and K. K. Lehmann, "Cavity enhanced absorption spectroscopy using abroadband prism cavity and a supercontinuumsource," *Optics Express*, vol. 16, pp. 15013–15023, Sep 2008.

[119] Brillouin, "Diffusion of light and of X-rays by a transparent homogeneous body," *Annalen Der Physik*, vol. 17, pp. 88–122, 1922.

[120] N. Gupta, "Acousto-optic tunable filters," *Optics and Photonics News*, vol. 8, no. 11, pp. 23–27, 1997.

[121] M. Bass, ed., *Handbook of Optics: Volume II - Design, Fabrication, and Testing; Sources and Detectors; Radiometry and Photometry, Third Edition.* McGraw-Hill Professional: New York, Chicago, San Francisco, Lisbon, London, Madrid, Mexico City, Milan, New Delhi, San Juan, Seoul, Singapore, Sydney, Toronto, 2010.

[122] "Acousto-optic theory application notes," tech. rep., AA Opto Electronic, Orsay, France, 2013.

[123] ISOMET, Springfield, USA, *Acousto Optic Tuneable Filters, Basic Theory And Design Considerations*, 1998.

[124] C. Zhang, Z. Zhang, Y. Yang, and H. Wang, "Design and analysis of a noncollinear acousto-optic tunable filter," *Optics Letters*, vol. 32, no. 16, pp. 2417–2419, 2007.

[125] A. Farina, P. Taroni, A. Pifferi, and I. Bargigia, "Note: Comparison between a prism-based and an acousto-optic tunable filter-based spectrometer for diffusive media," *Review of Scientific Instruments*, vol. 84, no. 1, pp. 1–3, 2013.

[126] ISOMET, Springfield, USA, *Maximizing AO Diffraction efficiency*, 2006.

[127] G. M. Hale and M. R. Querry, "Optical constants of water in the 200-nm to 200-μm wavelength region," *Applied Optics*, vol. 12, no. 3, pp. 555–563, 1973.

[128] A. Gherardi, F. Piccinini, and A. Bevilacqua, "Vignetting correction by exploiting an optical microscopy image sequence," *Proceedings of the Annual International Conference of the IEEE Engineering in Medicine and Biology Society, EMBS*, vol. 2011, pp. 6166–6169, 2011.

[129] F. J. W.-M. Leong, M. Brady, and J. O. McGee, "Correction of uneven illumination (vignetting) in digital microscopy images," *Journal of Clinical Pathology*, vol. 56, no. PART 8, pp. 619–621, 2003.

[130] F. Banterle, A. Artusi, K. Debattista, and A. Chalmers, *Advanced High Dynamic Range Imaging : theory and Practice*. A K Peters, Ltd, 2011.

[131] S. Mann and R. Picard, "Being 'undigital' with digital cameras: Extending dynamic range by combining differently exposed pictures," Tech. Rep. 323, M.I.T. Media Lab Perceptual Computing Section, Boston, Massachusetts, 1994. Also appears, IS&T's 48th annual conference, Cambridge, Massachusetts, May 1995.

[132] M. Robertson, S. Borman, and R. Stevenson, "Estimation-theoretic approach to dynamic range enhancement using multiple exposures," *Journal of Electronic Imaging*, vol. 12, no. 2, pp. 219–228, 2003.

[133] B. Tromberg, L. Svaasand, T. Tsay, and R. Haskell, "Properties of photon density waves in multiple-scattering media," *Applied Optics*, vol. 32, no. 4, pp. 607–616, 1993.

[134] M. Compton, A. Durkin, A. E. Cerussi, E. Gratton, B. J. Tromberg, and A. Leproux, "Assessing tumor contrast in radiographically dense breast tissue using diffuse optical spectroscopic imaging (DOSI)," *Breast Cancer Research*, vol. 15, no. 5, pp. 1–12, 2013.

[135] J. E. Gunther, E. Lim, H. K. Kim, M. Flexman, S. Refice, M. Brown, K. Kalinsky, D. Hershman, and A. H. Hielscher, "Predicting tumor response in breast cancer patients using diffuse optical tomography," *Proceedings of the SPIE - the International Society for Optical Engineering*, vol. 8799, p. 87990P, 2013.

[136] D. Khoptyar, A. A. Subash, S. Johansson, M. Saleem, A. Sparén, J. Johansson, and S. Andersson-Engels, "Broadband photon time-of-flight spectroscopy of pharmaceuticals and highly scattering plastics in the VIS and close NIR spectral ranges," *Optics Express*, vol. 21, pp. 20941–20953, Sep 2013.

[137] T. Svensson, E. Alerstam, M. Einarsdottir, K. Svanberg, and S. Andersson-Engels, "Towards accurate in vivo spectroscopy of the human prostate," *Journal of Biophotonics*, vol. 1, no. 3, pp. 200–203, 2008.

[138] M. Mazurenka, L. Di Sieno, G. Boso, D. Contini, A. Pifferi, A. Dalla Mora, A. Tosi, H. Wabnitz, and R. Macdonald, "A non-contact time-domain scanning brain imaging system: First in-vivo results," *Proceedings of the SPIE - the International Society for Optical Engineering*, vol. 8799, p. 87990L, 2013.

[139] T. Svensson, E. Alerstam, D. Khoptyar, J. Johansson, S. Folestad, and S. Andersson-Engels, "Near-infrared photon time-of-flight spectroscopy of turbid materials up to 1400 nm," *Review of Scientific Instruments*, vol. 80, no. 6, p. 063105, 2009.

[140] M. S. Patterson, B. Chance, and B. C. Wilson, "Time resolved reflectance and transmittance for the non-invasive measurement of tissue optical properties," *Applied Optics*, vol. 28, pp. 2331–2336, Jun 1989.

[141] C. Abrahamsson, T. Svensson, S. Svanberg, S. Andersson-Engels, J. Johansson, and S. Folestad, "Time and wavelength resolved spectroscopy of turbid media using light continuum generated in a crystal fiber," *Optics Express*, vol. 12, pp. 4103–4112, Aug 2004.

[142] C. Abrahamsson, *Time-Resolved Spectroscopy for Pharmaceutical Applications*. PhD thesis, Lund Institute of Technology, Department of Physics, 2005.

[143] J. Dudley, X. Gu, L. Xu, M. Kimmel, E. Zeek, P. O'Shea, R. Trebino, S. Coen, and R. Windeler, "Cross-correlation frequency resolved optical gating analysis of broadband continuum generation in photonic crystal fiber: simulations and experiments," *Optics Express*, vol. 10, no. 21, pp. 1215–1221, 2002.

[144] A. A. Subash, "Wide-bandwidth time-of-flight spectroscopy of turbid media," Master's thesis, Lund University, 2012.

[145] W. Becker, *The bh TCSPC Handbook*. Becker & Hickl GmbH, Berlin, Germany, 5 ed., 2012.

[146] I. Bargigia, A. Tosi, A. B. Shehata, A. D. Frera, A. Farina, A. Bassi, P. Taroni, A. D. Mora, F. Zappa, and A. Pifferi, "Time-resolved diffuse optical spectroscopy up to 1700 nm using a time-gated InGaAs/InP single-photon avalanche diode," in *Novel Biophotonic Techniques and Applications*, p. 80900U, Optical Society of America, 2011.

[147] N. Ghosh, A. Datta, and P. Gupta, "Diffuse reflectance studies of edible fats," *Applied Spectroscopy*, vol. 56, no. 8, pp. 1094–1097, 2002.

[148] E. Alerstam and T. Svensson, "Observation of anisotropic diffusion of light in compacted granular porous materials," *Physical Review E*, vol. 85, no. 4, pp. –, 2012.

[149] T. Svensson, R. Savo, E. Alerstam, K. Vynck, M. Burresi, and D. S. Wiersma, "Exploiting breakdown of the similarity relation for diffuse light transport: simultaneous retrieval of scattering anisotropy and diffusion constant," *Optics Letters*, vol. 38, no. 4, pp. 437–439, 2013.

[150] K. Takagi, H. Haneishi, N. Tsumura, and Y. Miyake, "Alternative oblique-incidence reflectometry for measuring tissue optical properties," *Optical Review*, vol. 7, no. 2, pp. 164–169, 2000.

[151] Menon, Su, and Grobe, "Determination of g and μ using multiply scattered light in turbid media," *Physical Review Letters*, vol. 94, no. 15, pp. 153904/1–4, 2005.

[152] M. Jäger, F. Foschum, and A. Kienle, "Computation of the optical properties of turbid media from slope and curvature of spatially resolved reflectance curves," *Physics in Medicine and Biology*, vol. 58, no. 15, p. N211, 2013.

[153] J. Qin and R. Lu, "Measurement of the absorption and scattering properties of turbid liquid foods using hyperspectral imaging," *Applied spectroscopy*, vol. 61, no. 4, pp. 388–396, 2007.

[154] P. Fischer and E. J. Windhab, "Rheology of food materials," *Current Opinion in Colloid & Interface Science*, 2010.

[155] P. Sacoto, F. Lanza, H. Suarez, and L. H. Garcia-Rubio, "A novel automatic dilution system for on-line particle size analysis," in *ACS Symposium Series*, vol. 693, pp. 23–29, ACS Publications, 1998.

[156] B. Dissing, L. Clemmesen, H. Lje, B. Ersbœll, and J. Adler-Nissen, "Temporal reflectance changes in vegetables," in *Computer Vision Workshops (ICCV Workshops), 2009 IEEE 12th International Conference on*, pp. 1917–1922, IEEE, 2010.

[157] D.-W. Sun, ed., *Hyperspectral imaging for food quality analysis and control*. Academic Press, 2010.

[158] J. Carstensen, M. Hansen, N. Lassen, P. Hansen, B. Ersbøll, and T. Jørgensen, "Creating surface chemistry maps using multispectral vision technology," in *9th MICCAI - Workshop on Biophotonics Imaging for Diagnostics and Treatment*, IMM-Technical Report-2006-17, 2006.

[159] A. Nielsen, "Spectral mixture analysis: Linear and semi-parametric full and iterated partial unmixing in multi-and hyperspectral image data," *Journal of Mathematical Imaging and Vision*, vol. 15, no. 1, pp. 17–37, 2001.

[160] F. van der Meer, "Imaging spectrometry for geological remote sensing," *Geologie en Mijnbouw*, vol. 77, no. 2, pp. 137–151, 1998.

[161] A. Gowen, C. O'Donnell, P. Cullen, G. Downey, and J. Frias, "Hyperspectral imaging-an emerging process analytical tool for food quality and safety control," *Trends in Food Science & Technology*, vol. 18, no. 12, pp. 590–598, 2007.

[162] M. Kim, Y. Chen, and P. Mehl, "Hyperspectral reflectance and fluorescence imaging system for food quality and safety," *Transactions of the ASAE*, vol. 44, no. 3, pp. 721–729, 2001.

[163] Y. Peng and R. Lu, "Analysis of spatially resolved hyperspectral scattering images for assessing apple fruit firmness and soluble solids content," *Postharvest Biology and Technology*, vol. 48, no. 1, pp. 52–62, 2008.

[164] F. Yasuma, T. Mitsunaga, D. Iso, and S. Nayar, "Generalized assorted pixel camera: Postcapture control of resolution, dynamic range, and spectrum," *Image Processing, IEEE Transactions on*, vol. 19, no. 9, pp. 2241–2253, 2010.

[165] Y. Chen, K. Chao, and M. Kim, "Machine vision technology for agricultural applications," *Computers and Electronics in Agriculture*, vol. 36, no. 173Á/191, 2002.

[166] W. Wang and J. Paliwal, "Near-infrared spectroscopy and imaging in food quality and safety," *Sensing and Instrumentation for Food Quality and Safety*, vol. 1, no. 4, pp. 193–207, 2007.

[167] Y. Peng and R. Lu, "An lctf-based multispectral imaging system for estimation of apple fruit firmness. part 2. selection of optimal wavelengths and development of prediction models.," *Transactions of the ASAE*, vol. 49, no. 1, pp. 269–275, 2006.

[168] J. Gómez-Sanchís, L. Gómez-Chova, N. Aleixos, G. Camps-Valls, C. Montesinos-Herrero, E. Moltó, and J. Blasco, "Hyperspectral system for early detection of rottenness caused by penicillium digitatum in mandarins," *Journal of Food Engineering*, vol. 89, no. 1, pp. 80–86, 2008.

[169] N. Joshi, C. Donner, and H. W. Jensen, "Noninvasive measurement of scattering anisotropy in turbid materials by nonnormal incident illumination," *Optics Letters*, vol. 31, pp. 936–938, Apr 2006.

[170] M. Bourne, *Food texture and viscosity: concept and measurement*. Access Online via Elsevier, 2002.

[171] D. D. Muir and E. A. Hunter, "Sensory evaluation of fermented milks: vocabulary development and the relations between sensory properties and composition and between acceptability and sensory properties," *International Journal of Dairy Technology*, vol. 45, no. 3, pp. 73–80, 1992.

[172] E. R. Vedamuthu, "The yogurt story: past, present and future. iv," *Dairy, food and environmental sanitation*, vol. 11, no. 7, pp. 371–374, 1991.

[173] A. Law, "Effects of heat treatment and acidification on the dissociation of bovine casein micelles," *Journal of Dairy Research*, vol. 63, pp. 35–48, 1996.

[174] W. Lee and J. Lucey, "Structure and physical properties of yogurt gels: Effect of inoculation rate and incubation temperature," *Journal of Dairy Science*, vol. 87, no. 10, pp. 3153–3164, 2004.

[175] A. Tamime and R. Robinson, *Yoghurt: science and technology*. Woodhead Publishing, 1999.

[176] D. J. O'Callaghan, C. P. O'Donnell, and F. Payne, "Review of systems for monitoring curd setting during cheesemaking," *International journal of dairy technology*, vol. 55, no. 2, pp. 65–74, 2002.

[177] C. Fagan, M. Leedy, M. Castillo, F. Payne, C. O'Donnell, and D. O'Callaghan, "Development of a light scatter sensor technology for on-line monitoring of milk coagulation and whey separation," *Journal of Food Engineering*, vol. 83, no. 1, pp. 61 – 67, 2007. Future of Food Engineering - Selected Papers from the 2nd International Symposium of CIGR Section VI on Future of Food Engineering.

[178] R. Mezzenga, P. Schurtenberger, A. Burbidge, and M. Michel, "Understanding foods as soft materials," *Nature materials*, vol. 4, no. 10, pp. 729–740, 2005.

[179] D. Weitz, J. Zhu, D. Durian, H. Gang, and D. Pine, "Diffusing-wave spectroscopy: The technique and some applications," *Physica Scripta*, vol. 1993, no. T49B, p. 610, 1993.

[180] J. Lucey, "Formation and physical properties of milk protein gels," *Journal of Dairy Science*, vol. 85, no. 2, pp. 281 – 294, 2002.

[181] M. Castillo, "Cutting time prediction methods in cheese making," *Encyclopedia of Agricultural, Food, and Biological Engineering; Heldman, D., Ed., Taylor & Francis Group: Boca Raton, FL*, pp. 1–7, 2006.

[182] M. Castillo, F. Payne, C. Hicks, and M. Lopez, "Predicting cutting and clotting time of coagulating goat's milk using diffuse reflectance: effect of ph, temperature and enzyme concentration," *International Dairy Journal*, vol. 10, no. 8, pp. 551–562, 2000.

[183] M. Craft-Jenkins and F. Payne, "Development of a noncontact sensor for monitoring milk coagulation and cutting time prediction in cheese making," *American Society of Agricultural and Biological Engineers Annual International Meeting 2012*, vol. 2, pp. 906–921, 2012.

[184] D. Montgomery, *Design and analysis of experiments*. John Wiley & Sons Inc, 2008.

[185] J. Lucey, M. Tamehana, H. Singh, and P. Munro, "A comparison of the formation, rheological properties and microstructure of acid skim milk gels made with a bacterial culture or glucono-δ-lactone," *Food Research International*, vol. 31, no. 2, pp. 147–155, 1998.

[186] T. Cootes, C. Taylor, D. Cooper, J. Graham, *et al.*, "Active shape models-their training and application," *Computer vision and image understanding*, vol. 61, no. 1, pp. 38–59, 1995.

[187] C. Olson, "On choosing a test statistic in multivariate analysis of variance.," *Psychological Bulletin*, vol. 83, no. 4, p. 579, 1976.

[188] J. Lucey and H. Singh, "Formation and physical properties of acid milk gels: a review," *Food Research International*, vol. 30, no. 7, pp. 529–542, 1997.

[189] I. Sodini, F. Remeuf, S. Haddad, and G. Corrieu, "The relative effect of milk base, starter, and process on yogurt texture: a review," *Critical reviews in food science and nutrition*, vol. 44, no. 2, pp. 113–137, 2004.

[190] C. Phadungath, "The mechanism and properties of acid-coagulated milk gels," *Songklanakarin J Sci Tech*, vol. 27, no. 2, pp. 433–448, 2005.

[191] S. G. Anema, "Effect of temperature and rate of acidification on the rheological properties of acid skim milk gels," *Journal of Food Processing and Preservation*, vol. 32, no. 6, pp. 1016–1033, 2008.

[192] P. Walstra, P. Walstra, J. T. Wouters, and T. J. Geurts, *Dairy science and technology*. CRC press, 2010.

[193] J. Curcio and C. Petty, "The near infrared absorption spectrum of liquid water," *JOSA*, vol. 41, no. 5, pp. 302–302, 1951.

[194] M. Alexander and D. G. Dalgleish, "Application of transmission diffusing wave spectroscopy to the study of gelation of milk by acidification and rennet," *Colloids and Surfaces B: Biointerfaces*, vol. 38, no. 1, pp. 83–90, 2004.

[195] M. Alexander and D. Dalgleish, "Dynamic light scattering techniques and their applications in food science," *Food Biophysics*, vol. 1, no. 1, pp. 2–13, 2006.

[196] W. Labs, "Inline monitoring aids in food safety and quality: What you don't measure could kill your brand," *Food Engineering Magazine*, vol. 85, pp. 51–52, 54, 56–59, May 2013.

[197] M. Navrátil, C. Cimander, and C.-F. Mandenius, "On-line multisensor monitoring of yogurt and filmjölk fermentations on production scale," *Journal of Agricultural and Food Chemistry*, vol. 52, pp. 415–420, February 2004.

[198] A. Garcia-*Ü*ribe, J. Zou, M. Duvic, J. H. Cho-Vega, V. G. Prieto, and L. V. Wang, "*In vivo* diagnosis of melanoma and nonmelanoma skin cancer using oblique incidence diffuse reflectance spectrometry," *Cancer Research*, vol. 72, pp. 2738–2745, 2012.

[199] G. Marquez and L. Wang, "White light oblique incidence reflectometer for measuring absorption and reduced scattering spectra of tissue-like turbid media," *Optics Express*, vol. 1, no. 13, p. 454, 1997.

[200] P. Sun, X. Cao, R. Yang, F. Xie, J. Ding, and F. Zhang, "Basic research on determining optical properties of tissues in vivo by measuring diffuse reflectance with a charge-coupled device," *Optica Applicata*, vol. 3, pp. 541–555, 2011.

[201] A. J. Jääskeläinen, K.-E. Peiponen, and J. A. Räty, "On reflectometric measurement of a refractive index of milk," *Journal of Dairy Science*, vol. 84, pp. 38–43, January 2001.

[202] P. E. Debevec and J. Malik, "Recovering high dynamic range radiance maps from photographs," in *Proceedings of SIGGRAPH 97*, pp. 369–378, August 1997.

[203] S.-P. Lin, "Oblique-incidence fiber-optic reflectometry for measuring absorption and scattering in turbid media," Master's thesis, Rice University, 1996.

[204] O. H. A. Abildgaard, *Broadband optical characterization of material properties*. PhD thesis, Technical University of Denmark, 2014.

[205] S. Chitchian and N. M. Fried, "Near-ir optical properties of canine prostate tissue using oblique-incidence reflectometry," *Photonic Therapeutics and Diagnostics VI*, vol. 7548, no. 1, pp. 75480Z–75480Z–6, 2010.

[206] A. Kienle, F. K. Forster, and R. Hibst, "Influence of the phase function on determination of the optical properties of biological tissue by spatially resolved reflectance," *Optics Letters*, vol. 26, pp. 1571–1573, Oct 2001.

[207] A. V. Kalinin, V. N. Krasheninnikov, and V. N. Krivtsun, "Short wave near infrared spectrometry of back scattering and transmission of light by milk for multi-component analysis," *Journal of Near Infrared Spectroscopy*, vol. 21, pp. 35–41, 2013.

[208] C. Abrahamsson, A. Löwgren, B. Strömdahl, T. Svensson, S. Andersson-Engels, J. Johansson, and S. Folestad, "Scatter correction of transmission near-infrared spectra by photon migration data: Quantitative analysis of solids," *Applied Spectroscopy*, vol. 59, pp. 1381–1387, Nov 2005.

[209] F. Foschum and A. Kienle, "Broadband absorption spectroscopy of turbid media using a dual step steady-state method.," *Journal of Biomedical Optics*, vol. 17, no. 3, p. 037009, 2012.

[210] J. W. Pickering, S. A. Prahl, N. van Wieringen, J. F. Beek, H. J. C. M. Sterenborg, and M. J. C. van Gemert, "Double-integrating-sphere system for measuring the optical properties of tissue," *Applied Optics*, vol. 32, pp. 399–410, Feb 1993.

[211] W. Saeys, M. A. Velazco-Roa, S. N. Thennadil, H. Ramon, and B. M. Nicolaï, "Optical properties of apple skin and flesh in the wavelength range from 350 to 2200 nm," *Applied Optics*, vol. 47, pp. 908–919, Mar 2008.

[212] F. Foschum, M.-T. Heine, and A. Kienle, "Determination of the reduced scattering and absorption coefficients by spatially resolved reflectance and total reflectance measurements," in *Diffuse Optical Imaging III*, p. 80881N, Optical Society of America, 2011.

[213] A. Lin, M. Koike, K. Green, J. Kim, A. Mazhar, T. Rice, F. LaFerla, and B. Tromberg, "Spatial frequency domain imaging of intrinsic optical property contrast in a mouse model of alzheimer's disease," *Annals of Biomedical Engineering*, vol. 39, no. 4, pp. 1349–1357, 2011.

[214] T. D. O' Sullivan, A. E. Cerussi, D. J. Cuccia, and B. J. Tromberg, "Diffuse optical imaging using spatially and temporally modulated light," *Journal of Biomedical Optics*, vol. 17, no. 7, pp. 071311–1–071311–14, 2012.

[215] A. Krainov, A. Mokeeva, E. Sergeeva, S. Zabotnov, and M. Kirillin, "Nanoparticles as contrasting agents in diffuse optical spectroscopy," in *Society of Photo-Optical Instrumentation Engineers (SPIE) Conference Series*, vol. 8699 of *Society of Photo-Optical Instrumentation Engineers (SPIE) Conference Series*, Feb. 2013.

[216] S. Narasimhan, M. Gupta, C. Donner, R. Ramamoorthi, S. Nayar, and H. Jensen, "Acquiring scattering properties of participating media by dilution," *ACM Transactions on Graphics*, vol. 25, 2006.

[217] A. Jääskeläinen, K.-E. Peiponen, and J. Räty, "On reflectometric measurement of a refractive index of milk," *Journal of Dairy Science*, vol. 84, no. 1, pp. 38–43, 2001.

[218] B. W. Pogue and M. S. Patterson, "Review of tissue simulating phantoms for optical spectroscopy, imaging and dosimetry," *Journal of Biomedical Optics*, vol. 11, no. 4, pp. 041102–041102–16, 2006.

[219] K. F. Palmer and D. Williams, "Optical properties of water in the near infrared," *Journal of the Optical Society of America*, vol. 64, pp. 1107–1110, Aug 1974.

[220] A. Pifferi, A. Torricelli, A. Bassi, P. Taroni, R. Cubeddu, H. Wabnitz, D. Grosenick, M. Möller, R. Macdonald, J. Swartling, T. Svensson, S. Andersson-Engels, R. L. P. van Veen, H. J. C. M. Sterenborg, J.-M. Tualle, H. L. Nghiem, S. Avrillier, M. Whelan, and H. Stamm, "Performance assessment of photon migration instruments: the medphot protocol," *Applied Optics*, vol. 44, pp. 2104–2114, Apr 2005.

[221] P. Walstra and R. Jenness, *Dairy Chemistry and Physics*. Wiley Interscience, New York, USA, 1984.

[222] R. Re, D. Contini, M. Caffini, R. Cubeddu, L. Spinelli, and A. Torricelli, "A compact time-resolved system for near infrared spectroscopy based on wavelength space multiplexing," *Review of Scientific Instruments*, vol. 81, pp. 113101–113101–8, Nov 2010.

[223] A. Pifferi, A. Torricelli, L. Spinelli, D. Contini, R. Cubeddu, F. Martelli, G. Zaccanti, A. Tosi, A. Dalla Mora, F. Zappa, and S. Cova, "Time-resolved diffuse reflectance using small source-detector separation and fast single-photon gating," *Physical Review Letters*, vol. 100, p. 138101, Mar 2008.

[224] G. V. Dyatlov, K. V. Gilev, M. A. Yurkin, and V. P. Maltsev, "An optimization method with precomputed starting points for solving the inverse mie problem," *Inverse Problems*, vol. 28, no. 4, p. 045012, 2012.

[225] X. Wang, Pogue, S. Jiang, X. Song, Paulsen, Kogel, Poplack, and Wells, "Approximation of mie scattering parameters in near-infrared tomography of normal breast tissue in vivo," *Journal of Biomedical Optics*, vol. 10, no. 5, pp. 51704–1–8, 2005.

[226] X. Li, Z. Chen, A. Taflove, and V. Backman, "Epuiphase-sphere approximation for analysis of light scattering by arbitrarily shaped nonspherical particles," *Applied Optics*, vol. 43, no. 23, pp. 4497–4505, 2004.

[227] I. Bargigia, A. Tosi, A. B. Shehata, A. D. Frera, A. Farina, A. Bassi, P. Taroni, A. D. Mora, F. Zappa, R. Cubeddu, and A. Pifferi, "Time-resolved diffuse optical spectroscopy up to 1700 nm by means of a time-gated ingaas/inp single-photon avalanche diode," *Applied Spectroscopy*, vol. 66, pp. 944–950, Aug 2012.

[228] T. Lunghi, C. Barreiro, O. Guinnard, R. Houlmann, X. Jiang, M. A. Itzler, and H. Zbinden, "Free-running single-photon detection based on a negative feedback ingaas apd," *Journal of Modern Optics*, vol. 59, no. 17, pp. 1481–1488, 2012.

[229] M. W. Fishburn and E. Charbon, "Monolithic single-photon avalanche diodes: Spads," *Springer Series in Optical Sciences*, vol. 160, pp. 123–157, 2011.

[230] M. A. Itzler, X. Jiang, and M. Entwistle, "Power law temporal dependence of ingaas/inp spad afterpulsing," *Journal of Modern Optics*, vol. 59, no. 17, pp. 1472–1480, 2012.

[231] N. Namekata and S. Inoue, "Afterpulsing-free 80mhz single-photon detection at 1550 nm using an ingaas/inp avalanche photodiode operated with sinusoidal gating," in *Lasers and Electro-Optics, 2007 and the International Quantum Electronics Conference. CLEOE-IQEC 2007. European Conference on*, pp. 1–1, 2007.

[232] Z. Lu, W. Sun, J. Campbell, X. Jiang, and M. Itzler, "Single photon detection with sine gated dual ingaas/inp avalanche diodes," in *Photonics Conference (IPC), 2012 IEEE*, pp. 98–99, 2012.

[233] Z. Yan, D. R. Hamel, A. K. Heinrichs, X. Jiang, M. A. Itzler, and T. Jennewein, "An ultra low noise telecom wavelength free running single photon detector using negative feedback avalanche diode," *Review of Scientific Instruments*, vol. 83, no. 7, pp. –, 2012.

[234] "Tcspc at wavelengths from 900 nm to 1700 nm," tech. rep., Becker & Hickl GmbH, Nahmitzer Damm 30 , 12277 Berlin, Germany. http://www.becker-hickl.com/pdf/id-220-tcspc-04.pdf.

[235] W. Becker and A. Bergmann, *Detectors for High-Speed Photon Counting*. Becker & Hickle.

[236] A. P. Simopoulos, "Omega-3 fatty acids in health and disease and in growth and development," *American Journal of Clinical Nutrition*, vol. 54, pp. 438–463, 1991.

[237] O. Torrisen, R. Hardy, and K. Shearer, "Pigmentation of salmonids - carotenoid deposition and metabolism," *Reviews in Aquatic Sciences*, vol. 1, no. 2, pp. 209–225, 1989.

[238] R. Baker, A.-M. Pfeiffer, F.-J. Schöner, and L. Smith-Lemmon, "Pigmenting efficacy of astaxanthin and canthaxanthin in fresh-water reared atlantic salmon, salmo salar," *Animal Feed Science and Technology*, vol. 99, no. 1-4, pp. 97–106, 2002.

[239] E. Fernandez-Ahumada, J. M. Roger, B. Palagos, J. E. Guerrero, D. Perez-Marin, and A. Garrido-Varo, "Multivariate near-infrared reflection spectroscopy strategies for ensuring correct labeling at feed bagging in the animal feed industry," *Applied Spectroscopy*, vol. 64, no. 1, pp. 83–91, 2010.

[240] G. P. Sabin, M. C. Breitkreitz, A. M. de Souza, P. da Fonseca, L. Calefe, M. Moffa, and R. J. Poppi, "Analysis of pharmaceutical pellets: An approach using near-infrared chemical imaging," *Analytica Chimica Acta*, vol. 706, no. 1, pp. 113–119, 2011.

[241] M. G. Ljungqvist, S. Frosch, M. E. Nielsen, and B. K. Ersbøll, "Multispectral image analysis for robust prediction of astaxanthin coating," *Applied Spectroscopy*, vol. 67, July 2013. Accepted for publication.

[242] M. G. Ljungqvist, K.-i. Kobayashi, S. Frosch, M. E. Nielsen, B. K. Ersbøll, and S. Nakauchi, "Near-infrared hyper-spectral image analysis of astaxanthin concentration in fish feed coating," *Proceedings of the IEEE International Conference on Imaging Systems and Techniques*, pp. 136–141, July 2012. http://dx.doi.org/10.1109/IST.2012.6295524.

[243] N. Scherer, J. E. Jureller, T. Birks, W. Wadsworth, and P. S. J. Russell, "Widely tunable femtosecond pulses from a tapered fiber for ultrafast microscopy and multiphoton applications," in *The Thirteenth International Conference on Ultrafast Phenomena*, p. TuE41, Optical Society of America, 2002.

[244] G. McConnell and E. Riis, "Photonic crystal fibre enables short-wavelength two-photon laser scanning fluorescence microscopy with fura-2," *Physics in Medicine and Biology*, vol. 49, no. 20, p. 4757, 2004.

[245] L. K. H. Clemmensen and B. K. Ersbøll, "Multispectral recordings and analysis of psoriasis lesions," *MICCAI 06 - Workshop on Biophotonics Imaging for Diagnostics and Treatment, October 6, 2006 proceedings, 9th MICCAI Conference*, 2006.

[246] B. Dissing, B. Ersbøll, and J. Adler-Nissen, *New vision technology for multidimensional quality monitoring of food processes*. PhD thesis, Technical University of Denmark (DTU), 2011.

[247] J. M. Carstensen and J. Folm-Hansen, "An apparatus and a method of recording an image of an object, ep1051660," November 2003.

[248] J. Folm-Hansen, *On chromatic and geometrical calibration*. PhD thesis, Technical University of Denmark, 1999.

[249] E. Bligh and W. Dyer, "A rapid method of total lipid extraction and purification," *Canadian Journal of Biochemistry and Physiology*, vol. 37, no. 8, pp. 911–917, 1959.

[250] J. Serra, *Image Analysis and Mathematical Morphology*. Academic Press, London, 1982.

[251] B. S. Dissing, J. M. Carstensen, and R. Larsen, "Multispectral colormapping using penalized least square regression," *Journal of Imaging Science and Technology*, vol. 54, no. 3, pp. 0304011–0304016, 2010.

[252] P. Geladi, H. Isaksson, L. Lindqvist, S. Wold, and K. Esbensen, "Principal component analysis of multivariate images," *Chemometrics and Intelligent Laboratory Systems*, vol. 5, no. 3, pp. 209 – 220, 1989.

[253] A. Rinnan, F. van den Berg, and S. B. Engelsen, "Review of the most common pre-processing techniques for near-infrared spectra," *TrAC Trends in Analytical Chemistry*, vol. 28, no. 10, pp. 1201–1222, 2009.

[254] M. Sjöström, S. Wold, W. Lindberg, J.-Å. Persson, and H. Martens, "A multivariate calibration problem in analytical chemistry solved by partial least-squares models in latent variables," *Analytica Chimica Acta*, vol. 150, pp. 61–70, 1983.

[255] P. C. Williams and D. C. Sobering, "Comparison of commercial near infrared transmittance and reflectance instruments for analysis of whole grains and seeds.," *Journal of Near Infrared Spectroscopy*, vol. 1, no. 1, pp. 25–32, 1993.

[256] L. Nørgaard, A. Saudland, J. Wagner, J. P. Nielsen, L. Munck, and S. B. Engelsen, "Interval partial least-squares regression (ipls): A comparative chemometric study with an example from near-infrared spectroscopy," *Applied Spectroscopy*, vol. 54, no. 3, pp. 413–419, 2000.

[257] K. Sjöstrand, L. H. Clemmensen, R. Larsen, and B. Ersbøll, "Spasm: A matlab toolbox for sparse statistical modeling," *Journal of Statistical Software*, 2006. Accepted for publication 2012.

[258] S. Amarie, U. Förster, N. Gildenhoff, A. Dreuw, and J. Wachtveitl, "Excited state dynamics of the astaxanthin radical cation," *Chemical Physics*, vol. 373, no. 1-2, pp. 8–14, 2010.

[259] M. Buchwald and W. P. Jencks, "Optical properties of astaxanthin solutions and aggregates," *Biochemistry*, vol. 7, no. 2, pp. 834–843, 1968.

[260] J.-P. Yuan and F. Chen, "Identification of astaxanthin isomers in haematococcus lacustris by hplc-photodiode array detection," *Biotechnology Techniques*, vol. 11, no. 7, pp. 455–459, 1997.

[261] K.-i. Kobayashi, K. Nishino, B. S. Dissing, M. Mori, T. Toyota, and S. Nakauchi, "Design of characteristics of optical filter set for prediction and visualization of fat content in raw beef cuts," *Scandinavian Workshop on*

Imaging Food Quality 2011 : Ystad, May 27, 2011 - Proceedings, pp. 23–28, 2011.